QUARTZ-ENHANCED PHOTOACOUSTIC SPECTROSCOPY AND ITS ASSOCIATION WITH FIBER-OPTIC DEVICES

CAO YINGCHUN

Ph.D

The Hong Kong Polytechnic University

2013

The Hong Kong Polytechnic University

Department of Electrical Engineering

QUARTZ-ENHANCED PHOTOACOUSTIC SPECTROSCOPY AND ITS ASSOCIATION WITH FIBER-OPTIC DEVICES

CAO YINGCHUN

A thesis submitted in partial fulfillment of the requirements for the degree of Doctor of Philosophy

August 2012

CERTIFICATE OF ORIGINALITY

I hereby declare that this thesis is my own work and that, to the best of my knowledge and belief, it reproduces no material previously published or written, nor material that has been accepted for the award of any other degree or diploma, except where due acknowledgement has been made in the text.

_____ (Signed)

CAO YINGCHUN (Name of Student)

Abstract

Photoacoustic spectroscopy (PAS), in which the light absorption in analyte is converted into localized heat production and consequent acoustic pressure wave by modulation, is a powerful tool for trace gas detection. Among various acoustic detection techniques, quartz-enhanced photoacoustic spectroscopy (QEPAS), in which a tiny quartz tuning fork (QTF) is employed as acoustic transducer via piezoelectric effect, shows a number of advantages, including high sensitivity, compact size, low cost, and so on, over other methods.

Beginning with a detailed review of the development of PAS, we mainly focused on the gas detection based on QEPAS method and its association with fiber-optic devices in this thesis. The basic principles and theoretical descriptions of QEPAS, including gas absorption line, acoustic generation, resonance and loss mechanism in a cylindric cavity, resonance model of QTF, and wavelength modulation (WM) method, were introduced to provide a theoretical basis for the whole thesis.

We developed a numerical model with finite element method to simulate the multiple physical processes in the spectrophone of QEPAS. The model was calibrated by experimental results and found to be reliable. The position of the laser beam was optimized to be 0.6 mm down from the opening of the QTF gap. With varying resonant tube dimensions, unusual acoustic signal evolution and resonance curves were found. The results were explained by the acoustic coupling and QTF vibration. A set of parameters of spectrophone was suggested for optimal QEPAS gas detection. The numerical model provides an efficient approach in better understanding the acoustic coupling and energy conversion in QEPAS, and demonstrates a theoretical guidance for the spectrophone optimization. The detailed model setup procedure might be also instructive in the simulation of multiple

physical processes.

An experiment of QEPAS gas sensing was carried out by using a near-IR DFB laser. The acoustic signal was amplified by a pair of rigid tubes with optimized dimension and accumulated in a resonant QTF. Considering the property of diode laser, the influence of residual intensity modulation (RIM) on WM was analyzed theoretically and compared with experimental results. It shows that the acoustic signal profile is deformed and an extra phase delay is induced for optimal acoustic detection. By using a DFB laser with an output power of 8.44 mW and a wavelength of 1.53 μm, acetylene detection with a minimum detectable concentration limit of 2 ppm was achieved, corresponding to a normalized noise equivalent absorption (1σ) coefficient of 6.16×10^{-8} cm^{-1} $W/Hz^{1/2}$.

In order to simplify the optical collimating/focusing components in conventional open-path QEPAS, we proposed a novel evanescent-wave photoacoustic spectroscopy (EPAS) by using a tapered optical micro/nano fiber. As the diameter of an optical fiber is reduced to the scale of wavelength or even smaller, a considerable portion of light propagating outside of the fiber can be used to generate an acoustic wave by photoacoustic effect. By using a high sensitive QTF as the acoustic detector, a tapered optical fiber with a diameter of 1.1 μm, passing through the middle of the gap between two prongs of QTF, was demonstrated for EPAS acetylene detection with a comparable normalized acoustic signal with bare-QTF based QEPAS. The normalized noise equivalent absorption coefficient was estimated to be 1.5×10^{-6} cm^{-1} $W/Hz^{1/2}$ and possible enhancement approaches were suggested. The EPAS gas sensing method greatly simplifies the QEPAS system and promises a potential multiplexing gas sensing in fiber-optic network.

We also developed an all-optical gas sensing method based on a miniature diaphragm-type extrinsic Fabry-Perot interferometer (EFPI). The F-P cavity of the EFPI is used as the gas cell, and the diaphragm is served as acoustic responser. With

a polymer diaphragm of 2.75 mm in diameter and ~ 2 μm in thickness, an all-optical PAS system was demonstrated for acetylene detection with a detectable concentration limit of 4.3 ppm at atmospheric pressure by using an 8-mW DFB laser. The method incorporates the acoustic generation and detection in a same optical device for the first time, to the best of our knowledge, and pushes the sensor size into millimeter scale. This work might inspire the realization ways for all-optical multiplexing gas sensing.

Publications

Journal articles

1. **Yingchun Cao**, Wei Jin, Hoi Lut Ho, and Zhibo Liu, "Evanescent-wave photoacoustic spectroscopy with optical micro/nano fibers," *Optics Letters* **37**, 214-216 (2012).
2. **Yingchun Cao**, Hoi Lut Ho, and Wei Jin, "Optimization of spectrophone performance for quartz-enhanced photoacoustic spectroscopy," *Sensors and Actuators B: Chemical* **174**, 24-30 (2012).
3. **Yingchun Cao**, Wei Jin, Hoi Lut Ho, Lifeng Qi, and Yuanhong Yang, "Acetylene detection based on diode laser QEPAS: combined wavelength and residual amplitude modulation," *Applied Physics B*, DOI: 10.1007/s00340-012-5221-4.

Conference proceedings

1. **Yingchun Cao**, Wei Jin, and Hoi Lut Ho, "Gas detection with evanescent-wave quartz-enhanced photoacoustic spectroscopy," *Third Asia Pacific Optical Sensors Conference, Proc. SPIE* **8351**, 835121 (2012).
2. **Yingchun Cao**, Wei Jin, and Hoi Lut Ho, "NIR diode laser-based QEPAS for acetylene detection," *Optical Sensing and Detection II, Proc. SPIE* **8439**, 843928 (2012).
3. Wei Jin, Lifeng Qi, Hoi Lut Ho, and **Yingchun Cao**, "Gas detection with micro and nano-engineered optical fibers," *Imaging and Applied Optics Technical Digest, OSA*, STu4F.3 (2012).
4. **Yingchun Cao**, Wei Jin, and Hoi Lut Ho, "Numerical modeling and performance optimization of QEPAS spectrophone," *The 22nd International Conference on Optical Fiber Sensors*, *Proc. SPIE* **8421**, 842167 (2012).

Acknowledgements

Any achievement results in applause and happiness, but is resulted from continuous hardworking, useful guidance and various support. The complement of my thesis and PhD study cannot be separated from my perseverance, but more importantly the worthy guidance from my supervisor and the consistent support from my family.

I would like to express my deepest appreciation to my chief supervisor, Professor Wei Jin, for his continuous guidance and extraordinary care in my academic study. His research attitude sets an excellent example for me in my future career. His direct gives me invaluable help and inspiration. And his encouragement makes me full of confidence and impetus.

I would also like to give my deepest thanks to my beloved family. The endless support and care from my parents makes me full of gratitude. The encouragement from my wife, Han Dong, gives me the biggest confidence and motivation.

Special thank goes to Dr. Hoi Lut Ho and Dr. Jian Ju for their great assistance in my experimental work. I also want to take this opportunity to acknowledge all my colleagues for their kindly help and support in my study and life.

Contents

List of Figures

List of Tables

Chapter 1

Introduction

1.1 Literature review

Trace gas detection and quantification is of importance in many areas including environmental monitoring, industrial process control, medical diagnostics, mine safety, et al. The most efficient method for gas detection is infrared (IR) spectroscopy, which utilizes the gas absorption in the IR spectral range through its molecular transition between the energy levels. Due to the appearance of high quality light sources and high sensitivity detection techniques, gas detection has gained a remarkable development over the past several decades. Among various gas detection methods, photoacoustic spectroscopy (PAS) shows outstanding characteristics due to its zeros background noise, compact size, high sensitivity, and so on [1].

Different from conventional direct optical absorption spectroscopy based on Beer-Lambert law which states the exponential attenuation of transmitted intensity of light in the detection medium, PAS is a zero background calorimetric method governed by photoacoustic effect, which can be dated back to Bell's famous discovery in 1880 that modulated sunlight can generate sound when absorbed by solid or gaseous medium as shown in Figure 1.1 [2]. In PAS, the periodic light absorption in gases is converted into localized heating then acoustic pressure wave, which is subsequently detected by a high sensitive microphone to address the gas information.

Figure 1.1 Bell's setup for the discovery of photoacoustic effect [3]. A, ear phone to collect the acoustic signal; B, chopper to modulate the light intensity; C, reflecting mirror; D, support used to adjust the mirror.

Due to the lack of high-quality light source and sensitive acoustic detection techniques, PAS has been almost forgotten for half a century until the invention of laser sources. The unceasing appearance of high sensitive acoustic detection techniques further accelerates the development of PAS. The development of PAS will be reviewed along three main lines as follows:

1.1.1 Light sources

Light source is the first key component for PAS, the selection of which is governed by several considerations: a) the wavelength must be consistent with gas absorption line (generally in mid-IR or near-IR); b) with a large and stable output power to provide a constant absorption; c) with narrow line width to precisely select the desired absorption line.

In Bell's experiment, the light source is sunlight. But the quantitative measurement is impossible. Not until 1938, Viengerov introduced the first PAS gas detection system [3], in which he used a blackbody as the light source and the photoacoustically generated pressure wave was detected in a resonant space. An important breakthrough happened for the first use of continuous wave (cw) CO_2 laser as the light source for PAS carbon dioxide detection in 1968 [4]. Laser was a brand new light source with superior beam quality, very narrow line width and high radiative power, which provide a perfect light source for PAS. Subsequent research

by Kreuzer achieved a methane concentration limit of 10 part-per-billion (ppb) by using a He-Ne laser [5]. Since 1970s, PAS for gas detection booms due to the availability of high power lasers in the mid-IR range, which falls into the fundamental absorption range of many gas species. Line-tunable high power (1 W) CO and CO_2 gas laser was first used as PAS light source by Kreuzer et al. in 1972 [6]. They successfully detected the ethylene concentration as small as 5 ppb in air. In current state-of-the-art experiments, CO and CO_2 gas laser with output power over several ten watts can be easily available, which pushes the gas concentration detection sensitivity to the sub-ppb level or even smaller [7-9].

Although mid-IR gas laser exhibits excellent capability for PAS trace gas detection, their large size, complex control and expensive cost prevent them from finding more applications in practice. In recent years, plenty of novel laser sources, including tunable diode lasers (TDLs) [10-12], distributed feedback (DFB) lasers [13-16], mid-IR quantum cascade lasers (QCLs) [17-21], laser-pumped optical parametric oscillators (OPOs) [22,23] and difference frequency generators (DFGs) [24] , and fiber lasers [25,26], applied to the PAS system promoted the full development of PAS gas detection for various applications.

Tunable diode laser has the advantages of compact size, low cost, high stability and reliability, long lifetime et al., which can be continuously tunable in 20-100 nm bandwidth range with an electrical signal at room temperature. Both of the wavelength and intensity can be modulated at a high frequency. However, the output power is only in the ~mW range and the wavelength in the near-IR band (0.8-1.62 μm), which corresponds to the relatively weak absorption of molecules. With the assist of erbium-doped fiber amplifier (EDFA), the power can be amplified to as high as ~500 mW, and the gas concentration detection can be enhanced to ppb level [27, 28].

DFB laser is a kind of even smaller semiconductor laser that based on the

periodic Bragg grating structure oscillator. The wavelength of DFB laser is distributed in the near-IR communication band (1.3-1.6 μm) and the output power ranges from 1-10 mW. The gas concentration detection sensitivity based on DFB laser is typically in the ~ppm level. The more and more favor of using DFB laser in PAS system is due to its high stability, long lifetime, fast response, narrow line width and compact size. The fiber pigtail feature of this kind of laser makes it be more easily connected into the communication and detection system.

The invention of QCL by Faist et al. from Bell laboratories in 1994 [29] opens up a new area for PAS in the mid-IR spectral region. Different from other semiconductor laser, the emission wavelength of QCL is determined by its geometrical structure rather than the semiconductor material, thus the emission wavelength from 4-12 μm can be realized by properly control the laser structure. Compared with CO and CO_2 gas laser, QCL can emit light at any wavelength, theoretically at least, in the mid-IR region with power up to >100 mW [30]. The room temperature operation currently makes it more versatile in many applications. The tuning rang can be extended to typically ±5% of the central wavelength for external cavity QCLs [31]. All these features enables QCL represent the most promising light sources for gas sensing applications. Nevertheless, light propagation and detection in mid-IR range is still a big problem, which is especially apparent for remote sensing application.

Another alternative for mid-IR light source is based on nonlinear optical process, i.e., OPO and DFG. With this method, light source with any wavelength in the range of 3-15 μm can be achieved, depending on the nonlinear materials. An often used nonlinear material is periodically poled LiNbO3, also known as PPLN, which provides tuning in the important 3-4.5 μm range. The cw power of DFG is typically in the μW-mW range while up to 2 W for OPO [32]. The drawback of this kind of light source is its expensive cost and complicated setup.

Most recently, PAS gas detection based on a near-IR tunable erbium doped fiber laser (TEDFL) was proposed by Q. Yu's group [25]. Ammonia concentration limit of 3 ppb was achieved by them with an EDFA to boost the light power to 500 mW before entering the gas cell. Since the erbium doped fiber (EDF) has a broad gain bandwidth from 1520-1610 nm, which covers a number of gas absorption lines in the near-IR region, multi-gas sensing is permitted without using multi-lasers with specifically designed wavelength in most other gas sensing cases. Fiber laser-based PAS also possesses the advantages of easy access to the amplification and multiplexing system.

The main characteristics of IR tunable laser source are listed in Table 1.1.

Table 1.1 Main characteristics of IR tunable laser sources for PAS gas sensing system [32].

Laser sources	Wavelength (μm)	Tuning property	Power	Operation	Fiber lead out
CO laser	2.8-4.1, 4.8-8.4	line tunable	50 mW - ~W	RT	No
CO_2 laser	9-11	line tunable	Watts	RT	No
Solid State[a]	2.2-3.1, 3.9-4.5	0.5-1 μm	1 W cw (pulsed)	RT(Cryo)	No
TDL	0.8-1.62	20-100 nm	~mW	RT	Yes
DFB laser	1.3-1.65	few nm	1-10 mW	RT	Yes
QCL	4-25	cm^{-1} - >100 cm^{-1}	mW-W	Cryo/TE/RT	No
OPO[b]	3-16	~μm	>1 W	RT	No
DFG[b]	3-16	~μm	μW-mW	RT	No
Fiber laser[c]	1.52-1.61	up to 60 nm	Watts	RT	Yes

[a] Examples: Cr^{2+}:ZnSe laser (Fe^{2+}:ZnSe laser), etc.

[b] Examples: PPLN, $AgGaSe_2$, $LiInS_2$, $LiInSe_2$, etc.

[c] Examples: Erbium-doped fiber laser.

1.1.2 Acoustic enhancement methods

Acoustic signal can be apparently enhanced in a well-designed PA cell before detected. PA cell operation at its resonance mode by tuning the laser modulation frequency to one of the resonant frequencies of the gas cell was introduced by Dewey et al. [33] and Kamm [34]. This resonant gas cell operation can significantly

enhance the acoustic signal via the acoustic energy accumulation in the gas cell. The signal enhancement is embodied by the quality factor (*Q*-factor) of the acoustic resonator, which is typically in the range of 10-50 for the longitudinal resonance [35, 36], but much higher (several hundreds) for cylindrical resonators with radial or azimuthal resonances [37]. The optimized design of an acoustic resonator is significant for improving the sensitivity of a PAS gas sensing system by enhancing the acoustic signal in the gas cell, due to the constructive acoustic interference caused by the boundaries, and suppressing the influence of background noises. A variety of gas cells were summarized in the review paper [38] as shown in Figure 1.2.

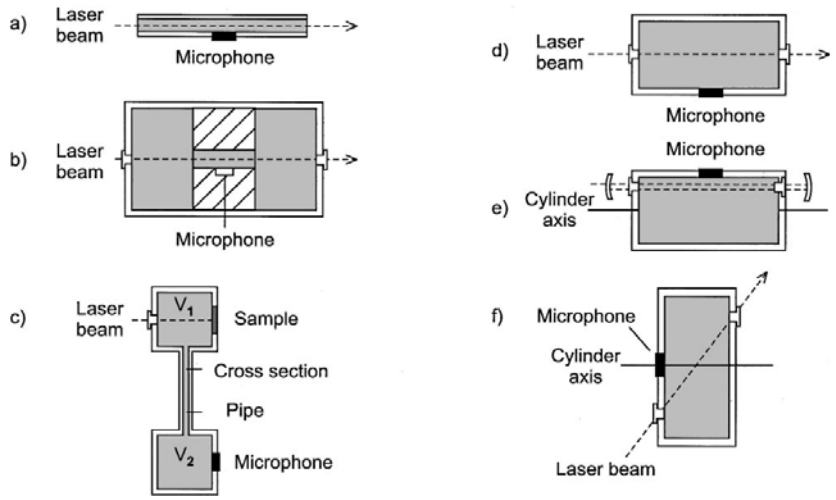

Figure 1.2 Different kinds of resonant PA cells. (a) Simple tube for excitation of longitudinal modes; (b) Tube with two buffer volumes; (c) Helmholz resonator with separate sample and detection chambers for solid samples; (d) Coaxial excitation in a cylinder; (e) Asymmetric multipass arrangements for azimuthal modes excitation in a cylinder; (f) Cylindrical cell suitable for excitation of the first radial mode with suppression of the window noise [38].

Generally, the PA cell can be classified into three types: 1-dimensional (1-D) resonant tube, Helmholz resonator and resonant cavity [39]. However, the mostly used PA cell is 1-D type, i.e., the dimension of the cross section is far smaller than the wavelength of acoustic signal in the cell, for its simplicity, compact size, high

frequency operation, and high sensitivity.

Another important means for acoustic enhancement is achieved by multipass absorption [40, 41] or cavity enhancement [42, 43]. Hao et al. developed a multipass Lissajous system for laser PAS gas detection by using a pair of cylindrical concave mirrors at appropriate spacing in a spheric cell [40]. The effective optical power in the absorption cell was enhanced by 45 times. Rey et al. investigated the optimized condition in a high absorption multipass PA cell for the first longitudinal acoustic mode [41]. The first cavity-enhanced PAS was reported by Rossi et al. [42]. The light intensity was amplified by using an external feedback-controlled Fabry-Perot cavity and the detection sensitivity down to tens ppb for gas absorption in the region between 1.5-1.7 μm was obtained. Hippler et al. recently introduced a novel method of cavity-enhanced resonant PAS gas detection by using optical feedback cw diode laser [43]. The laser power accumulated in the gas cell was amplified by ~1000 times due to the high finesse of optical cavity.

1.1.3 Acoustic detection techniques

The acoustic detection technique is the last important part that can ultimately limit the gas detection sensitivity. In photoacoustic effect discovery experiment, Bell used human ear as acoustic detector, which cannot quantitatively measure the acoustic signal. As the development of microelectronics, high sensitive electric microphone had been used for the acoustic detect in PAS system since 1980s [44]. In most cases, the acoustic detector in PAS gas sensing system was inclined to be an electric capacitive microphone, the electric signal of which is linearly related to the amplitude of the detected acoustic signal, due to its simplicity, and stability. Since the size of the microphone is very small, multiple microphone detectors are easy implemented as point sensor. Nägele et al. used a microphone array (16 microphones) for the detection of first longitudinal acoustic resonant mode distribution of a

multipass gas cell [45]. However, the wide response bandwidth and low sensitivity limits it to be used for high sensitive gas detection. Beside capacitive microphone, there are two new alternative techniques for acoustic wave detection.

The first one utilizes a miniature quartz tuning fork (QTF) as the acoustic transducer that was proposed by Kosterev et al. from Rice University in 2002 [46]. The sensing method is called quartz-enhanced photoacoustic spectroscopy (QEPAS), in which the photoacoustic induced sound wave applied on the prong of QTF is converted into electric signal through piezoelectric effect of QTF. The QTF is commercially available with very low cost and commonly used in wrist watches. The resonant frequency of this kind of acoustic detector is about 32.768 kHz in vacuum and ~ 10 Hz lower in atmospheric pressure. The higher frequency response makes it be immune to the environmental noise and the high *Q*-factor (~ 10000 in air) ensures a very high sensitivity of it. The PA cell of QEPAS can be greatly reduced compared with microphone-based PAS due the compact size of QTF [47, 48]. With optimized spectrophone, the sensitivity up to 3.3×10^{-9} cm^{-1} W $Hz^{-1/2}$ was achieved with this method [49]. Replacing of most on-beam detection schemes (Figure 1.3 (a)), the QTF can be also placed beside the resonant tube near the side-opening as off-beam configuration as shown in Figure 1.3 (b) [50, 51]. The assembly of the spectrophone is more convenient with comparable sensitivity to on-beam QEPAS.

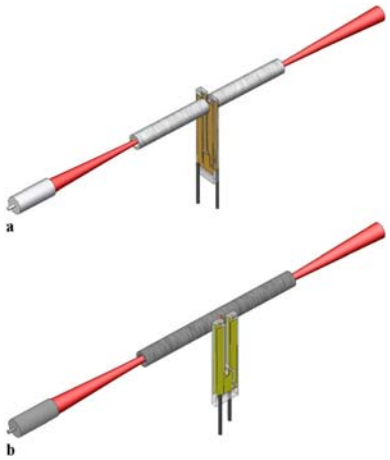

Figure 1.3 (a) On beam and (b) off-beam schemes for QEPAS gas detection [49].

Another method for PAS gas detection is based on a microcantilever and associated with an external Michelson interferometer which was first proposed by Kauppinen's group from the University of Turku (Finland) in 2003 [52]. The resonant acoustic wave in the gas cell pushes the cantilever with a deflection, which is measured by a Michelson interferometer as shown in Figure 1.4 [53]. The dimensions of the cantilever are generally 4mm×2mm×5μm [54]. Because of the bend of the free end instead of stretch in the middle, the movement at the free end of a cantilever is up to two orders larger in magnitude than in the middle of a tightened membrane for capacitive microphone. The cantilever-enhanced PAS (CEPAS) has the advantages of high sensitivity and thermal stability, immune to electromagnetic interference due to optical detection, etc., over general microphone based PAS. Laurila et al. carried out the first diode laser-based CEPAS with a DFB laser at 1572 nm for carbon dioxide detection in 2005 [55], and a noise equivalent sensitivity of 2.8×10^{-10} cm^{-1} $W/Hz^{1/2}$ was obtained. Later, they enhanced the sensitivity to 1.7×10^{-10} cm^{-1} $W/Hz^{1/2}$ by optimizing the cantilever-based PA cell [56], which was the best reported sensitivity ever, to the best of our knowledge, and at least one order larger than any other detection methods in tunable diode laser PAS (TDLPAS). However, due to the high requirement for the fabrication and assembly of the cantilever, and the complexity of the system brought by Michelson-type interferometric detection, the application of cantilever based PAS is limited for its expense. In addition, the cantilever-type PAS is more susceptible to the environmental and sample gas flow noise.

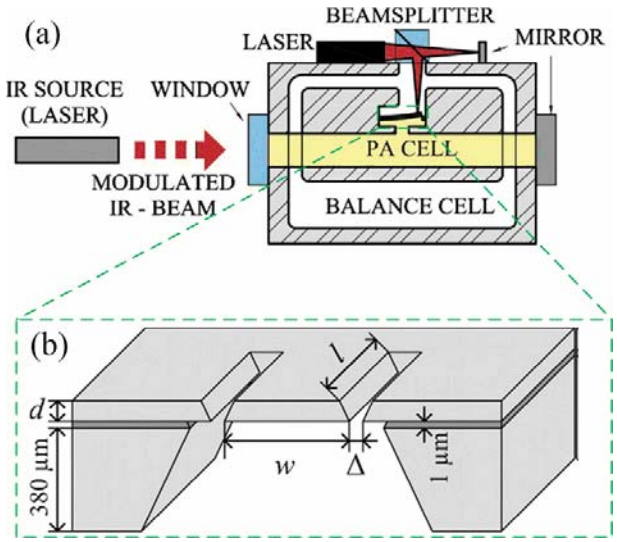

Figure 1.4 (a) Scheme of cantilever-enhanced PAS gas sensing system and (b) close-up figure of cantilever [53].

More recently, a novel detector based on electromechanical film (EMFi) was introduced for acoustic transducer in PAS gas sensing application [57, 58]. The frequency response of the EMFi is flat and wide (hundreds of kHz), and its easier formable and stackable, flexible, durable and low cost properties, high sensitivity to acoustic wave (down to 27 ppb for NO_2 detection at 436 nm) makes it be a competitive transducer material in the future.

In the applications of remote and multiplex gas sensing, fiber-based detection is required. As early as 1995, Breguet et al. proposed the first optical microphone for PAS gas detection as shown in Figure 1.5 [59]. They wound and glued the optical fiber on a thin plate as one arm of a Michelson interferometer. The acoustic pressure in the cylindric gas cell, one end of which was sealed by the thin plate, was excited as the first longitudinal acoustic resonant mode. As the acoustic pressure applied on the thin plate, it will be deformed and induce the length of the optical fiber, which will affect the interferometric output intensity. By utilizing both a Michelson interferometer and a Sagnac interferometer with fiber length of 4.5 km, respectively, the authors achieved the detection sensitivity down to 14 ppbv of ethanol vapor with 0.6 W CO_2 laser as light source.

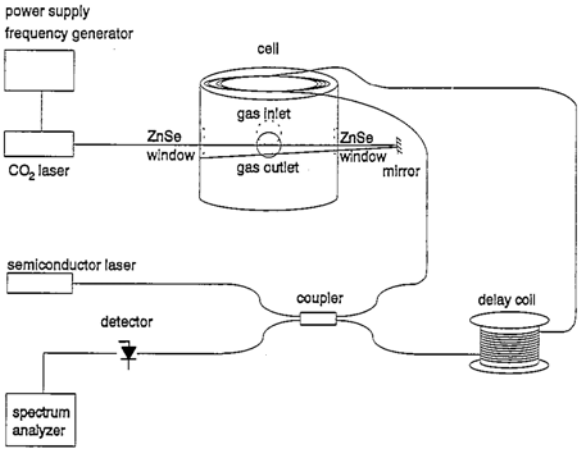

Figure 1.5 Experimental setup by Breguet et al. for Sagnac interferometric PAS acoustic detection [59].

An all-optical PAS approach with a diaphragm-based Fabry-Perot interferometric acoustic detector was reported for acetylene detection in 2011 as shown in Figure 1.6 [60]. A 4-mm-diameter polymer diaphragm with a thickness of 6 μm was sealed on the flat end of a ferrule, and a single mode fiber was plugged in with a section of cavity between them to form a Fabry-Perot interferometer. The acoustic pressure wave deforms the polymer diaphragm and can be read out from the interferometric system. A concentration limit of 1.56 ppb for acetylene detection was achieved by them with an erbium-doped fiber laser and an EDFA.

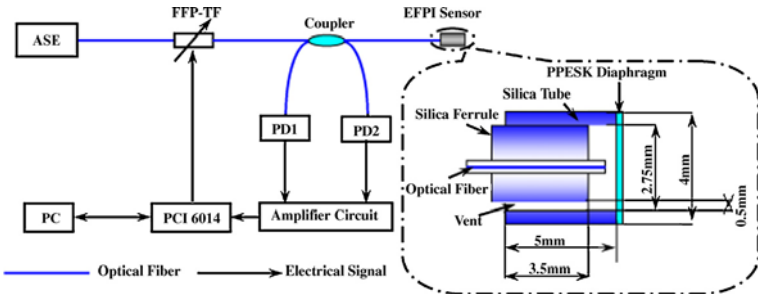

Figure 1.6 Diaphragm-based Fabry-Perot interferometric detection system for all-optical PAS gas detection [60].

Most recently, our group proposed an evanescent-wave PAS (EPAS) method based on micro/nano fibers [61]. The acoustic wave was excited by the periodic

interaction between the evanescent field of a microfiber and the gas analyte, and detected with a QTF. Acetylene sensitivity of 1.96×10^{-6} cm^{-1} $W/Hz^{1/2}$ was obtained by us with a 1.1-μm-diameter tapered optical fiber and bare QTF detection.

1.2 Motivation of this work

Trace gas detection with PAS gained much success in the past two decades. Since the acoustic signal is generated from the absolute optical absorption, there is no background signal without gas absorption. Among different detection methods, QEPAS, in which the acoustic signal is detected by a tiny QTF at its resonance mode via piezoelectric effect, draws many attentions for its compact size, low cost and high sensitivity. To better understand the physical process and improve its gas sensing ability is the first motivation of this thesis.

Although many experimental works have been done on QEPAS, the systematic introduction of each part of QEPAS is had to be found. Thus we set up several models to theoretical demonstrate the behavior of QTF vibration, and acoustic signal amplification in the micro-resonator. Further more, a numerical method is thought to be necessary to quantitatively describe the acoustic coupling in the spectrophone and provide a useful guidance for the optimization of spectrophone parameters.

Wavelength modulation (WM) and second harmonic detection is usually adopted for gases with well-resolved absorption lines in QEPAS. For semiconductor diode laser, a modulation on the laser wavelength can simultaneously cause the modulation of laser intensity, which added to the second harmonic signal can affect the signal amplitude and optimal detection phase. Therefore, a theoretical deviation of this combined wavelength modulation and residual intensity modulation might be useful for the understanding of modulation process and selecting of optimal modulation parameters. Experimental work will be carried out to verify the theoretical results and also provides a method for the determination of the laser

modulation information.

Considering the complicated light focusing/alignment components in conventional open-path QEPAS, we try to simplify this part by using a compact and efficient fiber-optic method, i.e., evanescent-wave PAS gas detection method based on a tapered optical micro/nano fiber. As the diameter of an optical fiber is reduced to the scale of wavelength or even smaller, a considerable portion of light power will propagate outside the physical boundary of the fiber as evanescent field. This part of light can interact with ambient gas analyte and generate acoustic wave by periodic modulation. PA excitation based on evanescent field avoids the use of complicated optical collimating/focusing system and makes the light propagate more freely. Moreover, the compact size, low cost, and potential multiplexing capability promises its bright future in gas sensing application.

As the development of fiber network and near-IR diode laser sources, remote gas sensing and multiple points monitoring is required in some applications. However, up to date, almost all of the reported investigations on PAS gas detection are based on open-path coupling or electric detection. Although the sensitivity can be extremely high with large-power light source, multiplexing and multi-point sensing is not possible. Therefore, we try to find the solution of the combination of high sensitive PAS detection technique, such as QEPAS, and fiber based devices, or even the all-optical gas detection system in this work.

1.3 Thesis outline

The thesis structure is arranged as follows:

Chapter 1 We review the development and background of PAS from three different main lines: the development of light source, the enhancement approaches of acoustic wave before detected and the different acoustic detection methods. And then the motivation of this work is talked about which followed by the thesis structure.

Chapter 2 In this chapter, we will introduce the principle of PAS in detail, including the gas absorption line, photoacoustic effect in gases, acoustic generation and resonance in a cylindric PA cell, and also the acoustic loss scheme.

Chapter 3 Theoretical description of quartz-enhanced photoacoustic spectroscopy will be presented in this chapter. Three different models, mechanical, electrical and piezoelectric, are developed to describe the properties of QTF. Then the acoustic enhancement in an ideal 1-D resonant tube will be derived for QEPAS. The wavelength modulation method, which is usually used in QEPAS, for an actual semiconductor in PAS scheme will be investigated in detail.

Chapter 4 A numerical model will be setup for the investigation on the behavior of a spectrophone in QEPAS, including the acoustic generation, coupling and distribution in PA cell, and the vibration property and piezoelectric effect of QTF. Finally, the optimized parameters for the design of a spectrophone will be suggested.

Chapter 5 Experimental research on QEPAS will be carried out. We will experimentally determine the property of our laser source and QTF first. Then the experimental research of QEPAS gas sensing will be demonstrated. The influence of residual amplitude modulation on wavelength modulation will be discussed and the performance of our sensing system will be evaluated.

Chapter 6 We will propose a novel evanescent-wave PAS method for acoustic excitation by using an optical micro/nano fiber. First, the fabrication and property of a micro/nano fiber will be presented. Subsequently, the method will be employed for acetylene detection with a QTF as the acoustic detector. The method will be analyzed and improvement possibility will be discussed.

Chapter 7 In this chapter, an all-optical gas sensing method based on PAS by using a diaphragm-based extrinsic Fabry-Perot interferometer (EFPI) as the sensing element will be presented. The principle of EFPI will be demonstrated and the acoustic response of diaphragm will be theoretically addressed and experimentally

examined. Then the sensing system for gas detection will be evaluated.

Chapter 8 The conclusion of the whole work will be drawn and the future work will be suggested in this chapter.

1.4 Summary

In this chapter, we mainly introduced the background knowledge of this thesis, including the development of photoacoustic spectroscopy for trace gas detection from the aspects of light source evolution, gas cell enhancement and alternative acoustic detection techniques. The main motivation of this thesis is demonstrated and the outline for each specific chapter is listed.

References of Chapter 1

1. C. Haisch, "Photoacoustic spectroscopy for analytical measurements," *Meas. Sci. Technol.* 23, 012001 (2012).
2. A. G. Bell, "On the production and reproduction of sound by light," *Am. J. Sci.* 20, 305-324 (1880).
3. M. L. Viegerov, "Eine Methode der gasanalyse, beruhend auf der optisch-akustischen tyndall- röntgenerscheinung," *Dokl. Akad. Nauk SSSR* 19, 687-688 (1938).
4. E. L. Kerr and J. G. Atwood, "The laser illuminated absorptivity spectrophone: a method for measurement of weak absorptivity in gases at laser wavelengths," *Appl. Opt.* 7, 915-921 (1968).
5. L. B. Kreuzer, "Ultralow gas concentration infrared absorption spectroscopy," *J. Appl. Phys.* 42, 2934-2943 (1971).

6. L. B. Kreuzer, N. P. Kenyon, and C. K. N. Patel, "Air pollution: sensitive detection of ten pollutant gases by carbon monoxide and carbon dioxide lasers," *Science* 177, 347-349 (1972).
7. F. J. M. Harren, J. Reuss, E. J. Woltering, and D. D. Bicanic, "Photoacoustic measurements of agriculturally interesting gases and detection of C_2H_4 below the ppb level," *Appl. Spectrosc.* 44, 1360-1368 (1990).
8. P. L. Meyer and M. W. Sigrist, "Atmospheric pollution monitoring using CO_2-laser photoacoustic spectroscopy and other techniques," *Rev. Sci. Instrum.* 61, 1779-1807 (1990).
9. F. J. M. Harren, R. Berkelmans, K. Kuiper, S. te Lintel Hekkert, P. Scheepers, R. Dekhuijzen, P. Hollander, and D. H. Parker, "On-line laser photoacoustic detection of ethene in exhaled air as biomarker of ultraviolet radiation damage of the human skin," *Appl. Phys. Lett.* 74, 1761-1763 (1999).
10. Z. Bozóki, J. Sneider, G. Szabó, A. Miklós, M. Serényi, G. Nagy, and M. Fehér, "Intracavity photoacoustic gas detection with an external cavity diode laser," *Appl. Phys. B* 63, 399-401 (1996).
11. A. Boschetti, D. Bassi, E. Iacob, S. Iannotta, L. Ricci and M. Scotoni, "Resonant photoacoustic simultaneous detection of methane and ethylene by means of a 1.63-μm diode laser," *Appl. Phys. B* 74, 273-278 (2002).
12. M. Scotoni, A. Rossi, D. Bassi, R. Buffa, S. Iannotta, and A. Boschetti, "Simultaneous detection of ammonia, methane and ethylene at 1.63 μm with diode laser photoacoustic spectroscopy," *Appl. Phys. B* 82, 495-500 (2006).
13. S. Schäfer, M. Mashni, J. Sneider, A. Miklós, P. Hess, H. Pitz, K.-U. Pleban, and V. Ebert, "Sensitive detection of methane with a 1.65 μm diode laser by photoacoustic and absorption spectroscopy," *Appl. Phys. B* 66, 511-516 (1998).
14. S. Schilt, A. Vicet, R. Werner, M. Mattiello, L. Thevenaz, A. Salhi, Y. Rouillard, and J. Koeth, "Application of antimonide diode lasers in photoacoustic

spectroscopy," *Spectrochim. Acta Part A* 60, 3431-3436 (2004).

15. M. Szakáll, Z. Bozóki, Á. Mohácsi, A. Varga, and G. Szabó, "Diode Laser based photoacoustic water vapor detection system for atmospheric research," *Appl. Spectrosc.* 58, 792-798 (2004).
16. M. Wolff, M. Germer, H.G. Groninga, and H. Harde, "Photoacoustic CO_2 sensor based on a DFB diode laser at 2.7 μm," *Eur. Phys. J. Special Topics* 153, 409-413 (2008).
17. D. Hofstetter, M. Beck, J. Faist, M. Nägele, and M. W. Sigrist, "Photoacoustic spectroscopy with quantum cascade distributed-feedback lasers," *Opt. Lett.* 26, 887-889 (2001).
18. S. Barbieri, J.-P. Pellaux, E. Studemann, and D. Rosset, "Gas detection with quantum cascade lasers: An adapted photoacoustic sensor based on Helmholtz resonance," *Rev. Sci. Instrum.* 73, 2458-2461 (2002).
19. S. Schilt, L. Thévenaz, M. Niklès, L. Emmenegger, and C. Hüglin, "Ammonia monitoring at trace level using photoacoustic spectroscopy in industrial and environmental applications," *Spectrochim. Acta Part A* 60, 3259-3268 (2004).
20. A. Elia, C. D. Franco, P. M. Lugarà, and G. Scamarcio, "Photoacoustic spectroscopy with quantum cascade lasers for trace gas detection," *Sensors* 6, 1411-1419 (2006).
21. J. Lima, H. Vargas, A. Mikls, M. Angelmahr, and P. Hess, "Photoacoustic detection of NO_2 and N_2O using quantum cascade lasers," *Appl. Phys. B* 85, 279-284 (2006).
22. D. Costopoulos, A. Miklos, and P. Hess, "Detection of N_2O by photoacoustic spectroscopy with a compact, pulsed optical parametric oscillator," *Appl. Phys. B* 75, 385 (2002).

23. J. Ng, A. H. Kung, A. Miklós, and P. Hess, "Sensitive wavelength-modulated photoacoustic spectroscopy with a pulsed optical parametric oscillator," *Opt. Lett.* 29, 1206-1208 (2004).
24. A. Bohren and M. W. Sigrist, "Optical parametric oscillator based difference frequency laser source for photoacoustic trace gas spectroscopy in the 3 mm mid-IR Range," *Infrared Phys. Technol.* 38, 423-435 (1997).
25. Y. Peng, W. Zhang, L. Li, and Q. Yu, "Tunable fiber laser and fiber amplifier based photoacoustic spectrometer for trace gas detection," *Spectrochim. Acta Part A* 74, 924-927 (2009).
26. J. Wang, W. Zhang, L. Li, and Q. Yu, "Breath ammonia detection based on tunable fiber laser photoacoustic spectroscopy," *Appl. Phys. B* 103, 263-269 (2011).
27. M. E. Webber, M. Pushkarsky, and C. K. N. Patel, "Fiber-amplifier-enhanced photoacoustic spectroscopy with near-infrared tunable diode lasers," *Appl. Opt.* 42, 2119-2126 (2003).
28. J. P. Besson, S. Schilt, E. Rochat, and L. Thévenaz, "Ammonia trace measurements at ppb level based on near-IR photoacoustic spectroscopy," *Appl. Phys. B* 85, 323-328 (2006).
29. J. Faist, F. Capassso, D. L. Sivco, C. Sirtori, A. L. Hutchinson, and A. Y. Cho, "Quantum cascade laser," *Science* 264, 553-556 (1994).
30. A. Wittmann, M. Giovannini, J. Faist, L. Hvozdara, S. Blaser, D. Hofstettter, and E. Gini, "Room temperature, continuous wave operation of distributed feedback quantum cascade lasers with widely spaced operation frequencies," *Appl. Phys. Lett.* 89, 141116 (2006).
31. G. Wysocki, R. F. Curl, F. K. Tittel, R. Maulini, J. M. Bulliard, and J. Faist, "Widely tunable mode-hop free external cavity quantum cascade laser for high resolution spectroscopic applications," *Appl. Phys. B* 81, 769-777 (2005).

32. M. Sigrist, R. Bartlome, D. Marinov, J. Rey, D. Vogler, and H. Wächter, "Trace gas monitoring with infrared laser-based detection schemes," *Appl. Phys. B* 90, 289-300 (2008).
33. C. F. Dewey, R. D. Kamm, and C. E. Hackett, "Acoustic amplifier for detection of atmospheric pollutants," *Appl. Phys. Lett.* 23, 633-635 (1973).
34. R. D. Kamm, "Detection of weakly absorbing gases using a resonant optoacoustic method," *J. Appl. Phys.* 47, 3550-3558 (1976).
35. A. Keller, M. Rüegg, M. Forster, M. Loepfe, R. Pleisch, P. Nebiker, and H. Burtscher, "Open photoacoustic sensor as smoke detector," *Sens. Actuators B* 104, 1-7 (2005).
36. J. Li, X. Gao, L. Fang, W. Zhang, and H. Cha, "Resonant photoacoustic detection of trace gas with DFB diode laser," *Opt. Laser Technol.* 39, 1144-1149 (2007).
37. S. Schilt, L. Thévenaz, E. Courtois, and P. A. Robert, "Ethylene spectroscopy using a quasi-room-temperature quantum cascade laser," *Spectrochim. Acta Part A* 58, 2533-2539 (2002).
38. A. Miklós, P. Hess, and Z. Bozóki, "Application of acoustic resonators in photoacoustic trace gas analysis and metrology," *Rev. Sci. Instrum.* 72, 1937-1955 (2001).
39. P. Hess, "Resonant photoacoustic spectroscopy," *Top. Curr. Chem.* 111, 1-32 (1983).
40. L. Hao, S. Qiang, G. Wu, L. Qi, D. Feng, and Q. Zhu, "Cylindrical mirror multipass Lissajous system for laser photoacoustic spectroscopy," *Rev. Sci. Instrum.* 73, 2079-2085 (2002).
41. J. M. Rey, D. Marinov, D. E. Vogler, and M. W. Sigrist, "Investigation and optimisation of a multipass resonant photoacoustic cell at high absorption levels," *Appl. Phys. B* 80, 261-266 (2005).

42. A. Rossi, R. Buffa, M. Scotoni, D. Bassi, S. Iannotta, and A. Boschetti, "Optical enhancement of diode laser-photoacoustic trace gas detection by means of external Fabry-Perot cavity," *Appl. Phys. Lett.* 87, 041110 (2005).
43. M. Hippler, C. Mohr, K. A. Keen, and E. D. McNaghten, "Cavity-enhanced resonant photoacoustic spectroscopy with optical feedback cw diode lasers: A novel technique for ultratrace gas analysis and high-resolution spectroscopy," *J. Chem. Phys.* 133, 044308 (2010).
44. P. Korpiun, and B. Büchner, "Photoacoustic signal in gas-microphone cells for all thermal lengths below acoustic-resonance," *Journal de Physique Colloques* 44, C6-85-C6-89 (1983).
45. M. Nägele and M. W. Sigrist, "Mobile laser spectrometer with novel resonant multipass photoacoustic cell for trace-gas sensing," *Appl. Phys. B* 70, 895-901 (2000).
46. A. A. Kosterev, Y. A. Bakhirkin, R. F. Curl, and F. K. Tittel, "Quartz-enhanced photoacoustic spectroscopy," *Opt. Lett.* 27, 1902-1904 (2002).
47. A. A. Kosterev, F. K. Tittel, D. V. Serebryakov, A. L. Malinovsky, and I. V. Morozov, "Applications of quartz tuning forks in spectroscopic gas sensing," *Rev. Sci. Instrum.* 76, 043105 (2005).
48. A. Elia, P. M. Lugarà, C. D. Franco, and V. Spagnolo, "Photoacoustic techniques for trace gas sensing based on semiconductor laser sources," *Sensors* 9, 9616-9628 (2009).
49. L. Dong, A. A. Kosterev, D. Thomazy, and F. K. Tittel, "QEPAS spectrophones: design, optimization, and performance," *Appl. Phys. B* 100, 627-635 (2010).
50. K. Liu, X. Guo, H. Yi, W. Chen, W. Zhang, and X. Gao, "Off-beam quartz-enhanced photoacoustic spectroscopy," *Opt. Lett.* 34, 1594-1596 (2009).
51. K. Liu, H. Yi, A. A. Kosterev, W. Chen, L. Dong, L. Wang, T. Tan, W. Zhang, F. K. Tittel, and X. Gao, "Trace gas detection based on off-beam quartz

enhanced photoacoustic spectroscopy: optimization and performance evaluation," *Rev. Sci. Instrum.* 81, 103103 (2010).

52. K. Wilcken and J. Kauppinen, "Optimization microphone for photoacoustic spectroscopy," *Appl. Spectroscopy* 57, 1087-1092 (2003).
53. V. Koskinen, J. Fonsen, K. Roth, and J. Kauppinen, "Progress in cantilever enhanced photoacoustic spectroscopy," *Vib. Spectrosc.* 48, 16-21 (2008).
54. J. Kauppinen, K. Wilcken, I. Kauppinen, and V. Koskinen, "High sensitivity in gas analysis with photoacoustic detection," *Microchem. J.* 76, 151-159 (2004).
55. T. Laurila, H. Cattaneo, V. Koskinen, J. Kauppinen, and R. Hernberg, "Diode laser-based photoacoustic spectroscopy with interferometrically-enhanced cantilever detection," *Opt. Express* 13, 2453-2458 (2005).
56. V. Koskinen, J. Fonsen, K. Roth, and J. Kaupinnen, "Cantilever enhanced photoacoustic detection of carbon dioxide using a tunable diode laser source," *Appl. Phys. B* 86, 451-454 (2007).
57. A. Manninen, J. Sand, J. Saarela, T. Sorvajärvi, J. Toivonen, and R. Hernberg, "Electromechanical film as a photoacoustic transducer," *Opt. Express* 17, 16994-16999 (2009).
58. J. Saarela, J. Sand, T. Sorvajrvi, A. Manninen, and J. Toivonen, "Transversely excited multipass photoacoustic cell using electromechanical film as microphone," *Sensors* 10, 5294-5307 (2010).
59. J. Breguet, J. P. Pellaux, and N. Gisin, "Photoacoustic detection of trace gases with an optical microphone," *Sens. Actuators A* 48, 29-35 (1995).
60. Q. Wang, J. Wang, L. Li, and Q. Yu, "An all-optical photoacoustic spectrometer for trace gas detection," *Sens. Actuators B* 153, 214-218 (2011).
61. Y. Cao, W. Jin, L. H. Ho, and Z. Liu, "Evanescent-wave photoacoustic spectroscopy with optical micro/nano fibers," *Opt. Lett.* 37, 214-216 (2012).

Chapter 2

Photoacoustic spectroscopy

2.1 Introduction

Photoacoustic spectroscopy, or PAS, is a molecular detection method based on spectral absorption in target medium. Different from direct absorption spectroscopy, in which the absorption in analyte is determined by the transmitted optical power, the light absorption in PAS is converted into acoustic energy via photoacoustic effect by the proper modulation of the light source, the acoustic wave is accumulated and amplified in a well designed PA cell, and finally detected by a high sensitive acoustic detector. A detailed theoretical description of PAS in this chapter, although which might appear elsewhere similarly, is regarded to be helpful for better understanding the physical process in it and assisted-designing the sensing system. Obviously, PAS is also an absorption spectroscopy, which strongly depends on the gas absorption line. Thus, the theory of the gas absorption line will be introduced first.

2.2 Gas absorption line

When an optical light beam with specific wavelength interacts with gases, part of the light energy will be absorbed by the gas to excite the gas molecules under lower energy level to jump to a higher energy level. The absorption wavelengths and intensities are unique for each gas molecule, which allows for gas species and concentration identification.

2.2.1 Intensity of the gas absorption line

The absorption spectroscopy is governed by the Beer-Lambert law, i.e., the transmitted optical intensity through an absorption medium with length l is expressed as [1]:

$$I_{out}(\nu) = I_0(\nu)\exp\left(-\alpha(\nu)l\right), \tag{2.1}$$

where $I_0(\nu)$ is the incident light intensity at wavenumber ν (in cm^{-1}), and $\alpha(\nu)$ is the absorption coefficient in cm^{-1}, which is determined by the gas line strength, lineshape, line width and concentration as:

$$\alpha(\nu) = N\sigma(\nu) = CN_{tot}Sg(\nu), \tag{2.2}$$

where $C = N / N_{tot}$ is gas molecular concentration with N and N_{tot} are the target gas molecular and total molecular density in mol/cm^3, respectively, cross section $\sigma(\nu) = Sg(\nu)$ is described by the line strength S (in $cm^{-1}/(mol\ cm^{-2})$) and normalized lineshape function $g(\nu)$. The total gas molecular density at temperature T (in Kelvin) and pressure p (in atm) can be expressed by:

$$N_{tot} = N_L \frac{296}{T} p, \tag{2.3}$$

where N_L=2.479×10^{19} mol·cm^{-3}·atm^{-1} is the Loschmidt number.

The line strength S of an absorption transition is a function of the population in the lower quantum state N_n, and the probability of the transition between lower state n and higher state m (determined by Einstein coefficient B_{nm}) as [2]

$$S = \frac{N_n}{N}\frac{h\nu_{nm}}{c}B_{nm}\left[1-\exp\left(\frac{hc\nu_{nm}}{kT}\right)\right], \tag{2.4}$$

where c is light velocity in vacuum and k is Boltzmann constant. The value of line strength for a specific absorption line of various familiar gases can be found in

[3]. Absorption lines for several gases in the near-IR spectral region are plotted in Figure 2.1 for example.

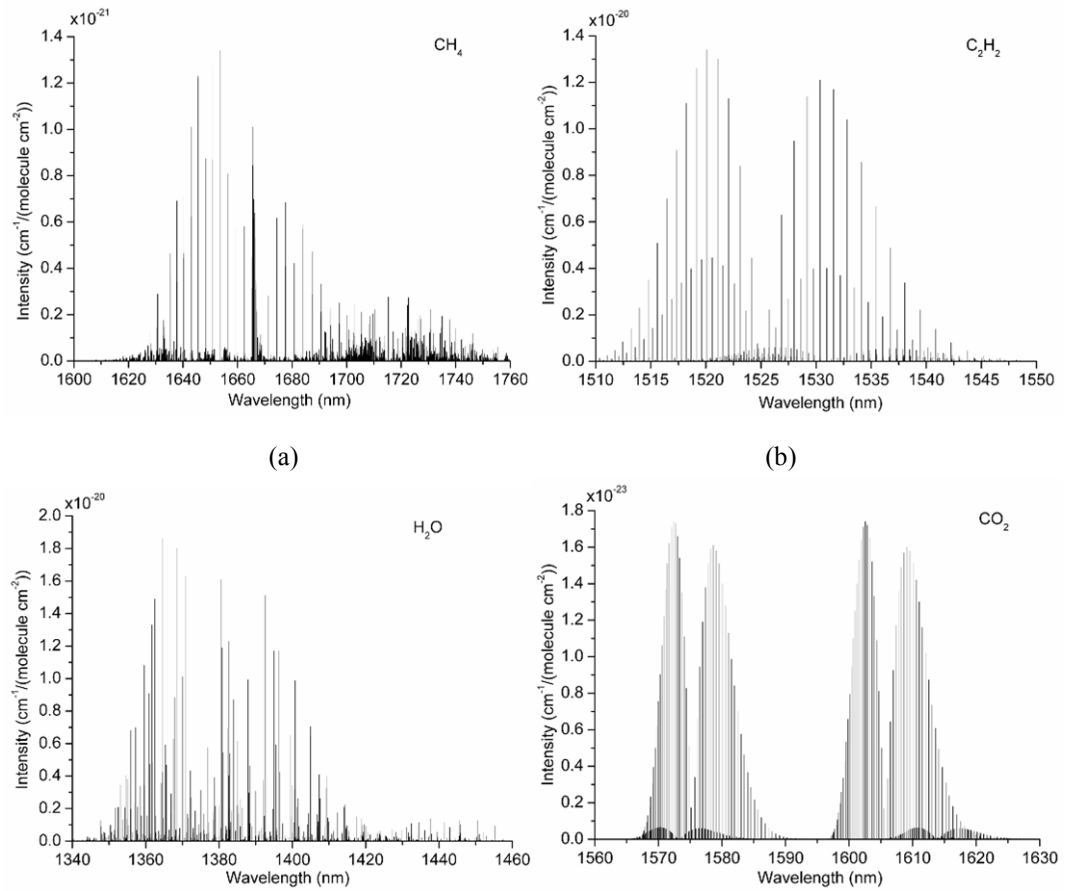

Figure 2.1 Absorption lines for four different familiar gases in the near-IR region. (a) CH_4, (b) C_2H_2, (c) H_2O and (d) CO_2.

2.2.2 Spectral shape of the absorption line

Broadening due to the environment can greatly affect the absorption transition of gas molecules, which results in different absorption lineshapes. The lineshape provides important information such as the temperature, gas concentration and pressure. Three significant lineshape functions (Gaussian, Lorentzian and Voigt) and their broadening mechanisms will be described below.

(a) Gaussian lineshape

The Gaussian lineshape function results from inhomogeneous broadening mechanism such as Doppler broadening, which is caused by the random thermal motion of gas molecules. The lineshape function is expressed as

$$g_D(\nu) = \frac{1}{\gamma_D}\sqrt{\frac{\ln 2}{\pi}}\exp\left[-ln2\left(\frac{\nu-\nu_0}{\gamma_D}\right)^2\right], \tag{2.5}$$

where γ_D (in cm^{-1}) is Doppler half width of half maximum (HWHM) of absorption line and can be calculated by

$$\gamma_D = \nu_0\sqrt{\frac{2kT\ln 2}{mc^2}} = 3.5812\times10^{-7}\nu_0\sqrt{\frac{T}{M}}, \tag{2.6}$$

where ν_0 (in cm^{-1}) is line center wavenumber, T (in Kelvin) is temperature and M (in atomic mass unit) is the molecular weight of the target gas. The peak value of Gaussian lineshape function is

$$g_D(\nu_0) = \frac{1}{\gamma_D}\sqrt{\frac{\ln 2}{\pi}}. \tag{2.7}$$

(b) Lorentzian lineshape

Lorentzian lineshape function is the result of two homogeneous broadening mechanisms, natural lifetime broadening and collisional broadening. Natural broadening is caused by the uncertainty in energy of the states in a finite lifetime of absorption transition described by the Heisenberg Uncertainty Principle. While collisional broadening is produced by the collision between particles in the process of emission and absorption. In most cases, natural broadening can be neglected because of the relatively long lifetime of the energy levels. Both of these two broadenings have the Lorentzian profile, so the Lorentzian lineshape function is expressed by

$$g_L(\nu) = \frac{1}{\pi}\frac{\gamma_L}{\left(\nu-\nu_0\right)^2+\gamma_L^2}, \tag{2.8}$$

where γ_L (in cm^{-1}) is Lorentzian HWHM, ν_0 (in cm^{-1}) is line center wavenumber. The peak value of Lorentzian lineshape function is

$$g_L(\nu_0) = \frac{1}{\pi\gamma_L}. \tag{2.9}$$

(c) Voigt lineshape

In practice, Doppler broadening often dominates at low pressure and collisional broadening dominates at high pressure. Therefore, the actual overall broadening is a combination of Doppler, natural and collisional broadening. The lineshape is given by the Voigt profile in the case of independent broadening

$$g_V(\nu) = \int_{-\infty}^{+\infty} g_D(u) g_L(\nu - u) du. \tag{2.10}$$

The above equation can be further written as

$$g_V(\nu) = g_D(\nu_0) \frac{a}{\pi} \int_{-\infty}^{+\infty} \frac{\exp(-y^2)}{a^2 + (w-y)^2} dy, \tag{2.11}$$

where the Voigt parameter *a*, non-dimensional line position *w* and integral variable *y* are defined as

$$a = \sqrt{\ln 2}\gamma_L / \gamma_D, \tag{2.12a}$$

$$w = \sqrt{\ln 2}\left(\nu - \nu_0\right) / \gamma_D, \tag{2.12b}$$

$$y = \sqrt{\ln 2} u / \gamma_D. \tag{2.12c}$$

The line width (HWHM) of Voigt lineshape can be estimated by [4]

$$\gamma_V = 0.5346\gamma_L + \sqrt{0.2166\gamma_L^2 + \gamma_D^2}. \tag{2.13}$$

The peak value of Voigt lineshape function is expressed by [5]

$$g_V(\nu_0) = g_D(\nu_0) \frac{a}{\pi} \int_{-\infty}^{+\infty} \frac{\exp(-y^2)}{a^2 + y^2} dy = \frac{\sqrt{\pi} + 1}{\pi(\gamma_L + \gamma_{ED})}, \tag{2.14}$$

where $\gamma_{ED} = \gamma_D / \sqrt{\ln 2}$ is effective HWHM of Doppler broadening.

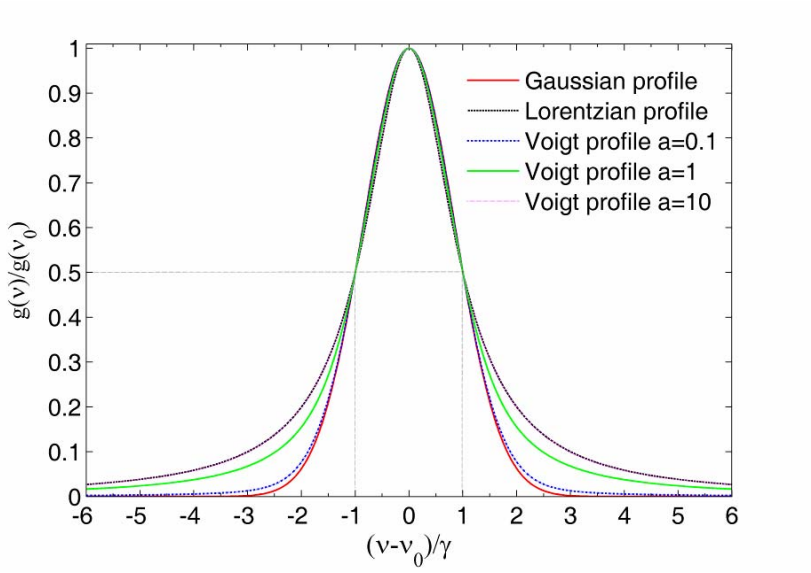

Figure 2.2 The absorption lineshapes of different broadening profiles with the same HWHM.

Figure 2.2 shows the comparison between these three lineshape profiles on a normalized scale of frequency and intensity. It reveals that the Lorentzian profile has a relatively larger intensity than Gaussian profile for frequencies far from the center. For small Voigt parameter *a*, Doppler broadening dominates in the absorption, so Voigt profile approaches Gaussian profile. Otherwise, Collisional broadening dominates, and Voigt profile shows a Lorentzian-like behavior.

2.3 The photoacoustic effect in gases

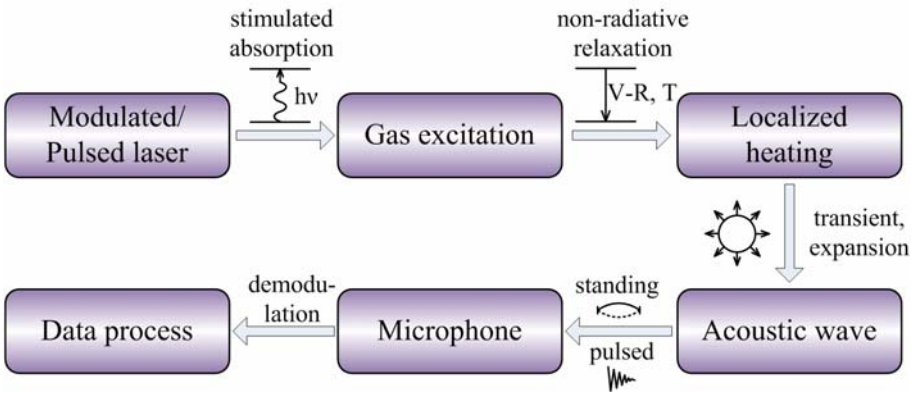

Figure 2.3 Schematic of physical processes in photoacoustic effect in gas.

The photoacoustic effect, first discovered by Bell in 1880, is the basic principle that governs the PAS. Photoacoustic effect in gas-phase medium is composed by the following processes [6]:

1) A modulated or pulsed laser source with specific wavelength interacts with the molecules with target gas to excite the gas molecules in lower energy level to higher energy level by stimulated absorption;
2) The relaxation of excited gas molecules due to the molecular collision in the form of *R*-*T*, *V*-*R*, *T* and *E*-*V*, *R*, *T* processes leads to localized transient heating;
3) The expansion of localized transient heating causes the acoustic and thermal wave generation;
4) The standing acoustic wave in an acoustic resonator or a localized pulsed acoustic wave is detected by a microphone;
5) The signal from a microphone is demodulated and analyzed by data process.

Photons of the laser source absorbed by the gas molecules result in the excitation of the molecular energy levels (rotational, vibrational, or electronic). The high energy level is not stable, which will return the initial state in the form of radiation processes, such as spontaneous/stimulated emission, and/or non-radiative reactivation by molecular collision. In the case of vibrational excitation, radiative emissions and chemical reactions do not play an important role because of the relatively long radiative lifetimes of vibrational levels compared with the time need for collisional deactivation at common used pressure in PAS and the too small photon energy to induce chemical reactions [7, 8]. Therefore, the absorbed light energy is completely converted into localized heating in practice, the release of which appears as translation (kinetic) energy of the gas molecules. The deposit heat power density is proportional to the incident optical power and the gas absorption coefficient.

The thermal and acoustic wave generation governed thermodynamics and fluid dynamics will be described in the following section theoretically. The resonance property and loss scheme will be analyzed. When the magnitude of the acoustic wave applied on the microphone is fixed, the detection acoustic signal is totally depended on the type and geometry of PA detectors. Finally, the acoustic signal is demodulated and analyzed to achieve the gaseous information of the analyte.

2.4 Acoustic signal generation

Photoacoustic gas sensing is based on the detection of the acoustic signal, which behaves as the sound pressure and is caused by the expansion and contraction of the deposit heating. The generation of photoacoustic signal can be split into two steps. The first step is the heat production in the gas medium, which describes the energy transfer from vibrational to translational degrees of freedom (*V-T* relaxation) for excited gas molecules, and the second step deals with the acoustic wave generation, which is directly related to the heat production [2].

2.4.1 Heat production rate

Heat production in a gas sample induced by a modulated laser can be described by the molecular population levels [9]. To simplify the problem, a two-level system for the absorbing gas molecule with a molecular density of N is assumed. The population density of the excited vibrational state $N^{'}$ can be derived from the following rate function:

$$\frac{dN^{'}}{dt} = \left(N - N^{'}\right)\sigma\phi - N^{'}\sigma\phi - N^{'}/\tau\,, \tag{2.15}$$

where σ is the absorption cross section and ϕ is photon flux, time τ related to the time constants of non-radiative and radiative relaxation can be expressed as

$$\frac{1}{\tau}=\frac{1}{\tau_n}+\frac{1}{\tau_r}. \tag{2.16}$$

It is known from Eq. (2.15) that the derivative of the molecular density in the upper level is determined by the absorption of the photons (1st term on the right-hand side), stimulated emission (2nd term), and spontaneous emission of phonons and non-radiative relaxation (3rd term). Take into consideration that for typical atmospheric conditions, τ_n (in the order of 10^{-6}-10^{-9} s) is much smaller than τ_r (in the order of 10^{-1}-10^{-3} s) [10], so $\tau \approx \tau_n$ is applied. Further more, for weak absorption, excitation rate $\sigma\phi$ is very small, so the density of the excited state is considerably smaller than the total molecular density. Thus Eq. (2.15) can be simplified as

$$\frac{dN'}{dt}=N\sigma\phi-N'/\tau_n. \tag{2.17}$$

For a modulated photon flux with form $\phi=\phi_0\left(1+e^{i\omega t}\right)$, where ω is the angular modulation frequency, the solution of Eq. (2.17) can be expressed as

$$N'=\frac{N\sigma\phi_0\tau_n}{\sqrt{1+(\omega\tau_n)^2}}e^{i(\omega t-\varphi)}, \tag{2.18}$$

where $\varphi=\arctan(\omega\tau_n)$ represents the phase lag between the molecular density of the excited state N' and the incident photon flux ϕ.

The heat production rate *H* (by volume and unit time) is related to N' by

$$H=N'\frac{hc\Delta\nu}{\tau_n}, \tag{2.19}$$

where $hc\Delta\nu$ is the average thermal energy released due to the non-radiative relaxation of the excited state. If the molecule is de-excited to the ground state, as is the case in two-level system, then $\Delta\nu\cong\nu_{laser}$. Therefore, the heat production rate in

Eq. (2.19) is rewritten as

$$H = H_0 e^{i(\omega t - \varphi)}, \tag{2.20}$$

with

$$H_0 = \frac{N\sigma I_0}{\sqrt{1+(\omega\tau_n)^2}}, \tag{2.21}$$

where $I_0 = \phi_0 hc\nu_{laser}$ is the incident laser intensity.

For low modulation frequency $\omega << 10^6$, $\omega\tau_n << 1$, the heat production rate is further obtained to be

$$H = H_0 e^{i\omega t}, \tag{2.22}$$

and

$$H_0 = N\sigma I_0 = \alpha I_0, \tag{2.23}$$

where α is the absorption coefficient of target gas. For most gas sensing system, the condition $\omega\tau_n << 1$ is satisfied since the modulation frequencies are generally in the kHz range or smaller. However, in some particular cases, the $\omega\tau_n << 1$ condition is not sufficed any more even for modulation frequency in the kHz range because τ_n^{-1} can be the same order in magnitude of ω.

2.4.2 Acoustic wave generation

Acoustic/thermal wave generation in PAS is governed by the laws of the energy, the momentum, mass conservation and thermomechanic equation of the state. The physical property of the acoustic and thermal processes can be quantitatively characterized by pressure $p(\mathbf{r},t)$, temperature $T(\mathbf{r},t)$, gas density $\rho(\mathbf{r},t)$ and the three components of fluid velocity vector $\mathbf{v}(\mathbf{r},t)$. All these parameters are considered as relative quantities compared to their equilibrium values, so they can be

regarded as small quantities and their higher order products can be neglected. Therefore, the linearized Navier-Stokes equation can be used to include thermal conduction and frication in the fluid [11]

$$\frac{\partial \mathbf{v}}{\partial t} = -\frac{1}{\rho_0}\nabla p(\mathbf{r},t) + D_v \nabla\left(\nabla \cdot \mathbf{v}_l\right), \tag{2.24}$$

where ρ_0 is the density of gas sample, $\mathbf{v}_l$ is the longitudinal component of fluid velocity vector $\mathbf{v}$, and $D_v = 4\eta/3\rho_0 + \eta_b/\rho_0$, where η and η_b represent the coefficients of shear viscosity and bulk viscosity (or volume viscosity), respectively.

A thermal diffusivity equation can be derived to describe the combination of sound pressure and temperature fluctuations as

$$\frac{K}{\rho_0 C_p}\nabla^2 T(\mathbf{r},t) = \frac{\partial}{\partial t}\left(T(\mathbf{r},t) - \frac{\gamma - 1}{\gamma \beta_T}\kappa_T p(\mathbf{r},t)\right) - \frac{H(\mathbf{r},t)}{\rho_0 C_p}, \tag{2.25}$$

where K is the thermal conductivity, C_p is the heat capacity at constant pressure, $\gamma = C_p / C_V$ is the ratio of the specific heat at constant pressure to constant volume, β_T is the thermal expansion coefficient, κ_T is the isothermal compressibility and $H(\mathbf{r},t)$ is heat power deposit density.

By further considering the mass-density continuity equation

$$\frac{\partial \rho(\mathbf{r},t)}{\partial t} + \rho_0 \nabla \cdot \mathbf{v}_l = 0, \tag{2.26}$$

and the thermodynamic equation

$$\rho(\mathbf{r},t) = \frac{\gamma}{c_s^2}\left(p(\mathbf{r},t) - \frac{\beta_T}{\kappa_T}T(\mathbf{r},t)\right), \tag{2.27}$$

where c_s is the sound velocity in gas and defined by

$$c_s = \sqrt{\gamma RT/M}, \tag{2.28}$$

$\mathbf{v}_l$ and $\rho(\mathbf{r},t)$ can be eliminated as

$$\nabla^2 p(\mathbf{r},t)=\frac{\gamma}{c_s^2}\left(\frac{\partial^2}{\partial t^2}-D_v\nabla^2\right)\left(p(\mathbf{r},t)-\frac{\beta_T}{\kappa_T}T(\mathbf{r},t)\right), \tag{2.29}$$

Two independent solutions can be obtained from the coupled Eq. (2.25) and (2.29): a weakly damped propagating acoustic wave with wavelength in the range of centimeter and a heavily damped thermal wave with wavelength in the range of submillimeter and can only propagate within a few wavelengths. Therefore, thermal and acoustic wave are separated in space and can be observed independently. The detection of the former one corresponds to the photothermal techniques [12, 13], and the latter one is photoacoustic spectroscopy, which is based on the acoustic wave detection using a microphone.

In practice, the acoustic wave is typically generated and detected in a PA cell, the dimension of which is greatly larger than the propagation distance of the thermal wave, so the second derivatives of $T(\mathbf{r},t)$ can be neglected due to its heavy damping property in PAS, which results a unique pressure equation by combining Eq. (2.25) and (2.29)

$$\nabla^2 p(\mathbf{r},t)-\frac{1}{c_s^2}\frac{\partial^2 p(\mathbf{r},t)}{\partial t^2}+\frac{1}{c_s^2}D_v\nabla^2 p(\mathbf{r},t)=-\frac{(\gamma-1)}{c_s^2}\frac{\partial H(\mathbf{r},t)}{\partial t}. \tag{2.30}$$

This equation is a damping wave equation, with the last term of the left-hand side as a viscosity loss term and the right-hand side part as the source term. The loss term makes this equation impossible to be solved analytically. To simplify this problem, we neglect this damping term in first approximation, which will be analyzed in the following section as a perturbation of the solution, and consider the equation below

$$\nabla^2 p(\mathbf{r},t)-\frac{1}{c_s^2}\frac{\partial^2 p(\mathbf{r},t)}{\partial t^2}=-\frac{(\gamma-1)}{c_s^2}\frac{\partial H(\mathbf{r},t)}{\partial t}. \tag{2.31}$$

To solve this equation, time Fourier transform on both side is applied and the solution $p(\mathbf{r},t)$ is expressed as an infinite series expansion of the normal mode

solution $p_j(\mathbf{r},t)$. After Fourier transform, Eq. (2.31) becomes

$$\left(\nabla^2+\frac{\omega^2}{c_s^2}\right)p(\mathbf{r},\omega)=\frac{(\gamma-1)}{c_s^2}i\omega H(\mathbf{r},\omega), \tag{2.32}$$

where

$$p(\mathbf{r},t)=\int_{-\infty}^{\infty}p(\mathbf{r},\omega)e^{-i\omega t}d\omega, \tag{2.33a}$$

$$H(\mathbf{r},t)=\int_{-\infty}^{\infty}H(\mathbf{r},\omega)e^{-i\omega t}d\omega. \tag{2.33b}$$

In order to find the normal mode solutions of the homogeneous wave equation, a boundary condition should be given. As most of the PAS gas detection is carried out in a cylindrical cavity, where the acoustic wave is generated and detected, the normal modes for a cylindrical cavity with length L, radius R_c and volume V_c are given by [14]

$$p_j(\mathbf{r},\omega)=p_j\cos(m\Phi)\cos\left(k\frac{\pi z}{L}\right)J_m\left(\alpha_{mn}\frac{\pi r}{R_c}\right),\qquad j=[k,m,n], \tag{2.34a}$$

$$p_j(\mathbf{r},\omega)=p_j\cos(m\Phi)\sin\left(k\frac{\pi z}{L}\right)J_m\left(\alpha_{mn}\frac{\pi r}{R_c}\right),\qquad j=[k,m,n], \tag{2.34b}$$

for both ends closed and both end open cases, respectively, where p_j is the normalization coefficient determined by the mode orthogonality

$$\int p_i^*(\mathbf{r},\omega)p_j(\mathbf{r},\omega)dV=\delta_{ij}V_c, \tag{2.35}$$

J_m are the first kind Bessel functions and α_{mn} is the n^{th} root of the equation involving the m^{th} order Bessel function

$$\frac{d}{dr}J_m\left(\alpha_{mn}\frac{\pi r}{R_c}\right)\Big|_{r=R_c}=0,\quad m=0,1,2,\ldots;n=0,1,2,\ldots,. \tag{2.36}$$

The values of $\pi\alpha_{mn}$ for the first several azimuthal (denoted by m) and radial (denoted by n) modes of a cylindrical acoustic cavity are listed in Table 2.1. Thus the coefficient p_j is given by

$$\frac{1}{p_j}=\frac{J_m(\pi\alpha_{mn})}{\sqrt{\varepsilon_{km}}}\sqrt{1-\left(\frac{m}{\pi\alpha_{mn}}\right)^2}\,, \tag{2.37}$$

where $\varepsilon_{00}=1$, $\varepsilon_{01}=\varepsilon_{10}=2$ and $\varepsilon_{km}=4$ for $k+m>1$. The eigenfrequencies are the same for an open-open and closed-closed cylindrical cavity and given by

$$\omega_j=2\pi f_j=\pi c_s\sqrt{(k/L)^2+(\alpha_{mn}/R_c)^2}\,. \tag{2.38}$$

The eigenvalues (*k, m, n*) represent the longitudinal, azimuthal and radial indices of the acoustic resonant mode.

Table 2.1 Values of $\pi\alpha_{mn}$ for the first several azimuthal and radial modes of a cylindrical acoustic cavity.

$\pi\alpha_{mn}$	n=0	n=1	n=2	n=3	n=4
m=0	0	3.8318	7.0156	10.1734	13.3236
m=1	1.8412	5.3315	8.5364	11.7060	14.8636
m=2	3.0543	6.7062	9.9695	13.1703	16.3476
m=3	4.2012	8.0153	11.3460	14.5858	17.7888
m=4	5.3176	9.2824	12.6819	15.9642	19.1961

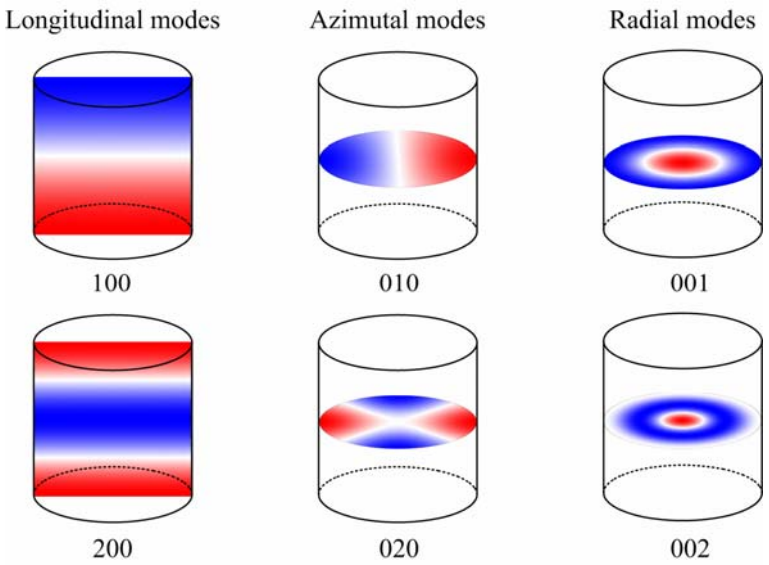

Figure 2.4 The first two longitudinal, azimuthal and radial eigenmodes for acoustic wave in a both-ends closed cylindrical acoustic cavity. The light color areas denote the nodes of the acoustic wave while the deep color (red or blue) areas represent the antinodes of the acoustic wave.

The first two eigenmodes for the pure longitudinal, azimuthal and radial modes in a closed-closed cylindrical acoustic cavity are shown in Figure 2.4. It can be found from Eq. (2.38) that the resonant frequencies of the longitudinal modes are overtones of the fundamental mode, i.e., $\omega_{k00}=k\pi c_s/L=k\omega_{100}$, while the azimuthal and radial modes are not, which are determined by the Bessel functions.

The acoustic pressure $p(\mathbf{r},\omega)$ in the gas cell is the sum of all the eigenmodes as

$$p(\mathbf{r},\omega)=\sum_j A_j(\omega)p_j(\mathbf{r},\omega). \tag{2.39}$$

Substituting Eq. (2.39) in Eq. (2.32) and considering that $p_j(\mathbf{r},\omega)$ is a solution of the homogeneous wave equation, we obtain

$$\sum_j A_j(\omega^2-\omega_j^2)p_j(\mathbf{r},\omega)=i\omega(\gamma-1)H(\mathbf{r},\omega). \tag{2.40}$$

By multiplying $p_j^*(\mathbf{r},\omega)$ on both sides of the equation and integrating it over the whole cavity, we can get the amplitude of the mode $p_j(\mathbf{r},\omega)$ as

$$A_j(\omega)=-i\omega\frac{\gamma-1}{V_c}\frac{\int p_j^*(\mathbf{r},\omega)H(\mathbf{r},\omega)dV}{\omega_j^2-\omega^2}, \tag{2.41}$$

The integral on the right-hand side of Eq. (2.41) demonstrates the coupling between the acoustic normal mode and heat source. It seems that $A_j(\omega)$ will become infinite as ω approaches ω_j from Eq. (2.41). It is physically unreasonable because of the neglecting of acoustic loss in Eq. (2.31). This problem might be corrected by introducing a quality factor Q_j into Eq. (2.41) as

$$A_j(\omega)=-i\omega\frac{\gamma-1}{V_c}\frac{\int p_j^*(\mathbf{r},\omega)H(\mathbf{r},\omega)dV}{\omega_j^2-\omega^2-i\omega\omega_j/Q_j}. \tag{2.42}$$

The quantitative achievement of Q_j will be discussed in section 2.5.

In order to connect the acoustic signal with the absorption, we need to replace

$H(\mathbf{r},\omega)$ in Eq. (2.42) by using Eq. (2.22) and (2.23) as

$$A_j(\omega)=-i\omega\frac{\gamma-1}{V_c}\frac{\alpha P_0 L}{\omega_j^2-\omega^2-i\omega\omega_j/Q_j}\frac{1}{L}\int p_j^*(\mathbf{r},\omega)g(\mathbf{r},\omega)dV\,, \tag{2.43}$$

where light intensity

$$I_0(\mathbf{r},\omega)=P_0 g(\mathbf{r}) \tag{2.44}$$

is expressed as the total optical power P_0 and normalized distribution $g(\mathbf{r})$. The photoacoustic signal is proportional to the absorption coefficient, optical power, absorption length, and inversely proportional to cavity volume and modulation frequency.

In most cases, the light beam is Gaussian profile with radius of *a*, so

$$g(\mathbf{r})=\frac{2}{\pi a^2}\exp\left(-2\frac{r^2}{a^2}\right), \tag{2.45}$$

and the integral in Eq. (2.43) becomes

$$I_j=\frac{1}{L}\int p_j^*(\mathbf{r},\omega)g(\mathbf{r},\omega)dV=p_j e^{-\mu_j}\,, \tag{2.46}$$

where p_j is the normalization coefficient defined by Eq. (2.37) and $1/\mu_j$ is the coupling factor between the optical beam and the acoustic mode $p_j(\mathbf{r},\omega)$. The acoustic energy is proportional the square of pressure and given by [11]

$$E_j(\omega)=\frac{\left|A_j(\omega)\right|^2}{\rho c_s^2}=\frac{(\gamma-1)^2(\alpha P_0 L p_j e^{-\mu_j})^2}{\rho c_s^2 V_c^2}\frac{\omega^2}{\left(\omega_j^2-\omega^2\right)^2+\left(\omega\omega_j/Q_j\right)^2}\,, \tag{2.47}$$

Near the resonant frequency ω_j,

$$\omega_j^2-\omega^2=\left(\omega_j-\omega\right)\left(\omega_j+\omega\right)\approx 2\omega_j\left(\omega_j-\omega\right), \tag{2.48}$$

so the acoustic energy is given by

$$E_j(\omega)=\frac{\left|A_j(\omega)\right|^2}{\rho c_s^2}=\frac{(\gamma-1)^2(\alpha P_0 L p_j e^{-\mu_j})^2}{4\rho c_s^2 V_c^2}\frac{1}{\left(\omega_j-\omega\right)^2+\left(\omega_j/2Q_j\right)^2}\,, \tag{2.49}$$

which shows a Lorentzian distribution with a half-width at half-maximum (HWHM) given by

$$\Delta\omega_j=\omega_j/2Q_j, \tag{2.50}$$

coherent with the definition of quality factor

$$Q_j=\omega_j/2\Delta\omega_j. \tag{2.51}$$

From Eq. (2.43) and (2.46), the acoustic signal at the resonant frequency becomes

$$A_j(\omega_j)=\frac{Q_j}{\omega_j}\frac{\alpha P_0(\gamma-1)p_jL}{V_c}e^{-\mu_j}. \tag{2.52}$$

As the modulation frequency is tuned to one of the eigenfrequencies of the acoustic cavity, the absorbed optical energy for many cycles is accumulated in the cavity as an acoustic standing wave and the cavity acts as an acoustic amplifier. The amplification is equal to the quality factor Q_j, which is determined by the total losses of the resonator. In other words, the acoustic amplitude at resonance is Q_j times larger than that out of resonance.

Assuming that the light absorption and acoustic generation happens in a one-pass cylindrical cavity with light beam passing along the axis of the cylinder, Eq. (2.52) can be expressed by considering Eq. (2.51) as

$$A_j(\omega_j)=\frac{\alpha P_0(\gamma-1)p_j}{2\pi R_c^2\Delta\omega_j}e^{-\mu_j}. \tag{2.53}$$

The acoustic pressure is inversely proportional to the square of the cylindrical cavity radius, which implies that the acoustic signal could be greatly enhanced by reducing the cavity diameter. However, as the diameter of the resonator decreases to a specific value, the losses of the resonator becomes significant, which greatly broadens the acoustic resonant line width, i.e., $\Delta\omega_j$ increases fast to counteract the effect of resonator thining. This part will be discussed in section 2.5 in detail.

The acoustic signal at 0^{th}-order resonance (k=m=n=0, ω_0=0) corresponds to a uniform acoustic pressure variation in the cell as

$$p(\mathbf{r},t)=A_0(\omega)e^{i\omega t}, \tag{2.54}$$

with

$$A_0(\omega)=\frac{i}{\omega}\frac{\gamma-1}{V_c}\alpha P_0 L. \tag{2.55}$$

This is the case of non-resonance, which happens for the modulation frequency is much smaller than the lowest resonant frequency. The dimension of the gas cell is far smaller than the acoustic wavelength at modulation frequency, so the acoustic wave can not propagate and the standing wave can not be formed.

It is shown in Eq. (2.55) that the acoustic signal at non-resonance is proportional to absorption coefficient and optical power, which is the same as the resonance case, but inversely proportional to the modulation frequency and area of the cross section of the gas cell. This might be an efficient approach for acoustic signal generated and detected in a tiny cavity with a low modulation frequency.

To compare the efficiency of non-resonance configuration and resonance configuration, the amplitude over of the two acoustic signals is expressed below with assumption that the acoustic mode excitation is optimal (μ_j<<1) and $\alpha P_0/V_c$ is identical for both of them

$$\left|\frac{p_j(\mathbf{r},\omega_j)}{p_0(\mathbf{r},\omega)}\right|=\frac{\omega}{\omega_j}p_j Q_j. \tag{2.56}$$

It reveals that the resonance configuration can provide a much larger acoustic signal due to the high quality factor of the resonator. Moreover, the noise level could be also much smaller for resonant system due to its higher operation frequency, which greatly reduces the 1/*f* noise in the system.

2.5 Loss mechanism in gas cell

2.5.1 Loss sources

Acoustic energy accumulation in the resonance cell as a standing wave is much larger than the energy loss in a single period, which is why the acoustic signal can be amplified in the gas cell. However, the amplification is limited by various acoustic dissipation processes in the cavity. Basically, the dissipation can be divided into two main categories: surface effects and volumetric effects.

Surface effects are due to the interaction between the acoustic standing wave and solid boundaries of the acoustic cavity, which mainly includes [15]:

1) Acoustic wave reflection losses on the surface of the cavity wall due to its compliance;
2) Thermal and viscous dissipation inside the boundary layers at the smooth internal surface;
3) Losses due to the introduction of microphone;
4) Dissipation due to wave scattering at the surface obstructions such as gas inlet/outlet, microphone, light windows, etc.

Wave reflection losses are related to the gas density, sound velocity and the cavity material, which can be determined by acoustic laws [14]. By carefully selecting the rigid cavity material, these losses can be controlled at a relatively low level. The losses at the microphone due to its vibration and energy conversion are interrelated with the acoustic resonance setup in the cavity and depend on the microphone type, size and material. Fortunately, since most of the microphone surface (~ mm^2) is much smaller than the cavity surface, these losses can be neglected [15].

Thermal and viscous dissipation are significant in limiting the acoustic amplification, especially for the longitudinal resonance mode with a thin resonator.

Thermal dissipation occurs due to the nonadiabatic process of heat expansion and contraction near the wall of resonator because of its high thermal conductivity. This process happens in a heat conduction transition region, known as thermal boundary layer. The thickness of the thermal boundary layer is given by [14]

$$d_{th,j}=\sqrt{\frac{2KM}{\rho_0\omega_j C_p}}, \tag{2.57}$$

where is K gas thermal conductivity, M is the molar mass of the gas and C_p is the heat capacity at constant pressure.

Similarly, viscous dissipation happens in the transition layer of the velocity field in the gas cell, known as viscous boundary layer. In the inner volume of gas cell, the acoustic velocity is proportional the gradient of the pressure, while at the surface, the tangential component of the acoustic velocity is zero because of the viscosity η. The thickness of the viscous boundary layer is expressed as

$$d_{\eta,j}=\sqrt{\frac{2\eta}{\rho_0\omega_j}}. \tag{2.58}$$

The thermal and viscous boundary layers are both inversely proportional to the square root of the resonant frequency. They can be expressed in a simple form at atmospheric air and standard temperature as

$$d_{th}=\sqrt{\frac{2KM}{\rho_0\omega C_p}}\approx 2.5\frac{1}{\sqrt{f}}\ \ [mm], \tag{2.59a}$$

$$d_{\eta}=\sqrt{\frac{2\eta}{\rho_0\omega}}\approx 2.1\frac{1}{\sqrt{f}}\ [mm]. \tag{2.59b}$$

The frequency dependence of the thicknesses of these two boundary layers is plotted in Figure 2.5. It is shown that the thicknesses of the boundary layers are very close and reduces quickly for the higher modulation frequency. For example, the boundary layer for viscosity loss is about 200 μm at 100 Hz while is reduced to 2 μm at 1 MHz.

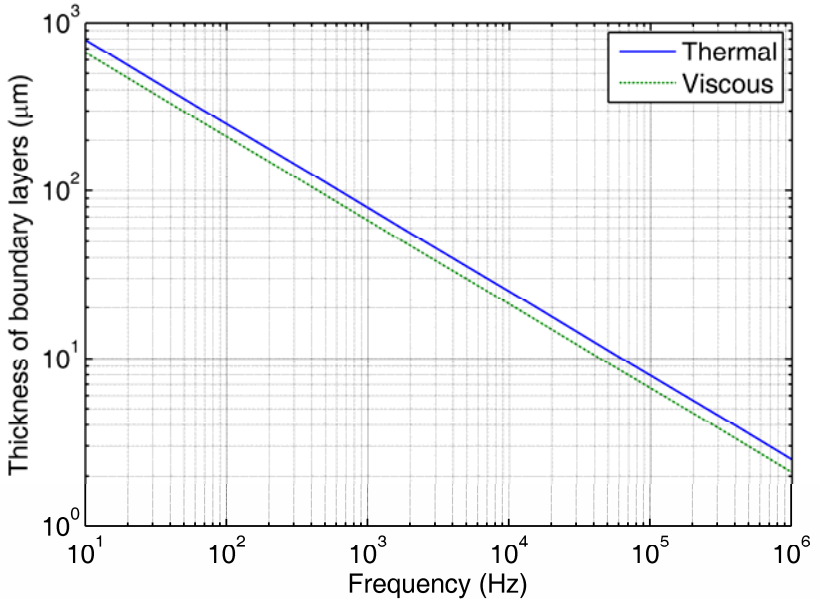

Figure 2.5 Dependence of the thickness of the thermal and viscous boundary layers on modulation frequency.

It should be noticed that there is no viscosity loss on the lateral surface for the pure radial modes (*k=m=0*) because sound velocity contains only a radial component. The total energy loss is thus much lower for radial modes than longitudinal and azimuthal modes for a properly designed gas cell. That is why extremely high quality factors (~ 2000-10000) can be achieved for carefully designed spherical resonators [16], in which only radial resonant modes exist.

Another source of acoustic dissipation is the volumetric losses, including free space thermal and viscous dissipation, diffusion effects, relaxation and radiation losses, etc., which caused by processes that tend to establish equilibrium in the propagating acoustic wave [14]. Thermal losses could be resulted from the transfer of organized energy into dispersed heat due to the temperature gradient in the gas while viscous losses is caused by the friction induced by molecular compressional motion. Diffusion effects are usually negligible [17] but molecular relaxation is much more important when acoustic wave propagates through polyatomic gases. Losses caused by molecular relaxation is greatly affected by the presence, even in

small quantities, of certain polyatomic impurities like water vapor, which greatly affect the energy transfer rates between translational, vibrational and rotational states. The determination of the relaxation time of energy transfer processes among different gas components, possibly done from the resulting dispersion frequency and the strong broadening of the resonance profile [18], plays an important role in accurately prediction the relaxation losses. The last radiation dissipation is negligible for a closed acoustic cavity due to the perfect reflection of the sound at the walls.

2.5.2 Influence on quality factor

Quality factor Q is an important parameter that determines the acoustic amplification in an acoustic resonator. The physical definition of Q is [17]

$$Q = \frac{2\pi \cdot accumulated\ energy}{energy\ lost\ over\ one\ period} = \frac{f_0}{\Delta f}, \tag{2.60}$$

where f_0 is the resonant frequency and Δf is the line width of the resonance profile. Quality factor is mainly determined by the surface losses and volumetric losses. For a cylindrical cavity, the quality factor contributed by surface losses is given by [18]

$$Q_{surf,j} = \frac{\omega_j}{\rho_0 c_s^2} \frac{\int \left| p_j(\mathbf{r},\omega_j) \right|^2 dV}{\frac{1}{2} R_{\eta,j} \int \left| u_{\parallel}(\mathbf{r},\omega_j) \right|^2 ds + \frac{1}{2} R_{th,j} \int \left| p_j(\mathbf{r},\omega_j) \right|^2 ds}, \tag{2.61}$$

where

$$R_{\eta,j} = \rho_0 \omega_j d_{\eta,j}, \tag{2.62a}$$

$$R_{th,j} = \frac{\gamma - 1}{\rho_0 c_s^2} \omega_j d_{th,j}, \tag{2.62b}$$

$d_{th,j}$ and $d_{\eta,j}$ are given by Eq. (2.57) and (2.58), respectively.

For pure radial and longitudinal modes, Eq. (2.61) is shown as the following equations, respectively:

$$Q_{surf,j}^{rad} = \frac{L}{d_{\eta,j} + (\gamma - 1) d_{th,j} (1 + L / R_c)}, \tag{2.63}$$

$$Q_{surf,j}^{long} = \frac{R_c}{d_{\eta,j} + (\gamma - 1) d_{th,j} (1 + 2R_c / L)}. \tag{2.64}$$

Quality factor contributed by volumetric losses can be expressed by

$$\frac{1}{Q_{vol,j}} = \frac{\omega_j}{2c_s^2} \left[\frac{4}{3} \frac{\eta}{\rho_0} + (\gamma - 1) \frac{\kappa}{\rho_0 C_p} + \frac{\eta_b}{\rho_0} \right], \tag{2.65}$$

where κ is compressibility, and η_b is an effective viscosity coefficient that contains the effect of relaxation losses.

The total quality factor that contains both surface and volumetric losses is then given by

$$\frac{1}{Q} = \frac{1}{Q_{surf}} + \frac{1}{Q_{vol}}. \tag{2.66}$$

When gas pressure is higher than 0.1 atm, the relaxation processes are negligible and the surface losses are dominant in PAS systems [19]. Therefore, the quality factor in Eq. (2.66) approaches surface quality factor given in Eq. (2.61).

2.6 Summary

In this chapter, we have introduced the basic principle of PAS. As the PAS method is also an absorption spectroscopy, the intensity and profile of gas absorption line is introduced. Starting from the photoacoustic effect in gases, we provide the derivation of acoustic generation and resonance in a cylindrical cavity in detail. The loss scheme in a cylindrical PA cell is also discussed at end of this chapter.

References of Chapter 2

1. G. Stewart, J. Norris, D. F. Clark, and B. Culshaw, “Evanescent-wave chemical

sensors-a theoretical evaluation," *Int. J. Optoelectron.* 6, 227-238 (1991).

2. J.-P. Besson, *Photoacoustic spectroscopy for multi-gas sensing using near infrared lasers*, Ph.D. Thesis, Swiss Federal Institute of Technology, 2006.
3. L. S. Rothman, I. E. Gordon, A. Barbe, D. C. Benner, P. F. Bernath, M. Birk, V. Boudon, L. R. Brown, A. Campargue, J.-P. Champion, K. Chance, L. H. Coudert, V. Dana, V. M. Devi, S. Fally, J.-M. Flaud, R. R. Gamache, A. Goldman, D. Jacquemart, I. Kleiner, N. Lacome, W. Lafferty, J.-Y. Mandin, S. T. Massie, S. N. Mikhailenko, C. E. Miller, N. Moazzen-Ahmadi, O. V. Naumenko, A. V. Nikitin, J. Orphal, V. I. Perevalov, A. Perrin, A. Predoi-Cross, C. P. Rinsland, M. Rotger, M. Simeckova, M. A. H. Smith, K. Sung, S. A. Tashkun, J. Tennyson, R. A. Toth, A. C. Vandaele, J. V. Auwera, "The HITRAN 2008 molecular spectroscopic database," *J. Quant. Spectrosc. Radiat. Transf.* 110, 533-572 (2009).
4. J. J. Olivero and R. L. Longbothum, "Empirical fits to the Voigt line width: A brief review," *J. Quant. Spectrosc. Radiat. Transf.* 17, 233-236 (1977).
5. F. Mayinger and O. Feldmann, *Optical measurements-techniques and applications (Heat and mass transfer)*, 2nd ed. (Springer, ISBN: 3-540-66690-7, 2001).
6. A. Miklos, S. Schäfer, and P. Hess, *Photoacoustic spectroscopy, Theory*, in Encyclopedia of Spectroscopy and Spectrometry (Academic Press, New York, 1999).
7. L. B. Kreuzer, *The physics of signal generation and detection*, in Optoacoustic Spectroscopy and Detection, Y-H. Pao, Ed. (Academic Press, New York, 1977).
8. P. Hess, "Resonant photoacoustic spectroscopy," *Top. Curr. Chem.* 111, 1-32 (1983).
9. A. C. Tam, *Ultra sensitive laser spectroscopy*, (Academic press, New York, 1983).
10. P. L. Meyer and M. Sigrist, "Atmospheric pollution monitoring using CO_2-laser

photoacoustic spectroscopy and other techniques," *Rev. Sci. Instrum.* 61, 1779-1807 (1990).

11. J. P. M. Trusler, *Physical acoustics and metrology of fluids*, Series in Measurement Science and Technology (Bristol, 1991).
12. W. B. Jackson, N. M. Amer, A. C. Boccara, and D. Fournier, "Photothermal detection spectroscopy and detection," *Appl. Opt.* 20, 1333-1344 (1981).
13. A. C. Tam, "Applications of photoacoustic sensing techniques," *Rev. Mod. Phys.* 58, 381-431 (1986).
14. P. M. Morse and K. U. Ingard, *Theoretical Acoustics*, (McGraw-Hill, New York, Chap. 6, 1968).
15. R. D. Kamm, "Detection of weakly absorbing gases using a resonant optoacoustic method," *J. Appl. Phys.* 47, 3550-3558 (1976).
16. J. B. Mehl and M. R. Moldover, "Precision acoustic measurements with a spherical resonator: Ar and C_2H_4," *J. Chem. Phys.* 74, 4062-4077 (1981).
17. A. Miklós, P. Hess, and Z. Bozóki, "Application of acoustic resonators in photoacoustic trace gas analysis and metrology," *Rev. Sci. Instrum.* 72, 1937-1955 (2001).
18. A. Karbach and P. Hess, "High precision acoustic spectroscopy by laser excitation of resonator modes," *J. Chem. Phys.* 83, 1075-1084 (1985).
19. C. F. Dewey Jr, *Design of optoacoustic systems*, in Optoacoustic Spectroscopy and Detection, edited by Y-H. Pao (Academic Press, New York, 1977).

Chapter 3

Theoretical description of quartz-enhanced photoacoustic spectroscopy

3.1 Introduction

Quartz-enhanced photoacoustic spectroscopy, or QEPAS, first proposed by Kosterev et al. in 2002 [1], is a novel photoacoustic spectroscopic gas detection technique that employs a tiny quartz tuning fork, or QTF, as the acoustic detector. The acoustic energy is accumulated in the highly resonant QTF instead of the photoacoustic resonator. The acoustic pressure causes the mechanical oscillation of the tuning fork, and results in a piezoelectric current signal via piezoelectric effect of the QTF. QTF is a frequency standard that commonly used in wrist electronic watches or clocks. Its resonant frequency is around 32.768 kHz with a quality factor ~20000 in vacuum and ~8000 at atmospheric pressure. The acoustic detection principles and acoustic enhancement in a 1-D resonance cell, and modulation method will be theoretically introduced in this chapter.

3.2 Properties of quartz tuning fork

A QTF is a tuning fork structure that made of quartz material. Typically, QTF that used in QEPAS as an acoustic detector has a dimension of 6mm×1.4mm×0.2mm, and each prong has a length of 3.8 mm and width of 0.6 mm, with a gap of 0.2 mm between them. The resonant frequency is around 32768 (i.e., 2^{15}) Hz with a quality

factor as high as 10^4 at atmospheric air due to its low oscillation loss [1]. Mechanical and electrical properties of a QTF have gained intensive investigation in relation with their application in ultrasensitive force detection and high resolution scanning microscopy [2-5].

3.2.1 Mechanical properties

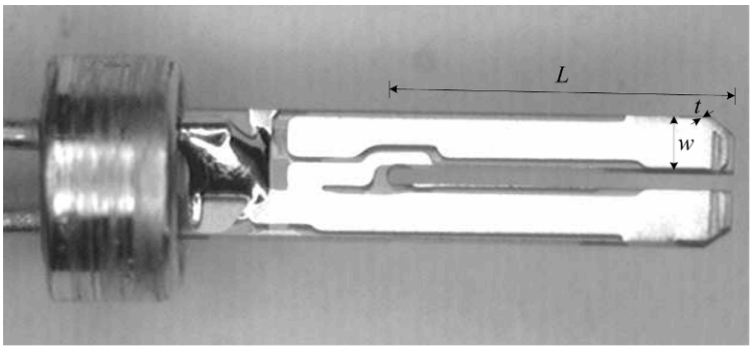

Figure 3.1 An image of a typical quartz tuning fork.

Mechanically, a QTF can be viewed as two identical cantilevers, connected by a low-loss quartz bridge as shown in Figure 3.1. When a modulated force applied at the prongs of QTF, it vibrates at the out-of-phase mode, in which the two prongs deflect at opposite direction, due to asymmetric placement of the two conducting electrodes during the fabrication. The resonant frequency of QTF can be approximated by the vibration frequency of a cantilever as [6]

$$f_0 = \frac{1}{2\pi}\sqrt{\frac{k}{m_{eff}}} \approx 1.015\frac{w}{2\pi L^2}\sqrt{\frac{E}{\rho}}, \tag{3.1}$$

where L, w, t are the length, width and thickness of the QTF prong as pictured in Figure 3.1, k is the static stiffness of the quartz cantilever given by $k = Etw^3/(4L^3)$, the effective mass m_{eff} is defined by $m_{eff} = 0.2427\rho(Lwt)$, E and ρ are the Young's modulus and density of quartz material.

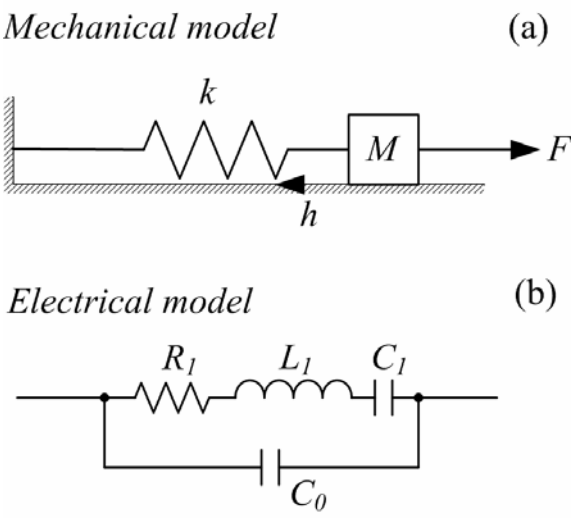

Figure 3.2 Mechanical model (a) and electrical model (b) of a QTF. k is spring constant, M is the effective mass, F is the driven force and h is the friction for mechanical model. In electrical model, R_1, L_1, C_1 are resistor, inductor and capacitor of a series RLC resonator, C_0 is the equivalent capacitance parallel to the series resonator.

The movement of the QTF prong can be described by a classical harmonic oscillator model as shown in Figure 3.2 (a). The governed equation is expressed as

$$M\frac{d^2x}{dt^2}+h\frac{dx}{dt}+kx=Fe^{i\omega t}, \tag{3.2}$$

where x is the displacement of the prong, mass m is equal to the effective mass of QTF prong and spring constant k can be replaced by the stiffness of QTF, the damping term h is originated from the friction of prong vibration with ambient air. The solution of Eq. (3.2) has a form of

$$x(t)=\frac{F/M}{\omega_0^2-\omega^2+i\omega_0\omega/Q}e^{i\omega t}, \tag{3.3}$$

where $\omega_0=\sqrt{k/M}$ is the resonant frequency, $Q=\sqrt{kM}/h$ is the quality factor. The amplitude of displacement can be expressed as

$$|x|=\frac{F/M}{\sqrt{\left(\omega_0^2-\omega^2\right)^2+\left(\omega_0\omega/Q\right)^2}}. \tag{3.4}$$

It should be noticed that the maximum value of displacement happens at a frequency

$$\omega_{x_{\max}} = \omega_0 \sqrt{1 - \frac{1}{2Q^2}}, \tag{3.5}$$

a little bit lower than the resonant frequency, which corresponding to the maximum displacement of

$$x_{\max}(t) = \frac{F}{\omega_0 h} / \sqrt{1 - \frac{1}{4Q^2}} \exp\left[i(\omega t + \theta_{x_{\max}}) \right], \tag{3.6}$$

where

$$\theta_{x_{\max}} = \arctan\left(-2Q \sqrt{1 - \frac{1}{2Q^2}} \right) \approx -\frac{\pi}{2}, \tag{3.7}$$

is the phase delay of displacement compared to the driving force.

The maximum displacement of QTF is proportional to the applied force and inversely proportional to the friction coefficient. The frequency dependent displacement of QTF by amplitude and phase delay to driving force is plotted in Figure 3.3. It is shown that the phase of displacement varies drastically at the resonance peak and it is about -90° at the resonant frequency.

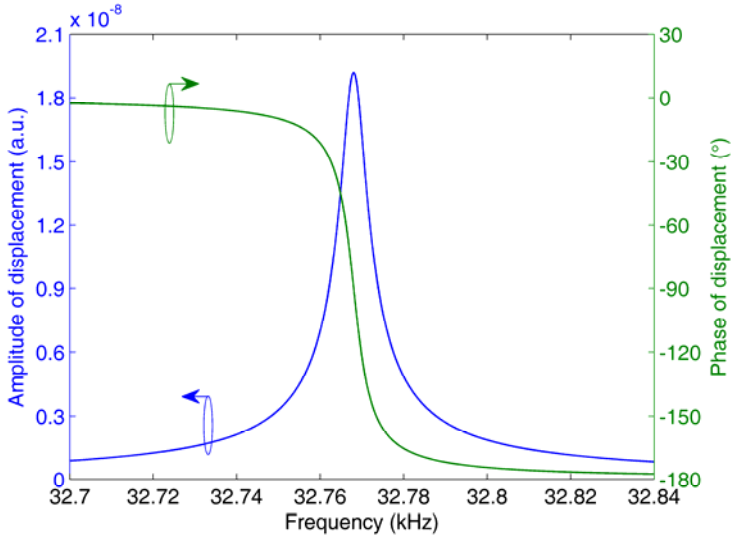

Figure 3.3 Diagram of the frequency response of the amplitude and phase of the QTF vibration.

3.2.2 Electrical properties

The QTF can be also operated at electrical mode as an AC voltage added to it. The electrical model of it can be described by a damped series *RLC* resonant circuit as shown in Figure 3.2 (b). The series R_1, L_1 and C_1 are equivalent resistance, inductor and capacitance of the QTF. The parallel capacitance C_0 is a package capacitance acting as a damping term which results in an anti-resonance at a frequency above the resonant frequency as demonstrated by Qin et al. [7]. The conductance of the equivalent electrical mode is

$$\begin{aligned} Y(\omega) &= j\omega C_0 + \frac{1}{R_1 + j\omega L_1 + 1/j\omega C_1} \\ &= j\omega C_0 + \frac{\omega^2 C_1^2 R_1 + j(1-\omega^2/\omega_0^2)\omega C_1}{(1-\omega^2/\omega_0^2)^2 + \omega^2 R_1^2 C_1^2} \end{aligned}, \tag{3.8}$$

where $\omega_0 = 1/\sqrt{L_1 C_1}$ is the resonant angular frequency of this electrical mode. The current of electrical mode determined by Eq. (3.8) is plotted near the resonant frequency for its amplitude and phase as shown in Figure 3.4. The anti-resonance is clearly seen above the resonant frequency at

$$f_a = f_0\sqrt{1 + C_0/C_1}, \tag{3.9}$$

where $f_0 = \omega_0/2\pi$ is resonant frequency. The current will achieve its minimum value at anti-resonant frequency. When the frequency of the driving source is away from the resonant frequency, the electrical model is dominated by the parallel package capacitance, resulting a conductance of $Y_0(\omega) = j\omega C_0$.

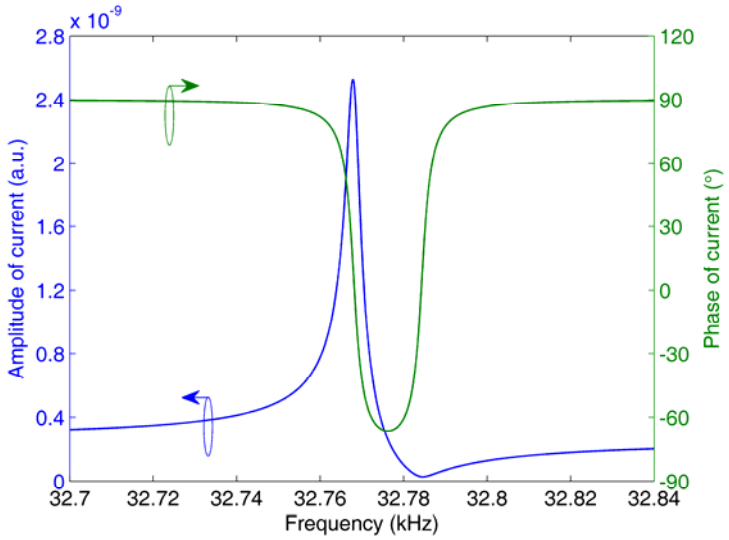

Figure 3.4 Diagram of the frequency response of the current signal for a QTF.

The anti-resonance of QTF can be eliminated by placing a proper capacitance parallel to the electrical model with anti-phase voltage, and then the current is transferred to voltage through a transimpedance amplifier with a feedback resistance of R_f and a capacitance of C_f as shown in Figure 3.5. The gain curve is expressed by

$$G(f) = V_{out} / U = Z_g Y(f) = \frac{Z_g}{R_1} \frac{f_0 f}{Q} / \sqrt{\left(f_0^2 - f^2\right)^2 + \left(\frac{f_0 f}{Q}\right)^2}, \qquad (3.10)$$

where $Q = \sqrt{L_1 / C_1} / R_1$ is the quality factor and $Z_g = R_f \sqrt{1 + (2\pi f R_f C_f)^2}$ is the gain impedance. The resonance curve exhibits a perfect Lorentzian profile with a maximum gain of $G_{\max} = Z_g / R_1$ at the resonant frequency. Thus the variable capacitance gives the value of C_0 (~ pF). f_0, Q and $G_{\max}$ can be found out from the Lorentzian fit of the resonance curve. Therefore, the values of the series *RLC* resonator are yielded by $R_1 = Z_g / G_{\max}$ (~ 100 kΩ), $L_1 = R_1 Q / (2\pi f_0)$ (~ 10 kH) and $C_1 = 1/(4\pi^2 f_0^2 L_1)$ (~ fF) [7].

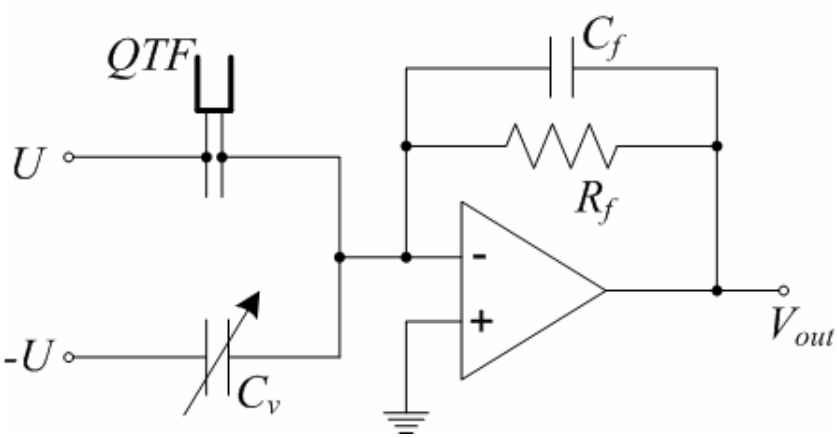

Figure 3.5 Measurement setup for the determination of equivalent quantities of the electrical model of QTF. U is the driving voltage; a variable capacitance parallel to QTF is used to eliminate the package capacitance of QTF, and a transimpedance amplifier with a feedback resistance R_f and a parallel capacitance C_f to convert the current into voltage.

3.2.3 Piezoelectrical properties

Table 3.1 Summary of equivalent quantities between the resonant mechanical model and electrical model shown in Figure 3.2.

Model	**Mechanical**	**Electrical**
variable	x (displacement)	q (electric charge)
derivative of variable	$v = dx/dt$ (velocity)	$i = dq/dt$ (current)
mass	M (effective mass)	L_1 (inductor)
spring constant	k (stiffness)	$1/C_1$ (capacitance)
damping	h (friction)	R_1 (resistance)
driving source	F (force)	U (voltage)
equation	$M\ddot{x} + h\dot{x} + kx = F$	$L_1\ddot{q} + R_1\dot{q} + q/C_1 = U$
quality factor	$Q = \sqrt{kM}/h$	$Q = \sqrt{L_1/C_1}/R_1$
resonant frequency	$\omega_0 = \sqrt{k/M}$	$\omega_0 = 1/\sqrt{L_1C_1}$

The comparison and corresponding parameters of mechanical and electrical model of a QTF is summarized and listed in Table 3.1. The connection between mechanical property and electrical property of QTF is governed by the piezoelectric effect of quartz material. Generally, the generated piezoelectric current of QTF is proportional to the displacement of the QTF prongs for small displacement amplitude, which is always the case in PAS trace gas detection, as [8]

$$i = \beta x \,, \tag{3.11}$$

where β is the piezoelectric coefficient of QTF representing the piezoelectric characteristics of it.

Due to the intrinsic systematic noise, there is a fundamental limit for the measurement of QTF resonance. This fundamental limit can be determined experimentally by measuring the output voltage noise with input voltage grounded as in Figure 3.5. It has been demonstrated that the noise is mainly comprised by the Johnson noise of the feedback resistor in the transimpedance amplifier,

$$\sqrt{4k_B T R_f}\ V/\sqrt{Hz}\,, \tag{3.12}$$

and thermal noise associated with mechanical dissipation in the tuning fork, which is represented by R in the equivalent series RLC resonant circuit,

$$\sqrt{4k_B T R_1}\,\frac{Z_g}{R_1}\frac{f_0 f}{Q}\Big/\sqrt{\left(f_0^2 - f^2\right)^2 + \left(\frac{f_0 f}{Q}\right)^2}\ V/\sqrt{Hz}\,, \tag{3.13}$$

where k_B is Boltzmann constant and T is temperature. The Johnson noise is dominated as the frequency is away from the resonant frequency. However, the thermal noise of QTF is dominated at the resonance due to its $\sqrt{R_f / R_1}$ times larger than the Johnson noise. Therefore, the rms voltage noise of QTF at the output of transimpedance amplifier at the resonant frequency is given by

$$\sqrt{\left\langle V_N^2 \right\rangle} = R_f \sqrt{4k_B T \Delta f / R_1}\,, \tag{3.14}$$

where Δf is the detection bandwidth, which should be far smaller than the bandwidth of QTF.

3.3 Acoustic enhancement in a 1-D resonant tube

In QTF-based PAS system, a pair of rigid tubes is usually introduced as an acoustic resonator to enhance the acoustic signal [1, 9]. The two tubes with length of *l* and inner diameter of *ID* are positioned beside the facets of QTF with a small gap as shown in Figure 3.6. Light propagates through the two tubes and the gap between the prongs of QTF for photoacoustic gas absorption. The generated acoustic wave is resonant in the tubes with an enhancement as high as 30 times by properly selecting the dimensions of resonant tubes [10]. So, the resonant tubes are also known as micro-resonator (mR).

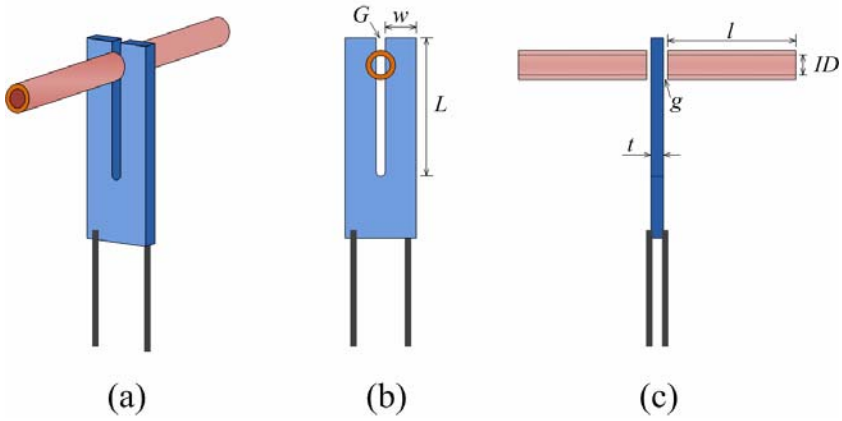

Figure 3.6 Structure design and dimension definition of the QTF and acoustic resonators. *L*, *w* and *t* are the length, width and thickness of a prong for the QTF, *G* is the gap between the two prongs. A pair of rigid tubes with each length of *l* and inner diameter of *ID* is placed on the two sides of the QTF facet with a small gap of *g* to enhance the acoustic signal. (a)-(c) are the 3D view, front view and side view of the QTF.

In order to investigate the acoustic behavior in the resonant tubes, the tubes can be simplified as a one-dimensional (1-D) resonator for the initial approximation.

This is reasonable because the gap between the two tubes is much smaller than the tube dimension and the tube diameter (usually <1 mm) is far smaller than the acoustic wavelength (~10 mm) at the operation frequency (~32.768 kHz). Thus the acoustic distribution in the cross section of the tube can be regarded as uniform. The resonant tubes are regarded as an open-open 1-D resonator that only the longitudinal modes excited in it.

The acoustic pressure in the mR is expressed by combining Eq. (2.39) and (2.43) as

$$p(\mathbf{r},\omega)=\sum_j -i\omega\frac{\gamma-1}{V_c}\frac{\alpha P_0 L}{\omega_j^2-\omega^2-i\omega\omega_j/Q_j}I_j p_j(\mathbf{r},\omega). \tag{3.15}$$

When the laser beam is modulated at one of the eigenfrequency ω_j, only the j^{th} acoustic resonance mode is excited and the contribution from other distant resonances can be neglected [11]. So the sound pressure at the position is obtained as

$$p(\mathbf{r}_M,\omega_j)=(\gamma-1)\frac{Q_j}{\omega_j}\frac{\alpha P_0 L}{V_c}I_j p_j(\mathbf{r}_M,\omega_j). \tag{3.16}$$

The acoustic signal proportional to the sound pressure can then be expressed as

$$S_{PA}=p(\mathbf{r}_M,\omega_j)=C_j(\omega_j)\alpha P_0. \tag{3.17}$$

where

$$C_j(\omega_j)=(\gamma-1)\frac{Q_j}{\omega_j}\frac{L}{V_c}I_j p_j(\mathbf{r}_M,\omega_j) \tag{3.18}$$

is a parameter that describes the resonance characteristics of the resonator, known as cell constant, and independent of the absorption coefficient and laser power.

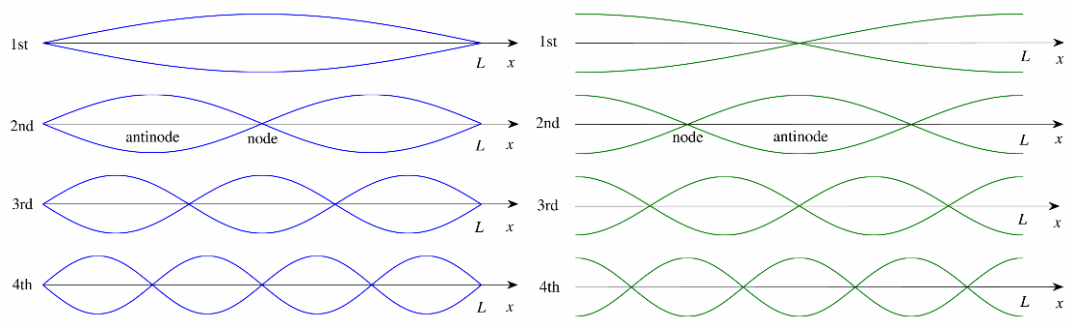

(a) (b)

Figure 3.7 First four resonance modes for 1-D (a) open-open and (b) closed-closed PA cell.

For a 1-D resonator with a length of L and inner radius of R_c, the pressure distribution in the cross section is uniform, therefore only longitudinal modes are excited. Figure 3.7 shows the first four resonance modes for open-open and closed-closed 1-D resonator, respectively. Thus, the resonant frequencies for open-open and closed-closed 1-D are given by [11]

$$f_n = \frac{nc_s}{2L_{eff}}, \quad n = 1,2,3,... \tag{3.19}$$

where L_{eff} is the effective length of resonator, which is $L_{eff} = L$ for closed-closed resonator but

$$L_{eff} = L + \frac{16}{3\pi} R_c \tag{3.20}$$

for open-open resonator by considering the additional acoustic buffering region at the open end of it. The acoustic distribution along the resonator is expressed as

$$p_n(x,\omega_n) = p_n \begin{pmatrix} \sin(n\pi x / L) \\ \cos(n\pi x / L) \end{pmatrix}, \tag{3.21}$$

for open-open and closed-closed resonators, respectively, by taking into account the acoustic resonance node at its end for open-open resonator while antinode for closed-closed resonator. Amplitude coefficient p_n is determined by

$$\int_0^L p_m^*(x,\omega_m) p_n(x,\omega_n) dx = \delta_{mn} L . \tag{3.22}$$

Therefore, we obtain $p_n = \sqrt{2}$ for both open-open and closed-closed resonators. Then, we have

$$I_n = \frac{1}{L}\int_0^L \sqrt{2}\begin{pmatrix}\sin(n\pi x/L)\\ \cos(n\pi x/L)\end{pmatrix}dx = \begin{pmatrix}\frac{\sqrt{2}}{n\pi}\left[1-(-1)^n\right]\\ 0\end{pmatrix}. \tag{3.23}$$

It is shown that the even acoustic modes in an open-open resonator and all the acoustic modes in a closed-closed 1-D resonator can not be excited. For odd acoustic modes in an open-open resonator, the cell constant in Eq. (3.18) shows a form of

$$C_n(x,\omega_n) = (\gamma-1)\frac{Q_n}{\omega_n}\frac{4}{n\pi^2 R_c^2}\sin(n\pi\frac{x}{L}),\ \ n=1,3,5,\ldots. \tag{3.24}$$

Since the first resonant mode is usually selected in QEPAS gas detection and the QTF is placed in the middle of the tubes, the cell constant is finally achieved as

$$C_1 = (\gamma-1)Q_1\frac{4L_{eff}}{\pi^3 R_c^2 c_s}. \tag{3.25}$$

When the gas detection is operated at atmospheric pressure, quality factor is mainly contributed by the surface loss. By combining Eq. (2.59) and (2.64), we obtain

$$Q_1 = \frac{R_c}{2.1+2.5(\gamma-1)(1+2R_c/L)}\sqrt{\frac{c_s}{2L_{eff}}}. \tag{3.26}$$

The resonant frequency, quality factor and cell constant of a 1-D PA cell at its first longitudinal acoustic mode is plotted in Figure 3.8. It is shown that the resonant frequency is approximately inversely proportional to the length of the cell and the frequency is over 30 kHz when the tube length is reduced down to 10 mm. Although the cell achieves a lower quality factor for the small tube radius, it results in a large enhanced cell constant, which determines the final acoustic signal as can be seen from Eq. (3.17).

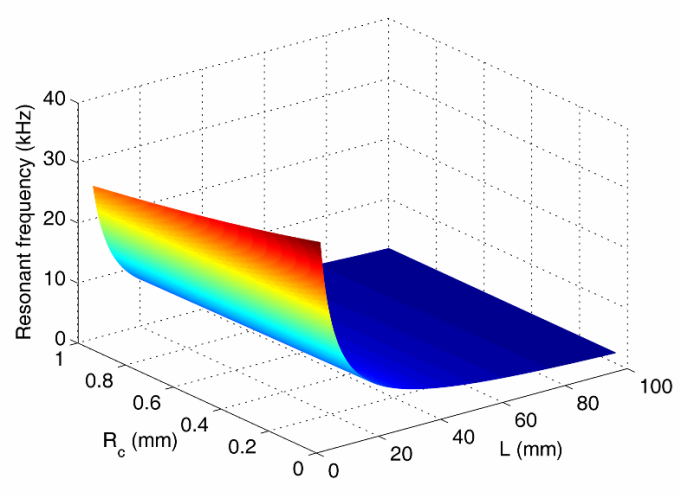

(a)

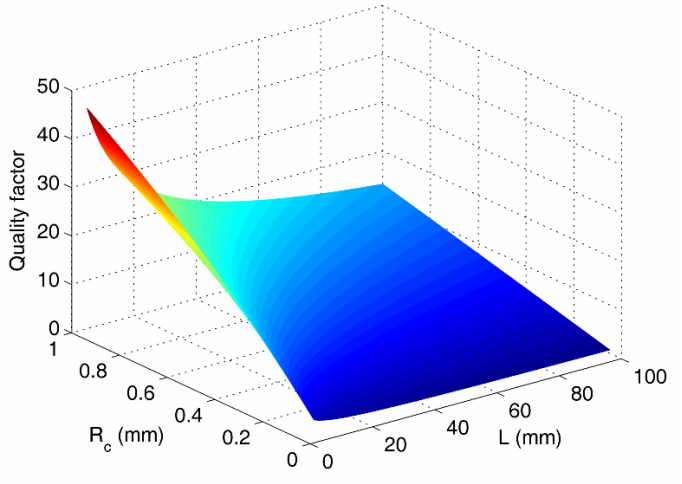

(b)

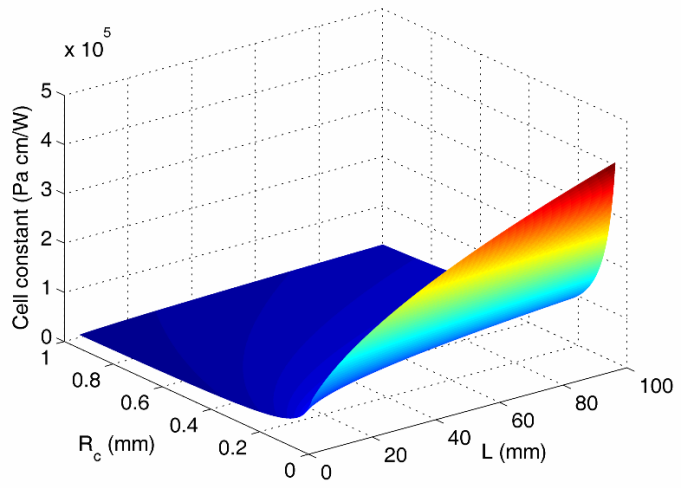

(c)

Figure 3.8 (a) Resonant frequency, (b) quality factor and (c) cell constant for 1-D PA cell with different radius and length at its first longitudinal mode.

In QTF-based PAS system, the frequency of the acoustic signal should be fixed at the resonant frequency of QTF, f_0, to ensure an efficient acoustic amplification and piezoelectrical output. Thus the effective length of the tube is optimally tailored to satisfy the resonant frequency condition as

$$L_{eff} = \frac{c_s}{2f_0} = \frac{\lambda_s}{2}, \tag{3.27}$$

where $\lambda_s = c_s / f_0$ is the sound wavelength in gas. At this frequency, the boundary layers near the inner surface of the tube are in the range of ~10 μm. To ensure a small acoustic loss, the tube radius should not be smaller than 10 times (i.e., 0.1 mm) of the boundary layer thickness. The quality factor of this resonator is several tens for tube radius less than 1 mm and the quality factor is larger with increasing tube radius as shown in Figure 3.9. However, the dependence of cell constant on tube radius displays very differently as compared to the quality factor and the cell constant increases extremely fast as the tube radius reduced down to ~ 0.2 mm. In order to find a tradeoff between the larger acoustic signal and easier assembly of the system, the tube radius is generally selected between 0.1-0.5 mm in practice.

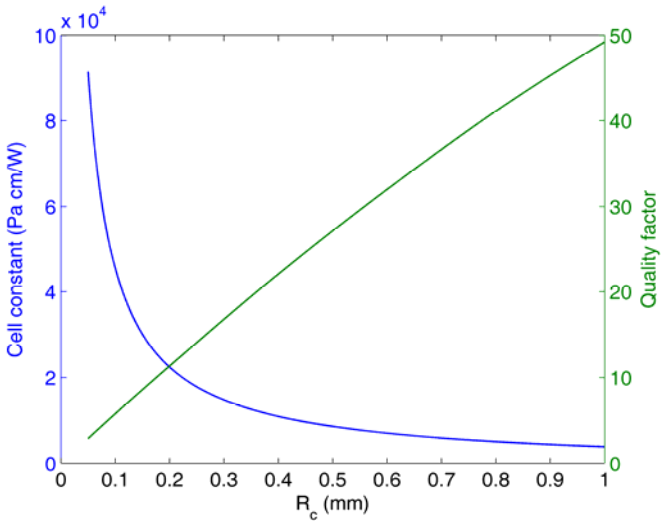

Figure 3.9 Cell constant and quality factor of the resonant tube at its first longitudinal mode.

In the initial research of QEPAS, the total length of the mR was selected to be equal to the half wavelength of sound, λ_s, in gas (~5.2 mm) by neglecting the gap influence on acoustic wave resonance and assuming the two tubes as one as shown in Figure 3.10 (a) [9]. However, subsequent study has found that the detected acoustic signal is much stronger when each tube length is equal to $\lambda_s/2$ [12]. The result suggested that the acoustic resonance in the two tubes is independent (Figure 3.10 (b)). However, an actual QEPAS mR structure should be the intermediate case with an unneglectable gap between the two tubes. The optimal length for each tube should be $\lambda_s/4<l<\lambda_s/2$ as shown in Figure 3.10 (c) [13]. Dong et al. carried out a series of experiment to investigate the dependence of acoustic signal on the tube length and diameter of the mR, even including the gap size between the tube and QTF plane [10]. And they suggested an optimal tube pairs with each tube length of 4.4 mm and inner diameter of 0.6 mm.

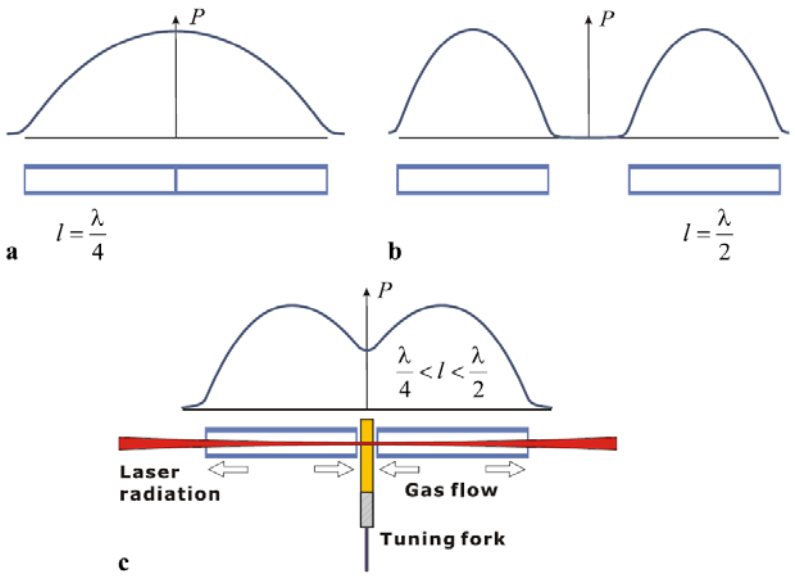

Figure 3.10 Schematic structures of the mR and acoustic distribution along the tube. (a) Two tubes stuck together without a gap; (b) two tubes separated by a large enough gap to make the acoustic wave resonate independently in the two tubes and (c) actual mR with a QTF between the two tubes. l is the length of each tube and P is the acoustic pressure [10].

3.4 Wavelength modulation method

Wavelength modulation (WM) [14-16] with second harmonic detection is generally used for acoustic signal detection in QEPAS. Compared with intensity modulation (IM), also known as amplitude modulation (AM), WM can efficiently reduce the background noise and gain high gas detection sensitivity. Different from IM-PAS modulation, where modulation of the optical power generates a localized acoustic wave with the same frequency due to photoacoustic absorption and acoustic signal is detected by the first harmonic, in WM-PAS scheme, the wavelength of the laser source is tuned to the absorption line and scanned across it periodically. Meanwhile, a sinusoidal current is injected into the laser controller to result in a modulation on the laser wavelength, which consequently induces a second harmonic acoustic wave near the absorption line center as shown in Figure 3.11. The acoustic signal is then demodulated by a lock-in amplifier with second harmonic detection.

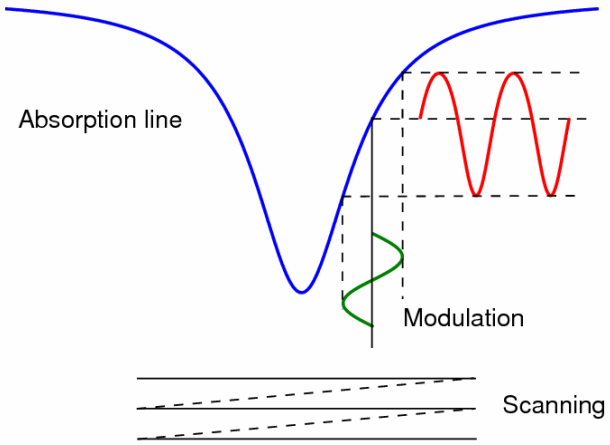

Figure 3.11 Schematic diagram of WM-PAS. The blue line is absorption line profile, the green line shows the wavelength modulation near the line center, and the red line is the induced acoustic signal.

However, for a semiconductor laser, a modulation on the laser inject current can simultaneously result in both the modulation of the laser wavelength (WM) and

optical power (IM). In most cases, the IM acts as an undesired residual signal. Therefore, IM accompanying with WM is called residual intensity modulation (RIM), which is an important effect that might affect the signal analysis.

Due to its high efficiency, WM method has been widely used in PAS for different gases detection (NH_3 [17, 18], H_2O [19, 20], CH_4 [21], etc.) with near-IR diode laser sources or mid-IR QCL [22, 23] and OPO sources [24, 25]. A theoretical description of WM-PAS was also proposed by Schilt et al. in 2006 [26]. Later, an algorithm was introduced and experimental detection for the higher harmonics of combined WM and IM spectroscopy was reported by Angelmahr et al. [27]. WM with various waveforms, sinusoidal, triangular, shaped, and quasi-square waves, was also investigated for PAS gas detection, and an enhancement factor up to 1.57 for quasi-square wave compared with conventional sinusoidal modulation [28].

A theoretical description of the WM can be started from the injected modulation current, which usually has a sinusoidal form of

$$i = i_0 \cos(\omega_m t). \tag{3.28}$$

Then, both the laser output power P (or light intensity) and wavenumber ν (or wavelength) will be modulated at the same frequency as

$$P(\nu) = P(\bar{\nu}) + \Delta P(\delta\nu)\cos(\omega_m t), \tag{3.29}$$

$$\nu = \bar{\nu} - \delta\nu \cos(\omega_m t - \psi), \tag{3.30}$$

where $\bar{\nu}$ is the central wavenumber of laser, ΔP and $\delta\nu$ are respectively the magnitudes of laser power and wavenumber modulation, ψ (>0) is the phase delay of modulated wavelength compared to the intensity modulation due to the time delay of wavelength response on varied laser inject current. The minus sign "-" before $\delta\nu$ in Eq. (3.30) shows the opposite phase between the intensity and wavenumber modulation. The phase relationships of current, laser power, wavelength and wavenumber modulation are shown in Figure 3.12.

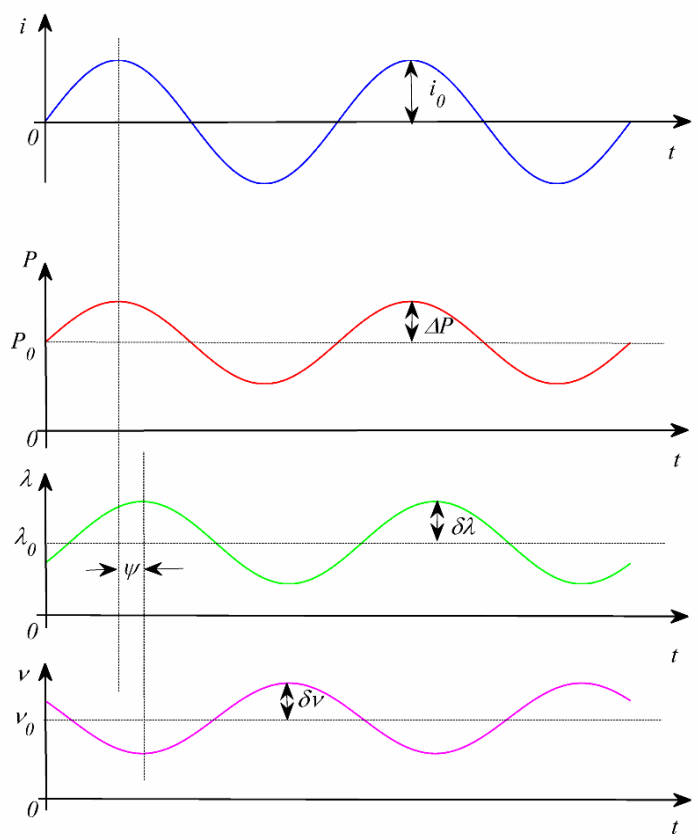

Figure 3.12 Phase relationships between inject current, laser output power, wavelength and wavenumber. ψ is the phase delay of laser wavelength compared to the output power.

By replacing the wavenumber with a normalized non-dimensional parameter as

$$\overline{x} = (\overline{\nu} - \nu_0) / \gamma_{line}, \tag{3.31}$$

where ν_0 is the wavenumber at the line center, γ_{line} ,in unit of cm^{-1},is the line width of the target absorption line, Eq. (3.29) can be rewritten as

$$P(\overline{x}) = P_0 \left(1 + p_\Omega \overline{x} + p_\omega m \cos(\omega_m t)\right), \tag{3.32}$$

where P_0 is the optical power at the center of the absorption line, p_Ω and p_ω are power coefficients for slow ramp (scanning) signal at frequency Ω and fast modulation signal at frequency ω_m, respectively, $m = \delta\nu / \gamma_{line}$ is modulation depth, γ_{line}, is absorption line width.

Since most of the absorption spectroscopic gas detection is carried out at atmospheric pressure and room temperature, the spectral shape of the absorption line approaches the Lorentzian distribution [29]. Thus the Lorentzian type absorption line is assumed in this work unless further claim made. The combination of Eq. (2.2) and (2.8) gives the absorption coefficient as

$$\alpha(\nu)=\frac{CN_{tot}S}{\pi\gamma_L}\cdot\frac{1}{1+\left[(\nu-\nu_0)/\gamma_L\right]^2}=\alpha_0\frac{1}{1+x^2}, \tag{3.33}$$

where $\alpha_0=CN_{tot}S/\pi\gamma_L$ is the peak absorption coefficient, and $x=(\nu-\nu_0)/\gamma_L$ is normalized wavenumber. The modulation of wavenumber as given in Eq. (3.30) results in a modulation of the absorption coefficient

$$\alpha(\bar{x})=\alpha_0\frac{1}{1+x^2}=\alpha_0\frac{1}{1+\left(\bar{x}-m\cos(\omega_m t-\psi)\right)^2}, \tag{3.34}$$

where

$$\begin{aligned}x&=(\nu-\nu_0)/\gamma_L=\left[(\bar{\nu}-\nu_0)-\delta\nu\cos(\omega_m t-\psi)\right]/\gamma_L\\&=\bar{x}-m\cos(\omega_m t-\psi)\end{aligned}, \tag{3.35}$$

is in the form of modulation.

To better analyze the components of absorption coefficient, Eq. (3.34) is expanded into Fourier series by

$$\alpha(\bar{x})=\alpha_0\left[H_0(\bar{x})+\sum_{n=1}^{\infty}H_1(\bar{x})\cos\left(n\omega_m t-n\psi\right)\right], \tag{3.36}$$

where

$$H_0(\bar{x})=\frac{1}{\pi}\int_0^{\pi}\frac{1}{1+\left(\bar{x}-m\cos(\theta)\right)^2}d\theta, \tag{3.37a}$$

$$H_n(\bar{x})=\frac{2}{\pi}\int_0^{\pi}\frac{\cos(n\theta)}{1+\left(\bar{x}-m\cos(\theta)\right)^2}d\theta, \tag{3.37b}$$

are the harmonic coefficients. It is shown that the *n*th harmonic will achieve its peak value at a detection phase $\Phi=-n\psi+k\pi$, where $k=0,\pm1,\pm2,\ldots$. The first four

harmonics of absorption coefficient with different modulation depth is plotted in Figure 3.13.

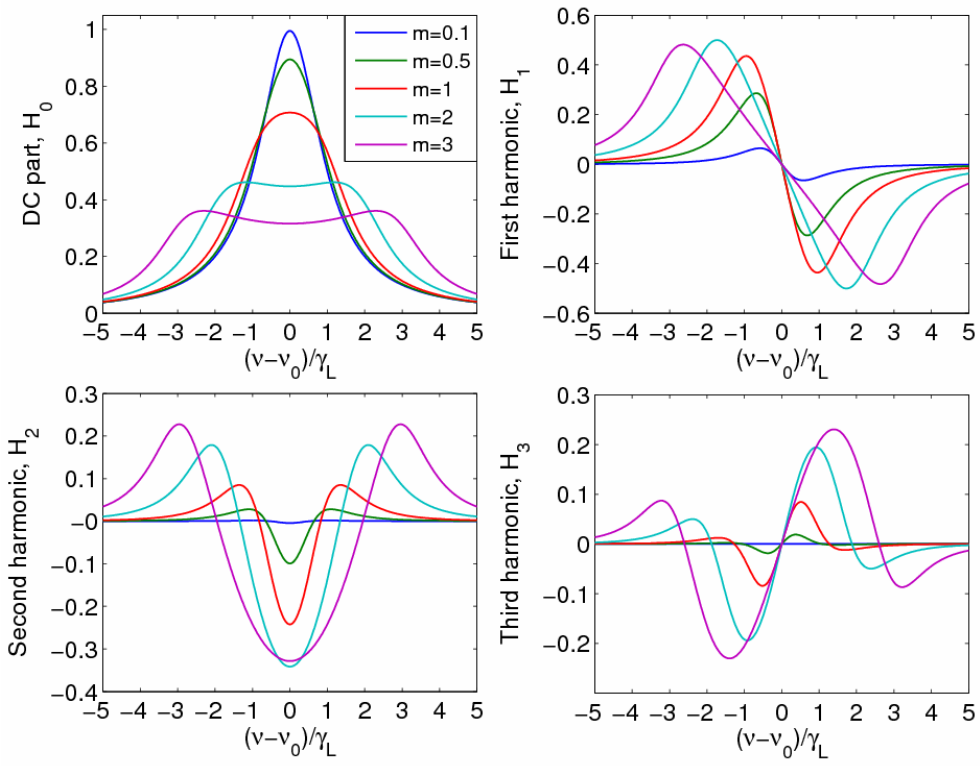

Figure 3.13 The first four harmonic coefficients for different modulation depth.

It is shown that the harmonic signals are broadened with increasing modulation depth. The value of the DC part (H_0) decreases in the central region of absorption line while increases far away from the center with increasing modulation depth. The odd harmonics exhibits a zero value at the absorption line center, while achieve their maximum value at a symmetric position away from the line center. The second harmonics shows a maximum value at the line center.

The most important harmonics is the first and second harmonics, which are usually used in IM and WM schemes, respectively. Their maximum values are depended on the modulation depth. In order to obtain a maximum acoustic signal, it is necessary to find the optimal modulation depth. Theoretical investigation has shown that the maximum value of the first harmonic (H_1) happens at [29]

$$\Delta = \pm \frac{\sqrt{3m^2+4}-1}{\sqrt{3}}, \tag{3.38}$$

where $\Delta = (\bar{\nu} - \nu_0)/\gamma_L$ is the relative walk-off from the line center, and the maximum value depended on modulation depth is expressed as

$$H_{1,\max} = \frac{\sqrt{3}}{2m} \frac{\sqrt{3m^2+4}-2}{\sqrt{\sqrt{3m^2+4}-1}}, \tag{3.39}$$

Similarly, the maximum value of the first harmonic (H_2) happens at $\Delta = 0$ and the maximum value is

$$H_{2,\max} = \frac{2}{m^2}\left(2 - \frac{m^2+2}{\sqrt{m^2+1}}\right). \tag{3.40}$$

The maximum values of H_1 and H_2 versus modulation depth m are plotted in Figure 3.14. It shows that the peak for maximum value of H_1 is 0.5002 (exactly be 0.5) at a walk-off $\Delta = \pm\sqrt{3}$ when the modulation depth is 2, and the peak for maximum value of H_2 is achieved for modulation depth equals to 2.2, the maximum value is 0.3431.

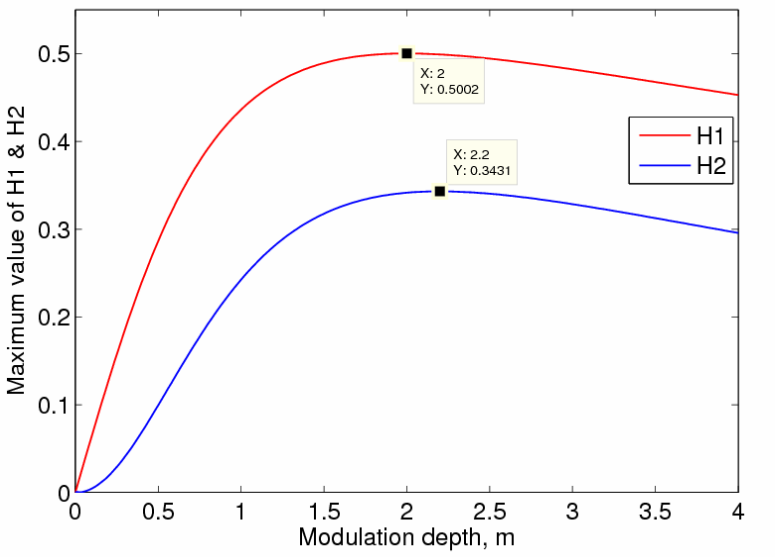

Figure 3.14 Maximum values for the first and second harmonics.

In PAS, the generated acoustic signal is proportional to the absorbed optical power in gases as can be seen from Eq. (2.39) and (2.52). Consider the case of small absorbance, the absorbed power can be derived from Beer-Lambert law as

$$P_{abs}(\nu) = P_0(\nu) - P_{out}(\nu) = P_0(\nu)\left[1 - \exp(-\alpha(\nu)L)\right] \approx P_0(\nu)\alpha(\nu)L\,. \qquad (3.41)$$

where L is the absorption length. Taking into account the intensity and wavelength modulation, Eq. (3.41) is evolved into

$$P_{abs}(\bar{x}) = P_0\alpha_0 L\left(1 + p_\Omega \bar{x} + p_\omega m\cos(\omega_m t)\right)\left[H_0(\bar{x}) + \sum_{n=1}^{\infty} H_1(\bar{x})\cos\left(n\omega_m t - n\psi\right)\right], \quad (3.42)$$

$P_{abs}(\bar{x})$ can be expanded as harmonics, and the first several harmonics are expressed from Eq. (3.42) as

$$P_{abs,DC}(\bar{x}) = P_0\alpha_0 L\left[\left(1 + p_\Omega \bar{x}\right)H_0(\bar{x}) + \frac{1}{2}p_\omega m H_1(\bar{x})\cos\left(\psi\right)\right], \qquad (3.43)$$

$$P_{abs,1f}(\bar{x}) = P_0\alpha_0 L\left[\begin{array}{l} p_\omega m H_0(\bar{x})\cos\left(\omega_m t\right) + \left(1 + p_\Omega \bar{x}\right)H_1(\bar{x})\cos\left(\omega_m t - \psi\right) \\ + \frac{1}{2}p_\omega m H_2(\bar{x})\cos\left(\omega_m t - 2\psi\right) \end{array}\right], \qquad (3.44)$$

$$P_{abs,2f}(\bar{x}) = P_0\alpha_0 L\left[\begin{array}{l} \frac{1}{2}p_\omega m H_1(\bar{x})\cos\left(2\omega_m t - \psi\right) + \left(1 + p_\Omega \bar{x}\right)H_2(\bar{x})\cos\left(2\omega_m t - 2\psi\right) \\ + \frac{1}{2}p_\omega m H_3(\bar{x})\cos\left(2\omega_m t - 3\psi\right) \end{array}\right], \qquad (3.45)$$

The harmonic in Eq. (3.43) shows the DC part of the absorbed optical power which is composed by the DC part of the absorption coefficient and first harmonic of the RIM as shown in Figure 3.15 (a). Eq. (3.44) and (3.45) shows the first and second harmonics of the absorption with each component displayed in Figure 3.15 (b) and (c).

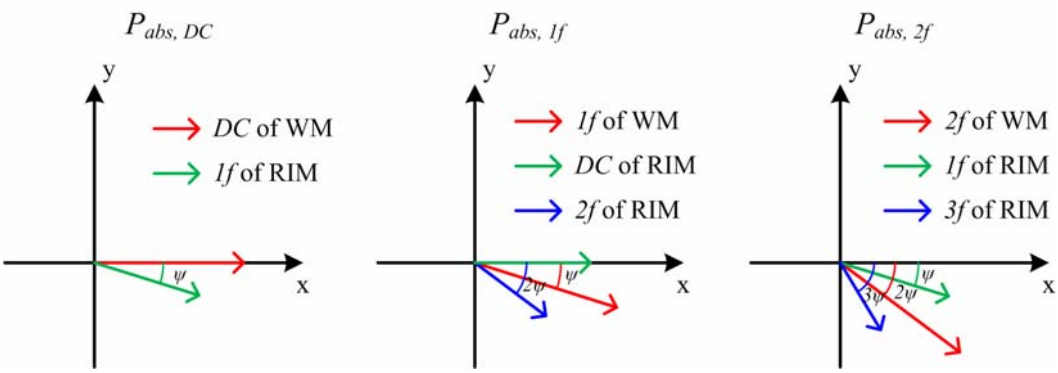

Figure 3.15 Phase relationships of the components for DC part, the first and second harmonics of the absorbed optical power in WM-PAS.

It is shown that each of the harmonic of WM is added by two harmonics of RIM with a phase shift, which will affect the signal profile and optimal detection phase for the acoustic signal. For the first and second harmonics, the signals can be decomposed into two orthogonal directions and the in-phase (p) and quadrature (q) signals with phase $-\psi$ and -2ψ respectively as

$$P_{abs,1f,p}(\bar{x}) = P_0\alpha_0 L\left[\left(1+p_\Omega\bar{x}\right)H_1(\bar{x}) + p_\omega m\left(H_0(\bar{x})+\frac{1}{2}H_2(\bar{x})\right)\cos(\psi)\right], \quad (3.46a)$$

$$P_{abs,1f,q}(\bar{x}) = P_0\alpha_0 L\left[p_\omega m\left(H_0(\bar{x})-\frac{1}{2}H_2(\bar{x})\right)\sin(\psi)\right], \quad (3.46b)$$

and

$$P_{abs,2f,p}(\bar{x}) = P_0\alpha_0 L\left[\left(1+p_\Omega\bar{x}\right)H_2(\bar{x}) + \frac{1}{2}p_\omega m\left(H_1(\bar{x})+H_3(\bar{x})\right)\cos(\psi)\right], \quad (3.47a)$$

$$P_{abs,2f,q}(\bar{x}) = P_0\alpha_0 L\left[\frac{1}{2}p_\omega m\left(H_1(\bar{x})-H_3(\bar{x})\right)\sin(\psi)\right]. \quad (3.47b)$$

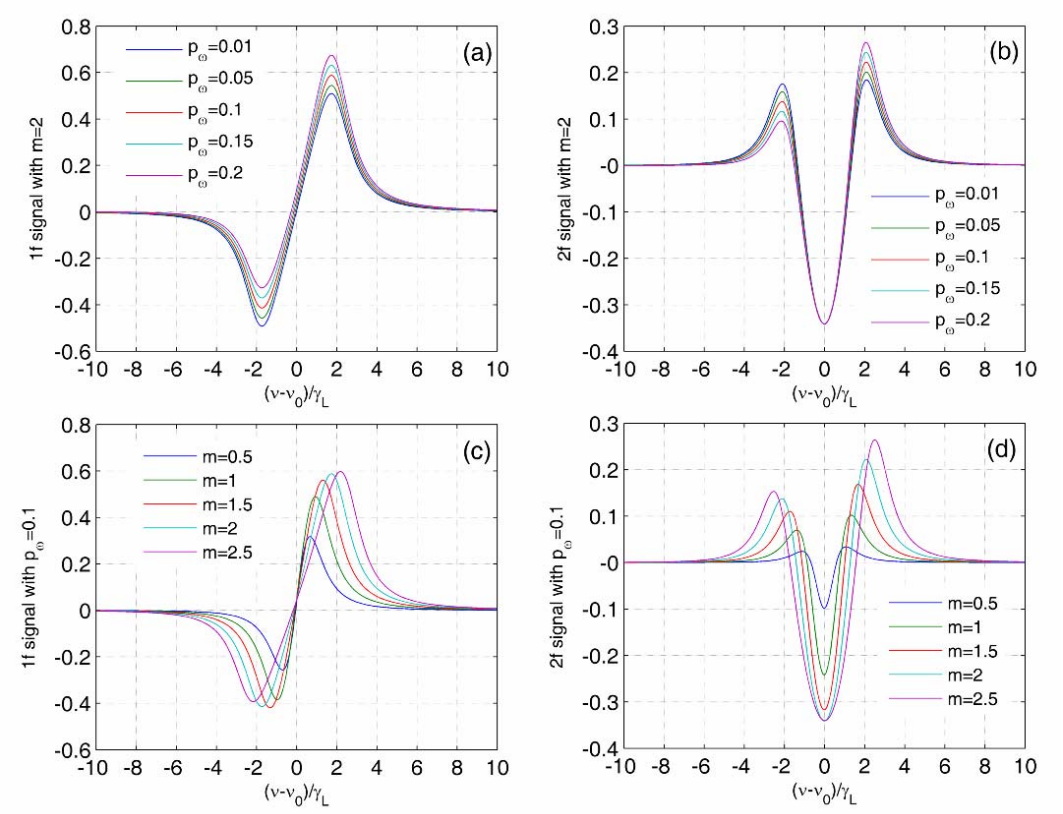

Figure 3.16 The first and second harmonic signals for different modulation depth and residual modulation intensity with a phase delay ψ=30°. (a), (c) are the first harmonic and (b), (d) are the second harmonics. For (a) and (b), the modulation depth is fixed at 2 with varied residual modulation intensity; For (c) and (d), the residual modulation intensity is fixed at p_ω=0.1 and modulation depth is varied from 0.5 to 2.5.

Figure 3.16 displays the first and second harmonic coefficients in the in-phase directions (the parts in the brace of Eq. (3.46a) and (3.47a) for different modulation depth and residual modulation intensity with a phase delay ψ=30°. It is shown that the residual modulation intensity mainly affects the relative amplitude of the two branches for the signals, which results in an asymmetric signal profile. However, the increasing modulation depth causes both the broadening and profile asymmetry of the signals. Pay attention that, in the central region of the absorption line, the second harmonic signal maintains its profile even for a large residual intensity modulation, this can be explained that the odd harmonics of the absorption coefficient has a zero

value at the line center.

In PAS gas detection, the WM is usually utilized with second harmonic detection. The *2f* PA signal for arbitrary detection phase Φ_{2f} is given by

$$S_{PA,2f}(\bar{x}) \propto P_{abs,2f}(\bar{x}) = P_{abs,2f,p}(\bar{x})\cos(\Phi_{2f} + 2\psi) + P_{abs,2f,q}(\bar{x})\sin(\Phi_{2f} + 2\psi), \tag{3.48}$$

The advantage is high sensitivity, independent signal profile on residual intensity modulation at the line center, lower environmental noise due to the second harmonic acoustic signal compared with first harmonic optical intensity noise.

3.5 Summary

In this chapter, we have demonstrated the theoretical models of QTF from mechanical, electrical and piezoelectrical properties. Then the acoustic enhancement in a 1-D resonator is approximated and discussed. The actual modulation for a semiconductor diode laser, i.e., combined wavelength modulation and residual intensity modulation, is analyzed to provide a theoretical guidance for the subsequent experiment.

References of Chapter 3

1. A. A. Kosterev, Y. A. Bakhirkin, R. F. Curl, and F. K. Tittel, “Quartz-enhanced photoacoustic spectroscopy,” *Opt. Lett.* 27, 1902-1904 (2002).
2. K. Karrai and R. D. Grober, “Piezoelectric tip-sample distance control for near field optical microscopes,” *Appl. Phys. Lett.* 66, 1842-1844 (1995).
3. J.-M., Friedt and É. Carry, “Introduction to the quartz tuning fork,” *Am. J. Phys.* 75, 415-422 (2007).
4. D. V. Serebryakov, A. P. Cherkun, B. A. Loginov, and V. S. Letokhov, “Tuning-fork-based fast highly sensitive surface-contact sensor for atomic force

microscopy near-field scanning optical microscopy," *Rev. Sci. Instrum.* 73, 1795-1802 (2002).

5. T. Akiyama, U. Staufer, N. F. de Rooij, P. Frederix, and A. Engel, "Symmetrically arranged quartz tuning fork with soft cantilever for intermittent contact mode atomic force microscopy," *Rev. Sci. Instrum.* 74, 112-117 (2003).
6. Y. Qin and R. Reifenberger, "Calibrating a tuning fork for use as a scanning probe microscope force sensor," *Rev. Sci. Instrum.* 78, 063704 (2007).
7. R. D. Grober, J. Acimovic, J. Schuck, D. Hessman, P. J. Kindlemann, J. Hespanha, A. S. Morse, K. Karrai, I. Tiemann, and S. Manus, "Fundamental limits to force detection using quartz tuning forks," *Rev. Sci. Instrum.* 71, 2776-2780 (2000).
8. J. Rychen, T. Ihn, P. Studerus, A. Herrmann, K. Ensslin, H. J. Hug, P. J. A. van Schendel, and H. J. Güntherodt, "Operation characteristics of piezoelectric quartz tuning forks in high magnetic fields at liquid helium temperatures," *Rev. Sci. Instrum.* 71, 1695-1697 (2000).
9. A. A. Kosterev, F. K. Tittel, D. V. Serebryakov, A. L. Malinovsky, and I. V. Morozov, "Applications of quartz tuning forks in spectroscopic gas sensing," *Rev. Sci. Instrum.* 76, 043105 (2005).
10. L. Dong, A. A. Kosterev, D. Thomazy, and F. K. Tittel, "QEPAS spectrophones: design, optimization, and performance," *Appl. Phys. B* 100, 627-635 (2010).
11. A. Miklós, P. Hess, and Z. Bozóki, "Application of acoustic resonators in photoacoustic trace gas analysis and metrology," *Rev. Sci. Instrum.* 72, 1937-1955 (2001).
12. S. Schilt, A. A. Kosterev, and F. K. Tittel, "Performance evaluation of a near infrared QEPAS based ethylene sensor," *Appl. Phys. B* 95, 813-824 (2009).
13. D. V. Serebryakov, I. V. Morozov, A. A. Kosterev, and V. S. Letokhov, "Laser microphotoacoustic sensor of ammonia traces in the atmosphere," *Quantum*

Electron. 40, 167-172 (2010).

14. P. Kluczynski and O. Axner, "Theoretical description based on Fourier analysis of wavelength-modulation spectrometry in terms of analytical and background signals," *Appl. Opt.* 38, 5803-5815 (1999).
15. P. Kluczynski, J. Gustafsson, Å. M. Lindberg, and O. Axner, "Wavelength modulation absorption spectrometry - an extensive scrutiny of the generation of signals," *Spectrochim. Acta Part B* 56, 1277-1354 (2001).
16. S. Schilt, L. Thevenaz, and P. Robert, "Wavelength modulation spectroscopy: combined frequency and intensity laser modulation," *Appl. Opt.* 42, 6728-6738 (2003).
17. A. Schmohl, A. Miklós, and P. Hess, "Detection of ammonia by photoacoustic spectroscopy with semiconductor lasers," *Appl. Opt*. 41, 1815-1823 (2002).
18. H. Huszár, A. Pogány, Z. Bozóki, Á. Mohácsi, L. Horváth, and G. Szabó, "Ammonia monitoring at ppb level using photoacoustic spectroscopy for environmental application," *Sens. Actuators B* 134, 1027-1033 (2008).
19. M. Szakáll, Z. Bozóki, Á. Mohácsi, A. Varga and G. Szabó, "Diode laser based photoacoustic water vapor detection system for atmospheric research," *Appl. Spectrosc.* 58, 792-798 (2004).
20. K. Song, S. Oh, E. C. Jung, D. Kim, and H. Cha, "Application of laser photoacoustic spectroscopy for the detection of water vapor near 1.38 μm," *Microchem. J.* 80, 113-119 (2005).
21. A. Boschetti, D. Bassi, E. Jacob, S. Iannotta, L. Ricci, and M. Scotoni, "Resonant photoacoustic simultaneous detection of methane and ethylene by means of a 1.63 μm diode laser," *Appl. Phys. B* 74, 273-278 (2002).
22. B. W. M Moeskops, S. M. Cristescu, and F. J. M. Harren, "Sub-part-per-billion monitoring of nitric oxide by use of wavelength modulation spectroscopy in combination with a thermoelectrically cooled, continuous-wave quantum

cascade laser," *Opt. Lett.* 31, 823-825 (2006).

23. A. Kosterev, G. Wysocki, Y. Bakhirkin, S. So, R. Lewicki, M. Fraser, F. Tittel, and R. F. Curl, "Application of quantum cascade lasers to trace gas analysis," *Appl. Phys. B* 90, 165-17 (2008).
24. A. K. Y. Ngai, S. T. Persijn, I. D. Lindsay, A. A. Kosterev, P. Groß, C. J. Lee, S. M. Cristescu, F. K. Tittel, K.-J. Boller, and F. J. M. Harren, "Continuous wave optical parametric oscillator for quartz-enhanced photoacoustic trace gas sensing," *Appl. Phys. B* 89, 123-128 (2007).
25. J. Ng, A. H. Kung, A. Miklós, and P. Hess, "Sensitive wavelength-modulated photoacoustic spectroscopy with a pulsed optical parametric oscillator," *Opt. Lett.* 29, 1206-1208 (2004).
26. S. Schilt and L. Thévenaz, "Wavelength modulation photoacoustic spectroscopy: Theoretical description and experimental results," *Infrared Phys. Technol.* 48, 154-162 (2006).
27. M. Angelmahr, A. Miklós, and P. Hess, "Wavelength- and amplitude-modulated photoacoustics: comparison of simulated and measured spectra of higher harmonics," *Appl. Opt.* 47, 2806-2812 (2008).
28. J. Saarela, J. Toivonen, A. Manninen, T. Sorvajärvi, and R. Hernberg, "Wavelength modulation waveforms in laser photoacoustic spectroscopy," *Appl. Opt.* 48, 743-747 (2009).
29. R. Arndt, "Analytical line shape for Lorentzian signal broadened by modulation," *J. Appl. Phys.* 36, 2522-2524 (1965).

Chapter 4

Numerical modeling and optimization for QEPAS spectrophone

4.1 Introduction

In QEPAS [1], a pair of rigid tubes, act as a micro-resonator (mR), is usually placed beside the QTF to accumulate the acoustic energy in resonance before detected by QTF. The materials of the resonant tubes are usually silica glass [2-6], or stainless steel [1, 7-10]. The enhancement factor of the mR mainly depends on the inner diameter and length of tubes. Sometimes, the size of the gap between the tubes and QTF could also play important roles in acoustic coupling between the two tubes [11]. In the early work of QEPAS, the length of each tube was selected to be 2.45 mm (~ $\lambda_s/4$) to form a first longitudinal resonance in the mR by neglecting the gaps between the two tubes [2-4]. The enhancement factor of ~ 10 was achieved by this kind of mR. However, a higher enhancement factor has been achieved by using a mR with each tube length ~$\lambda_s/2$ [7], indicating that the resonance in two tubes is somewhat independent. Further detailed studies revealed that the actual tube length for achieving optimal performance is somewhere between $\lambda_s/4$ and $\lambda_s/2$, and an enhancement factor as high as 30 times could be realized [11, 12]. The mR associated with QTF is usually called spectrophone, which is the key component in QEPAS system. Dong et al. [11] carried out experimental investigations on spectrophone optimization, but the samples are limited that it prevents a comprehensive investigation being carried out. Multiple parameters, including length

and inner diameter (ID) of the tube, gap between the tube and tuning fork, gas pressure, dimension of the tuning fork, could play important roles on the acoustic coupling and consequently the PA signal. Due to the complicated structure of spectrophone, no analytical method can be applied to calculate the acoustic coupling and resonance in the mR.

To better understand the acoustic behavior in mR and how it coupled to the tuning fork, and to optimize the performance of the spectrophone, we developed a numerical model based on COMSOL Multiphysics software with finite element method [13]. With this model, the influence of acoustic frequency, tuning fork position, and tube dimensions on the acoustic coupling and pressure distribution, and hence the generated acoustic signal are studied, and a set of parameters for optimal spectrophone performance is identified. Moreover, an improved mR structure is proposed and their performance is compared with the general mR structure.

4.2 Numerical modeling

As the physical processes involved in QEPAS are complicated and no simple analytical model can be applied, we developed a numerical model based on the COMSOL software. Two modules, Pressure Acoustics and Piezo Solid, are used for investigating acoustic coupling in mR and piezoelectric effect of QTF, respectively.

4.2.1 Geometry structure

The geometry structure of the spectrophone comprises a QTF, gas domain and an acoustic source (resonant tubes will be added in the following section). Considering the symmetry of the geometric structure, only half of the tuning fork (marked in blue) and the gas domain are included in our numerical model as shown in Figure 4.1. The gas domain is assumed to be of a spherical shape due to the spherical wave

propagation properties of the acoustic wave. An outer spherical shell is introduced as the perfectly matched layer (PML) to absorb the reflected acoustic wave from the boundary, thus to approach the numerical model to the practical relative infinite gas layer compared to the scale of the QTF. Since the diameter of the light beam through the resonant tubes is relatively small (~ 0.05 mm at waist [14]) compared to the gap between the QTF prongs (0.2 mm) and the ID of the tubes (typically ≥ 0.2 mm), the acoustic pressure wave may be regarded to be originated from a line source along the axis of the tube and propagate all around. Due to the anisotropy of the piezoelectric properties, tuning fork alignment to the assumed poling direction of the material (z-direction) is critical. Thus the QTF concerned in the numerical model is pointed to the y-direction, with the facet of prong perpendicular to the z-axis and vibration along x-direction. Acoustic line source from light absorption is along z-axis, passing through the gap between the prongs of QTF.

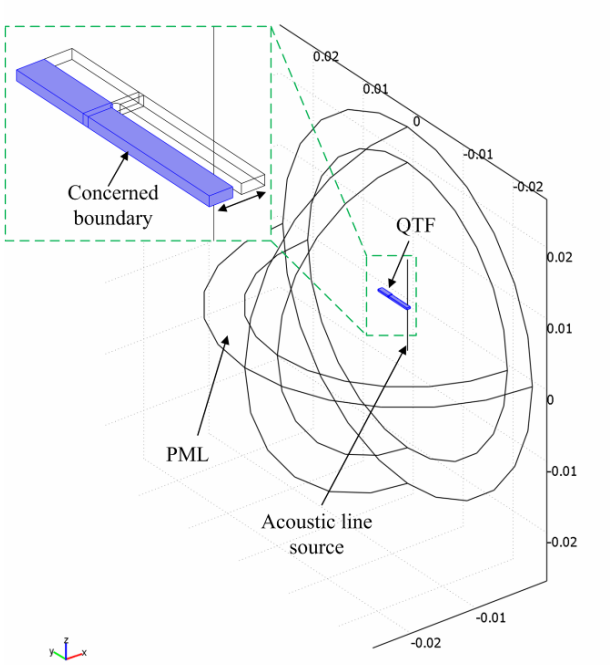

Figure 4.1 Numerical model of a QEPAS spectrophone with a bare QTF. The blue domains are QTF, the black line is acoustic source and the outer spherical shell is served as PML. The unit of scale is meter. The numerical model only includes half of the spectrophone considering the geometrical symmetry of it.

4.2.2 Source term and damping approximation

The source term setting in COMSOL is originated from the heat production via absorption and can be expressed by comparing the acoustic equation in COMSOL with Eq. (2.32) as

$$iS(\mathbf{r},\omega) = i\frac{(\gamma-1)}{\rho_0 c_s^2} H(\mathbf{r},\omega) = i\frac{(\gamma-1)}{\rho_0 c_s^2}\alpha I_0(\mathbf{r},\omega), \tag{4.1}$$

where i is the sign of imaginary part, γ is the adiabatic coefficient of target gas, ρ_0 and c_s are the gas density and the sound velocity in the gas, respectively, $H(\mathbf{r},\omega)$ is heat production rate and I_0 is the light intensity, α is the light absorption coefficient of the gas. Integrating the equation over the cross section of mR, Eq. (4.1) becomes

$$iS = i\frac{(\gamma-1)}{\rho_0 c_s^2}\alpha P_0, \tag{4.2}$$

where S is the flow source term and P_0 is the power of the light source. The above quantity has a unit of m^2/s.

In our simulation, the gas involved in the model is assumed to be at atmospheric pressure. Therefore the viscous damping will play important roles in limiting the *Q*-factor of QTF resonance via increasing the friction on the QTF facet during its vibration [15, 16]. The drag force applied on the surface of QTF is determined by the velocity and acceleration of the QTF prongs, which can be expressed as [16]

$$\mathbf{F}_r = \beta_1\mathbf{u} + \beta_2\dot{\mathbf{u}}, \tag{4.3}$$

where $\mathbf{u}$ is the velocity field at the surface of the QTF prong, β_1 describes the dissipative part of the drag force that proportional to the velocity while the second

part proportional to acceleration $\dot{\mathbf{u}}$ represents the inertial or reactive portion. Blom et al. proposed a means to fit the drag force in a cantilever to that of an oscillatory motion of a sphere with radius of *R* [17]. And the parameters are given by [18, 19]

$$\beta_1 = 6\pi\eta R\left(1+\frac{R}{d_\eta}\right), \tag{4.4}$$

$$\beta_2 = 3\pi R^2\sqrt{\frac{2\eta\rho_0}{\omega}}\left(1+\frac{2R}{9d_\eta}\right), \tag{4.5}$$

where η is the dynamic viscosity of target gas, ρ_0 is the gas density, ω is radial frequency, R is the equivalent spherical radius that fits the damping action of a cantilever and d_η is the thickness of viscous boundary layer given by Eq. (2.58)

$$d_\eta = \sqrt{\frac{2\eta}{\rho_0\omega}}. \tag{4.6}$$

In this numeric model, the value of *R* can be determined by fitting the result to the experimentally observed 8 Hz resonant frequency shift between operation in vacuum and atmospheric air [2]. The drag force, resulted from the acoustic pressure on the prong, is added as a damping term on the QTF to limit the *Q*-factor, thus the final acoustic signal, of the spectrophone. A better damping model might be implemented by coupling in additional COSMOL modules to determine the damping term.

4.2.3 Specific subdomains and boundaries settings

There are two modules, Piezo Solid module and Pressure Acoustics module, involved in our numerical model. Piezo Solid module is employed to investigate the piezoelectric properties of QTF on the ambient acoustic pressure, while Pressure Acoustics module is used to simulate the behavior of acoustic field in the

spectrophone. The acoustic field is originated from the absorption line source and propagates around. The re-radiation of the QTF vibration plays an important role in the acoustic coupling and distribution that much be considered in the model.

The QTF subdomains are only active in the Piezo Solid module, while the other subdomains are active in the Pressure Acoustics module.

1) Piezo Solid module settings

Piezo Solid module includes only the QTF subdomains. The dimension of the QTF used in this model is the same as in [20] (Raltron R38), i.e., 3.636×0.54×0.232 mm for each prong and 0.2 mm for the gap between the two prongs. To better match the actual structure, the base of the QTF that is exposed to the gas is subdivided into a fixed section with a length of 2 mm and a free section with a length of 0.1 mm with rounded corner. The material properties of tuning fork are taken from the COMSOL material library for quartz. The structural damping factor is set to $9.0*10^{-6}$ as to match approximately the observed *Q*-factor of QTF and the dielectric loss factor is set to $9.0*10^{-4}$ for quartz material as given by [21]. The boundary settings for Piezo Solid module is listed in Table 4.1 with the boundaries numbered in Figure 4.2 as the same in the numerical model. The user-defined constants and expressions are listed in Table 4.2 and 4.3 as referred to [19], respectively. The drag force in Table 4.1 for boundaries (9-12, 22) is given by Eq. (4.3) as

$$\text{drag}=(\text{beta1}+i*\text{Frad}*\text{beta2})*\text{u\_t\_smpz3d}/\text{Area}, \tag{4.7}$$

with beta1, beta2 defined in Table 4.3 according to Eq. (4.4) and (4.5).

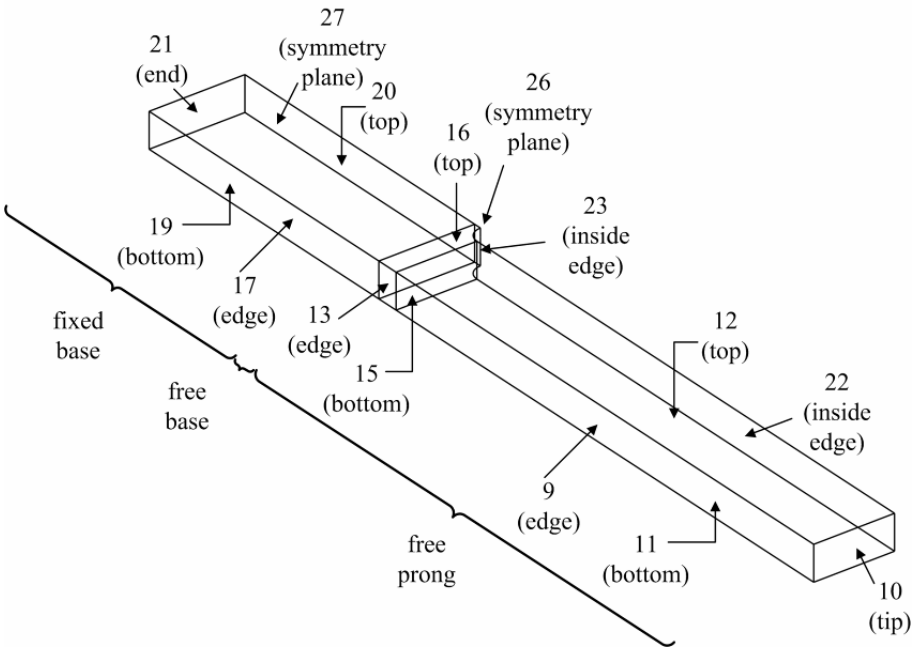

Figure 4.2 Close-up figure of QTF with its boundaries numbered as appears in the model.

Table 4.1 Boundary settings for Piezo Solid module.

Boundary No.	**Constraint**	**Load**	**Electric BC**
9, 11, 12, 22	Free	Fx=nx_acpr*p-drag Fy= ny_acpr*p Fz= nz_acpr*p	Ground
10	Free	Fx=nx_acpr*p-drag Fy= ny_acpr*p Fz= nz_acpr*p	Zero charge/ Symmetry
13, 15, 16, 23	Free	0	Zero charge/ Symmetry
17, 19, 20, 21	Fixed	0	Zero charge/ Symmetry
26, 27	Symmetry plane	0	Zero charge/ Symmetry

Table 4.2 User-defined constants.

Name	**Expression**	**Description**
Freq	32.536e3 [Hz]	Frequency (varied in parametric study)
E_quartz	7.8e10 [Pa]	Young's modulus for quartz
visc	1.983e-5 [Pa*s]	Dynamic viscosity of air at STP
dens	1.25 [kg/m^3]	Density of air at STP
R	515e-6 [m]	Radius of equivalent sphere for drag force
L	3.636e-3 [m]	Tine length
w	0.54e-3 [m]	Tine width
t	0.232e-3 [m]	Tine thickness
g	0.2e-3 [m]	Gap between tines

Table 4.3 User-defined expressions.

Name	**Expression**	**Description**
Frad	2*pi*Freq	Radial frequency
delta	sqrt(2*visc/(dens*Frad))	Boundary layer thickness
Area_ed	L*t	Cross-section area of prong edge
Area_fc	L*w	Cross-section area of prong face
Area_tp	w*t	Cross-section area of prong tip
Area	2*(Area_ed+Area_fc)+Area_tp	Total prong area
beta1	6*pi*visc*R*(1+R/delta)	beta1
beta2	3*pi*R^2*sqrt(2*visc*dens/Frad) *(1+2*R/(9*delta))	beta2

2) Pressure Acoustics module settings

In the Pressure Acoustics module, the subdomains include the gas domain and spherical PML boundary layer. For trace gas detection, the gas layer can be regarded

as atmospheric air. The line passes between the two prongs of QTF is set to flow source in the edge settings with its value obtained from Eq. (4.2). Acoustic wave originated from this line source propagates in the gas medium and detected by QTF. The boundary settings are kept as default except for the prong of QTF and the inner edge of free transition base (boundaries 9-12, 22, 23 in Figure 4.2) set to Normal acceleration condition with

$$a_n=nx\_smpz3d*u\_tt\_smpz3d+ny\_smpz3d*$$
$$v\_tt\_smpz3d+nz\_smpz3d*w\_tt\_smpz3d. \quad (4.8)$$

The acoustic pressure applied to the tuning fork prong excites mechanical oscillation of the QTF, which results in the electric charge accumulation in the inner and outer surface of QTF through piezoelectric effect. With an external connection between the two surfaces, an electric current signal is generated and it can be obtained by integrating the surface charge density ρ_s throughout the outer surface of QTF as

$$I_{out} = \omega \iint \rho_s dA, \quad (4.9)$$

where ω is the radial frequency of the acoustic wave. The current signal can be further converted into voltage signal through a transimpedance amplifier, which is demodulated by a lock-in amplifier. Pay attention to the fact that both the flow source (i.e., the acoustic line source) and generated current signal in this model are only half of actual case. For comparison with previous experimental results, the output current signal is normalized to absorption coefficient and laser power throughout this chapter.

4.3 Spectrophone performance

The numerical model is evaluated for QEPAS gas sensing for different spectrophones without/with resonant tubes, and with modified resonators.

4.3.1 Without mR

4.3.1.1 Frequency response

First, the numerical model is carried out for the simple bare QTF case to evaluate its feasibility. The numerical model is shown in Figure 4.1 and the deposit heat energy is normalized. Before the investigation of the frequency response of our model, the resonant frequency needs to be approximately estimated. As discussed in section 3.2.1, the resonant frequency of QTF is determined by its geometry, material and surrounding gas pressure, and can be estimated from Eq. (3.1) as

$$f_0 = \frac{1.015}{2\pi}\frac{w}{L^2}\sqrt{\frac{E_Q}{\rho_Q}}, \tag{4.10}$$

where E_Q and ρ_Q are the Young's modules (78.7 GPa) and density (2650 kg/m^3) of Quartz material, respectively, L and w are the length and width of QTF prong. For the dimensions of Raltron R38 QTF given in above, the theoretical resonant frequency is calculated to be 35.96 kHz. This is reasonably close to the experimental value of ~32.768 kHz, considering that the effect of the QTF base is not included in this simplified cantilever model.

In calculating the frequency response, a structural loss parameter of 9×10^{-6} and a dielectric loss factor of 0.0009 are used for Quartz material as stated before, these parameters were found to give a *Q*-factor approaching the experimental result of the QTF in vacuum [2]. In the following simulation, the loss factors are kept the same as above. The frequency response of the model without mR in vacuum, i.e., without

viscous damping, is plotted in Figure 4.3 as the green line. The resonant frequency is ~ 32.542 kHz and the *Q*-factor is calculated to be ~ 93,975, very close to the experimental result of 93,456 [2]. In reality, gas sensing is usually carried out at atmospheric pressure, so the acoustic re-radiation and viscous damping are two main factors that affect the energy loss of QTF. Therefore, the frequency response of the model at atmospheric pressure is also simulated and shown in Figure 4.3 as the blue line. The resonant frequency and *Q*-factor are found to be ~ 32.536 kHz and 22,035, respectively. The frequency shift from vacuum to atmosphere is ~ 6 Hz, but the *Q*-factor suffers a significant decrease, which is consistent with experimental observation [2], indicating the reasonability for the selection of fitting parameter *R* and structural loss parameter in the calculation.

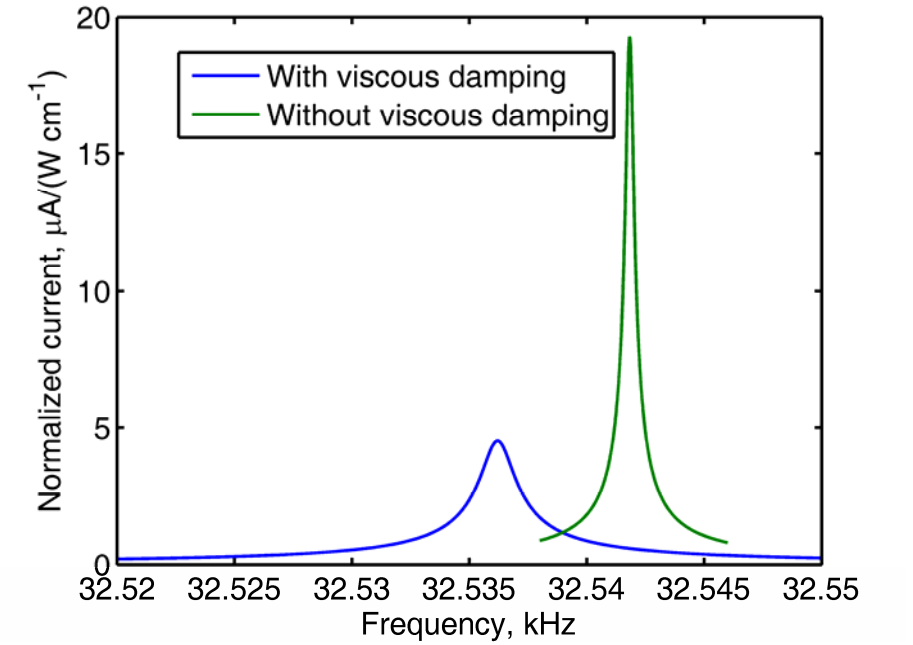

Figure 4.3 Frequency response of bare QTF without mR in vacuum (green line) and in atmospheric air (blue line).

4.3.1.2 Light beam position

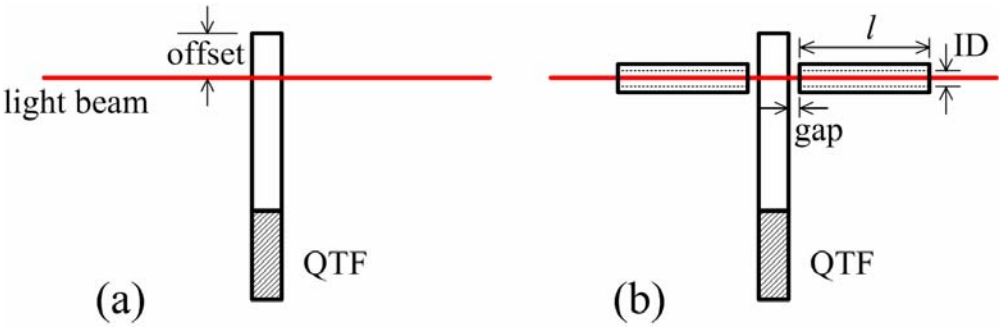

Figure 4.4 Schematic structure of spectrophone without (a) and with (b) mR. Light beam pass through the gap between prongs of QTF with an offset from the opening. ID: inner diameter.

For better acoustic detection, the light beam usually passes through the middle of the prong gap, with a small offset from the QTF opening as shown in Figure 4.4 (a). To obtain the optimal beam position, the light beam is moved from the opening of QTF step by step, and the corresponding normalized PA signal is recorded and plotted in Figure 4.5. The optimal offset is found to be ~ 0.6 mm, agreeing with the reported theoretical [14] and experimental [1] results. In the following section, the light beam is fixed at 0.6 mm down from the opening. To further test our model, we compare our result with the experimental result in Ref. [22] under the same condition. The PA signal in [22] was 2.869 mV with a feedback resistor of 10 MΩ, a laser power of 8 mW and an absorption coefficient of 0.01 cm^{-1}, corresponding to a normalized current signal ~ 3.6 μA/(W cm^{-1}). This is on the same order of magnitude as our simulation result of ~ 8.5 μA/(W cm^{-1}), indicating our numerical modeling is reasonably reliable.

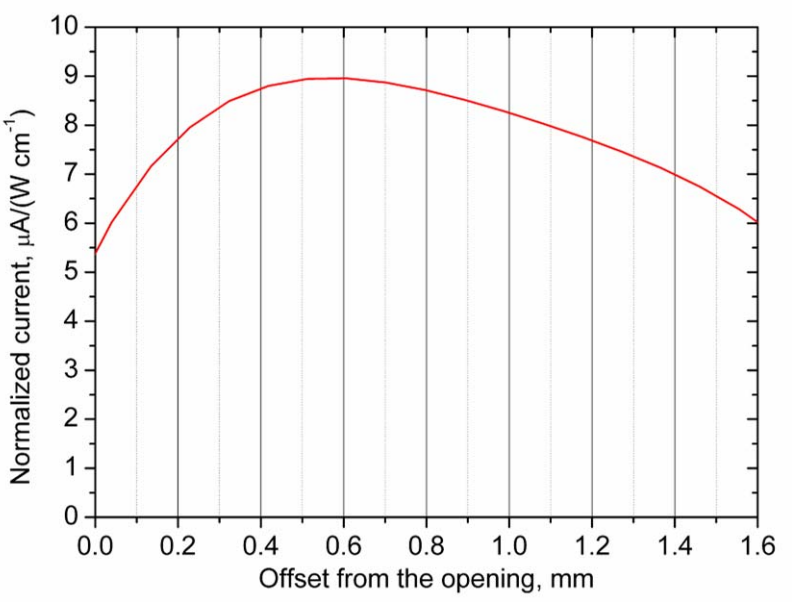

Figure 4.5 Normalized piezoelectric current as a function of beam offset from the QTF opening without resonant tubes.

4.3.2 With mR

In QEPAS, mR based scheme is usually adopted to enhance the acoustic signal in the resonant tubes before detection. The resonant tubes, or mR, are generally placed along the two sides of the QTF facet with a small gap as shown in Figure 4.4 (b). The corresponding numerical model is shown in Figure 4.6 by adding two sections of tubes (red regions) beside the QTF, with symmetric structure considered similarly. In order to simplify the problem, several assumptions are made for the mR-based numerical model:

1) The resonant tubes are perfectly hard, which are not involved in the acoustic behavior;

2) Viscous damping in the tubes is neglected if the diameter of tube is far larger than the thickness of viscous boundary layers defined in Eq. (4.6);

3) Viscous damping of QTF doesn't include the influence of resonant tube near it.

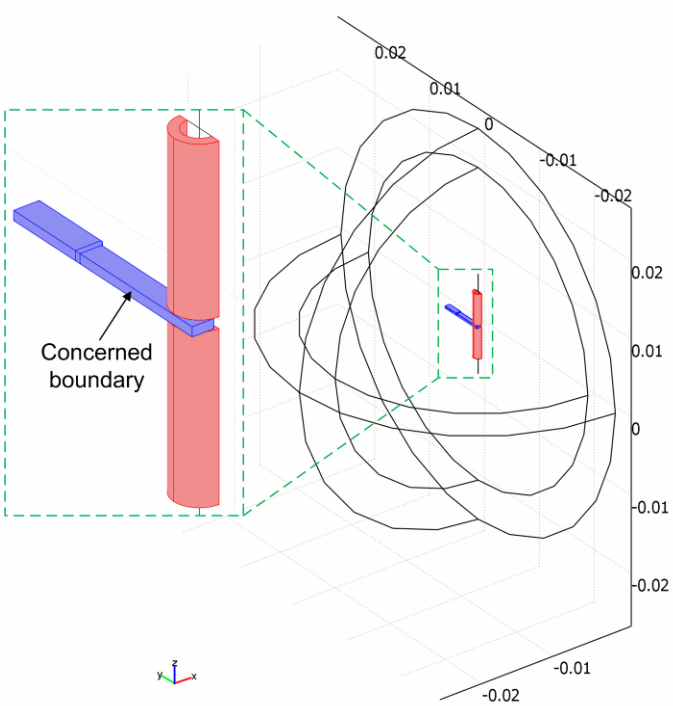

Figure 4.6 Numerical model of a QEPAS spectrophone comprising of a QTF and two rigid resonant tubes. The red domains are resonant tubes and the blue ones are QTF. The unit of scale is meter.

4.3.2.1 Dependence on the gap between the QTF and mR

In order to investigate the effect of gap size between the tube and QTF on the acoustic signal, we change the gap step by step and record the PA signals. Figure 4.7 reveals the dependence of PA current signal on the gap size for resonant tube with inner diameter of 1 mm and each length of 5 mm at frequency of 32.528 kHz. It is apparent that the PA signal decrease with increasing gap size. This is expected because a larger gap causes more acoustic energy leakage from the gap and reduces the acoustic coupling between the resonant tubes as can seen from Figure 4.8. A smaller gap is then more effective for acoustic coupling and QTF oscillation. However, if the gap is too small (<10 μm), the assembling of the QTF and the resonance tubes would be difficult; the viscous damping also becomes significant [23], which reduces the magnitude of the PA signal. Considering all these factors, we

select a gap of 20 μm for a tradeoff.

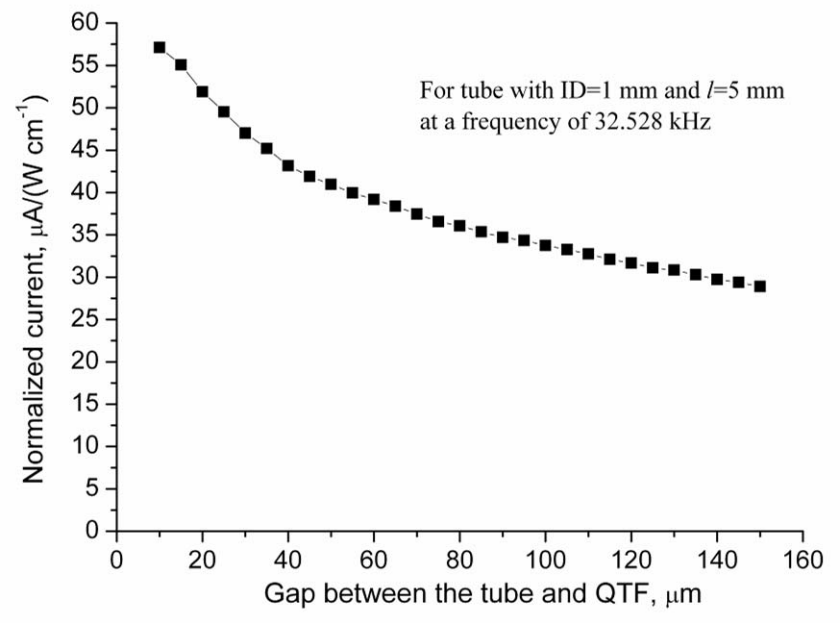

Figure 4.7 Dependence of PA signal on the gap size between the tube and QTF facet.

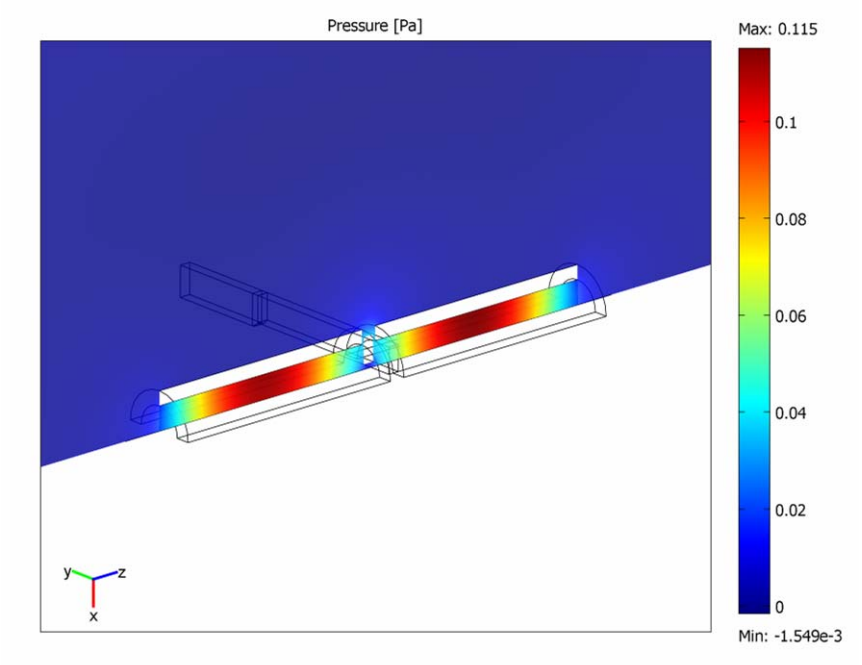

Figure 4.8 Pressure distributions along the resonant tubes.

4.3.2.2 Dependence on the dimension of mR

Another factor that significantly influences the PA signal is the dimensions, i.e., the length and ID, of the resonant tubes. The ID of tube is usually less than 1 mm and length between $\lambda_S/4$ and $\lambda_S/2$ for efficient acoustic amplification and detection. The normalized PA signal for different ID and length near the resonant frequency are simulated and shown in Figure 4.9. The ID of tube is changed from 0.2 to 0.8 mm and the length of each tube is varied from 2 to 6 mm step by step. On the whole, the PA signal decreases with increasing the tube ID. For different tube IDs, the optimum tube length changes. Even for a fixed tube ID, the resonant frequency of spectrophone varies with tube length.

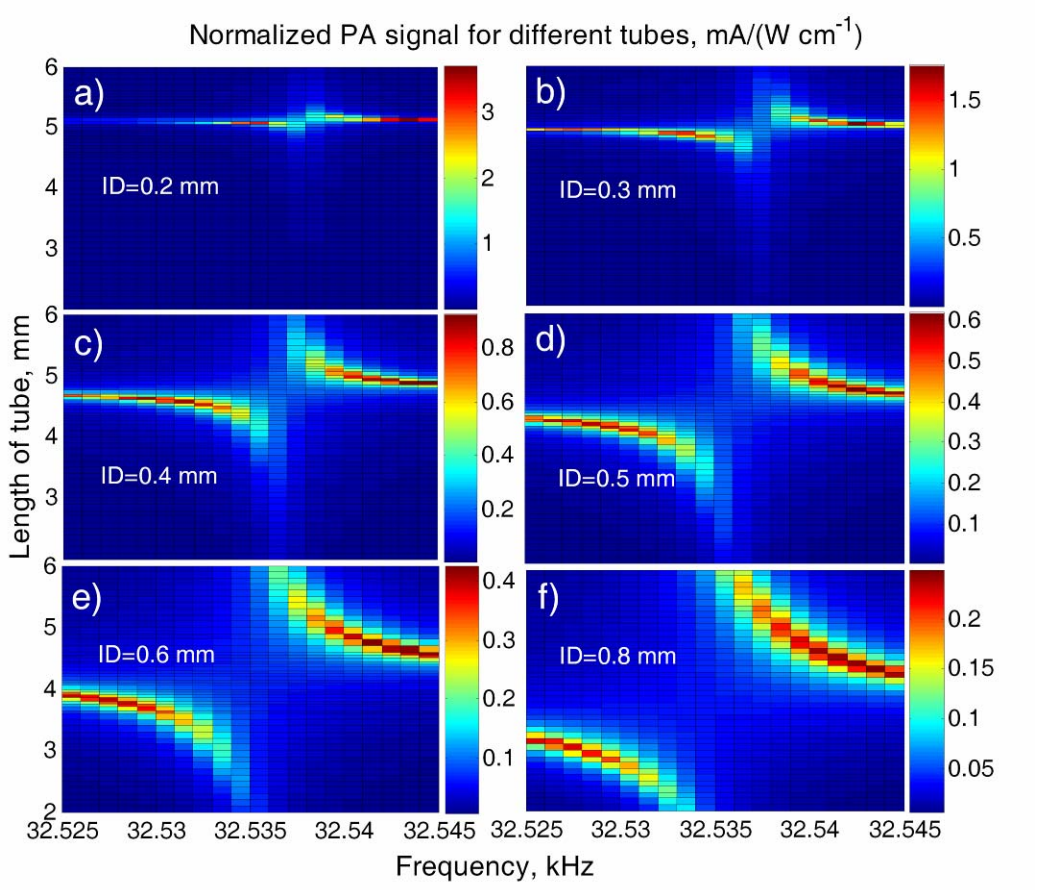

Figure 4.9 Normalized PA signal for resonant tube with different length and inner diameter. From a) to f) the ID of the tubes are 0.2, 0.3, 0.4, 0.5, 0.6 and 0.8 mm, respectively.

The maximum PA signal, resonant frequency and *Q*-factor of the setup for varying tube length and ID are calculated and plotted in Figure 4.10. It is shown again in Figure 4.10 a) that the PA signal increases with reduced tube ID. The tube lengths corresponding to maximum PA signals are 5.1, 4.98, 4.85, 4.72, 4.57, 4.3 mm for IDs of 0.2, 0.3, 0.4, 0.5, 0.6, 0.8 mm, respectively, exhibiting a nearly linear relationship. For each tube ID, there is a sharp drop of PA signal at the center of the resonance, this is referred as anti-resonance, and the corresponding tube length is referred as anti-resonant length. As shown in Figure 4.10 a), the anti-resonant length reduces with increasing tube ID. The smaller the tube ID, the sharper the resonant curve. Around the anti-resonant length, the resonant frequencies suffer from severe changes. They deviate significantly from the resonant frequency of the spectrophone without mR (i.e., bare QTF) around the anti-resonant length as shown in Figure 4.10 b). The *Q*-factor near the anti-resonant length achieves a minimum value and gradually approaches the value for the bare QTF when tube length is away from the anti-resonant length (Figure 4.10 c)). The thinner the resonant tube, the sharper of the resonant frequency and *Q*-factor curves.

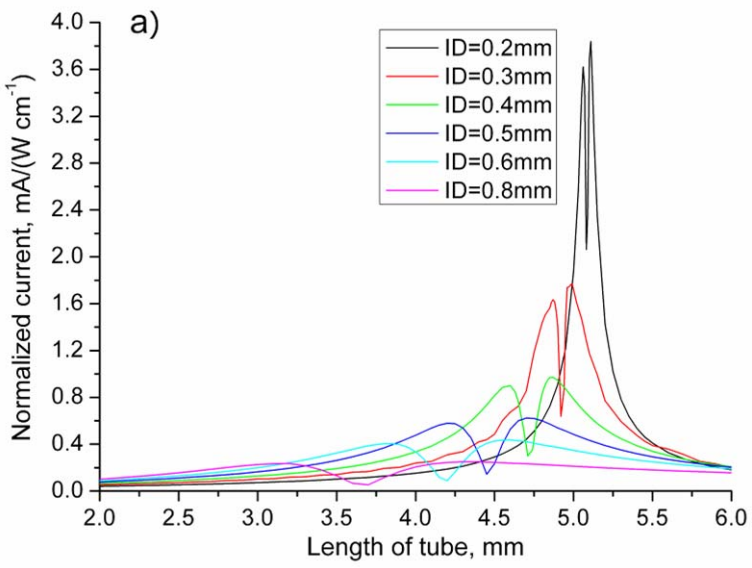

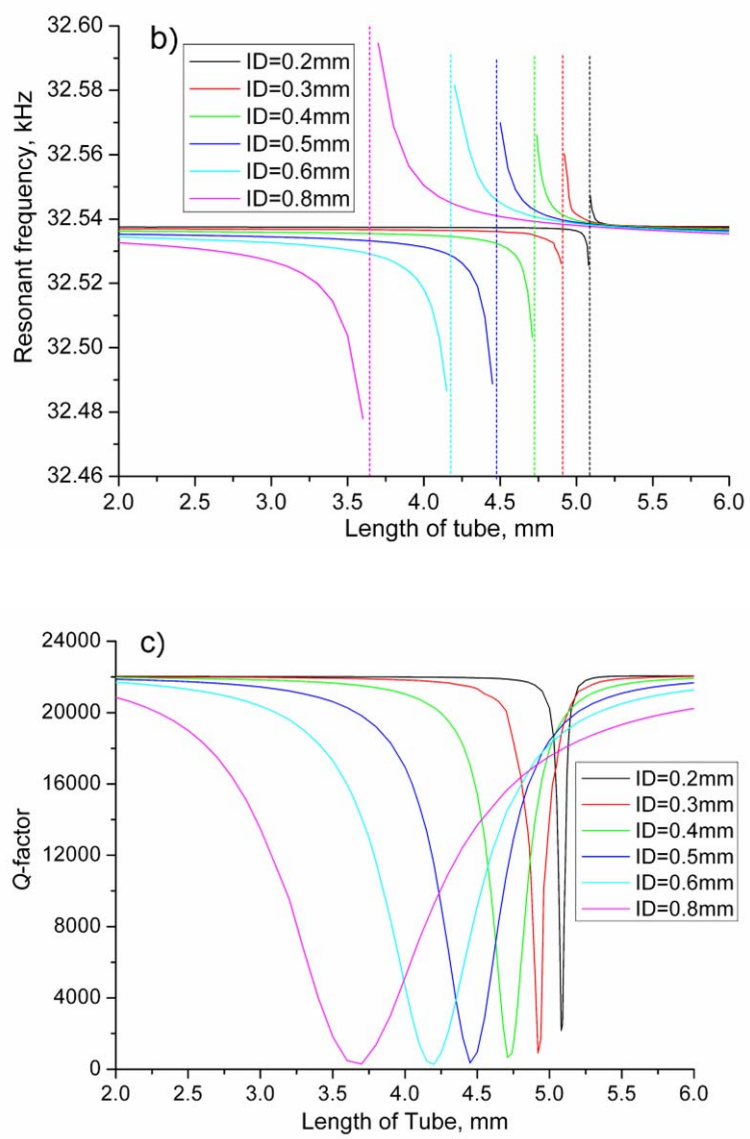

Figure 4.10 a) Maximum normalized PA signal, b) resonant frequency and c) *Q*-factor for spectrophone with different tube length and ID.

From Figure 4.9, it can be seen that the PA signal achieves its maximum value at around 32.542 kHz for all the tube IDs. For efficient PA signal detection, the frequency is fixed at 32.542 kHz and the simulated PA signals for several tube dimensions are shown in Figure 4.11. The signal is reduced and broadened for a larger tube ID, and the optimal tube length is shifted down from ~5.1 mm to ~4.4 mm. The peak value and corresponding total length of mR (the lengths of the two tubes plus the gap between them) are plotted in Figure 4.12. It reveals that the

optimal total length of mR decreases linearly with the ID of the tube, while the peak PA signal depends on the reciprocal of the square of tube ID.

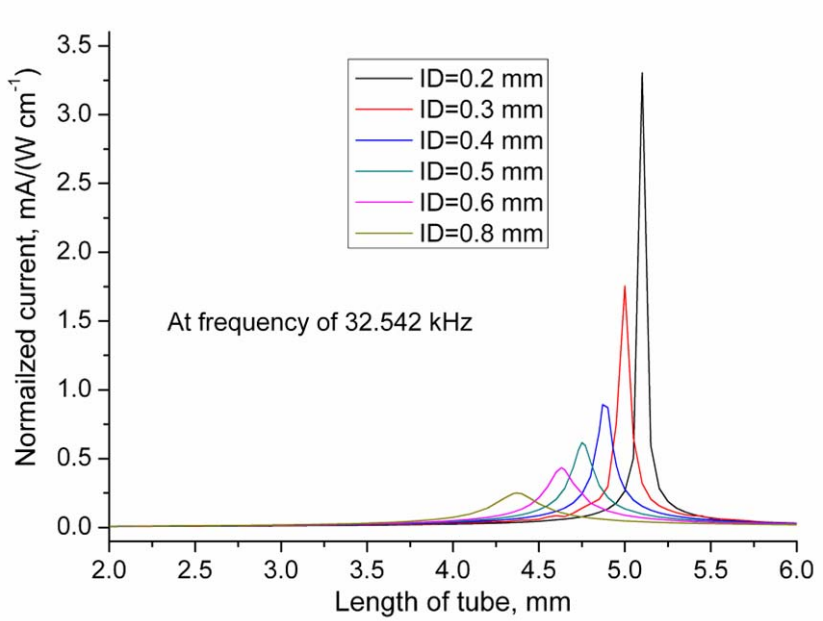

Figure 4.11 Normalized PA signal for tubes with different ID and length at frequency 32.542 kHz.

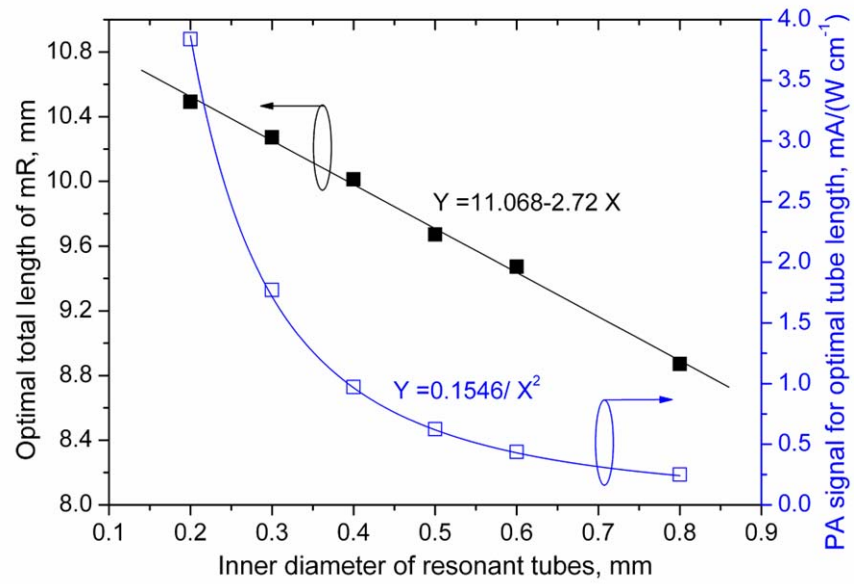

Figure 4.12 The total length of mR and normalized PA signal at resonance peak as functions of tube ID. The squares are numerically calculated data and the solid lines are fitted curves.

4.3.3 Modified mR structures

Considering the gap between the tubes introduced by the QTF, which might cause a considerable amount of acoustic energy loss around it, we modified the mR structure with reduced gap area in the middle of the resonant tubes as depicted in Figure 4.13. The two tubes in general QEPAS method are connected by two thin bridges or it can be seen as a whole tube is cut in the middle by two symmetric small slots, and the size of the slots is suitable for the QTF to be plugged in with a small gap between the tuning fork and the tube walls. In this way, the gap is further reduced to prevent the acoustic wave leakage in the middle of the tube, thus to enhance the signal. Considering the maximum deflection of the QTF prong is usually less than 1 μm, a gap with several tens μm will not affect the vibration of QTF much.

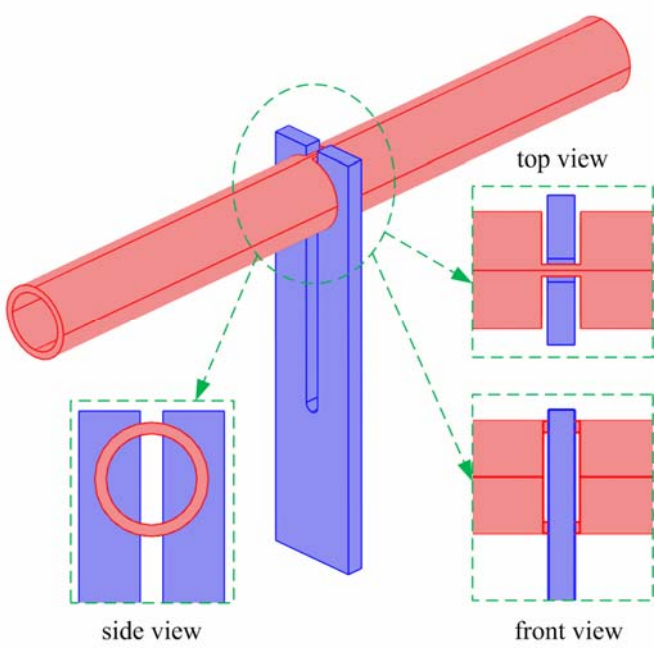

Figure 4.13 Modified spectrophone structure with three different views of the connection part of between resonant tube and QTF.

To evaluate the capability of our modified tube structure, we select a tube with inner diameter of 0.4 mm and sluts to leave a gap of 20 μm between the QTF and

tube walls. By varying the tube length, the optimal total tube length of 9.6 mm is found to obtain a maximum PA signal. The frequency response of the PA signal for this modified tube is shown in Figure 4.14. For typical resonant tubes, the optimal length for each tube is ~ 4.9 mm to ensure a maximum PA signal given by Figure 4.10 a). The calculated PA signal near the resonant frequency is shown in Figure 4.14. For comparison, we also simulate the typical spectrophone with optimal each tube length of 4.9 mm corresponding to an ID of 0.4 mm according to Figure 4.10 a), and the results are also displayed in Figure 4.14. Unexpectedly, the maximum PA signals for these two kinds of mRs are almost equivalent, with an operation frequency shift of 5 Hz between them. Therefore, the modified structure with two thins bridges could not distinctly improve the capacity of the spectrophone. These might imply that the small gap between the two prongs of QTF induce little influence to the spectrophone. Moreover, the fabrication of this kind of modified structure and assembly with the QTF is also a challenge. The separated two tube structure of mR is still preferred in practice.

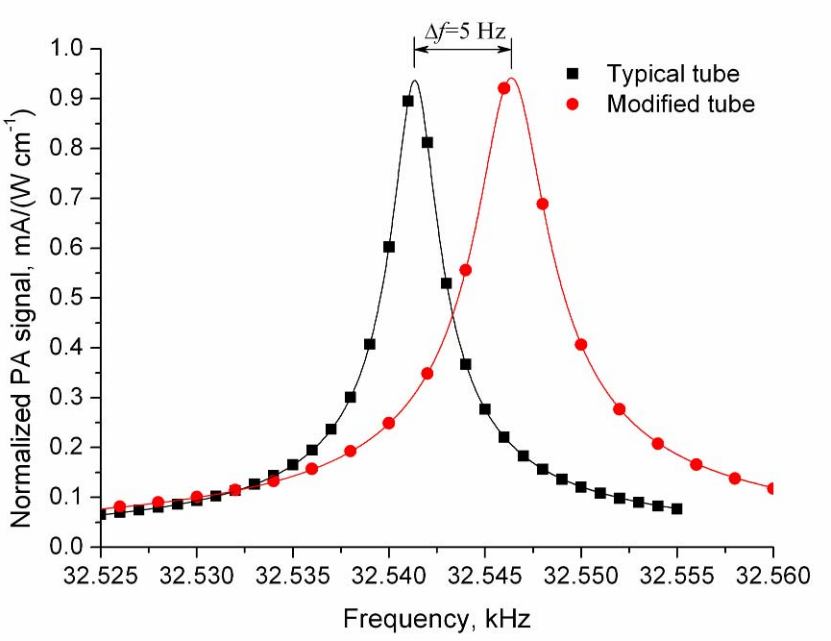

Figure 4.14 Frequency responses of the typical tube and modified tube with ID of 0.4 mm.

4.4 Analysis

The frequency response of the QEPAS spectrophone may be regarded as following approximately a two-step process: the built up of acoustic pressure at the gap between the two resonant tubes and the conversion of pressure to a piezoelectric current by the QTF. The conversion or transfer function of the QTF was found to be independent of the length and has only a weak dependence on the ID of the tubes. The acoustic pressure wave at the gap center is however a result of complex interaction between the resonant tubes and the QTF, and depends strongly on the dimensions of the tubes. The varying characteristic of the PA signal shown in section 4.3.2 is believed to be mainly due to the different acoustic coupling for tubes with varying dimensions.

As the ID of the tube is far smaller than the acoustic wavelength λ_s (~ 10.5 mm) in gas at around 32.536 kHz, the resonant tube can be regarded as a 1D acoustic resonator and the acoustic pressure distribution in the cross section of the tube may be regarded as uniform. As demonstrated by Dong et al. [11], the acoustic coupling between the two tubes results in an optimal tube length of between $\lambda_s/4$ and $\lambda_s/2$, where λ_s is related to acoustic frequency f and velocity c_s by $\lambda_s = c_s/f$. Hence, for a fixed tube length l, the acoustic resonance frequency for maximum pressure at the center between the two tubes falls between $c_s/4l$ and $c_s/2l$ and increases with reducing tube length.

In order to analyze the acoustic wave coupling and interaction with QTF, we numerically calculated the acoustic pressure in the middle of the QTF prongs at the gap center and QTF vibration at different excitation frequency for resonant tube with fixed ID of 0.8 mm as an example and various lengths. The amplitude and phase of acoustic pressure are plotted in Figure 4.15 and 4.16, respectively. And the frequency dependent QTF vibration is plotted in Figure 4.17 and 4.18 for amplitude and phase.

In Figure 4.15, the close-up figure shows the details of pressure variation around the resonant frequency of the QTF. As expected, the acoustic resonance peak shifts to lower frequency with increasing tube length because of the first longitudinal acoustic wave operation in the tube. The acoustic pressure shows dramatic variations near the resonant frequency of the QTF due to the re-radiation of QTF. This can also be seen from Figure 4.16 and 4.18 that the re-radiation from QTF results in an intense phase change for both acoustic wave and QTF vibration around the QTF resonant frequency. In other words, for a small tube length, the acoustic resonant frequency is larger than the QTF resonant frequency, thus near the QTF resonance, the acoustic wave is accumulated in the lower frequency side. While for a larger tube length, the relative lower acoustic frequency makes the acoustic energy accumulated in the higher frequency side of QTF resonant frequency. At the QTF frequency, the 90° phase lag between the QTF vibration and acoustic resonance results in an anti-resonance of the spectrophone as shown in Figure 4.19. Interestingly, at this anti-resonance frequency, the vibration of QTF and acoustic signal are independent on the tube length as displayed in Figure 4.15 and 4.17.

Pay attention that when the acoustic resonance of the tubes overlaps with the resonance of the QTF, anti-resonance occurs and a dip appears in the resonance curve. The tube length corresponding to the matching of the two resonances is the anti-resonant length. For tubes with a larger ID, stronger acoustic coupling occurs, and the acoustic resonance frequency is closer to $c_s/4l$ and the hence anti-resonant length is closer to $\lambda_s/4$. For smaller IDs, the anti-resonant length is closer to $\lambda_s/2$. This is consistent with the simulation results in section 4.3.2.

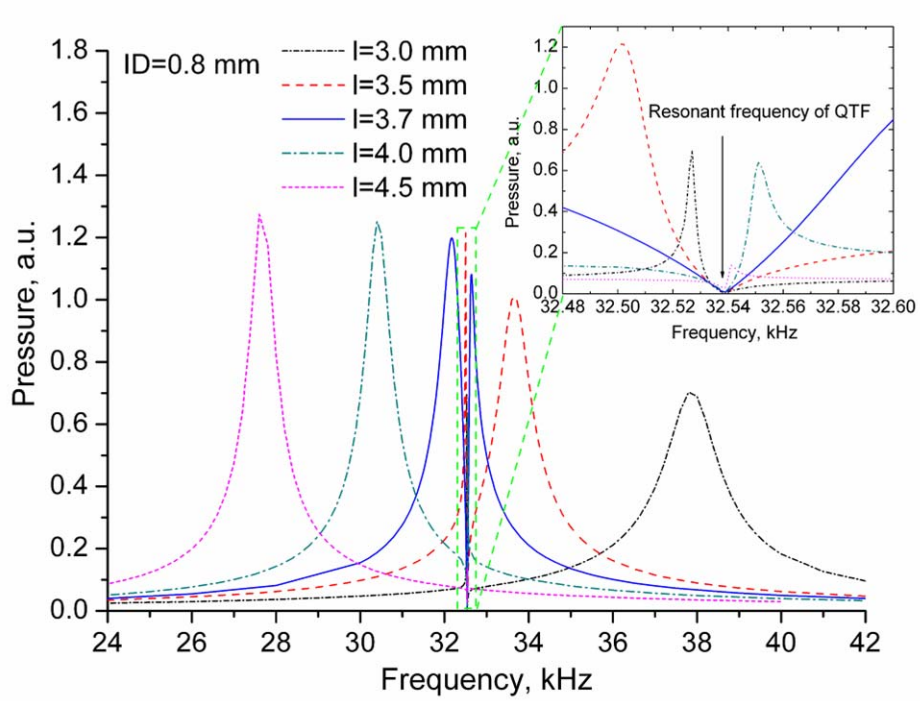

Figure 4.15 Amplitude of the acoustic pressure at the center of the gap between the two tubes for various tube lengths. The ID of the tubes is 0.8 mm. The close-up figure shows the details of pressure variation near the resonance of the QTF.

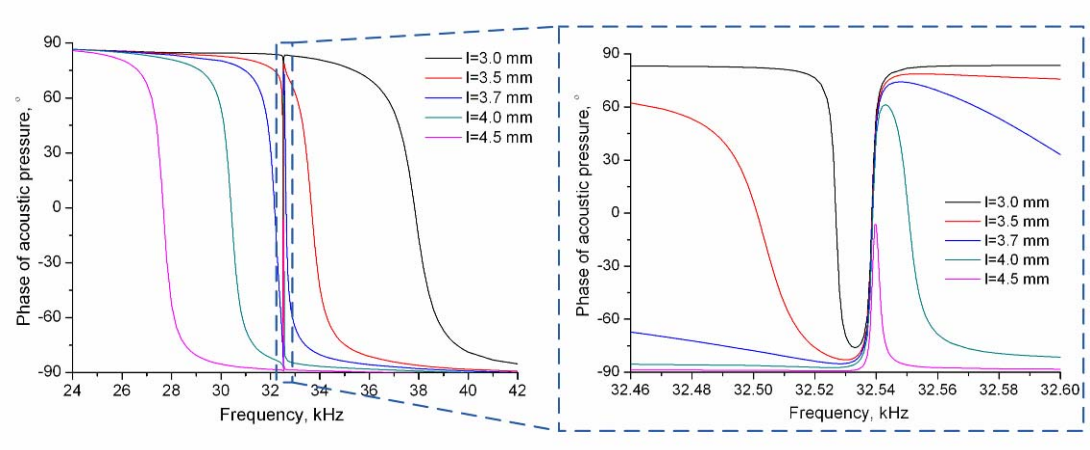

Figure 4.16 Phase of the acoustic pressure at the center of the gap between the two tubes for various tube lengths. The ID of the tubes is 0.8 mm. The close-up figure shows the details of pressure phase variation near the resonance of the QTF.

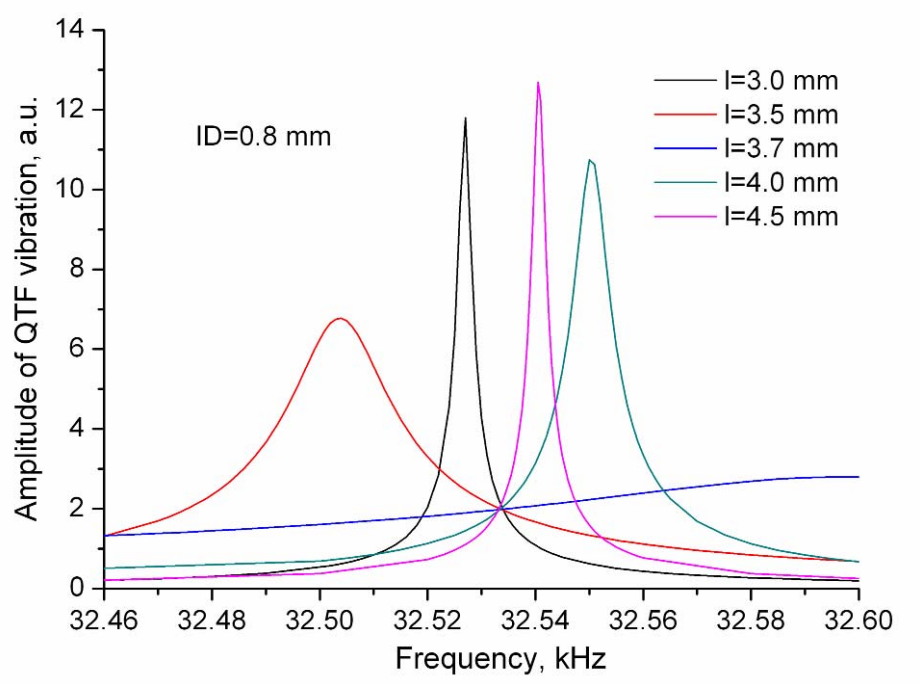

Figure 4.17 Amplitude of the QTF vibration at different operation frequency.

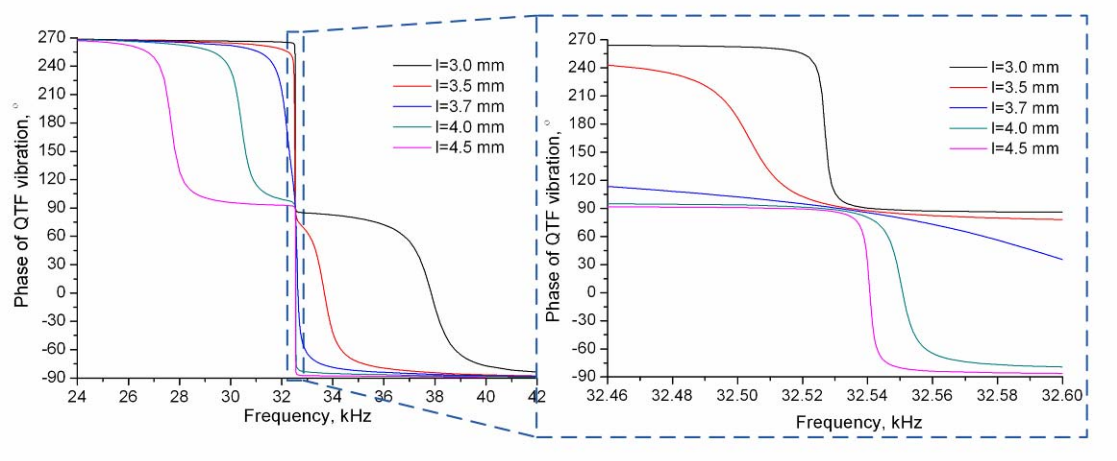

Figure 4.18 Phase of the QTF vibration at different operation frequency. The close-up figure shows the details of phase variation near the resonant frequency of QTF.

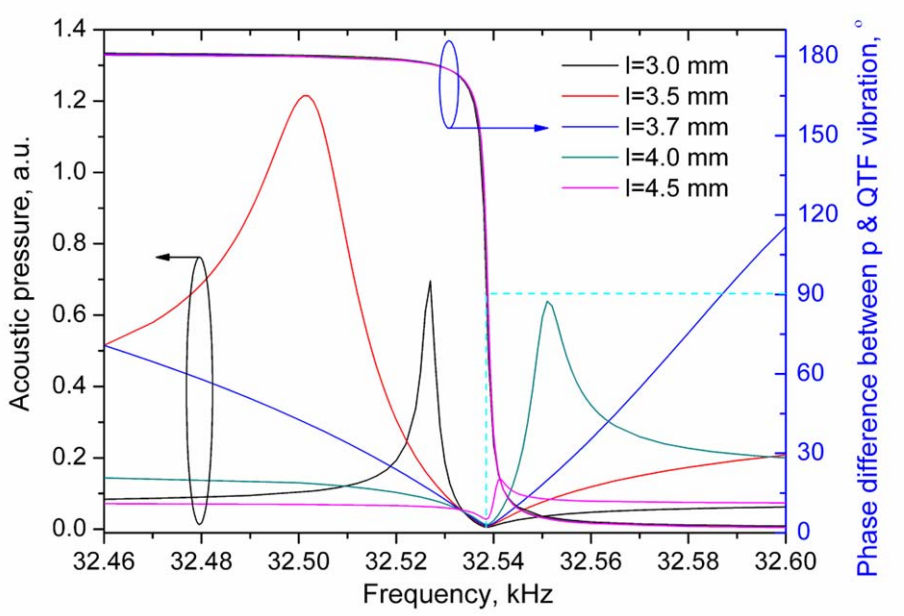

Figure 4.19 Dependence of acoustic pressure and phase difference between pressure and QTF vibration on operation frequency. The anti-resonance corresponding to a 90° phase lag of QTF vibration to acoustic wave.

The anti-resonance in the spectrophone might be explained from the pressure distribution along the tubes. It is shown in Figure 4.15 that for a tube ID of 0.8 mm, the anti-resonant length is around 3.7 mm. For tubes with a length shorter than the anti-resonant length, the acoustic pressure wave distribution along the mR is closer to the fundamental resonance of the mR as shown in Figure 4.20, and the acoustic energy is higher in the lower frequency side of anti-resonant frequency as shown in close-up of Figure 4.15. For tube length longer than the anti-resonant length, the second resonance mode dominates, and the acoustic energy is larger in the higher frequency side of anti-resonant frequency. For a specific tube ID, the combined effect of frequency dependent acoustic pressure and QTF conversion function pulls down/up the resonant frequency of the PA signal for tube length shorter/longer than the anti-resonant length. The shift of the resonant frequency can be significant around the anti-resonant length. For the same reason, the *Q*-factor of the spectrophone reaches a minimum value close to zero at the anti-resonant length and

increases gradually, approaching the value for bare-QTF when tube length is far away from the anti-resonant length.

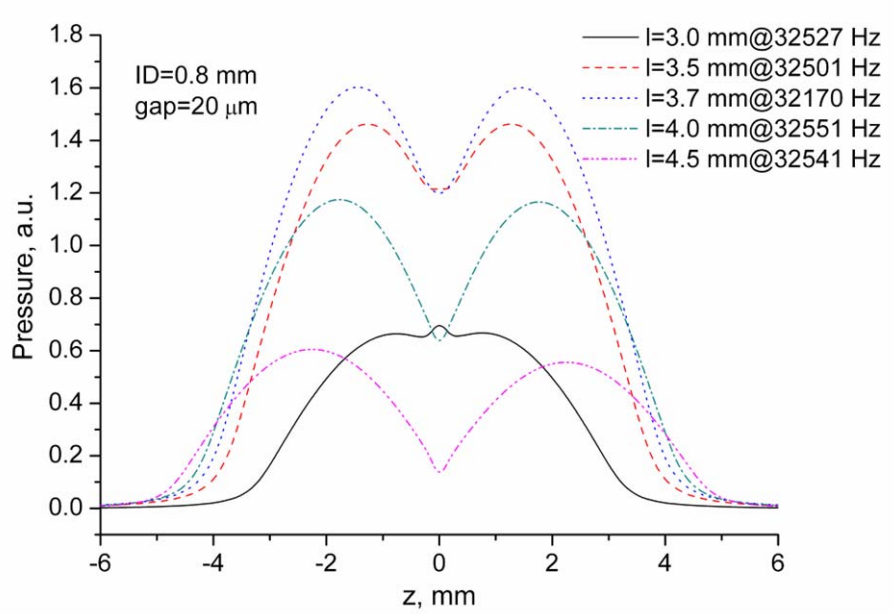

Figure 4.20 Acoustic pressure distribution along the mR for each tube lengths with a fixed ID=0.8 mm at their resonance peak around the resonance frequency of QTF.

As shown in Figure 4.12, the PA signal is inversely proportional to the square of tube ID, which agrees with the previous theoretical result as [2]

$$S = k\frac{\alpha P_0 l_R Q}{f_c V_R} = k\frac{\alpha P_0 Q}{f_c \pi r_R^2}, \tag{4.11}$$

where S is the PA signal detected by QTF with mR, k is a constant describing the transfer function of the spectrophone, α is absorption coefficient of gas, P_0 is laser power, l_R, V_R and r_R are the total length, volume and inner radius of the mR, Q and f_c are the Q-factor and resonant frequency of the spectrophone, respectively. However, a too small tube ID will result in large damping loss of the acoustic resonance and reduce the Q-factor of the system [23], and make the optical alignment difficult as well.

On the whole, the maximum PA signal is achieved for tubes with a relatively

small gap and ID, and a length slightly longer than the anti-resonant length. Considering the detection efficiency and also easier assembling, we suggest a spectrophone comprising of a Raltron R38 QTF and a pair of tubes with an ID of 0.2 mm and length of 5.1 mm, placed 0.6 μm down from the opening and 20 μm away from the facet of tuning fork.

4.5 Summary

In this chapter, we developed a numerical model for investigating the acoustic coupling and performance of QEPAS spectrophone by use of finite element method. The numerical method with multiple modules is introduced in detail. The spectrophone comprises of a QTF and a pair of tubes, and photoacoustic current generated from QTF is studied for different tube dimensions and relative position of QTF with respective to the tubes. A modified tube structure is proposed and compared with typical mR. The regulation for the acoustic coupling and interaction with QTF is attempted to be analyzed. Finally, a set of parameters is suggested for optimal gas detection under atmospheric pressure in QEAPS method. This work may provide useful theoretical understanding and guidance on QEPAS optimization and multiphysical process modeling.

References of Chapter 4

1. A. A. Kosterev, Y. A. Bakhirkin, R. F. Curl, and F. K. Tittel, “Quartz-enhanced photoacoustic spectroscopy,” *Opt. Lett.* 27, 1902-1904 (2002).
2. A. A. Kosterev, F. K. Tittel, D. V. Serebryakov, A. L. Malinovsky, and I. V. Morozov, “Applications of quartz tuning forks in spectroscopic gas sensing,” *Rev. Sci. Instrum.* 76, 043105 (2005).

3. A. A. Kosterev and F. K. Tittel, "Ammonia detection by use of quartz-enhanced photoacoustic spectroscopy with a near-IR telecommunication diode laser," *Appl. Opt.* 43, 6213-6217 (2004).
4. A. A. Kosterev, Y. A. Bakhirkin, F. K. Tittel, S. Blaser, Y. Bonetti, and L. Hvozdara, "Photoacoustic phase shift as a chemically selective spectroscopic parameter," *Appl. Phys. B* 78, 673-676 (2004).
5. M. Horstjann, Y. A. Bakhirkin, A. A. Kosterev, R. F. Curl, and F. K. Tittel, "Formaldehyde sensor using interband cascade laser based quartz-enhanced photoacoustic spectroscopy," *Appl. Phys. B* 79, 799-803 (2004).
6. A. A. Kosterev, T. S. Mosely, and F. K. Tittel, "Impact of humidity on quartz-enhanced photoacoustic spectroscopy based detection of HCN," *Appl. Phys. B* 85, 295-300 (2006).
7. S. Schilt, A. A. Kosterev, and F. K. Tittel, "Performance evaluation of a near infrared QEPAS based ethylene sensor," *Appl. Phys. B* 95, 813-824 (2009).
8. K. Liu, J. Li, L. Wang, T. Tan, W. Zhang, X. Gao, W. Chen, and F. K. Tittel, "Trace gas sensor based on quartz tuning fork enhanced laser photoacoustic spectroscopy," *Appl. Phys. B* 94, 527-533 (2009).
9. A. A. Kosterev, L. Dong, D. Thomazy, F. K. Tittel, and S. Overby, "QEPAS for chemical analysis of multi-component gas mixtures," *Appl. Phys. B* 101, 649-659 (2010).
10. A. A. Kosterev, P. R. Buerki, L. Dong, M. Reed, T. Day, and F. K. Tittel, "QEPAS detector for rapid spectral measurements," *Appl. Phys. B* 100, 173-180 (2010).
11. L. Dong, A. A. Kosterev, D. Thomazy, and F. K. Tittel, "QEPAS spectrophones: design, optimization, and performance," *Appl. Phys. B* 100, 627-635 (2010).
12. D. V. Serebryakov, I. V. Morozov, A. A. Kosterev, and V. S. Letokhov, "Laser microphotoacoustic sensor of ammonia traces in the atmosphere," *Quantum*

Electron. 40, 167-172 (2010).

13. http://www.comsol.com/.
14. N. Petra, J. Zweck, A. A. Kosterev, S. E. Minkoff, and D. Thomazy, "Theoretical analysis of a quartz-enhanced photoacoustic spectroscopy sensor," *Appl. Phys. B* 94, 673-680 (2009).
15. W. E. Newell, "Miniaturization of tuning forks," *Science* 161, 1320-1326 (1968).
16. M. Christen, "Air and gas damping of quartz tuning forks," *Sens. Actuators* 4, 555-564 (1983).
17. F. R. Blom, S. Bouwstra, M. Elwenspoek, and J. H. J. Fluitman, "Dependence on the quality factor of micromachined silicon beam resonators on pressure and geometry," *J. Vac. Sci. Technol. B* 10, 19-26 (1992).
18. L. D. Landau and E. M. Lifshitz, *Fluid Mechanics*, (Pergamon Press, London, pp. 88-98, 1959).
19. S. L. Firebaugh, F. Roignant, E. A. Terray, "Modeling the response of photoacoustic gas sensors," *Proceedings of Comsol Conference 2009*, Oct. 8-10, 2009, Newton, MA.
20. C. H. Yang, T. H. Chang, M. J. Yang, and W. J. Moore, "A low noise transimpedance amplifier for cryogenically cooled quartz tuning fork force sensors," *Rev. Sci. Instrum.* 73, 2713-2716 (2002).
21. S. C. Leonard and H. H. Race, "Calorimetric measurement of dielectric losses in solids," *Trans. Amer. Inst. Elect. Engrs.* 55, 1347-1356 (1936).
22. K. Liu, X. Guo, H. Yi, W. Chen, W. Zhang, and X. Gao, "Off-beam quartz-enhanced photoacoustic spectroscopy," *Opt. Lett.* 34, 1594-1596 (2009).
23. J.-P. Besson, *Photoacoustic spectroscopy for multi-gas sensing using near infrared lasers*, (Ph.D. Thesis, Swiss Federal Institute of Technology, 2006).

Chapter 5

Experimental investigation of QEPAS for gas detection

5.1 Introduction

QEPAS, which uses a tiny quartz tuning fork (QTF) for photoacoustically generated acoustic detection, shows several advantages, such as compact sensor size, low cost, immunity to environmental noise, etc., over the conventional PAS method with a microphone as acoustic detector. Since the first report of QEPAS in 2002 [1], it has been widely employed for various gases detection, including simple molecules, such as NH_3 [2-5], CH_4 [6], H_2O [2, 7], CO_2 [2, 8], CO [9, 10], C_2H_2 [2, 11, 12], C_2H_4 [13], etc., for a single rotational-vibrational line detection with WM method, and large molecules, such as Freon-134a or -125 [14-16], for broad, unresolved absorption spectra analysis with IM method. Besides the widely used on-beam QEPAS, in which the QTF is placed between the two tubes with its plane perpendicular to the optical beam, another configuration of QEPAS, called off-beam QEPAS, has also been proposed for trace gas detection, in which only one tube with a small slot on the tube side to let the acoustic wave be coupled out and detected by the QTF [17-19].

In this chapter, we will evaluate our QEPAS sensing system for gas detection by using a near-IR DFB laser as light source.

5.2 Absorption line selection and devices characterization

5.2.1 Absorption line selection

In absorption spectroscopy, gas detection is realized by the light absorption in the target gas at a specific spectral region. Since the fundamental absorption lines for most of the conventional gases are located in the mid-IR spectral region as depicted in Figure 5.1, the ideal absorption should happen at this range to ensure a strong absorption. Several QEPAS works based on the fundamental absorption lines were reported by using quantum cascade lasers (QCLs) [16, 20-22] or optical parametric oscillator (OPO) [23], and sensitivity up to 2 ppb has been achieved with cw external-cavity QCL. Although the absorption is much intense in this mid-IR region, the expensive source and detection system prevent its wide application in some areas. Moreover, the difficulty of the long distance light propagation in the mid-IR is also a big issue for remote gas sensing.

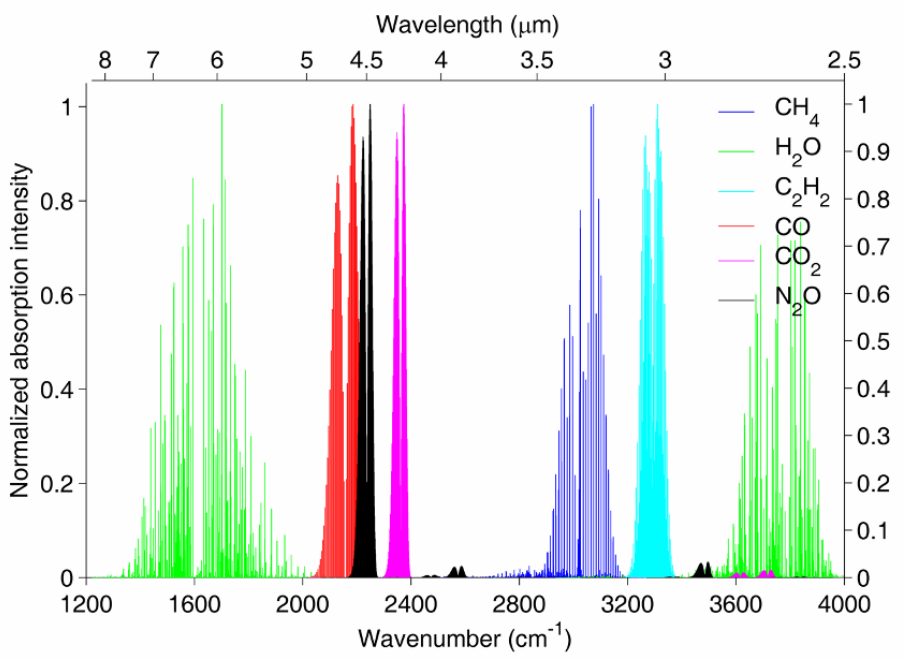

Figure 5.1 Fundamental absorption lines for conventional gases in the mid-IR spectral range according to the Spectroscopy of Atmospheric Gases website [24].

Therefore, we are interested in the QEPAS gas sensing in the near-IR. Although the absorption strength in this region is 1-2 orders smaller than the fundamental absorption lines, the light source and coupling system is easily available and it is quite convenient for the connection of the sensor to fiber based communication network for remote and multiplexing gas sensing. As an example, we select acetylene (C_2H_2) as our sensing gas for the evaluation of our QEPAS sensing system. Acetylene is a colorless and odorless gas, which is widely used as a fuel and a chemical building block in application. Although acetylene is not especially toxic, but the highly flammability makes it dangerous in many circumstances. Thus the concentration detection of acetylene is meaningful.

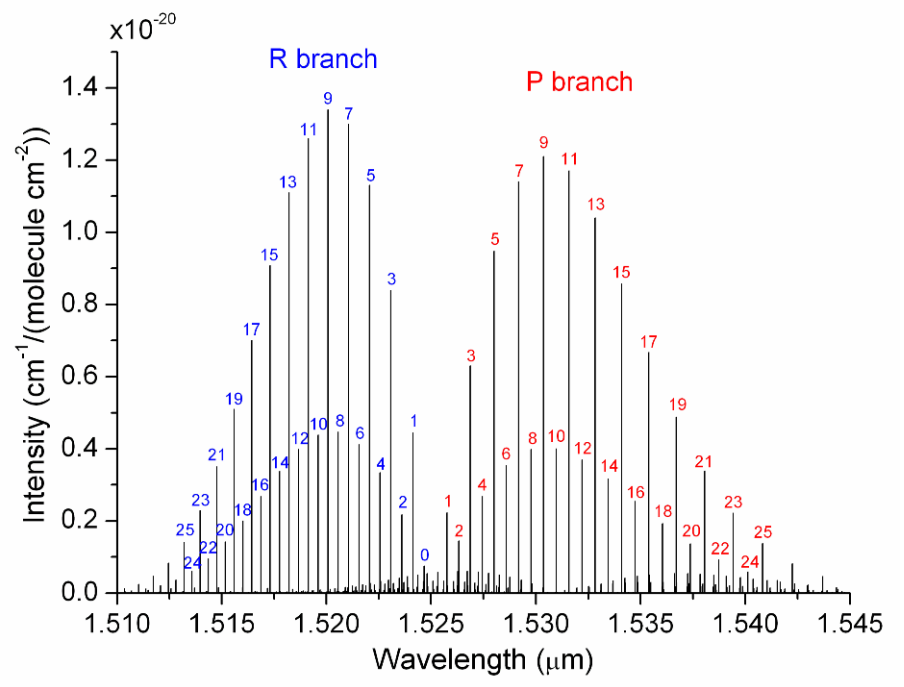

Figure 5.2 Absorption lines of C_2H_2 in the near-IR region with sequentially numbered on both P and R branches from HITRAN database.

The absorption intensity of C_2H_2 in near-IR is stronger than many other conventional gases, so it is usually selected for laboratorial gas sensing investigation. The absorption lines of C_2H_2 falling in the near-IR region is the ro-vibrational $\nu_1+\nu_3$

overtone band of it, with a distinct P-branch and R-branch structure, and plotted based on HITRAN database as shown in Figure 5.2 [25]. The main information for each absorption lines is also listed in Table 5.1.

Table 5.1 Main absorption lines of C_2H_2 in the near-IR spectral region.

No.	P Branch			R Branch		
	Wavenumber ν, cm^{-1}	Width γ, cm^{-1}	Intensity S, $cm^{-1}/(mol\ cm^{-2})$	Wavenumber ν, cm^{-1}	Width γ, cm^{-1}	Intensity S, $cm^{-1}/(mol\ cm^{-2})$
1	6554.1117	0.1114	2.222E-21	6561.0943	0.1043	4.441E-21
2	6551.7327	0.1043	1.448E-21	6563.3702	0.0985	2.170E-21
3	6549.3280	0.0985	6.299E-21	6565.6203	0.0940	8.385E-21
4	6546.8978	0.0940	2.675E-21	6567.8446	0.0903	3.337E-21
5	6544.4419	0.0903	9.475E-21	6570.0429	0.0875	1.134E-20
6	6541.9606	0.0875	3.539E-21	6572.2152	0.0852	4.117E-21
7	6539.4537	0.0852	1.144E-20	6574.3615	0.0834	1.303E-20
8	6536.9214	0.0834	3.977E-21	6576.4818	0.0820	4.456E-21
9	6534.3636	0.0820	1.211E-20	6578.5761	0.0808	1.340E-20
10	6531.7805	0.0808	4.002E-21	6580.6442	0.0796	4.380E-21
11	6529.1721	0.0796	1.165E-20	6582.6862	0.0787	1.264E-20
12	6526.5384	0.0787	3.693E-21	6584.7020	0.0777	3.977E-21
13	6523.8794	0.0777	1.035E-20	6586.6916	0.0768	1.107E-20
14	6521.1953	0.0768	3.165E-21	6588.6550	0.0756	3.369E-21
15	6518.4860	0.0756	8.572E-21	6590.5922	0.0746	9.078E-21
16	6515.7516	0.0746	2.539E-21	6592.5030	0.0733	2.677E-21
17	6512.9921	0.0733	6.665E-21	6594.3875	0.0719	7.000E-21
18	6510.2076	0.0719	1.915E-21	6596.2456	0.0704	2.004E-21
19	6507.3982	0.0704	4.882E-21	6598.0774	0.0688	5.092E-21
20	6504.5639	0.0688	1.363E-21	6599.8828	0.0671	1.418E-21
21	6501.7047	0.0671	3.379E-21	6601.6617	0.0653	3.504E-21
22	6498.8207	0.0653	9.178E-22	6603.4141	0.0635	9.495E-22
23	6495.9119	0.0635	2.214E-21	6605.1401	0.0616	2.285E-21
24	6492.9784	0.0616	5.855E-22	6606.8395	0.0597	6.030E-22
25	6490.0202	0.0597	1.375E-21	6608.5124	0.0578	1.414E-21

A DFB laser with wavelength ~ 1.53 μm is used as the light source in our QEPAS gas sensing system, which falls in the P branch of C_2H_2 absorption line. Consider the absorption intensity and the tunable range of our DFB laser, P(9)

absorption line, the maximum strength of P branch, of the $\nu_1+\nu_3$ overtone band of C_2H_2 is selected as the target absorption line. The line intensity is about 1.211×10^{-20} $cm^{-1}/(mol\ cm^{-2})$ and line width about 0.082 cm^{-1} (0.0192 nm) as given in Table 5.1. The line shape can be approximated by a Lorentzian profile at atmospheric pressure and room temperature as shown in Figure 5.3. The central wavelength, λ_0, of the P(9) line is ~ 1530.37 nm.

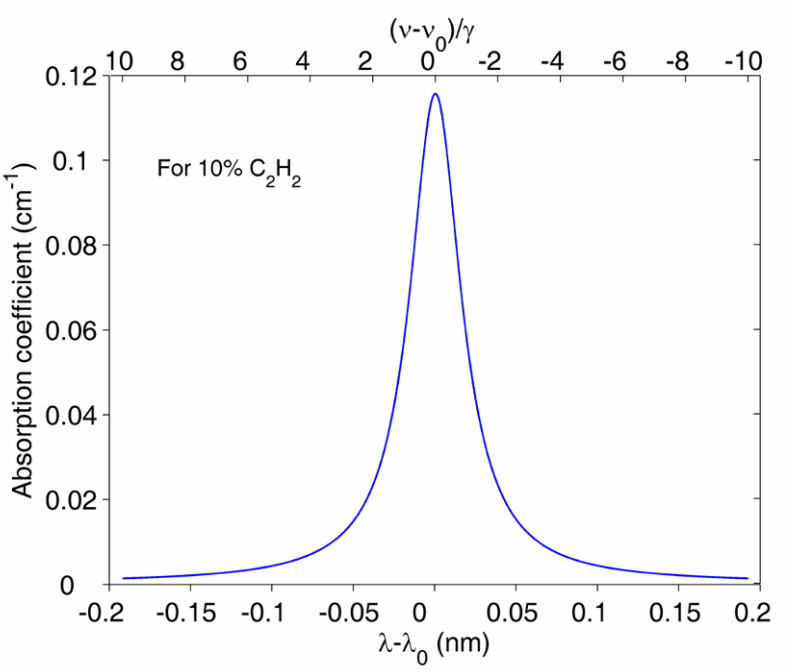

Figure 5.3 Line profile for the P(9) absorption line of C2H2.

5.2.2 Laser source characterization

As mentioned above, the light source used in our QEPAS system is a DFB diode laser with wavelength around 1.53 μm that made by Fujitsu Corp., coincide with the P(9) absorption line of C_2H_2 in the near-IR region as displayed in Figure 5.4. The wavelength also falls in the communication waveband that propagates in optical fiber with a very loss (0.02 dB/km).

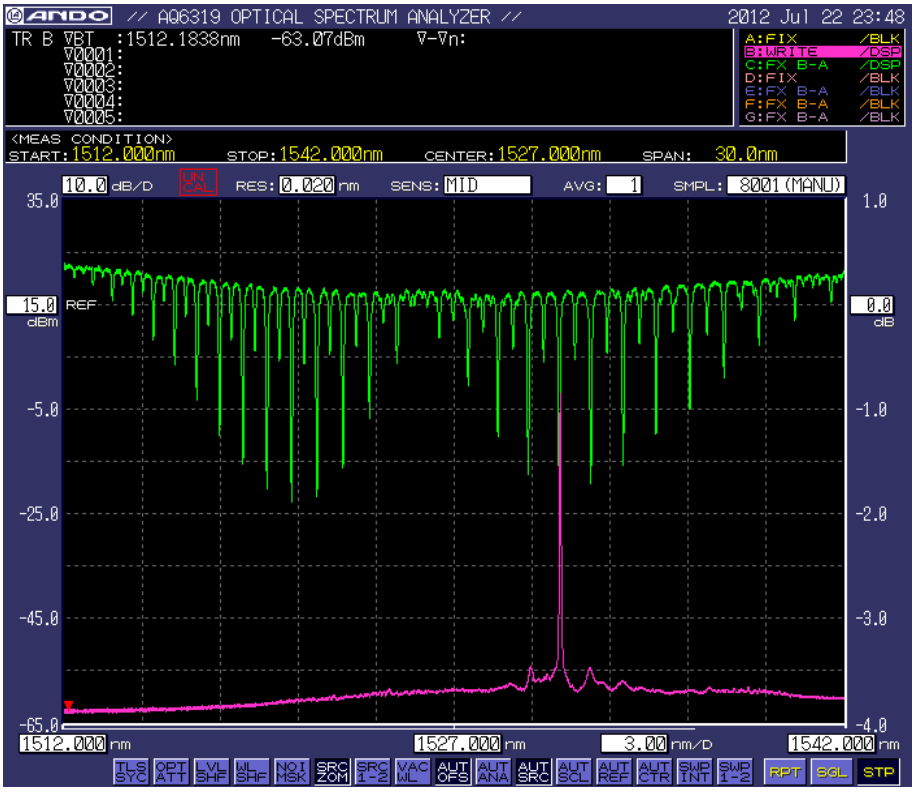

Figure 5.4 Spectrum of DFB (purple line) laser compared with the C_2H_2 absorption lines (green line) in the near-IR range.

The dependence of laser output power and wavelength on forward current is shown in Figure 5.5. It is shown that the laser is excited when the forward current is over 12 mA and the laser power shows an approximate proportional dependence on the driven current from 12-200 mA. As the forward current increases, the wavelength of the laser also varies as shown in Figure 5.6. The relationship between the forward current and laser wavelength can be regarded as linear in a small current range. However, for a larger current range, the laser wavelength seems increases fast for a larger driven current. This may be attributed to the nonlinear dependence of the laser temperature, which is proportional to the laser wavelength, on the driven current.

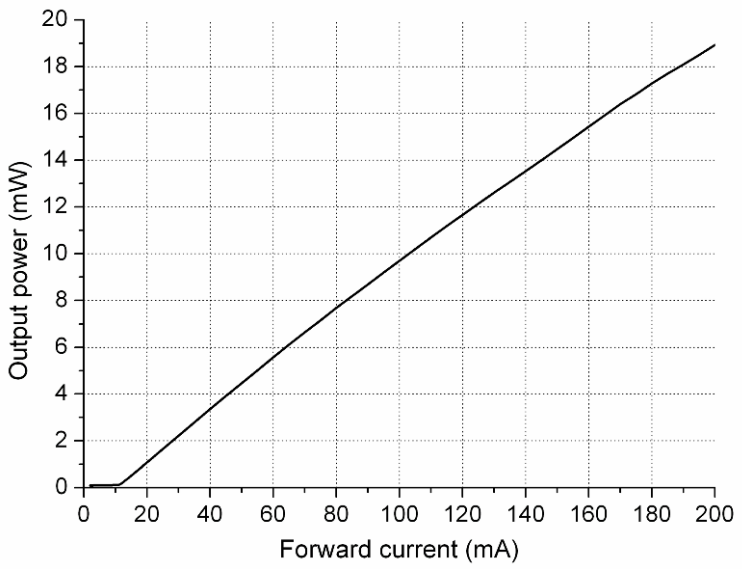

Figure 5.5 Dependence of laser output power on forward current.

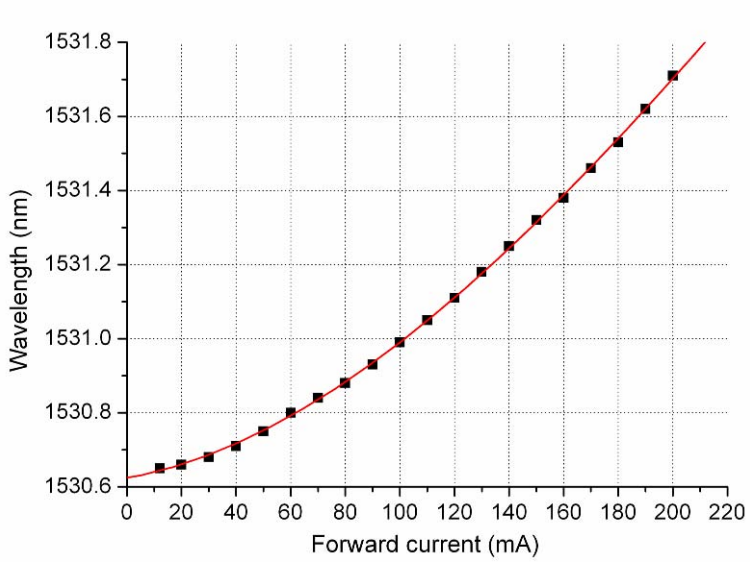

Figure 5.6 Dependence of laser wavelength on forward current.

One of the biggest advantages of DFB laser is its tunable wavelength property. The tuning range for a DFB laser is usually in ~nm range. The laser wavelength is controlled by a thermoelectric cooler (TEC) via temperature. When the laser temperature changes, the inner grating structure of DFB laser will vary, inducing the wavelength tuning. The temperature dependence of laser wavelength is examined

experimentally and plotted in Figure 5.7 with different forward current from 50 mA to 200 mA. It reveals that the laser wavelength shows a linear relationship with the temperature in the range 15-40 °C and a 1 °C temperature increase induces ~0.15 nm wavelength tuning. This means that temperature changing by 2-3 °C can result in the laser wavelength scanning across the whole absorption line of target gas as can be seen from Figure 5.3.

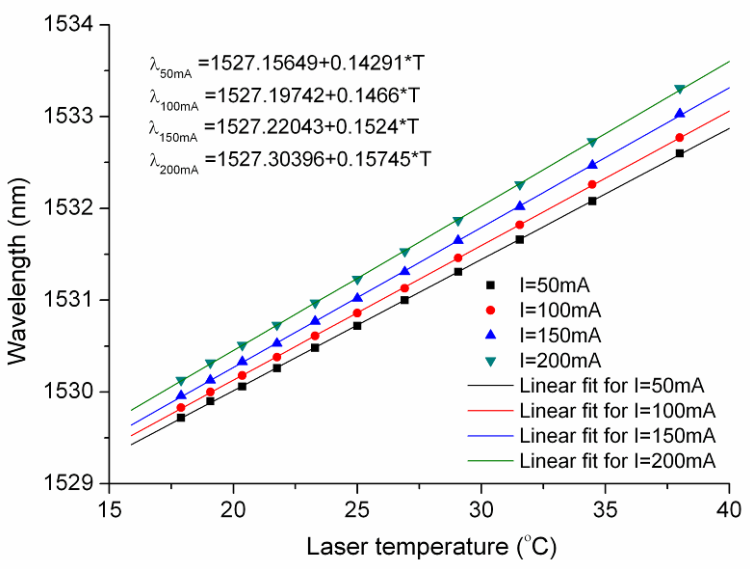

Figure 5.7 Dependence of laser wavelength on controlling temperature.

To obtain the influence of laser temperature changing on the output power, the laser power is also recorded with different temperature and forward current. The fitted results in Figure 5.8 show that the laser power hardly varies in a large temperature range, especially for a smaller forward current.

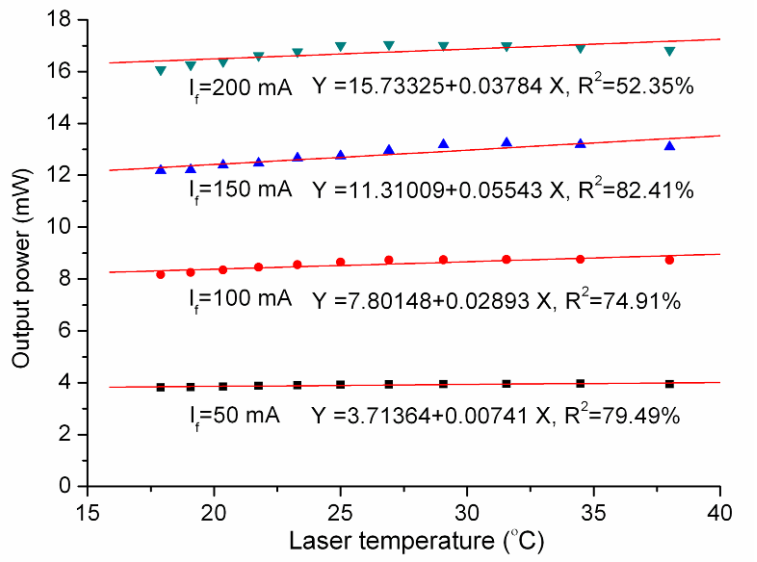

Figure 5.8 Dependence of laser output power on controlling temperature.

In the WM gas sensing experiment, the forward current is fixed at a specific point to provide a constant laser output power. And then an external sinusoidal current signal with a higher frequency is added to the forward current, which results in both the wavelength modulation and intensity modulation of the laser as described in section 3.4, thus to generate the periodic absorption. Before the gas sensing method, we need to find the relationship between the modulation signal and the wavelength and intensity modulation amplitude.

The modulation current added to the forward current results in a combined controlled current as

$$i = I_f + i_0 \cos(\omega_m t), \tag{5.1}$$

where I_f is the laser forward current, i_0 is the amplitude of the modulation current and ω_m is the modulation frequency. Then the laser output power and wavelength can be written respectively as

$$P = P_0 + \Delta P \cos(\omega_m t) = P_0 \left(1 + \frac{\delta P / P_0}{\delta i} \Delta i \cos(\omega_m t) \right), \tag{5.2}$$

$$\lambda = \lambda_0 + \Delta\lambda\cos(\omega_m t + \psi) = \lambda_0 + \frac{\delta\lambda/\gamma}{\delta i}\Delta i\gamma\cos(\omega_m t + \psi), \tag{5.3}$$

where P_0 and λ_0 are the power and wavelength at the fixed forward current, ΔP and $\Delta\lambda$ are the amplitudes of modulated power and wavelength, γ is the absorption line width (in nm). The next thing to do is to find the coefficients $\alpha_m = (\delta P/P_0)/\delta i$ and $\beta_m = (\delta\lambda/\gamma)/\delta i$, which represent the modulation characteristics of tunable laser, and also the phase delay ψ between the wavelength and intensity modulation.

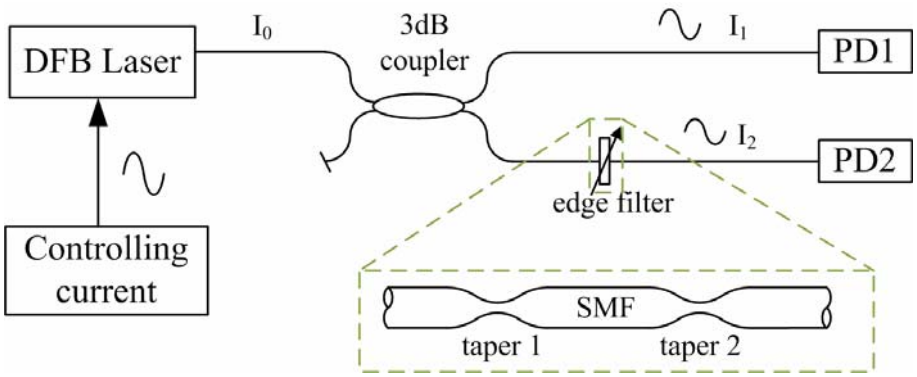

Figure 5.9 Diagram for determining the intensity and wavelength modulation coefficients. PD: photodetector.

The intensity modulation coefficient can be directly determined by measuring the dependence of laser power variation on the modulation current. However, the wavelength modulation coefficient can not be directly measured due to the fast variation of laser wavelength. Similar to the interferometric method proposed in [25], we designed a fiber optic interferometric system to simultaneously measure the intensity and wavelength modulation coefficients. The diagram is shown in Figure 5.9. Optical intensity of one arm is directly measured by a photodetector (PD1) and gives the form of α_m as

$$\alpha_m = \left(\frac{I_{1,\max} - I_{1,\min}}{I_{1,\max} + I_{1,\min}}\right)/\Delta i. \tag{5.4}$$

The other arm consists of an edge filter that made of a Mach-Zehnder interferometer (MZI) by the fabrication of two tapers on a single mode fiber as shown in the close-up figure of Figure 5.9. The laser wavelength is operated at the quadrature point of the MZI by carefully selecting the length between the two tapers to ensure an approximate linear relationship between the wavelength and transmitted light intensity [26]. The detected signal by photodetector 2 has the form of

$$I_2 = I_1 f(\lambda) = I_1(a + b\lambda)\,. \tag{5.5}$$

where $f(\lambda)$ is the transfer function of the edge filter and its coefficients, *a* and *b*, can be determined by scanning the laser wavelength and find the relationship between I_1 and I_2. Then in modulation case, laser wavelength can be determined by

$$\lambda = \frac{1}{b}\left(\frac{I_2}{I_1} - a\right), \tag{5.6}$$

so

$$\beta_m = \frac{ampl(I_2 / I_1)}{b\gamma\Delta i}, \tag{5.7}$$

$$\psi = phase(I_2 / I_1) - phase(I_1)\,. \tag{5.8}$$

where *ampl* and *phase* represent the amplitude and phase for detected signals.

Considering the WM method with second harmonic detection is used in the gas sensing experiment, the modulation frequency is fixed at the half of the resonant frequency of QTF (16.375 kHz in this experiment). The experimental results for $\Delta P / P_0$ versus Δi is plotted in Figure 5.10. It shows a linear relationship between them for small modulation and the fitted curve gives a value of $\alpha_m = 3.07\ A^{-1}$.

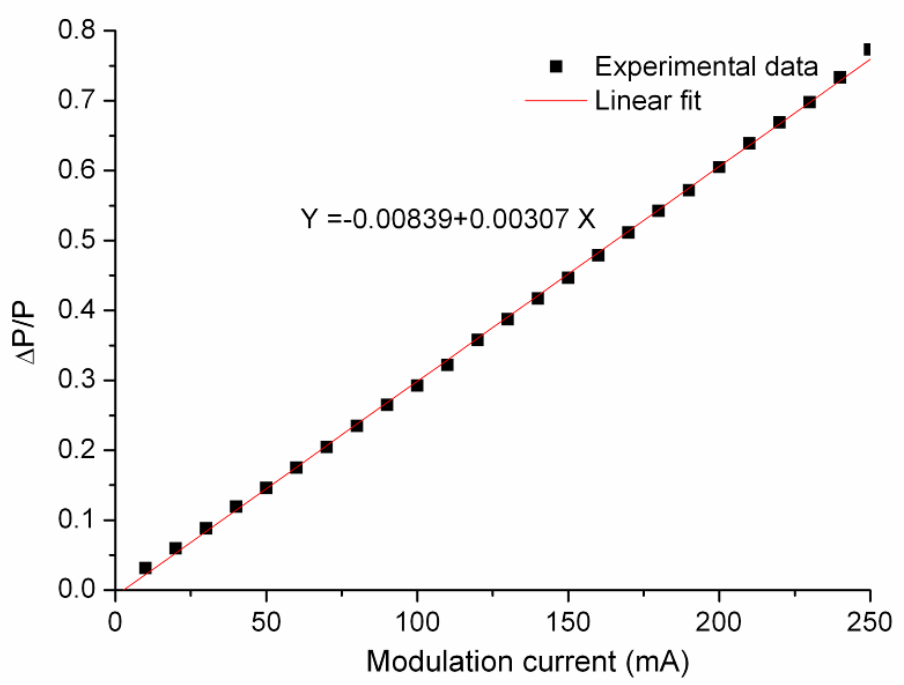

Figure 5.10 Dependence of power amplitude on the modulation current.

The transfer function of edge filter is obtained by scanning the laser wavelength near the quadrature point of the MZI and is shown in Figure 5.11. For a modulation frequency of 16.375 kHz, an example of I_1 and I_2 for modulation amplitude of 80 mA is plotted in Figure 5.12. The phase shift between I_2/I_1 and I_1, i.e., the phase shift between the wavelength modulation and intensity modulation, is found to be ~ -14°. The calculated amplitude of wavelength modulation dependent on the modulation current is plotted in Figure 5.13. And the fit curve gives a linear coefficient of 1.27 nm/A.

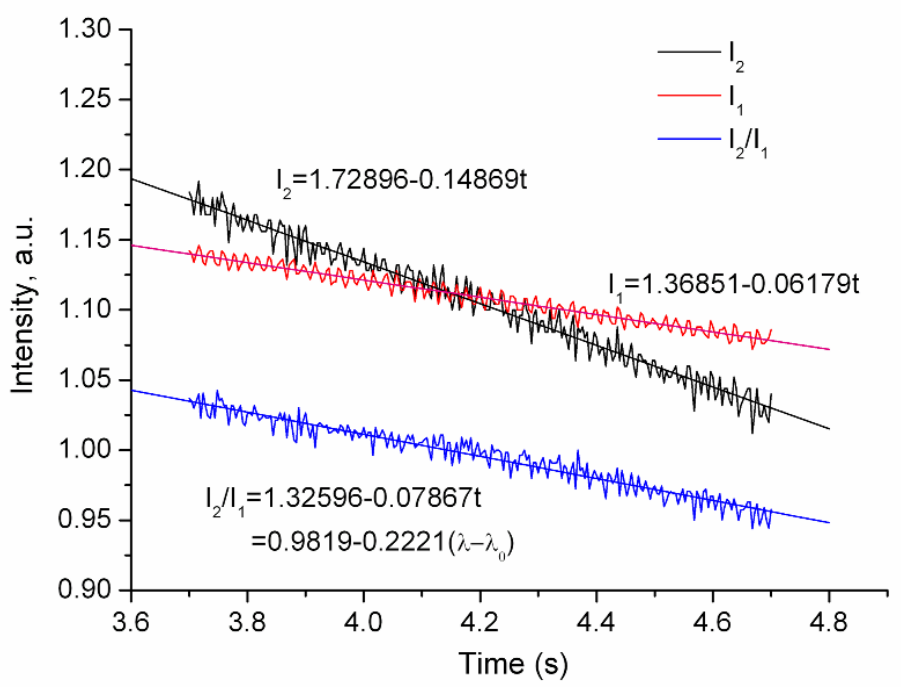

Figure 5.11 Dependence of I_1 and I_2 in Figure 5.9 on the laser wavelength as it is scanned around the quadrature point of MZI.

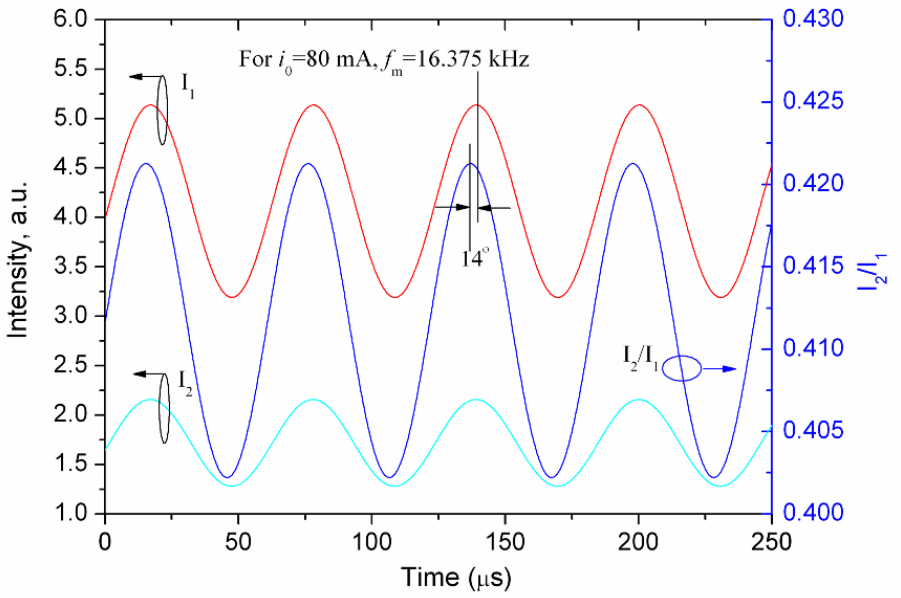

Figure 5.12 Wave signals for I_1, I_2 and I_2/I_1 at a modulation frequency of 16.375 kHz and modulation current of 80 mA.

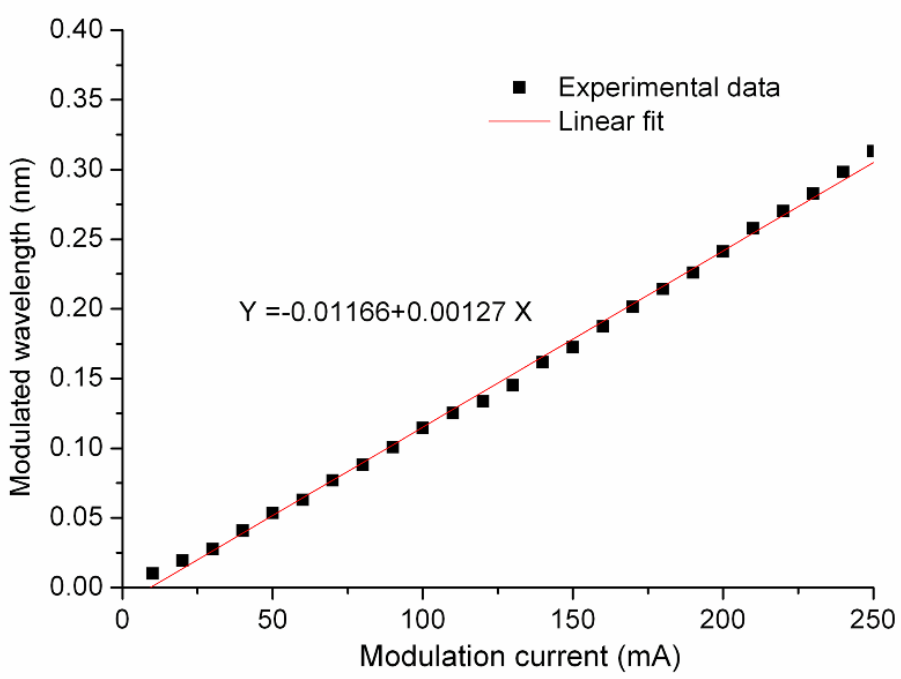

Figure 5.13 Dependence of modulated wavelength on the modulation current at a modulation frequency of 16.375 kHz.

5.2.3 Tuning fork performance

QTF, which is used to detect the generated PA signal in my experiment, is an important part in the spectrophone of QEPAS. An image of the QTF used in our experiment is displayed in Figure 5.14. Because of its high mechanical quality factor Q (10^3-10^5), QTF provides a build-in high gain and is very sensitive to sub-pN forces when used at or near its resonance frequency. Also, the high resonance frequency greatly reduces the 1/f noise in our PA sensing system. When a mechanical force is applied to the prongs of QTF, an electrical signal will be generated for the piezoelectric effect native to quartz crystals. The electrical signal is proportional to the applied force. Before the sensing experiment, the property of the QTF including the resonance frequency, quality factor and optimal position for applied force to get maximum signal should be accurately measured first.

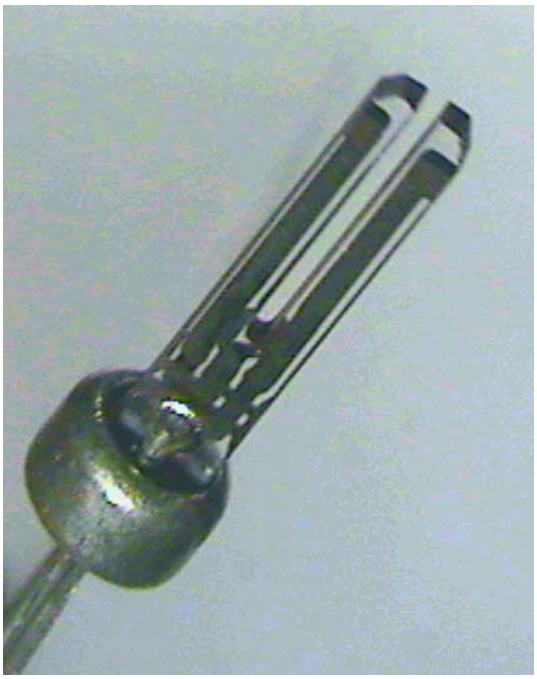

Figure 5.14 An image of the QTF used in our gas sensing system.

Generally, there are two ways to obtain the resonance curve of QTF [27]. One is to shake the QTF at its mechanical resonance and monitor the induced current (Figure 5.15 (a)), which is called mechanical configuration here. The other is to directly drive the QTF with an alternative voltage signal and measure the induced current (Figure 5.15 (b)). In both cases, the generated current signal is converted into voltage signal via a transimpedance amplifier with a feedback resistance R_f.

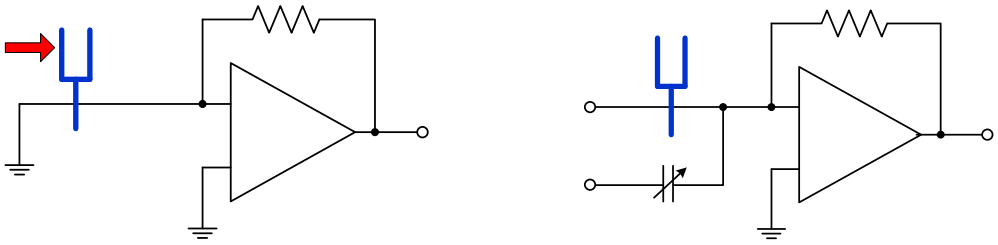

(a) (b)

Figure 5.15 Measurement configurations for resonance curve of the QTF: (a) mechanical configuration and (b) electrical configuration.

For the mechanical configuration, the optical beam is focused on the surface of one prong of the QTF, and then the optical power is modulated sinusoidally with a frequency scanning across the resonant frequency of QTF. The light beam with modulated power applied on the QTF provides a periodic force to the prong of QTF, which causes the prong of QTF oscillate and generate a piezoelectric current signal. The amplitude of the current signal is proportional to the displacement of QTF prong, and can be measured by a lock-in amplifier after the transimpedance amplifier [28]. With the amplitude of optical power fixed and QTF placed at atmospheric air, the dependence of lock-in signal on the modulation frequency is shown in Figure 5.16. Resonance frequency f_0 and quality factor Q can be calculated by Lorentzian fitting as shown in the figure. The asymmetry of the resonance curve is due to the equivalent package capacitance of QTF [27].

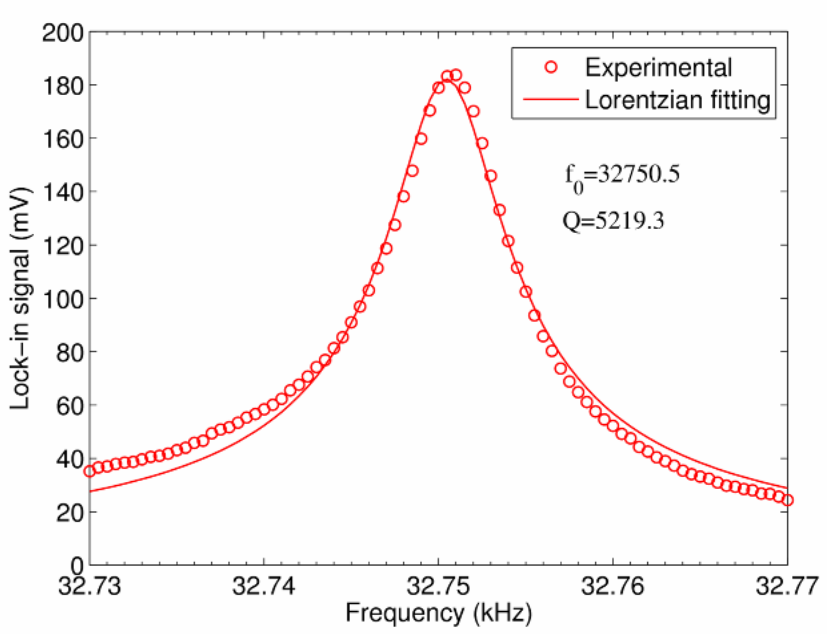

Figure 5.16 Resonance curve of QTF by mechanical configuration.

While for electrical configuration, a voltage signal with frequency around f_0 is directly applied to the QTF. In order to eliminate the effect from the QTF's package capacitance, another same voltage signal with opposite phase is applied to a variable

capacitor and added up to the generated current as shown in Figure 5.15 (b) [27]. Figure 5.17 shows the resonance curve of QTF in electrical configuration with the variable capacitance of 2 μF. Gain in Figure 5.17 represents V_{out}/V_{in}. It can be seen that the resonance curves match well with each other for different methods. And the resonance frequency of QTF is about 32.75 kHz and quality factor Q is higher than 5000, which proves that QTF is an efficient tool to detect the acoustic signal near its resonant frequency.

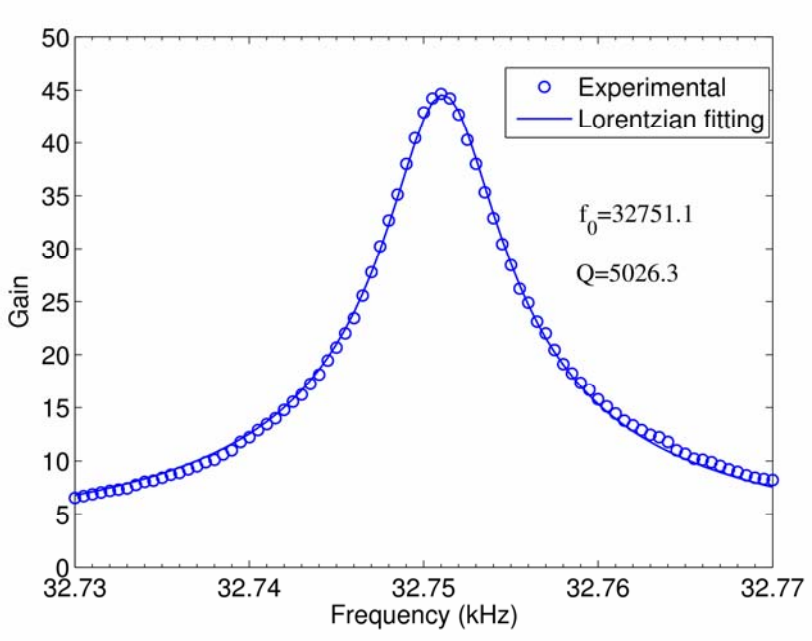

Figure 5.17 Resonance curve of QTF by electrical configuration.

5.3 Evaluation of QEPAS gas detection

QEPAS for C_2H_2 detection at atmospheric pressure and room temperature is carried out to evaluate the sensing ability of our system. The absorption is happened at the P(9) absorption line of the overtone band of C_2H_2 in the near-IR around 1.53 μm.

5.3.1 Experimental setup

The experimental setup of our gas sensing scheme is depicted in Figure 5.18. A DFB laser (FLD5F15CX-E9580, Fujitsu) with wavelength around 1.53 μm is employed as light source for photoacoustic excitation. The laser temperature is tuned by a slow varying triangle wave scanning signal from a computer-controlled DAQ device (NI USB-6009) and current is controlled by a fast varying sinusoidal modulation signal at half of the resonant frequency of QTF from lock-in amplifier simultaneously. 1% standard acetylene gas balanced by nitrogen diffused into the gas chamber serves as sample gas. The light from diode laser is fed into the gas chamber by SMF and focused through the gap between the two prongs of QTF by a collimator. A pair of stainless steel tubes, known as acoustic micro-resonator (mR), with a length of 4.4 mm and inner diameter of 0.5 mm as suggested in Ref. [29], is placed along the beam of laser light and beside the two facets of QTF to enhance the acoustic signal. A QTF (JU308, Yajingxin Electronics Co. Ltd) with a high Q-factor (~10,000) and resonant frequency ~32.75 kHz at atmospheric pressure is used as photoacoustic transducer. The piezoelectric current from QTF is transformed to voltage signal by a self-designed transimpedance amplifier with a feedback resistor R_f=10 MΩ and then demodulated by a lock-in amplifier (SR830 DSP, Stanford) for second harmonic detection. The time constant of lock-in amplifier is set to 1 s with a filter slope 18 dB/octave, which corresponds to a detection bandwidth of Δf_{BW}=0.094 Hz. The laser light after the spectrophone is refocused into a SMF for reference.

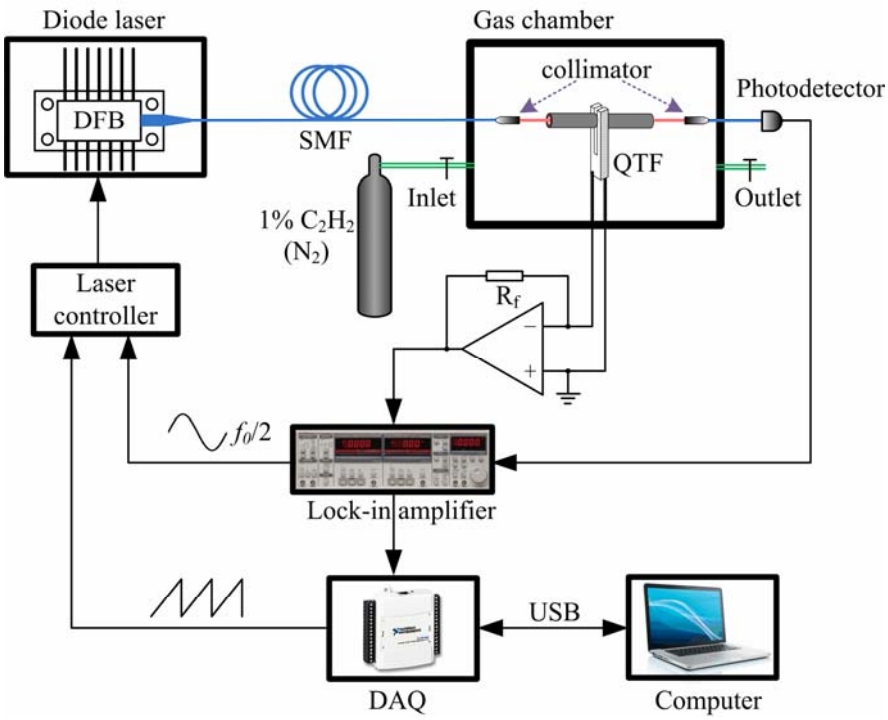

Figure 5.18 Experimental setup for DFB laser based QEPAS configuration. The feedback resistance of transimpedance amplifier is R_f=10 MΩ; the control current of DFB laser is modulated at half of the resonant frequency of QTF; DAQ, data acquisition. The blue line shows the optical fiber, the red line is optical beam in open path and the black line describes the electric path.

5.3.2 Gas concentration calibration

In laboratorial gas sensing research, the sample gas is usually prepared by injecting a standard gas flow into the gas chamber. For a small gas chamber, the sample gas concentration can reach that of the source gas in seconds, so it can be treated the same as the standard gas with its concentration level provided by its manufactory. However, optical alignment and focusing parts are included in our sensing gas chamber, which requires the gas chamber to have a relatively larger volume. A volume of ~11.9 L is estimated for our gas chamber. Thus a relatively longer time is needed for the gas concentration to reach that of the source gas. In order to precisely quantitate the instaneous gas concentration in the chamber and save the amount of

the source gas, which is to some extent meaningful in laboratory gas sensing research, we developed a simple but efficient method for the gas concentration calibration in the gas chamber.

Standard gas with a concentration of C_0 is assumed to be injected into a gas chamber with a volume V_c, at an instaneous gas flow rate of $Q_{flow}(t)$. The gas concentration within the chamber at an arbitrary time is $C(t)$ with an assumption that the gas in the chamber reaches a homogenous distribution in short time. The time derivative of the gas concentration may be expressed as

$$C'(t) = \left[C_0 - C(t)\right] Q_{flow}(t) / V_c . \tag{5.9}$$

For a constant gas flow rate Q_{flow}, the gas concentration in the chamber is derived as

$$C(t) = C_0 + \left[C(t_0) - C_0\right] \exp(-Q_{flow} t / V_c) , \tag{5.10}$$

where $C(t_0)$ is the initial gas concentration in the gas chamber.

As the photoacoustic signal is proportional to the gas concentration [11], the acoustic signal $S(t)$ should follow the below expression with a constant flow rate filling process with initial gas concentration of zero

$$S(t) = S_0 C(t) = S_0 C_0 \left[1 - \exp(-Q_{flow} t / V_c)\right], \tag{5.11}$$

where S_0 is a constant describing the sensitivity of the setup. Hence, if the signal $S(t)$ could be measured experimentally, the instaneous gas concentration $C(t) = S(t) / S_0$ and the constant gas flow rate Q_{flow} would be obtained by fitting the measured curve to Eq. (5.11).

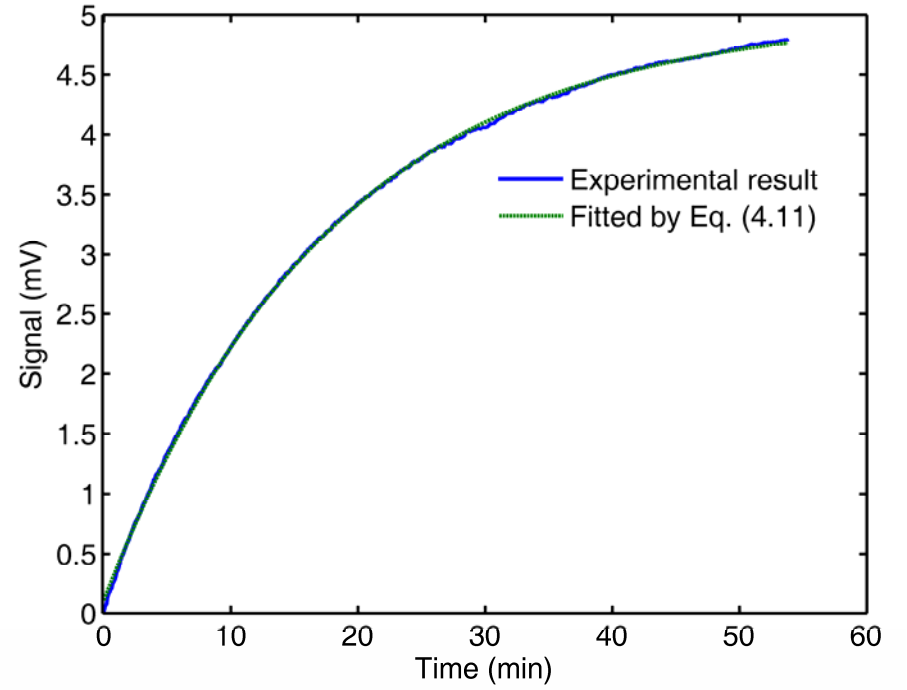

Figure 5.19 Experimental result (blue line) and fitting curve (green line) for photoacoustic signal during the constant flow rate filling process. The sensitivity and gas flow rate were found to be 0.489 μV/ppm and 673.5 SCCM for our gas chamber with a volume of ~11.9 L.

With DFB laser wavelength tuned to the peak of the gas absorption line, the signal from QTF was recorded by filling the ~1% acetylene into our gas chamber with a constant flow rate and is shown in Figure 5.19 as the blue line. The fitted curve from Eq. (5.11) is also plotted in Figure 5.19 as the green dash line. They matches perfect with each other, which proves the validity of the calibration method. The fitted value of the sensitivity is S_0=0.489 μV/ppm, and the flow rate is Q_{flow}=673.5 cm^3/min (SCCM). At the end of this recording (~54 min), the gas concentration is estimated to be ~0.95%. The gas chamber is then sealed and used to evaluate the performance of the system, as will be reported in the following sections.

5.3.3 Results and discussion

5.3.3.1 PA signal profile

In order to obtain the PA signal profile, the central wavelength of the laser source is scanned across the absorption line by controlling the laser temperature, which is linearly related to the wavelength as demonstrated in section 5.2.2. At the same time, the laser wavelength is fast modulated around the central wavelength by an external current with frequency fixed at 16.373 kHz (around the half the resonant frequency of QTF), and the current modulation amplitude is set to 100 mA to ensure a relatively larger PA signal. The second harmonic PA signal is detected by QTF and demodulated by a lock-in amplifier. The laser power passing through the gap between of QTF is measured to be 8.44 mW. The dependence of PA signal on laser temperature is shown in Figure 5.20 as the red line. It is shown the maximum PA signal is achieved around 21.7 °C, corresponding to the central wavelength of P(9) absorption line in the $\nu_1+\nu_3$ band of C_2H_2. The maximum value of PA signal is found to be 4.63 mA and peak to peak value to be 7.56 mV. The signal in the non-absorption region approaches to zero quickly as expected. For comparison, the PA signal without mR at the same gas concentration is also recorded and shown in Figure 5.20 as the black dash line. For better visibility, the PA signal without mR is amplified by 10 times. It is shown that the PA signal is amplified by over 20 times with a pair of mR compared with bare QTF case. And the signal profile almost maintains the same.

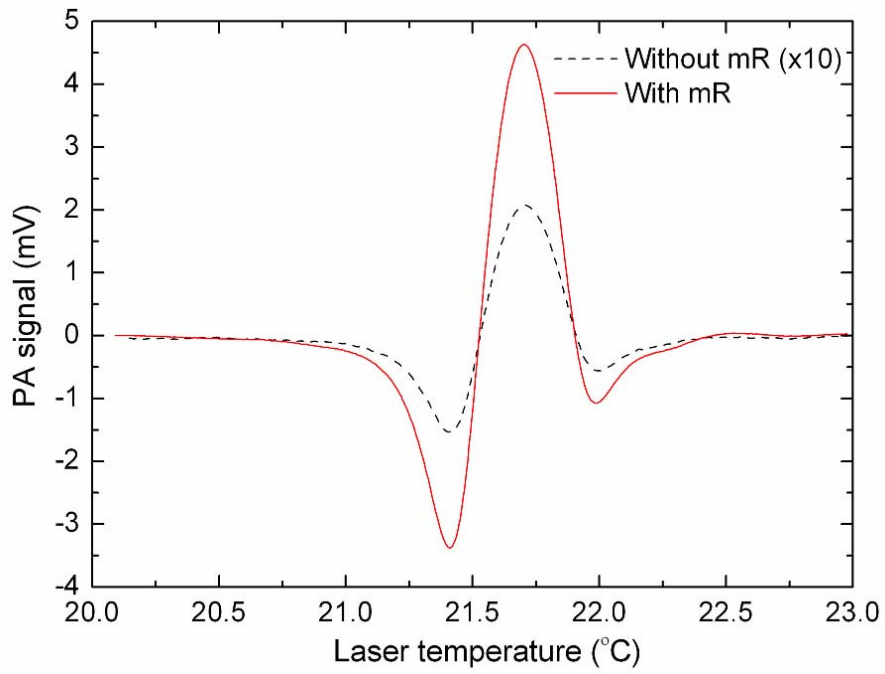

Figure 5.20 PA signal for system with and without mR depended on the laser temperature.

5.3.3.2 Frequency response

Since the detection in our system is extremely dependent on the operation frequency, the modulation frequency should be tuned properly to guarantee the excitation and detection of acoustic signal at the most sensitive frequency of tuning fork, i.e., the resonant frequency. Considering the second harmonic WM scheme used in our system, the modulation frequency of current signal is scanned around half of the resonant frequency of QTF with laser wavelength fixed at the peak absorption point and modulation current of 100 mA. The PA signal was recorded by varying the modulation frequency from 16.34 to 16.4 kHz, corresponding to the frequency response of QTF from 32.68 to 32.8 kHz, and shown in Figure 5.21 as the red dots. The data is fitted by Lorentzian profile to achieve its central frequency and *Q*-factor as 16,372.15 Hz and 4,433, indicating that the maximum PA signal happens for QTF vibrating at 32,744.3 Hz. To study the effect of mR on the resonance of QTF, the resonance curve for the non-mR case was also measured and shown in Figure 5.21

for comparison, with values also multiplied by 10 for visibility reason. The *Q*-factor and peak modulation frequency are calculated to be 8,699 and 16,373.3 Hz, corresponding to the QTF frequency of 32,746.6 Hz. That is to say, the resonant frequency of the system is down shifted by 2.3 Hz and *Q*-factor reduced by almost a half with the introduction of the mR. However, PA signal is amplified by ~ 22.5 times by the use of mR. These results agree with the numerical investigation of spectrophone of QEPAS.

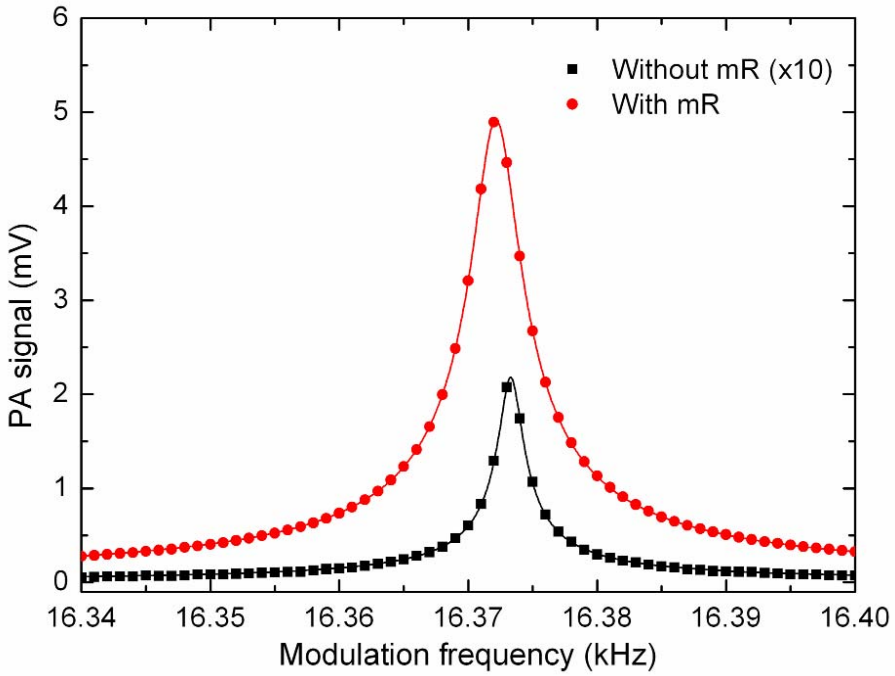

Figure 5.21 Frequency response of the PA signal on modulation frequency for spectrophone with and without mR. Both of the results are fitted by Lorentzian profile.

5.3.3.3 Modulation characterization

As stated previously, in WM scheme with a semiconductor laser source, a modulation current signal applied to the laser can result simultaneously the wavelength and intensity modulation of the laser source. The latter usually acts as a secondary factor that affects the signal profile and phase condition of the acoustic

detection, known as residual intensity modulation (RIM). The amplitude of the current modulation can significantly determine the magnitude of PA signal. Thus experimental investigation on the dependence of modulation on the PA signal and the effect of RIM on WM is necessary and meaningful.

The WM QEPAS experiment was carried out for acetylene detection at the P(9) absorption line, corresponding to a line intensity of 1.211×10^{-20} $cm^{-1}/(molecule\ cm^{-2})$, line width of 0.082 cm^{-1} and line center at 6534.3636 cm^{-1} [24]. The sample gas is 0.95% C_2H_2 balanced by N_2. Laser output power involved in gas absorption was measured to be 8.44 mW. And the relative magnitude of laser output power modulation was found to be $\Delta P/P_0=3.07\cdot i_0$, where i_0 (in Ampere) is the amplitude of current modulation applied to laser source. The phase delay between WM and RIM was found to be -25° at the modulation frequency of 16.373 kHz by using an interferometric method [27]. The second harmonic PA signal was also experimentally measured by tuning the laser wavelength across the gas absorption line and is plotted in Figure 5.22 as the green dashed line. For comparison, we also displayed the theoretical result according to the derivation in section 3.4 by using the measured parameters of the laser. It is shown that the profiles of the experimental and theoretical results match well with each other. And the asymmetry for the signal profile is due to the influence of RIM, which increases the PA signal in the short wavelength side while suppresses the signal in the long wavelength side as can be seen from Figure 3.16.

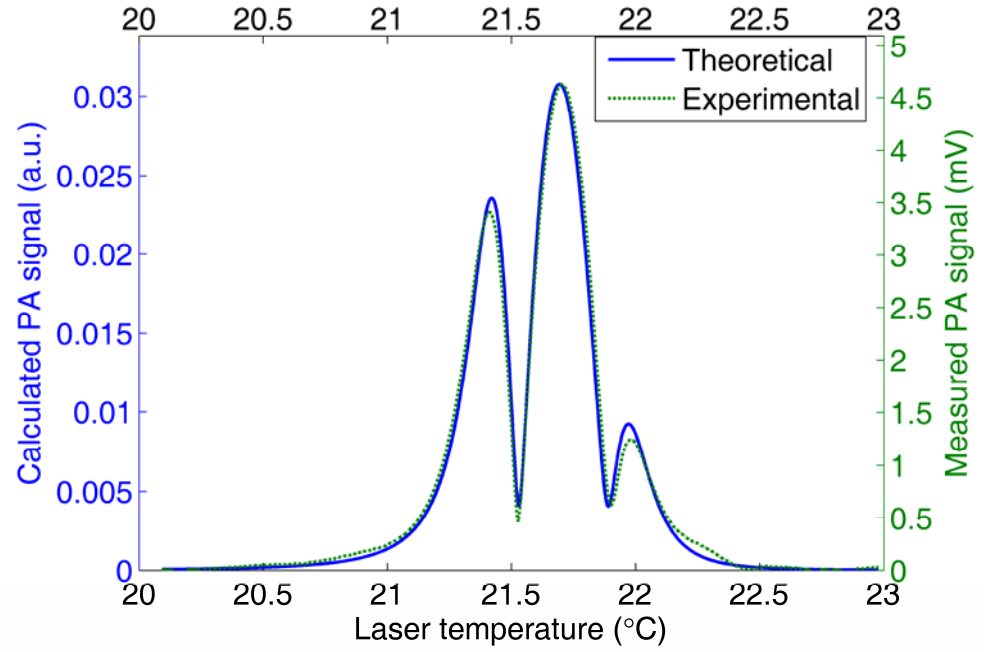

Figure 5.22 Magnitude of the PA signal for varied laser temperature around the absorption line for both experimental and theoretical results.

The dependence of maximum PA signal on modulation depth, regardless of the sign, for combined WM and RIM is experimentally measured and plotted in Figure 5.23 as the green circles. It reveal that the PA signal increases quickly with modulation depth before the modulation depth reaches a value around 2, where the PA signal achieves its maximum value. After that, the PA signal reduces with continue increasing the modulation depth. The efficiency of the sensor decreases quickly to prevent it from effective gas detection. By comparison, we also provide the theoretical result in Figure 5.23 as the blue line. They agree well with each other for small values of modulation depth. The optimal PA signal happens for the modulation depth equals to 2.184 (marked as red square), very close to the pure WM value of 2.2 [30]. By fitting the experimental date to the theoretical curve, a relationship between modulation current and the modulation depth was found to be $m=19.5i_0$. Hence the optimum modulation current for our experimental system can be calculated to be 112 mA. The departure between the theoretical and experimental

results for the larger modulation depth might be explained by the nonlinear relationship between the WM and PA signal. Thus higher order harmonics for the absorption must be included in the problem [31].

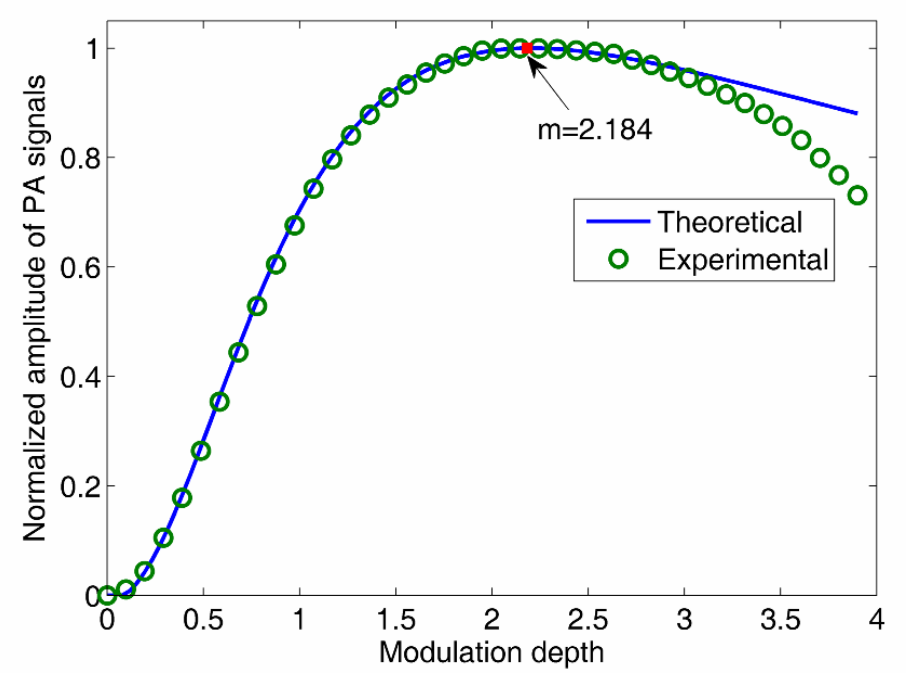

Figure 5.23 Normalized maximum PA signals for different modulation depth.

For different detection phase on the lock-in amplifier, the PA signal shows a different profile and amplitude as plotted in Figure 5.24. For pure WM, the PA signal will show a symmetric structure as the acoustic signal is detected at a phase equaling to or reversal with the twice of the phase delay of WM to the current modulation (i.e., 2ψ). However, the involvement of the RIM makes the phase detection complicated and the symmetric PA signal might not be achieved at 2ψ. From Figure 5.24 we can roughly find that PA signal achieves its positive maximum value around -180° while achieves negative maximum value near 0°.

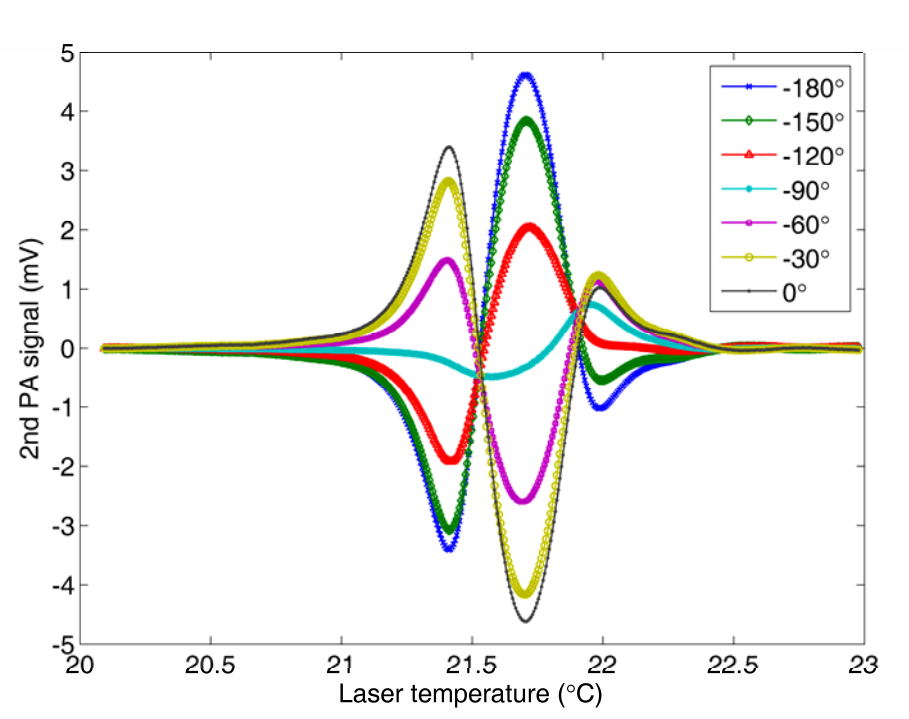

Figure 5.24 PA signals for different detection phase on the lock-in amplifier.

Regardless of the sign of the signal, the peak value of the second harmonic signal for varying detection phase angle was theoretically calculated and compared with experimental measurement. The maximum PA signal for each single detection phase is plotted in Figure 5.25 with normalization. The profile and relative amplitude agrees well with each other for experimental and theoretical results. The theoretical PA signal is maximized at a detection phase $\Phi_{max,\,theo}=-50°+n\cdot 180°$, where $n=0,\pm 1,\pm 2,...$, coherent with the previous conclusion. However, the experimental signal maximums occur at $\Phi_{max,\,exp}=-4°+n\cdot 180°$. Considering the sign of signals, a phase lag of 134° is found between the experiment and the theory. To understand the source of the phase delay, we measured the PA signal with different detection phases for a spectrophone without mR, and the maximum signal was achieved at -113°, which lags the theoretical result by 63° but leads the result of the mR-based QEPAS by 71°. Therefore, we may conclude that the 63° phase lag might be resulted

from the time delay in photoacoustic process and phase delay of the QTF [32], while the part of 71° mainly comes from the acoustic resonance setup and coupling in the tubes. This could be interpreted by the phase evolution in the acoustic resonance as described in section 3.2 and section 4.3.

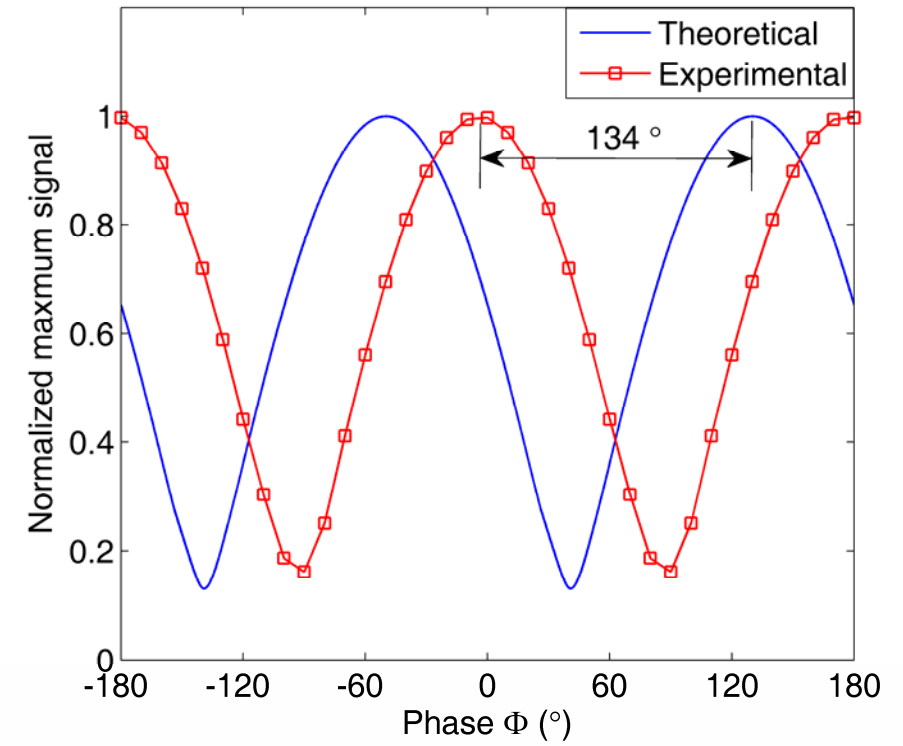

Figure 5.25 Normalized peak values of second harmonic PA signal for varying detection phase.

5.3.3.4 Noise analysis

As can be seen from Figure 5.19 and Eq. (5.11), the detected PA signal is approximately proportional to the gas concentration, with a sensitivity of 0.489 μV/ppm. In order to obtain the minimum detection limit (MDL) of the gas concentration for our sensing system, we need to achieve the noise level of our system first.

To evaluate the noise level of our sensing system, the laser wavelength was fixed at absorption line center, and the modulation frequency fixed at 16.372 kHz,

corresponding to the resonant frequency of QTF. The PA signal was recorded point to point with a 1 s integration time. A noise level of 2 μV was found from the standard deviation of the baseline measurements as shown in Figure 5.26. Considering a minimum distinguishable voltage level of 1.22 μV (2*10 mV/2^{14}) of our data acquisition device, this noise level is not reliable. So the laser wavelength was tuned to the non-absorption region and the DAQ device is selected with a smaller scale, this time a noise level of 1.02 μV was achieved as the blue line in Figure 5.26, consistent with the thermal noise level of QTF (1 μV) at current condition [11, 27]. Therefore, the SNR is estimated to be 4798, corresponding to a MDL of 2 ppmv and a normalized noise equivalent absorption coefficient (1σ) of 6.16×10^{-8} cm^{-1} W/ $Hz^{1/2}$.

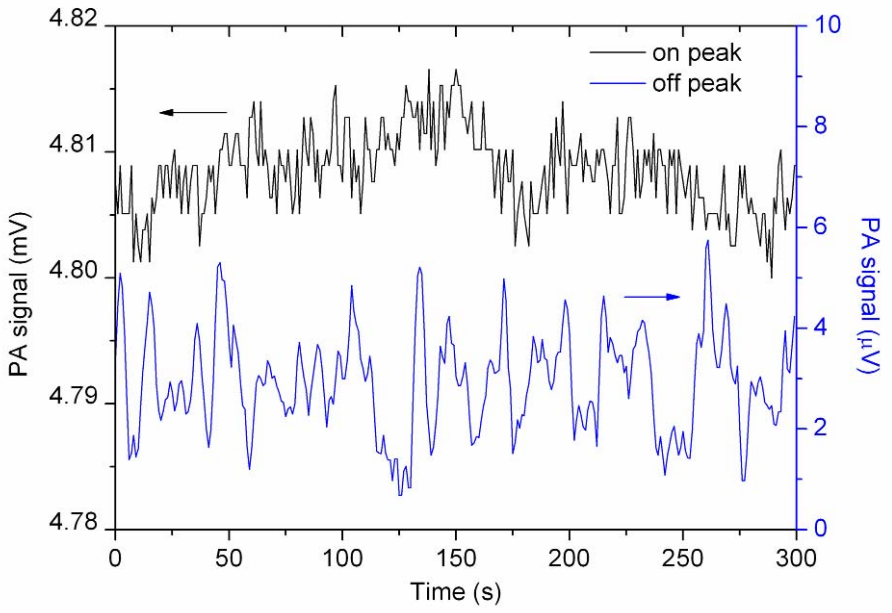

Figure 5.26 PA signals for 0.95% C_2H_2 on the absorption peak and off the absorption peak, respectively, to show the noise level of the QEPAS system.

To evaluate the long term stability of our system, the Allan variance analysis was also provided as shown in Figure 5.27 [33]. The black and blue lines show the Allan deviation of time series measurements for 0.95% C_2H_2 in N_2 and pure air,

respectively. The red line with a slope ~t demonstrates the linear drift of the signal due to the gas leakage of the chamber. For pure air, there is no gas leakage, so the Allan deviation shows a white noise behavior, as indicated by the green line with a slope ~$t^{-1/2}$. As can be seen, the stability time for present sensing system is 10 s for the both cases, which is mainly determined by the laser temperature stability time and gas chamber stability. Thus, the sensor sensitivity could be further improved with a longer integration time.

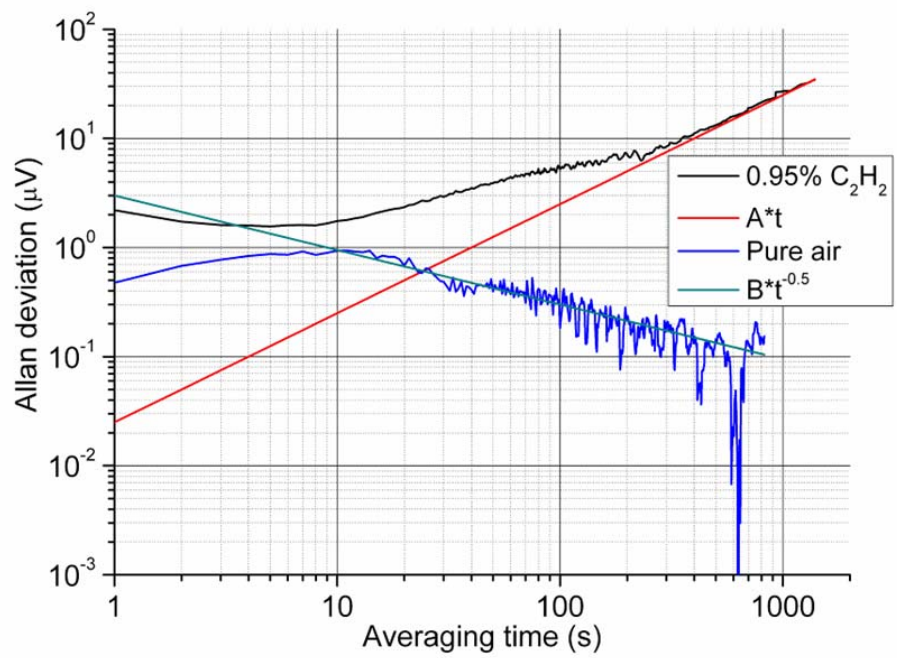

Figure 5.27 Allan deviations for time series measurement of signals for 0.95% C_2H_2 in N_2 and pure air. The red and green lines are fitting curves with slopes ~t and ~$t^{-1/2}$, respectively. A, B are fitting coefficients.

5.3.4 Conclusion

Our QEPAS system is experimentally evaluated in this section for C_2H_2 detection at the P(9) absorption line of the overtone band in the near-IR region. With a DFB laser operating at 1.53 μm and an output power of 8.44 mW, the PA signal is achieved as ~0.5 mV/ppmv with optimized spectrophone. Considering the noise level of 1.02 μV

for our setup with a 10 MΩ feedback resistance in the transimpedance amplifier, a minimum detectable concentration limit of 2 ppmv is obtained, corresponding to a normalized noise equivalent absorption coefficient (1σ) of 6.16×10^{-8} cm^{-1} W/ $Hz^{1/2}$.

5.4 Summary

In this chapter, we carried out the gas sensing experiment by our QEPAS system. Before the experiment, absorption spectrum of C_2H_2 was introduced, the characteristics of our DFB laser were examined, and the resonance curve of QTF used in our system was measured by different methods. An efficient gas concentration calibration method was presented. The influence of RIM on WM was analyzed and compared with theoretical results. With optimized spectrophone, the QEPAS was evaluated for C_2H_2 detection, resulting in a minimum detectable limit of 2 ppmv.

References of Chapter 5

1. A. A. Kosterev, Y. A. Bakhirkin, R. F. Curl, and F. K. Tittel, "Quartz-enhanced photoacoustic spectroscopy," *Opt. Lett.* 27, 1902-1904 (2002).
2. D. Weidmann, A. A. Kosterev, F. K. Tittel, N. Ryan, and D. McDonald, "Application of a widely electrically tunable diode laser to chemical gas sensing with quartz-enhanced photoacoustic spectroscopy," *Opt. Lett.* 29, 1837-1839 (2004).
3. A. A. Kosterev and F. K. Tittel, "Ammonia detection by use of quartz-enhanced photoacoustic spectroscopy with a near-IR telecommunication diode laser," *Appl. Opt.* 43, 6213-6217 (2004).
4. R. Lewicki, G. Wysocki, A. A. Kosterev, and F. K. Tittel, "Carbon dioxide and ammonia detection using 2μm diode laser based quartz-enhanced photoacoustic

spectroscopy," *Appl. Phys. B* 87, 157-162 (2007).

5. D. V. Serebryakov, I. V. Morozov, A. A. Kosterev, and V. S. Letokhov, "Laser microphotoacoustic sensor of ammonia traces in the atmosphere," *Quantum Electron.* 40, 167-172 (2010).
6. A. A. Kosterev, Y. A. Bakhirkin, F. K. Tittel, S. McWhorter, and B. Ashcraft, "QEPAS methane sensor performance for humidified gases," *Appl. Phys. B* 92, 103-109 (2008).
7. K. Liu, J. Li, L. Wang, T. Tan, W. Zhang, X. Gao, W. Chen, and F. K. Tittel, "Trace gas sensor based on quartz tuning fork enhanced laser photoacoustic spectroscopy," *Appl. Phys. B* 94, 527-533 (2009).
8. G. Wysocki, A. A. Kosterev, and F. K. Tittel, "Influence of molecular relaxation dynamics on quartz-enhanced photoacoustic detection of CO_2 at $\lambda = 2$ μm," *Appl. Phys. B* 85, 301-306 (2006).
9. A. A. Kosterev, Y. A. Bakhirkin, and F. K. Tittel, "Ultrasensitive gas detection by quartz-enhanced photoacoustic spectroscopy in the fundamental molecular absorption bands region," *Appl. Phys. B* 80, 133-138 (2005).
10. A. A. Kosterev, Y. A. Bakhirkin, F. K. Tittel, S. Blaser, Y. Bonetti, and L. Hvozdara, "Photoacoustic phase shift as a chemically selective spectroscopic parameter," *Appl. Phys. B* 78, 673-676 (2004).
11. A. A. Kosterev, F. K. Tittel, D. V. Serebryakov, A. L. Malinovsky, and I. V. Morozov, "Applications of quartz tuning forks in spectroscopic gas sensing," *Rev. Sci. Instrum.* 76, 043105 (2005).
12. Y. Cao, W. Jin and H. L. Ho, "NIR diode laser-based QEPAS for acetylene detection," *Proc. SPIE* 8439, 843928 (2012).
13. S. Schilt, A. A. Kosterev, and F. K. Tittel, "Performance evaluation of a near infrared QEPAS based ethylene sensor," *Appl. Phys. B* 95, 813-824 (2009).
14. M. D. Wojcik, M. C. Phillips, B. D. Cannon, and M. S. Taubmna, "Gas-phase

photoacoustic sensor at 8.41 μm using quartz tuning forks and amplitude-modulated quantum cascade lasers," *Appl. Phys. B* 85, 307-313 (2006).

15. M. C. Phillips, T. L. Myers, M. D. Wojcik, and B. D. Cannon, "External cavity quantum cascade laser for quartz tuning fork photoacoustic spectroscopy of broad absorption features," *Opt. Lett.* 32, 1177-1179 (2007).
16. R. Lewicki, G. Wysocki, A. A. Kosterev, and F. K. Tittel, "QEPAS based detection of broadband absorbing molecules using a widely tunable, cw quantum cascade laser at 8.4 μm," *Opt. Express* 15, 7357-7366 (2007).
17. K. Liu, X. Guo, H. Yi, W. Chen, W. Zhang, and X. Gao, "Off-beam quartz-enhanced photoacoustic spectroscopy," *Opt. Lett.* 34, 1594-1596 (2009).
18. K. Liu, H. Yi, A. A. Kosterev, W. Chen, L. Dong, L. Wang, T. Tan, W. Zhang, F. K. Tittel, and X. Gao, "Trace gas detection based on off-beam quartz enhanced photoacoustic spectroscopy: Optimization and performance evaluation," *Rev. Sci. Instrum.* 81, 103103 (2010).
19. H. Yi, K. Liu, W. Chen, T. Tan, L. Wang, and X. Gao, "Application of a broadband blue laser diode to trace NO_2 detection using off-beam quartz-enhanced photoacoustic spectroscopy," *Opt. Lett.* 36, 481-483 (2011).
20. A. Kosterev, G. Wysocki, Y. Bakhirkin, S. So, R. Lewicki, M. Fraser, F. Tittel, and R. F. Curl, "Application of quantum cascade lasers to trace gas analysis," *Appl. Phys. B* 90, 165-176 (2008).
21. M. Horstjann, Y. A. Bakhirkin, A. A. Kosterev, R. F. Curl, F. K. Tittel, C. M. Wong, and C. J. Hill, "Formaldehyde sensor using interband cascade laser based quartz-enhanced photoacoustic spectroscopy," *Appl. Phys. B* 79, 799-803 (2004).
22. L. Dong, R. Lewicki, K. Liu, P. R. Buerki, M. J. Weida, and F. K. Tittel, "Ultra-sensitive carbon monoxide detection by using EC-QCL based

quartz-enhanced photoacoustic spectroscopy," *Appl. Phys. B* 107, 275-283 (2012).

23. A. K. Y. Ngai, S. T. Persijn, I. D. Lindsay, A. A. Kosterev, P. Groß, C. J. Lee, S. M. Cristescu, F. K. Tittel, K.-J. Boller, and F. J. M. Harren, "Continuous wave optical parametric oscillator for quartz-enhanced photoacoustic trace gas sensing," *Appl. Phys. B* 89, 123-128 (2007).
24. L. S. Rothman, I. E. Gordon, A. Barbe, D. C. Benner, P. F. Bernath, M. Birk, V. Boudon, L. R. Brown, A. Campargue, J.-P. Champion, K. Chance, L. H. Coudert, V. Dana, V. M. Devi, S. Fally, J.-M. Flaud, R. R. Gamache, A. Goldman, D. Jacquemart, I. Kleiner, N. Lacome, W. Lafferty, J.-Y. Mandin, S. T. Massie, S. N. Mikhailenko, C. E. Miller, N. Moazzen-Ahmadi, O. V. Naumenko, A. V. Nikitin, J. Orphal, V. I. Perevalov, A. Perrin, A. Predoi-Cross, C. P. Rinsland, M. Rotger, M. Simeckova, M. A. H. Smith, K. Sung, S. A. Tashkun, J. Tennyson, R. A. Toth, A. C. Vandaele, J. V. Auwera, "The HITRAN 2008 molecular spectroscopic database," *J. Quant. Spectrosc. Radiat. Transf.* 110, 533-572 (2009).
25. S. Schilt and L. Thévenaz, "Experimental method based on wavelength-modulation spectroscopy for the characterization of semiconductor lasers under direct modulation," *Appl. Opt.* 43, 4446-4453 (2004).
26. P. Lu, L. Men, K. Sooley, and Q. Chen, "Tapered fiber Mach–Zehnder interferometer for simultaneous measurement of refractive index and temperature," *Appl. Phys. Lett.* 94, 131110 (2009).
27. R. D. Grober, J. Acimovic, J. Schuck, D. Hessman, P. J. Kindlemann, J. Hespanha, A. S. Morse, K. Karrai, I. Tiemann, and S. Manus, "Fundamental limits to force detection using quartz tuning forks," *Rev. Sci. Instrum.* 71, 2776-2780 (2000).
28. A. Pohlkötter, U. Willer, C. Bauer, and W. Schade, "Resonant tuning fork detector for electromagnetic radiation," *Appl. Opt.* 48, B119-B125 (2009).

29. L. Dong, A. A. Kosterev, D. Thomazy, and F. K. Tittel, “QEPAS spectrophones: design, optimization, and performance,” *Appl. Phys. B* 100, 627-635 (2010).
30. S. Schilt and L. Thévenaz, “Wavelength modulation photoacoustic spectroscopy: Theoretical description and experimental results,” *Infrared Phys. Technol.* 48, 154-162 (2006).
31. H. Li, G. B. Rieker, X. Liu, J. B. Jeffries, and R. K. Hanson, “Extension of wavelength-modulation spectroscopy to large modulation depth for diode laser absorption measurements in high-pressure gases,” *Appl. Opt.* 45, 1052-1061 (2006).
32. J.-M., Friedt and É. Carry, “Introduction to the quartz tuning fork,” *Am. J. Phys.* 75, 415-422 (2007).
33. P. Werle, “Accuracy and precision of laser spectrometers for trace gas sensing in the presence of optical fringes and atmospheric turbulence,” *Appl. Phys. B* 102, 313-329 (2011).

Chapter 6

Evanescent-wave photoacoustic spectroscopy based on optical micro/nano fibers

6.1 Introduction

PAS, in which an acoustic pressure wave is generated by light absorption of gas molecules and detected by an acoustic transducer, has been demonstrated for various gases detection with high sensitivities [1]. As a competitive representative of PAS, quartz-enhanced PAS (QE-PAS) [2-7], which uses a resonant quartz tuning fork (QTF) as the acoustic transducer, has been widely investigated with outstanding performance. However, in all of the PAS systems reported so far, open path PA cells were used, and complex and precise collimating/focusing optics are needed to minimize the optical insertion loss and improve the efficiency of PA generation. Moreover, the precise alignment for the invisible infrared light beam is also a challenge.

Therefore, we consider proposing an evanescent-wave PAS (EPAS) method based on tapered optical micro/nano fibers (OMNFs) for PA generation. The evanescent field of this kind of OMNFs interacts with sample gas and generates a localized acoustic pressure wave via photoacoustic effect, which can be detected by a high sensitive acoustic transducer to address the gas concentration information. As light propagates along the OMNF freely with a very low loss and small beam size in this method, no extra collimating/focusing devices are needed.

Although optical fiber sensors based on direct absorption spectroscopy have

been studied extensively and deployed for real-world applications [8-12], the sensitivity is limited because of the difficulty associated with fabricating a long-length absorption cell. For instance, evanescent-wave absorption spectroscopy by using a D-shaped optical fiber [9] or a tapered optical fiber [10] suffers from very low sensitivity due to the relatively small evanescent field or difficulty in fabricating a long fiber taper.

The above problems in optical fiber sensors are not believed to exist in our EPAS method. By reducing the fiber diameter down to wavelength or sub-wavelength scale, a considerable portion of light power can be ensured to fall in the evanescent field for gas sensing. Besides, since the acoustic signal in PAS isn't necessarily determined by the absorption length, a small section of tapered OMNFs (with a length of a few mm) would be sufficient for high sensitivity gas detection if a small-size acoustic detector, QTF for an instance, is used. In the following, EPAS associated with QTF-based acoustic detection will be demonstrated for gas detection.

6.2 Optical micro/nano fibers

Optical micro/nano fibers, or OMNFs, are a kind of thin optical fibers with diameter in the scale of micrometer or even nanometer. Generally, OMNFs are usually fabricated from conventional single mode fiber (SMF) by heating and stretching method [13, 14]. OMNFs has drawn much attention in the past decade due to its unique optical and mechanical properties, such as strong confinement, larger evanescent field, great configurability, low loss and easy availability [15]. In this section, the fabrication method and optical properties of OMNFs will be discussed.

6.2.1 Fabrication of OMNFs

OMNFs can be easily fabricated from general SMF by the well-known heating and

stretching method as demonstrated in Figure 6.1 [14-16]. A SMF is placed on a moveable translation stage with two ends fixed and coating removed in the middle section. Then a moveable flame heats along the fiber with controlled flame size and movement speed. Meanwhile, the translation stages are moved to the opposite direction with a desired speed to stretch the fiber. Thus the fiber is elongated with diameter reduced until the desired the fiber length and diameter achieved. During the fabrication process, a pair of light source and powermeter is employed to monitor the transmission loss of the fiber. By carefully controlling the flame size and speed, the fiber stretch rate and the heating time, a tapered optical fiber with diameter down to sub-wavelength scale can be made without much effort.

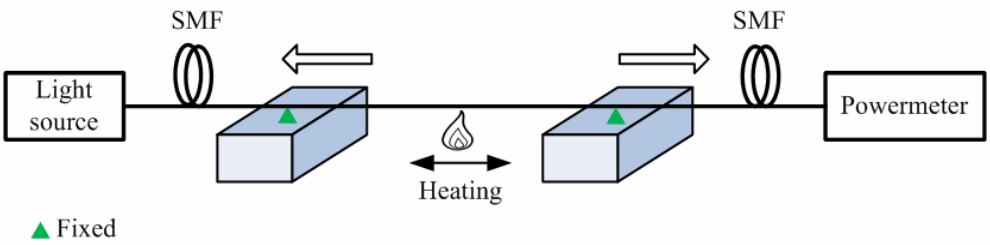

Figure 6.1 Scheme for the fabrication of OMNFs.

Several tapered OMNFs with wavelength from 1.1 to 2.4 μm were fabricated with losses of ~ 0.2 dB by using the above method. An image of one of the OMNFs is displayed in Figure 6.2. The fiber diameter is measured to be 1.4 μm, close to the communication wavelength in optical fiber. These OMNFs are ready for the following gas sensing experiment.

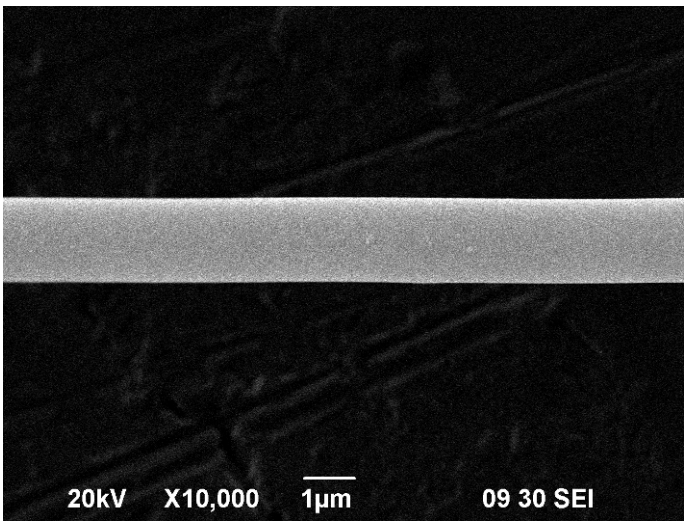

Figure 6.2 SEM image of an OMNF with diameter of 1.4 μm.

6.2.2 Optical properties of OMNFs

One of the most significant properties of OMNFs is the evanescent field located outside the physical boundary of optical fiber. Because part of the optical power propagates outside the fiber as evanescent field, OMNFs are frequently utilized for high-Q knot, loop and coil resonators [17-19], particle manipulation [20, 21] and sensing applications [22-24].

The two most important optical properties of the evanescent field are the power portion in it and the mode field radius of the fiber. We numerically investigated the dependence of these two parameters on the fiber diameter. Figure 6.3 shows the calculated effective refractive index of the tapered OMNFs with different diameters from 0.1-5 μm. In our calculation, the finite air layer with a diameter of 100 μm is included in our model. It is shown that as the diameter reduced, more and more optical power propagates outside of the fiber, so the effective refractive index decreases until approaching the refractive index of air, i.e., n_{eff}=1.

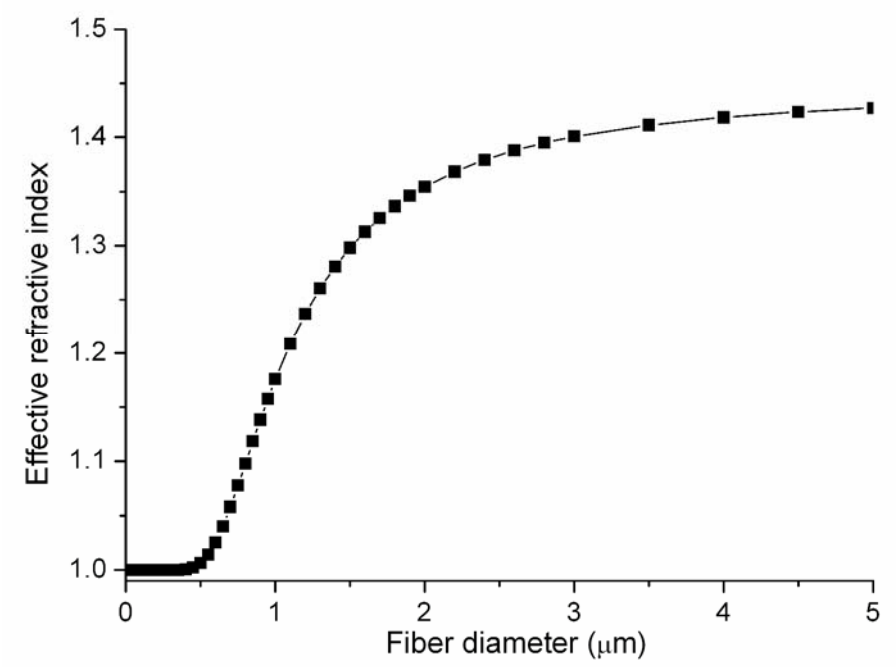

Figure 6.3 Dependence of effective refractive index of tapered OMNFs on fiber diameters.

The mode field of the OMNFs were also studied and plotted in Figure 6.4. It reveals that as the fiber diameter reduced, the mode field diameter (MFD) is reduced at first until the diameter reaches 1 μm and increases as the fiber diameter keeps on reducing. When the fiber diameter is smaller than 0.5 μm, the MFD increases fast. So the optical beam can not be efficiently confined in the fiber as can be seen from the mode field distribution of fiber with diameter of 0.2 μm. The curve of power percentage in air for the evanescent field of OMNFs exhibits a similar tendency with that of the MFD. It is shown in Figure 6.4 that when the diameter of the fiber equals 1.5 μm, the MFD approaches the fiber diameter, which demonstrates about 8% power percentage in the evanescent field. As the fiber diameter keeps on decreases, more and more optical power will distribute in the evanescent field of the optical fiber. For instance, the power percentage in evanescent field is about 26.6% for fiber diameter of 1 μm, 48% for diameter of 0.8 μm and 93.5% for diameter of 0.5 μm.

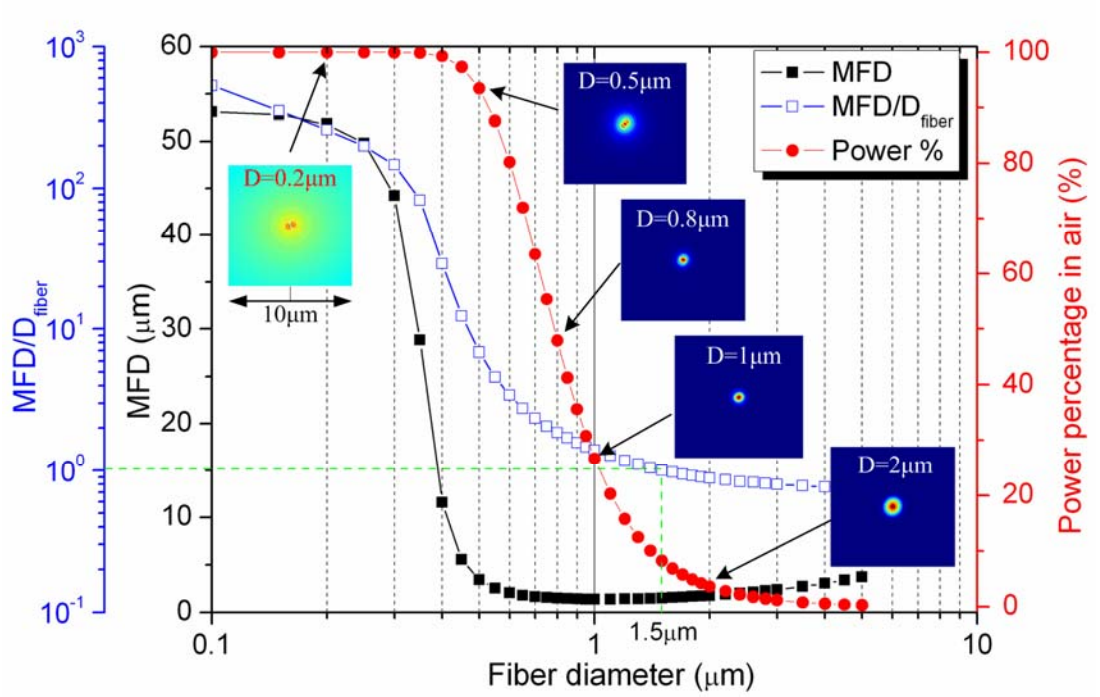

Figure 6.4 Optical mode field diameter (MFD) (black squares), MFD over fiber diameter (blue squares) and power percentage in air (red dots) for different fiber diameters. The mode field distributions for fibers with diameters from 0.2 to 2 μm are selectively shown as the figures inset.

6.3 Gas detection based on EPAS

As a considerable part of the optical power located outside of the fiber as evanescent field, the OMNFs are suitable for photoacoustic gas sensing, which can be referred as evanescent-wave photoacoustic spectroscopy, or EPAS. The generated acoustic wave can be detected by a quartz tuning fork as shown in Figure 6.5. Light is launched into the SMF end of OMNF and propagates with evanescent wave in the waist section of the fiber. Light energy in the evanescent field absorbed by the sensing gas induces a localized heat production, and then diffuses as acoustic wave on condition of light modulation. A QTF is placed with its facet perpendicular to the fiber and the fiber is threaded through the gap between the two prongs of QTF. The acoustic wave by photoacoustic absorption applies on the QTF to make it oscillate and generate a piezoelectric current signal, which is proportional to the light

absorption as in the QEPAS. So QTF based EPAS is also called quartz-enhanced EPAS (QE-EPAS).

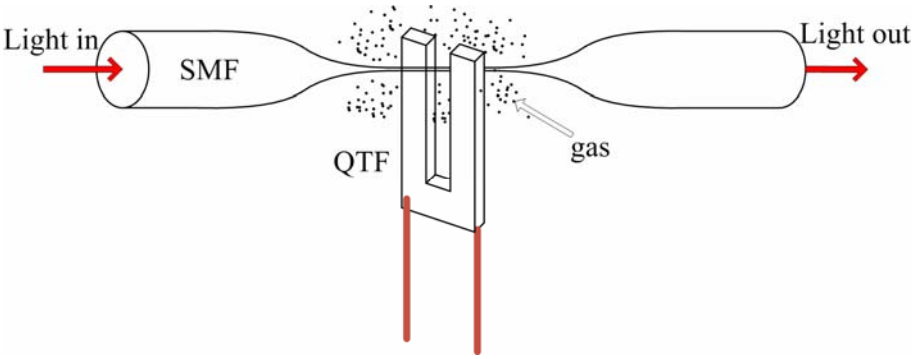

Figure 6.5 Schematic of quartz-enhanced EPAS with an OMNF.

6.3.1 Experimental setup

The experiment setup for our OMNF-based QE-EPAS system is shown in Figure 6.6. A distributed feedback (DFB) laser with a wavelength of ~1532.8 nm was used as the light source, which corresponds to the P(13) absorption line of acetylene in the overtone absorption band. A ramp signal generated from a computer scans the laser wavelength across the absorption line periodically. Simultaneously, a sinusoidal signal modulates the laser wavelength at a frequency $f_m=f_0/2$, where f_0=32.75 kHz is the resonant frequency of the QTF (KDS-DT38) in our experiment. The light signal is amplified by an erbium-doped fiber amplifier (EDFA) and split by a 10/90 fiber coupler. 10% of light is fed to the reference cell for gas concentration calibration by direct absorption, while the remaining 90% to the OMNF for PA-based gas absorption and detection. For optimized PA detection the OMNF was placed approximately in the middle of the gap between two prongs and ~ 0.7 mm below the QTF opening [2]. The dimension of the QTF used in this sensing system is 6mm×1.4mm×0.2mm, with measured quality factor Q=6341 at atmospheric pressure, and equivalent resistance R=220 kΩ. The output from the QTF passes through a

transimpedance amplifier (TA) with a feedback resistor of 10 MΩ and a preamplifier with a gain of 6 before entering into a lock-in amplifier for second harmonic detection. The time constant of the lock-in amplifier was set to 30 ms with an 18 dB/Oct slope filter, corresponding to a detection bandwidth of Δf=3.125 Hz.

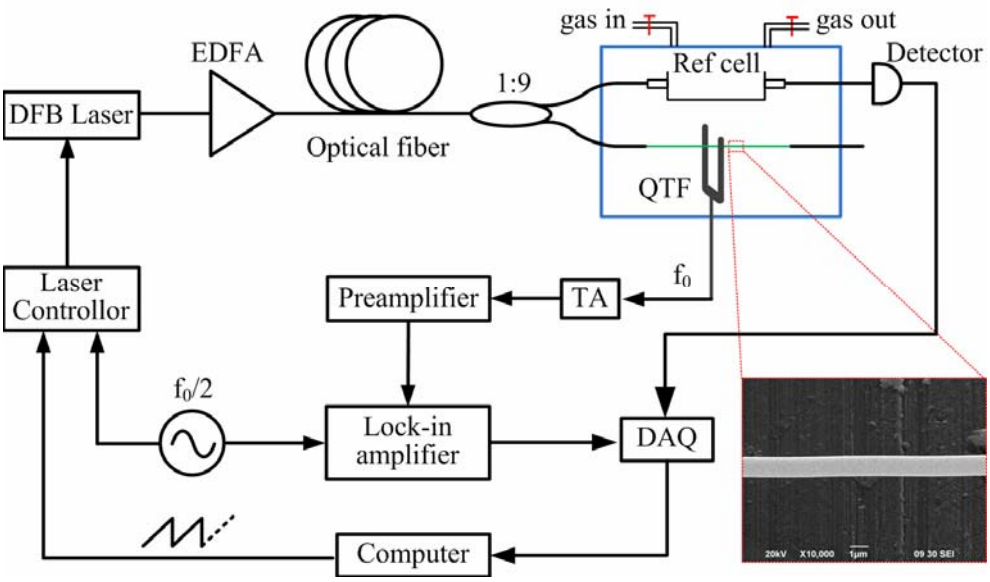

Figure 6.6 Experimental setup for QE-EPAS gas sensing based on an OMNF. EDFA: erbium-doped fiber amplifier; QTF: quartz tuning fork; Ref cell: open-path cell with 2 cm absorption length; TA: transimpedance amplifier with a feedback resistor R_f=10 MΩ; DAQ: data acquisition device; f_0: resonant frequency of QTF. The inset is a SEM image of OMNF, the diameter of which is measured to be 1.1 μm.

6.3.2 Results and discussion

Acetylene gas sensing for the absorption line of P(13) in the overtone absorption band is selected to evaluate the performance of our QE-EPAS configuration. The target absorption line with line strength of 1.035×10^{-20} $cm^{-1}/(mol\ cm^{-2})$ and line center of 6523.88 cm^{-1} is considered. So the laser wavelength is tuned to the center of the absorption line (~ 1532.8 nm). WM with modulation frequency fixed to half of the resonant frequency of QTF (~16.375 kHz) is carried out for acoustic generation, and acoustic signal is detected at the second harmonic.

6.3.2.1 For different fiber diameter

By controlling the flame velocity and the fiber stretching rate, four OMNF samples with different waist diameter were fabricated for the gas sensing experiment. The diameters of them were measured and power percentages in the evanescent field were calculated at 1532.83 nm when placed in atmospheric air as listed in Table 6.1.

Table 6.1 Performance of QE-EPAS gas detection system with tapered OMNFs of different diameters.

Taper	D_{fiber} [μm]	Power portion in air [%] [a]	P_0 [mW]	QTF signal [mV]	C_2H_2 concentration	Peak absorption coefficient α [cm^{-1}]	Normalized QTF signal [mV/(W ppmv)]
1	1.1	20	9.8	4.88	1.58%	0.024	0.032
2	1.4	10	9.8	6.19	4.14%	0.052	0.015
3	1.9	4	12.5	0.7	0.96%	0.0076	0.0058
4	2.4	2	8.4	1.08	4%	0.046	0.0032
Open path QEPAS with a bare QTF [b]			8	2.87	1.08% [c]	0.01	0.033

[a] calculated results at λ=1532.83nm;

[b] Result from Ref [10] for water vapor sensing at 7161.41 cm^{-1} without the use of an acoustic resonator;

[c] Sensing gas is water vapor.

The acoustic signals for the gas sensing system based on tapered OMNFs are plotted in Figure 6.7 for different laser power and gas concentration. For better comparison, the signals are normalized to laser power and absorption coefficient. The results are also listed in Table 6.1. The signal profiles are similar to each other in general and the peak acoustic signal happens for the laser operated at ~ 19 °C. For the fiber taper with a diameter of 1.1 μm (Taper 1), the measured (normalized) maximum second harmonic output signal is 0.0317 mV/(W ppmv). Considering the similar absorption line intensity of H_2O at 7176.41 cm^{-1} and the gain factor of the preamplifier used in [7], this value may be regarded as comparable to the value of QEPAS with a QTF alone without the use of an acoustic resonator. This suggests that the QE-EPAS would achieve a similar performance as an open-path PAS system.

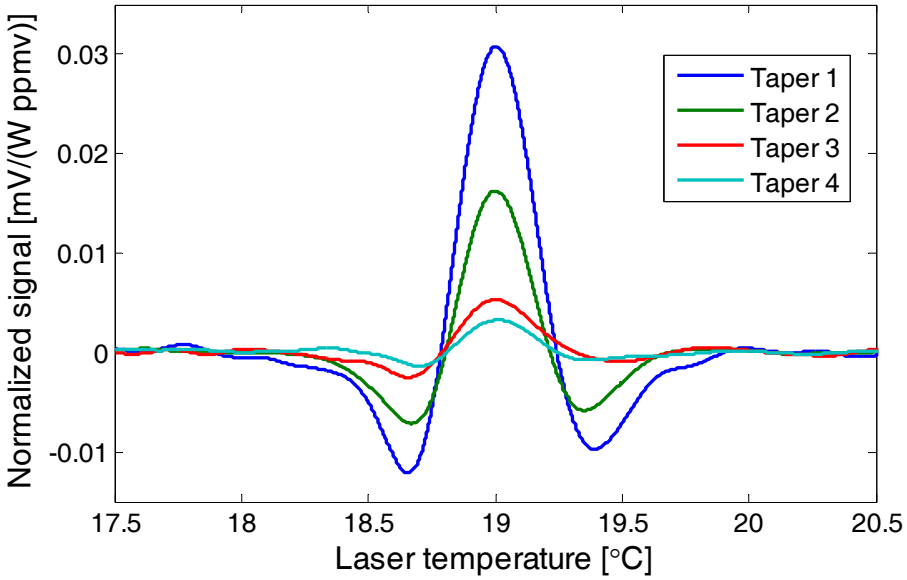

Figure 6.7 Normalized second harmonic acoustic signals for fiber tapers with different diameters.

It also can be shown that the normalized acoustic signal is larger for the thinner optical fiber. This can be explained by the evanescent field power portion of the fiber. By comparing the calculated fiber diameter dependent curve of power portion in air (as black line) and the measured normalized acoustic signals (as blue square) shown in Figure 6.8, we can find that the tendency of the acoustic signal agrees well with the power portion curve and the acoustic signal shows a linear relationship with the power portion in air as depicted in the inset of Figure 6.8. We are inspired from Figure 6.8 that the sensitivity may be further improved by reducing the diameter of the fiber taper. However, for fiber diameter smaller than 0.5 μm, the light confinement of the fiber is poor, so the acoustic excitation and detection might not be efficient.

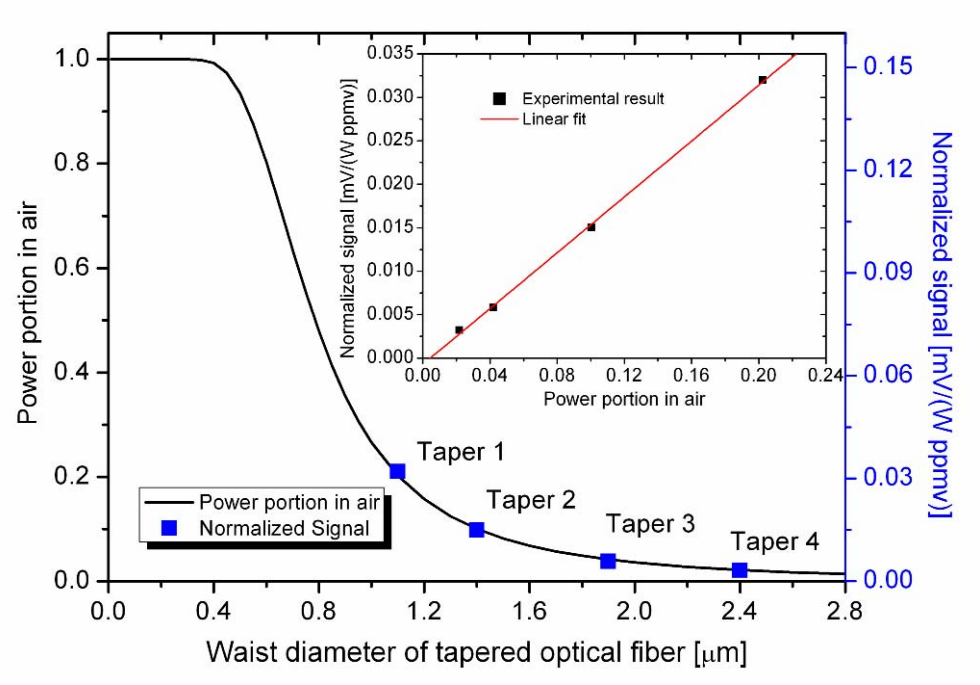

Figure 6.8 Calculated power portion in evanescent field for tapered OMNFs with diameter from 0~2.8 μm at λ=1532.83 nm (solid line) and measured normalized second harmonic signals for four different fiber tapers (solid blue squares). The inset shows the dependence of normalized signal on percentage of light power in air.

6.3.2.2 For different laser power

The dependence of acoustic signal on the laser power was tested for taper 2 as an example. The laser power is changed from 1.45 mW to 9.75 mW and the maximum acoustic signal was recorded point by point as shown in Figure 6.9. The average acoustic signal for each individual laser power was calculated and displayed in the inset of Figure 6.9. The linear fit indicates that the acoustic signal is proportional to the laser power as expected. Therefore, a smaller minimum detectable concentration limit could be achieved with a larger laser power.

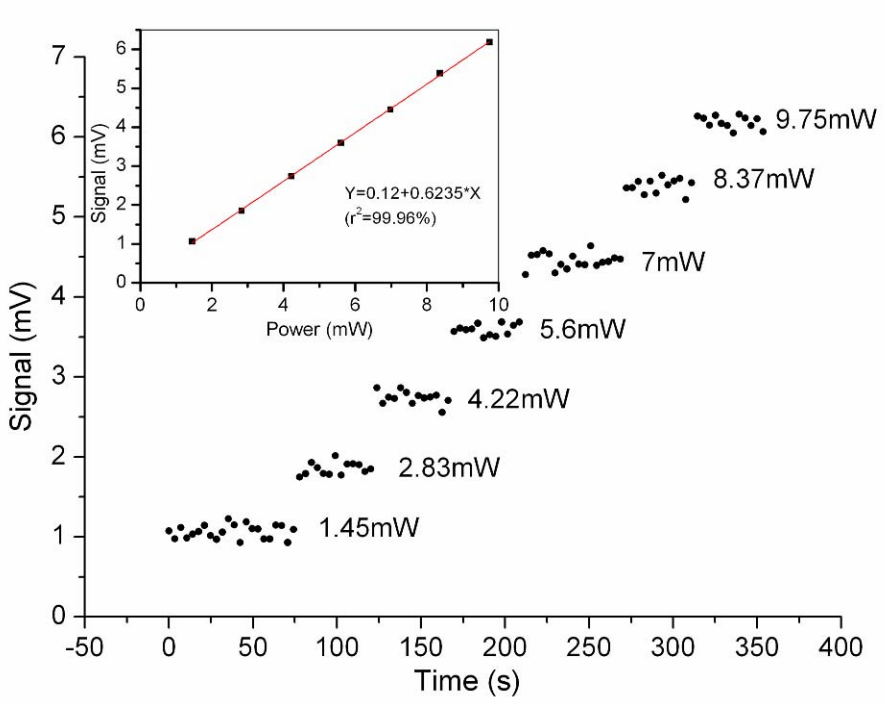

Figure 6.9 Acoustic signals for different laser power. The inset figure shows the average signal for each individual laser power and its linear fit.

6.3.2.3 For different modulation current

In WM, the harmonics signal is significantly depended on the wavelength modulation depth, or the modulation current of the light source. As the modulation current varied, the acoustic signal was recorded and depicted in Figure 6.10. The acoustic increases fast with modulation depth before the modulation current reaching 150 mA. After that the acoustic signal stays with small variation from 150 to 250 mA modulation current. The signal achieves a maximum value at a modulation current of 200 mA. The profile tendency of the curve matches well with the theoretical result as investigated in section 3.4.

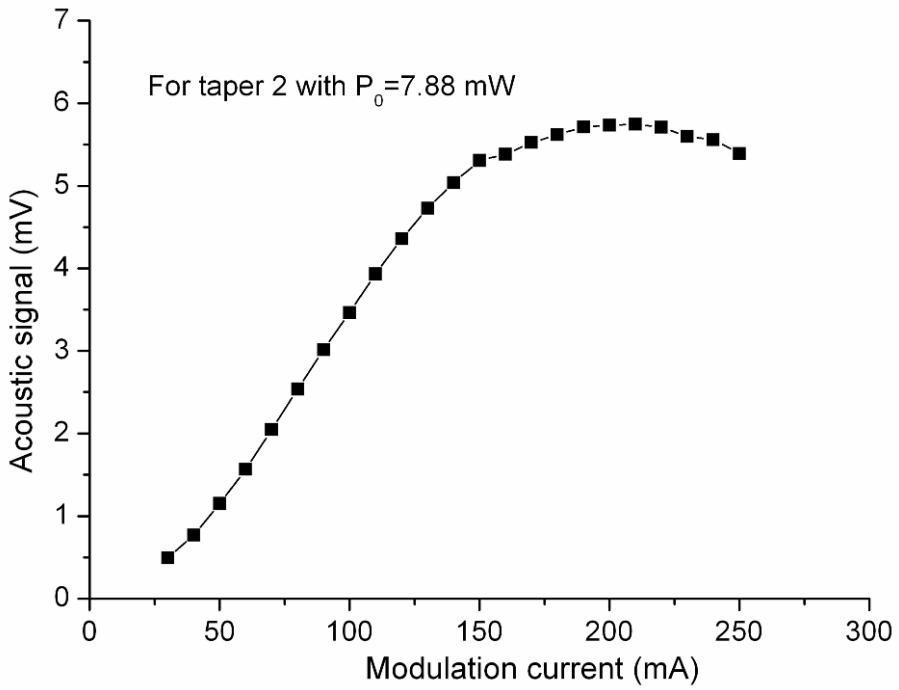

Figure 6.10 Dependence of acoustic signal on modulation current for taper 2 based gas sensing system. The operation laser power is 7.88 mW.

6.3.2.4 For different gas concentration

The gas concentration response of our system was carried out by using taper 4 with a diameter of 2.4 μm. The laser power used in this experiment is 8.37 mW. The gas concentration is calibrated by the reference cell with direct absorption as shown in Figure 6.6. Acoustic signal for different gas concentration was recorded as in Figure 6.11. It is shown that the acoustic signal decreases with reduced gas concentration. And the fitting curve indicates a linear relationship between the signal and the gas concentration.

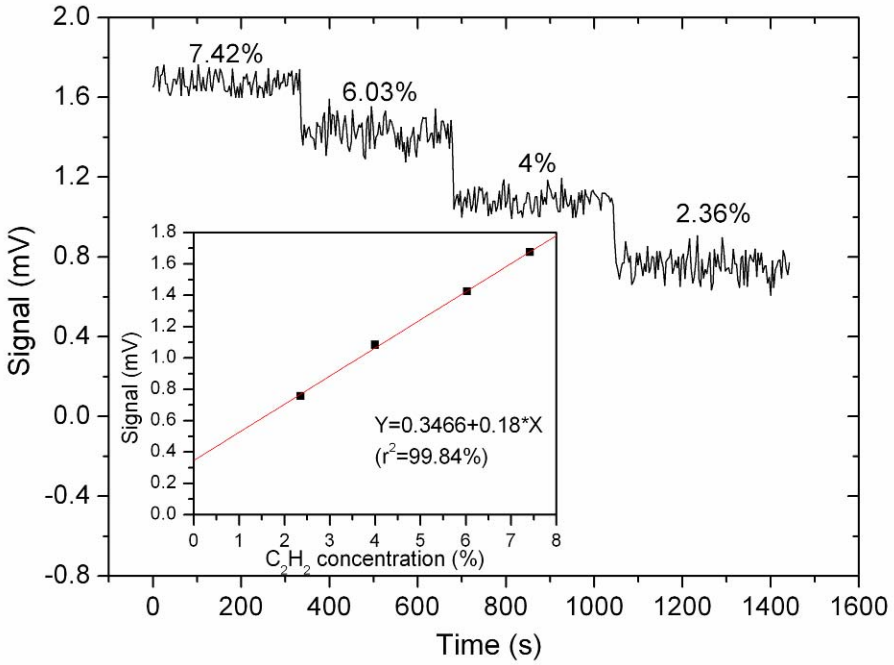

Figure 6.11 Acoustic signals for different C_2H_2 concentrations. Inset figure shows the average signal depended on the gas concentration and its linear fit.

6.3.2.5 Noise determination

In order to obtain the minimum detectable gas concentration limit of our system, the noise of the setup must be quantified first. From Figure 6.11 we can find that the intercept value between the linear fit and the vertical axis is ~ 0.347 mV, indicating the output would not be zero even when no acetylene is present. This might be resulted from the swinging of the tapered fiber which would affect the resonance property of the QTF. Moreover, the evanescent field would also beat on the prong of the QTF and induce a background signal if the fiber is placed too close to the tuning fork. This could be improved by properly fixing the fiber taper and placing it in the middle of the gap between prongs of QTF. The standard derivation of the noise was estimated to be 55 μV from the gas concentration response of taper 4 in Figure 6.11. This noise level is independent of fiber diameter, the laser power and gas concentration, and it is believed to be mainly due to the thermal noise of QTF and amplified by the preamplifier. The noise level seems a little bit higher than the

reported results by other researchers [3] because of the relative small time constant of 30 ms we used for signal demodulation, which will increase the thermal noise of QTF directly as determined by [25]

$$\sqrt{\left\langle V_N^2 \right\rangle} = R_f \sqrt{4k_B T \Delta f / R_1} \ , \tag{6.1}$$

where R_f is the feedback resistance in the transimpedance amplifier, R_1 is the equivalent resistance of QTF (220 kΩ), k_B is Boltzmann constant, T is temperature and Δf is the detection bandwidth of the system. Therefore the noise level would be reduced considerably if a longer integration time is used.

By using the current noise level, a minimum detectable concentration limit of 178 ppmv (corresponding to a signal to noise ratio (SNR) of 1) was deduced for taper 1 with 9.8 mW optical power and 30 ms integration time. The corresponding normalized noise equivalent absorption (NNEA) coefficient (1σ) can then be obtained from [26]

$$NNEA = \frac{\alpha_{\min} P_0}{\sqrt{\Delta f}} = \frac{\alpha P_0}{SNR\sqrt{\Delta f}} , \tag{6.2}$$

where $\alpha_{\min}$ is minimum detectable absorption coefficient, P_0=9.8 mW is laser power, Δf=3.125 Hz is detection bandwidth determined by lock-in amplifier. For taper 1, α=0.024 cm^{-1} and SNR can be estimated (by using the results in Table 1) to be 88.7. Therefore, the NNEA for taper 1 is calculated to be 1.5×10^{-6} cm^{-1} W/√Hz.

6.3.3 Conclusion

It is verified by experiment that the evanescent wave of an OMNF can be employed for photoacoustic signal generation and efficiently detected by a QTF. The acoustic signal is proportional to the power of the laser source and the gas concentration. By using an optical fiber with smaller diameter, the acoustic signal can be greatly

enhanced due to a larger evanescent field. Compared with the conventional open-path QEPAS, QE-EPAS can achieve a similar order acoustic signal while simplify the system by omitting the use of complicated optical collimating and focusing devices. By adding a proper acoustic resonant tube or using other sensitive acoustic detection techniques, such as a micro-cantilever-based interferometric detection method [27], the sensitivity would be further improved by 2-3 orders of magnitude. The fiber-optic devices of it also promise a bright potential application in all-optical multiplexing gas sensing area, etc.

6.4 Summary

EPAS with tapered OMNFs was demonstrated for the first time, to the best of our knowledge, for gas sensing in this chapter. The fabrication method and optical properties of OMNFs were introduced. With a fiber taper of 1.1 μm waist diameter and a QTF as the acoustic detector, we obtained a normalized output signal of 0.0317 mV/(W ppmv) and a NNEA coefficient (1σ) of 1.5×10^{-6} cm^{-1} $W/Hz^{1/2}$ for C_2H_2 detection at atmospheric pressure.

References of Chapter 6

1. A. Elia, P. M. Lugarà, C. D. Franco, and V. Spagnolo, “Photoacoustic techniques for trace gas sensing based on semiconductor laser sources,” *Sensors* 9, 9616-9628 (2009).
2. A. A. Kosterev, Y. A. Bakhirkin, R. F. Curl, and F. K. Tittel, “Quartz-enhanced photoacoustic spectroscopy,” *Opt. Lett.* 27, 1902-1904 (2002).
3. A. A. Kosterev, F. K. Tittel, D. V. Serebryakov, A. L. Malinovsky, and I. V. Morozov, “Applications of quartz tuning forks in spectroscopic gas sensing,” *Rev. Sci. Instrum.* 76, 043105 (2005).

4. S. Schilt, A. A. Kosterev, and F. K. Tittel, "Performance evaluation of a near infrared QEPAS based ethylene sensor," *Appl. Phys. B* 95, 813-824 (2009).
5. A. Kosterev and F. K. Tittel, "Ammonia detection by use of quartz-enhanced photoacoustic spectroscopy with a near-IR telecommunication diode laser," *Appl. Opt.* 43, 6213-6217 (2004).
6. L. Dong, A. A. Kosterev, D. Thomazy, F. K. Tittel, "QEPAS spectrophones: design, optimization, and performance," *Appl. Phys. B* 100, 627-635 (2010).
7. K. Liu, X. Guo, H. Yi, W. Chen, W. Zhang, and X. Gao, "Off-beam quartz-enhanced photoacoustic spectroscopy," *Opt. Lett.* 34, 1594-1596 (2009).
8. G. Whitenett, G. Stewart, K. Atherton, B. Culshaw, and W. Johnstone, "Optical fibre instrumentation for environmental monitoring applications," *J. Opt. A: Pure Appl. Opt.* 5, S140-S145 (2003).
9. G. Stewart, W. Jin, and B. Culshaw, "Prospects for fibre-optic evanescent-field gas sensors using absorption in the near-infrared," *Sens. Actuators B* 38, 42-47 (1997).
10. H. Tai, H. Tanaka, and T. Yoshino, "Fiber-optic evanescent-wave methane-gas sensor using optical absorption for the 3.392-μm line of a He-Ne laser," *Opt. Lett.* 12, 437-439 (1987).
11. Y. L. Hoo, W. Jin, C. Shi, H. L. Ho, D. N. Wang, and S. C. Ruan, "Design and modeling of a photonic crystal fiber gas sensor," *Appl. Opt.* 42, 3509-3515 (2003).
12. Y. L. Hoo, W. Jin, H. L. Ho, J. Ju, and D. N. Wang, "Gas diffusion measurement using hollow-core photonic bandgap fiber," *Sens. Actuators B* 105, 183-186 (2005).
13. L. M. Tong, R. R. Gattass, J. B. Ashcom, S. L. He, J. Y. Lou, M. Y. Shen, I. Maxwell, and E. Mazur, "Subwavelength-diameter silica wires for low-loss optical wave guiding," *Nature* 426, 816-819 (2003).

14. L. Tong, J. Lou, Z. Ye, G. T. Svacha, and E. Mazur, "Self-modulated taper drawing of silica nanowires," *Nanotechnology* 16, 1445-1448 (2005).
15. G. Brambilla, F. Xu, P. Horak, Y. Jung, F. Koizumi, N. P. Sessions, E. Koukharenko, X. Feng, G. S. Murugan, J. S. Wilkinson, and D. J. Richardson, "Optical fiber nanowires and microwires: fabrication and applications," *Adv. Opt. Photon.* 1, 107-161 (2009).
16. H. Xuan, W. Jin, and S. Liu, "Long-period gratings in wavelength-scale microfibers," *Opt. Lett.* 35, 85-87 (2010).
17. M. Sumetsky, Y. Dulashko, J. M. Fini, and A. Hale, "Optical microfiber loop resonator," *Appl. Phys. Lett.* 86, 161108 (2005).
18. X. Jiang, L. Tong, G. Vienne, X. Guo, A. Tsao, Q. Yang, and D. Yang, "Demonstration of optical microfiber knot resonators," *Appl. Phys. Lett.* 88, 223501 (2006).
19. F. Xu and G. Brambilla, "Embedding optical microfiber coil resonators in Teflon," *Opt. Lett.* 32, 2164-2166 (2007).
20. K. Grujic, O. G. Hellesø, J. S. Wilkinson, and J. P. Hole, "Optical propulsion of microspheres along a channel waveguide produced by Cs^+ ion-exchange in glass," *Opt. Commun.* 239, 227-235 (2004).
21. S. Gaugiran, S. Gétin, J. M. Fedeli, G. Colas, A. Fuchs, F. Chatelain, and J. Derouard, "Optical manipulation of microparticles and cells on silicon nitride waveguides," *Opt. Express* 13, 6956-6963 (2005).
22. J. Villatoro and D. Monzón-Hernández, "Fast detection of hydrogen with nano fiber tapers coated with ultra thin palladium layers," *Opt. Express* 13, 5087-5092 (2005).
23. L. Tong, J. Lou, R. Gattass, S. He, X. Chen, L. Liu, and E. Mazur, "Assembly of silica nanowires on silica aerogels for microphotonic devices," *Nano Lett.* 5, 259-262 (2005).

24. C. Y. Chao and L. J. Guo, "Design and optimization of microring resonators in biochemical sensing applications," *J. Lightwave Technol.* 24, 1395-1402 (2006).
25. R. D. Grober, J. Acimovic, J. Schuck, D. Hessman, P. J. Kindlemann, J. Hespanha, A. S. Morse, K. Karrai, I. Tiemann, and S. Manus, "Fundamental limits to force detection using quartz tuning forks," *Rev. Sci. Instrum.* 71, 2776-2780 (2000).
26. A. Elia, C. D. Franco, V. Spagnolo, P. M. Lugarà, and G. Scamarcio, "Quantum cascade laser-based photoacoustic sensor for trace detection of formaldehyde gas," *Sensors* 9, 2697-2705 (2009).
27. T. Laurila, H. Cattaneo, V. Koskinen, J. Kauppinen, and R. Hernberg, "Diode laser-based photoacoustic spectroscopy with interferometrically-enhanced cantilever detection," *Opt. Express* 13, 2453-2458 (2005).

Chapter 7

All-optical PAS gas detection with miniature extrinsic Fabry-Perot interferometer

7.1 Introduction

Trace gas detection based on PAS has achieved great development in the past decade. Different acoustic detection techniques, including the most widely used capacitive microphone [1-3], resonant quartz tuning fork [4, 5] and micro-cantilever associated with Michelson interferometric detection [6, 7], have been proposed with high gas detection sensitivity. All these methods are based on open-path light absorption and separated acoustic detection, the electrical detection approaches of which limits the application on remote gas detection and the multiplex sensing is difficult. Recently, researchers from Prof. Yu's group proposed an all-optical acoustic detection method by using an extrinsic Fabry-Perot interferometer (EFPI) with a polymer diaphragm and successfully used it for PAS gas detection [8]. However, they also used the conventional PA cell for acoustic generation in their system, which makes the system kind of complicated.

In this chapter, we propose a novel all-optical gas detection method by integrating the acoustic generation and detection of PAS in a same optical device, i.e., diaphragm-based EFPI. The sensor size is only in ~mm scale. The source light and detection light share a single optical fiber. This kind of novel gas sensor might possess advantages in the application of small space gas detection and multiplex gas

sensing with compact size, high sensitivity, immune to electromagnetic interference, and remote and distributed sensing ability, etc. In the subsequent sections, we will investigate the properties and fabrication of this kind of acoustic sensor, and evaluate its performance in PAS gas detection.

7.2 Acoustic detection based on EFPI

7.2.1 Basic principle of pressure sensor based on EFPI

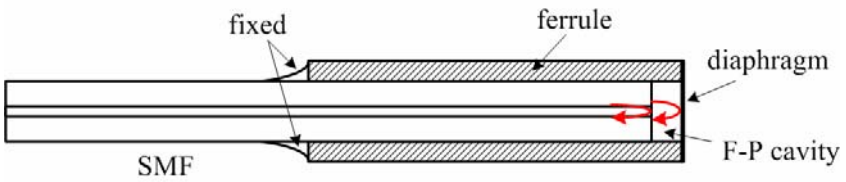

Figure 7.1 Schematic structure of EFPI. SMF: single mode fiber.

The basic principle guiding the diaphragm-type pressure sensor is F-P interference. As shown in Figure 7.1, the space between the fiber end and the diaphragm forms a F-P cavity. The reflected light from the two parallel planes of the F-P cavity interferes with each other. It is well known that the reflection spectrum of FPI can be expressed by [9]

$$R_e = \frac{I_r}{I_i} = \frac{F\sin^2(\delta/2)}{1+F\sin^2(\delta/2)}, \tag{7.1}$$

where I_i and I_r are the incident and reflected light intensity,

$$\delta = \frac{2\pi}{\lambda}2nL \tag{7.2}$$

is the phase difference between each succeeding reflection, and

$$F = \frac{4R}{(1-R)^2} \tag{7.3}$$

is the coefficient of finesse, R is the reflectance on both surfaces, n and L are

the refractive index and length of the F-P cavity. For different reflectance, the reflection spectra for FPI are plotted in Figure 7.2 with phase difference. It is shown that for a larger reflectance, the finesse is large and the spectrum becomes very sharp. For a small reflectance, the reflection spectrum approaches a sinusoidal distribution.

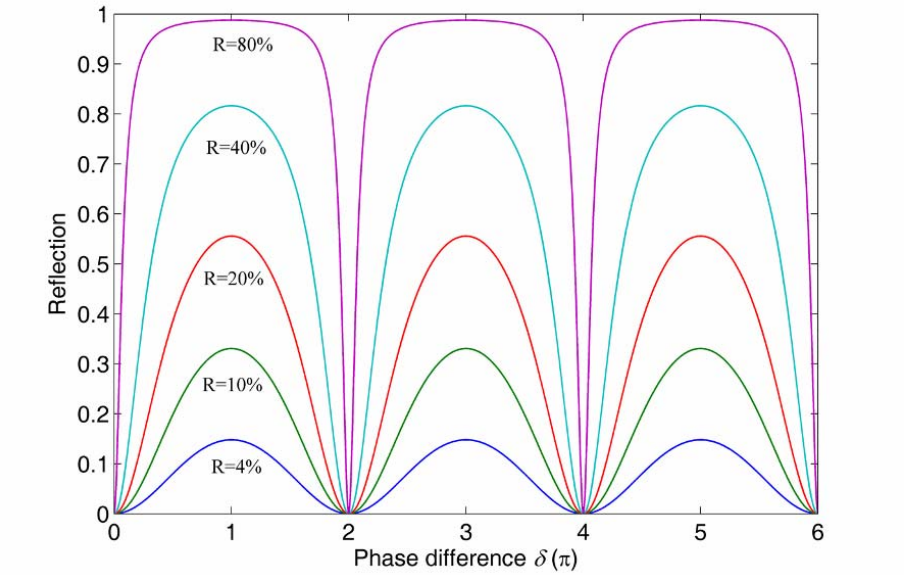

Figure 7.2 Reflection spectra for Fabry-Perot interferometer with different reflectance.

For fiber-optic FPI, the reflectance on the interface between silica and air is about 4%. Therefore the higher order reflection from the second interface can be neglected. The situation is simplified as two-beam interference. The reflected electric field is composed by the two components from the inner and outer interfaces as

$$\begin{aligned} E_r &= E_1 + E_2 \\ &= E_0\sqrt{r_1}\exp(i\varphi_0) + E_0(1-r_1)\sqrt{r_2}\exp\left(i(\delta+\pi+\varphi_0)\right) \end{aligned}, \tag{7.4}$$

where E_0 and φ_0 are the amplitude and initial phase of electric field of incident light, r_1 and r_2 are the reflectance at the inner and outer surfaces, δ is the phase delay in the F-P cavity, half-wave loss in the outer surface reflection is considered. The reflection intensity can be derived from Eq. (7.4) as

$$\begin{aligned} I_r &= \left|E_r\right|^2 = E_0^2 r_1 + E_0^2 (1-r_1)^2 r_2 - 2E_0^2 (1-r_1)\sqrt{r_1 r_2}\cos(\delta) \\ &= I_1 + I_2 - 2\sqrt{I_1 I_2}\cos(\delta) \end{aligned}, \tag{7.5}$$

where

$$I_1 = E_0^2 r_1 = I_0 r_1, \tag{7.6a}$$

$$I_2 = E_0^2 (1-r_1)^2 r_2 = I_0 (1-r_1)^2 r_2, \tag{7.6b}$$

are the reflected intensities from the inner and outer surfaces, respectively, I_0 is the incident light intensity. Eq. (7.5) can be rewritten as

$$R_e = I_r / I_0 = a\left[1 - b\cos(\delta)\right], \tag{7.7}$$

where

$$a = r_1 + (1-r_1)^2 r_2, \tag{7.8a}$$

$$b = \frac{2(1-r_1)\sqrt{r_1 r_2}}{r_1 + (1-r_1)^2 r_2}, \tag{7.8b}$$

are the reflection without interference and visibility of the F-P interferometer, respectively. For the silica fiber-optic FPI, $r_1 = r_2 = 0.033$, $a = 0.0639$, $b = 0.9994$. Therefore, only ~ 12.8% of the light intensity can be reflected at most. However, the visibility is close to 1, which provides a perfect interferometric spectrum with large contrast.

The dependence of reflection of FPI on the wavelength and length of F-P cavity is shown in Figure 7.3.

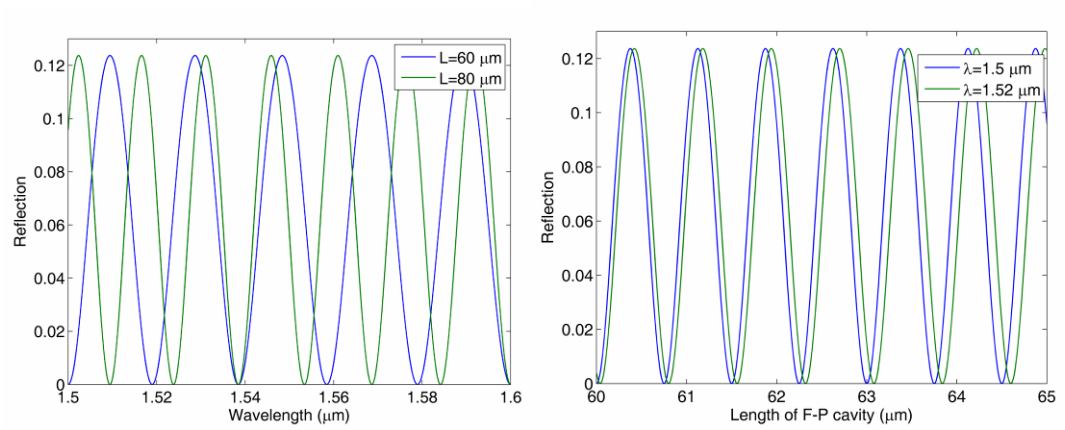

(a) (b)

Figure 7.3 Dependence of FPI reflections on (a) wavelength and (b) cavity length.

It is shown that a small variation of light wavelength or cavity length can result in a large change on the reflection. For a fixed cavity length, the wavelength of the adjacent reflection peaks or dips is related to the cavity length as

$$\frac{1}{\lambda_1}-\frac{1}{\lambda_2}=\frac{1}{2L}. \tag{7.9}$$

From the above equation, we can also derive the cavity length from the reflection spectrum as

$$L=\frac{\lambda_1\lambda_2}{2FSR}, \tag{7.10}$$

where $FSR=\left|\lambda_2-\lambda_1\right|$ is the free spectral range (FSR).

As an external pressure applied to the diaphragm of a pressure sensor, the diaphragm will be deformed due to its mechanical properties, which changes the cavity length of the EFPI and results in the reflected light intensity variation. This is the basic principle of diaphragm-based EFPI for pressure detection.

7.2.2 Pressure response of diaphragm

As stated in the previous section, a pressure applied to the diaphragm can make it

deformed and result in a variation for the reflected light intensity of an EFPI. Thus, the pressure response of the diaphragm plays a crucial role in the EFPI based pressure sensor. In this section, both of the static pressure and dynamic pressure response of the diaphragm will be investigated.

7.2.2.1 Under static uniform pressure

When the deformation of the diaphragm is less than 30% of its thickness, it can be considered as perturbation case that the magnitude of the diaphragm deformation is proportional to the external pressure. For a diaphragm with uniform thickness of *h*, radius of *a*, the deformation of it under external uniform pressure is expressed as [10]

$$Y(r) = \frac{3(1-\mu^2)P}{16Eh^3}\left(a^2 - r^2\right)^2, \tag{7.11}$$

where r is the distance from the center of the diaphragm, μ and E are the Poisson's ratio and Young's modulus of the diaphragm material, and P is pressure. It is shown that the deformation of the diaphragm achieves a maximum value in its center (r=0) while equals zeros at the outer boundary (r=a). For a silica diaphragm (E=73 GPa and μ=0.17) with thickness of 10 μm and radius of 100 μm and clamped at the edges, the distribution of its deformation under a uniform pressure of 1 kPa is calculated and shown in Figure 7.4. The maximum deformation is about 0.25 nm.

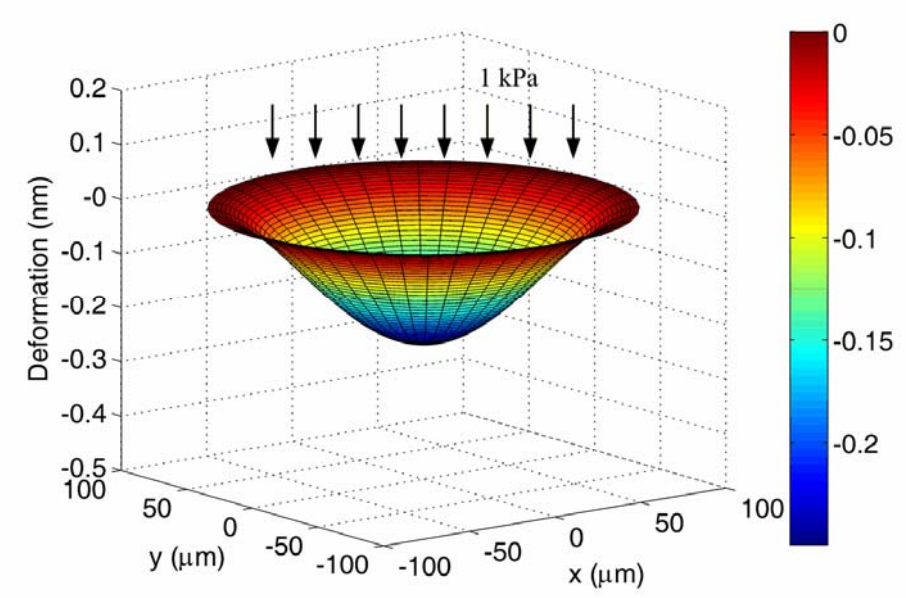

Figure 7.4 Deformation of a diaphragm with diameter of 200 μm and thickness of 10 μm at a 1 kPa uniform pressure.

The maximum deformation in the center of a diaphragm is

$$Y_{\max} = \frac{3(1-\mu^2)P}{16Eh^3}a^4, \tag{7.12}$$

which is proportional to pressure and the fourth order of diaphragm diameter, but reversely proportional to the Young's modulus and the third order of diaphragm thickness. When the diaphragm is selected, the maximum deformation is only proportional to the pressure, giving the pressure sensitivity of the diaphragm as

$$y_{sens} = Y_{\max}/P = \frac{3(1-\mu^2)}{16E}\frac{a^4}{h^3}. \tag{7.13}$$

In pressure detection experiment, the light beam is usually aligned to the center of the diaphragm to ensure a maximum sensitivity given by Eq. (7.13). The sensitivity is determined by both the diaphragm material and its dimension. Therefore, we can enhance the pressure detection sensitivity by selecting material with small Young's modulus and Poisson's ratio, reducing the diaphragm thickness or increasing the diameter of diaphragm. For instance, the pressure sensitivity of a

silica diaphragm at room temperature (25 °C) (E=73 GPa and μ=0.17) is expressed as

$$y_{sens} = 2.4943\times10^{-6}\frac{a^4}{h^3}\ \text{(nm/kPa)}, \tag{7.14}$$

where a and h in the unit of μm. While for a polymer material, taking mylar (E=5 GPa and μ=0.3) [11] as an example, the relatively small Young's modulus gives a pressure sensitivity as

$$y_{sens} = 3.4125\times10^{-5}\frac{a^4}{h^3}\ \text{(nm/kPa)}, \tag{7.15}$$

one order higher than the silica diaphragm with the same thickness and diameter. The pressure sensitivity of silica diaphragm with different diameter and thickness is plotted in Figure 7.5.

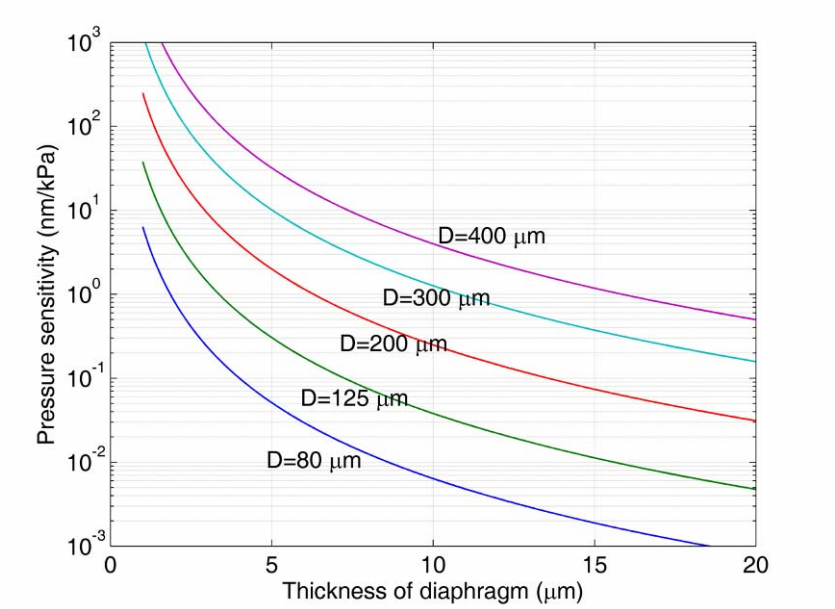

Figure 7.5 Pressure sensitivity of silica diaphragm with different diameter and thickness.

Since the linear relationship between the diaphragm deformation and pressure is only valid when the deformation is less than 30% of the diaphragm thickness, the thickness of the diaphragm should not be less than its minimum value to ensure a

linear pressure response. When the range of the pressure to be measured is known, the minimum diaphragm thickness can be estimated as

$$h_{\min} = \left(\frac{(1-\mu^2)P_{\max}}{1.6E} \right)^{1/4} a, \tag{7.16}$$

It is shown that the minimum diaphragm thickness is proportional to the quarter order of applied pressure and proportional to the diaphragm diameter. The dependence of minimum thickness for a silica diaphragm on the detected pressure and diaphragm diameter is plotted in Figure 7.6.

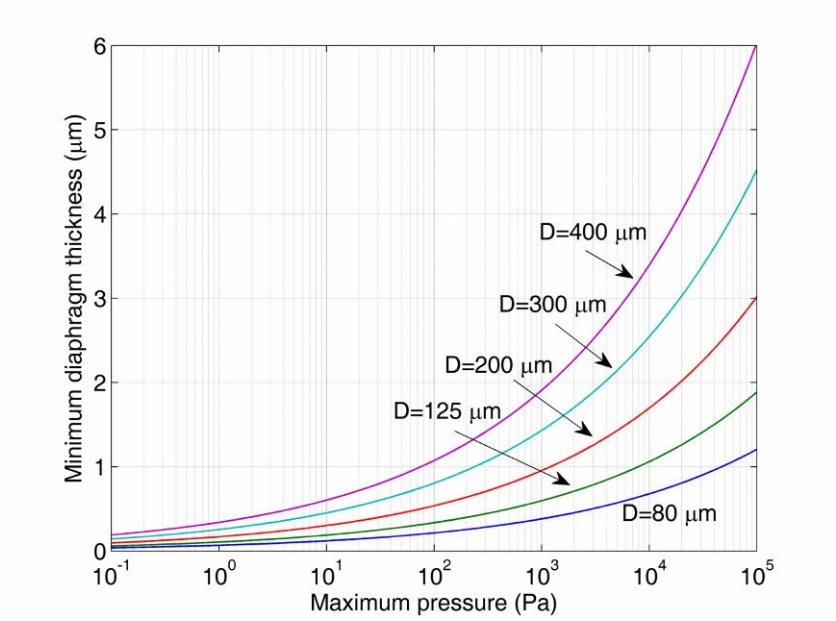

Figure 7.6 Dependence of minimum thickness on the maximum detected pressure and diaphragm diameter for a silica diaphragm.

7.2.2.2 Under dynamic acoustic field

The frequency response of a diaphragm is also a very important factor that determines the acoustic detector properties. The diaphragm can be regarded as a free vibration circular plate with its edges clamped. So the natural resonant frequency of it is expressed as [10, 12]

$$f_{mn} = \frac{\varphi_{mn}^2}{4\pi}\sqrt{\frac{E}{3\rho(1-\mu^2)}}\frac{h}{r^2}, \tag{7.17}$$

where φ_{mn} is a constant related to the vibration mode of the diaphragm, E, μ, and ρ are the Young's modulus, Poisson's ratio and mass density of diaphragm material, h and r are the thickness and effective radius of diaphragm. The nature resonant frequency of a diaphragm is proportional to its thickness while inversely proportional to the square of the effective radius. For the lowest vibration mode, φ_{00}=3.196. So the natural resonant frequency of the first vibration mode of a silica diaphragm can be calculated as

$$f_{00} = 2.742\times10^9\frac{h}{r^2}\ (\text{Hz}), \tag{7.18}$$

where *h* and *r* are in micrometer.

When the diaphragm is operated at forced vibration mode, the dynamic deformation $Y(r,\theta,t)$ of it can be described by the following damping equation as [12]

$$D\nabla^2 Y + \rho h\frac{\partial^2 Y}{\partial t^2} + \nu\frac{\partial Y}{\partial t} = pe^{i\omega_F t}, \tag{7.19}$$

where p and ω_F are the amplitude and angular frequency of the applied acoustic pressure, ν is the damping coefficient of the diaphragm, D is the flexural rigidity of the diaphragm defined by

$$D = \frac{Eh^3}{12(1-\mu^2)}\ (\text{N/m}^2). \tag{7.20}$$

By solving Eq. (7.19), we can obtain the diaphragm deformation as

$$Y_{mn}(\omega_F) = \frac{3(1-\mu^2)p}{16E}\frac{a^4}{h^3}\frac{\omega_{mn}^2}{\sqrt{(\omega_{mn}^2-\omega_F^2)^2+4\omega_F^2\xi^2}}, \tag{7.21}$$

where

$$\xi = \frac{\nu}{2\rho h} \tag{7.22}$$

is the damping term and

$$\omega_{mn} = \frac{\varphi_{mn}^2}{r^2}\sqrt{\frac{D}{\rho h}} = 2\pi f_{mn} \tag{7.23}$$

describes the natural angular frequency of diaphragm in air, f_{mn} and φ_{mn} are given by Eq. (7.17).

The enhancement coefficient between the dynamically forced diaphragm and static pressure with the same amplitude at each vibration mode is defined as

$$Q_{mn} = \frac{\omega_{mn}^2}{\sqrt{(\omega_{mn}^2 - \omega_F^2)^2 + 4\omega_F^2\xi^2}}. \tag{7.24}$$

The frequency response of the enhancement Q-factor at the fundamental vibration mode for a silica diaphragm with diameter of 1000 μm and thickness of 10 μm is calculated and shown in Figure 7.7 by neglecting the damping term (ξ=0).

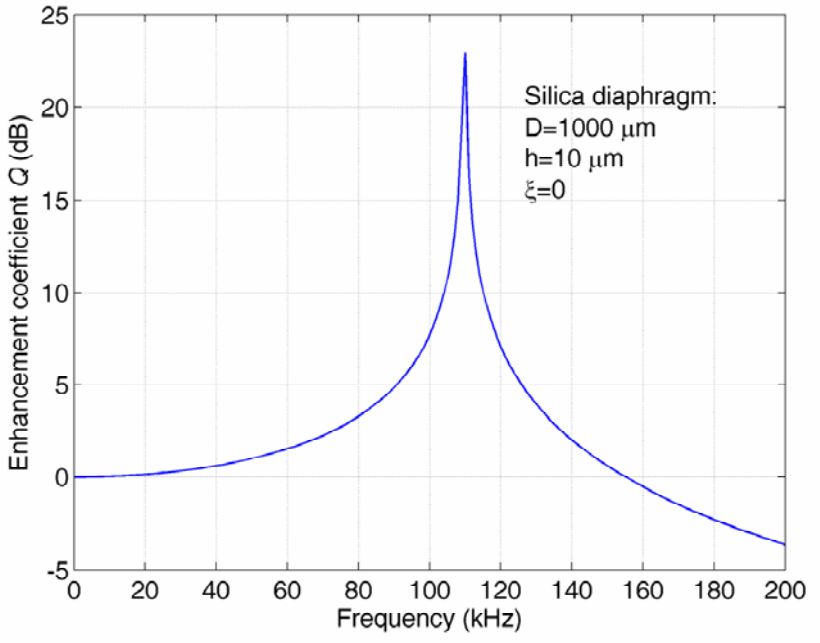

Figure 7.7 Frequency response of the enhancement factor at the fundamental vibration mode for a silica diaphragm.

It is shown that the resonant frequency is f_{00}=109.73 kHz. The enhancement curve shows a flat frequency response almost without an enhancement when the acoustic frequency is less than 40 kHz, and a strong resonance happens between 100-120 kHz frequency range, with a maximum enhancement factor as high as 200. These two frequency zones can be utilized for different applications:

1) If the pressure sensor works at a broadband detection, the diaphragm should be designed to ensure the resonant frequency of the fundamental vibration mode be 3 times of the detection frequency at least. Thus the deformation of the diaphragm is proportional to the applied acoustic pressure with a flat frequency response;
2) If the dynamic frequency is known or can be precisely controlled, the diaphragm can be designed to make the operation frequency coincide with the fundamental resonant frequency in order to gain a large enhancement. In this case, the sensor works at narrowband mode and the deformation of the diaphragm becomes

$$Y_{mn}(\omega_{mn}) = \frac{3(1-\mu^2)p}{16E}\frac{a^4}{h^3}\frac{\omega_{mn}}{2\xi}, \tag{7.25}$$

and enhancement coefficient becomes

$$Q_{mn} = \frac{\omega_{mn}}{2\xi} = \frac{\varphi_{mn}^2}{2\nu}\sqrt{\frac{\rho E}{3(1-\mu^2)}}\frac{h^2}{a^2}. \tag{7.26}$$

The final acoustic pressure sensitivity is

$$y_{mn}(\omega_{mn}) = Y_{mn}(\omega_{mn})/p = \frac{\varphi_{mn}^2}{32\nu}\sqrt{\frac{3\rho(1-\mu^2)}{16E}}\frac{a^2}{h}. \tag{7.27}$$

If the damping coefficient ν is a constant, the diaphragm properties result an inverse effect on the static pressure sensitivity and enhancement coefficient of the resonance. That is to say, if one selects diaphragm with smaller Young's modulus, larger diaphragm diameter and smaller thickness, the static pressure sensitivity is higher but the enhancement coefficient at the resonance is smaller.

Contradiction seems to appear. However, the combination effect of these two indicates that the final dynamic acoustic pressure sensitivity is still proportional to the square of diaphragm diameter, inversely proportional to the diaphragm thickness and square root of Young's modulus.

7.2.3 Signal demodulation method

For pressure detection, the deformation of the diaphragm induces the variation of the F-P cavity length, which results in the phase change of EFPI and the intensity at an individual wavelength also changes. In order to obtain the quantities of the deformation of the diaphragm, signal demodulation is necessary. There are generally two main demodulation methods for this kind of EFPI based pressure detection.

1) Spectrum phase trace method

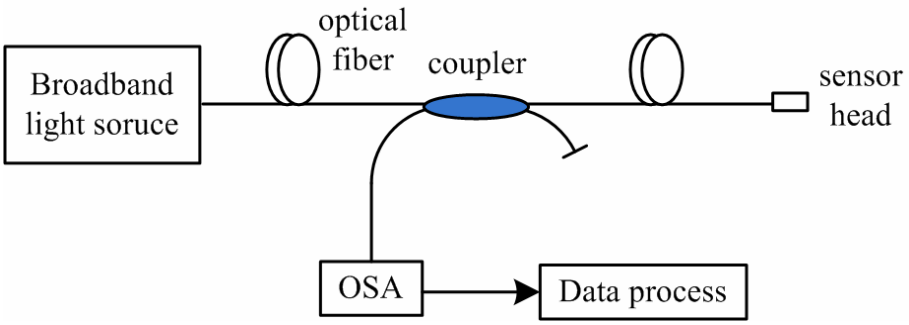

Figure 7.8 Scheme for spectrum phase trace demodulation method.

In this method, a broadband light source is coupled to the sensor, and the reflected light is coupled back to the optical spectrum analyzer (OSA) to monitor the spectrum of the light shown in Figure 7.8. As the diaphragm of the sensor is deformed by the pressure, a phase change will appear on the light spectrum as indicated in Figure 7.9. The diaphragm deformation can be calculated from

$$\Delta L = \frac{\lambda_{dip}}{2FSR}\Delta\lambda , \tag{7.28}$$

where λ_{dip} is the wavelength at the dip, $\Delta\lambda$ is the wavelength shift due to the

diaphragm deformation and FSR is the free spectral range.

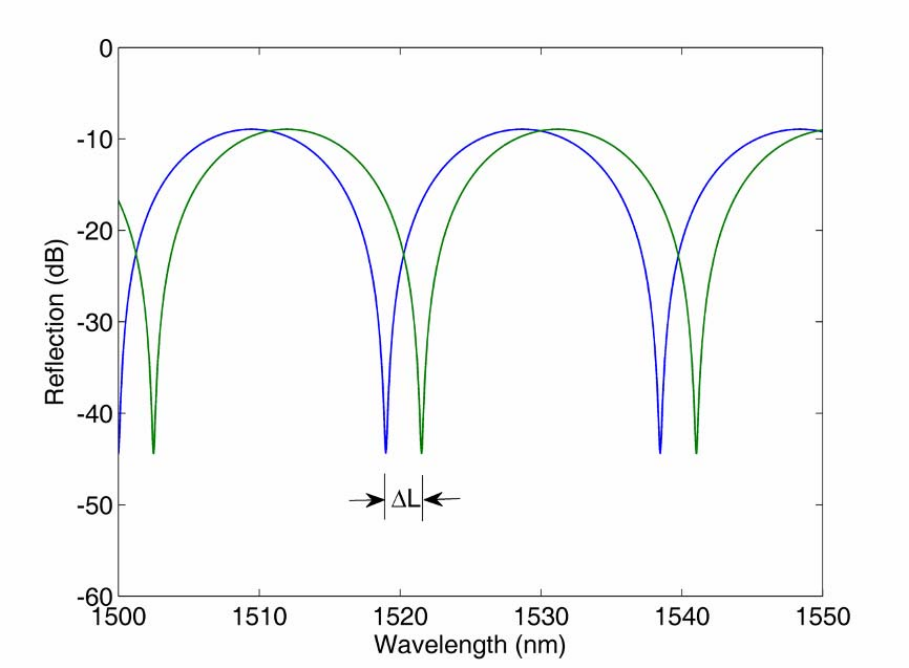

Figure 7.9 Spectrum shift of EFPI due to the deformation of diaphragm.

2) Interferometric intensity trace method

This method is especially efficient for dynamic acoustic pressure detection. When the periodic acoustic pressure applied to the diaphragm to cause it deformed periodically, the F-P cavity length shows a periodic variation. Therefore the reflection of EFPI in Eq. (7.7) is expressed as

$$R_e = a\left[1 - b\cos\left(\frac{4\pi}{\lambda}\left(L + \Delta L\sin(\omega t)\right)\right)\right], \tag{7.29}$$

where ω is the angular frequency of detected acoustic pressure. When the sensor is operated at different phase of interferometric fringe, the output signal is shown in Figure 7.10. When the demodulation is operated to ensure the phase variation within the linear range, the output signal shows a linear relationship with the cavity length variation as

$$R_e = a\left[1 - b\frac{4\pi}{\lambda}\Delta L\sin(\omega t)\right]. \tag{7.30}$$

In the nonlinear range, the sensitivity of the output signal is lower and the signal is distortion. The ideal condition for interferometric intensity demodulation is to fix the operation at the quadrature point (*Q*-point) as indicated in Figure 7.10 to ensure a maximum measurement sensitivity and range.

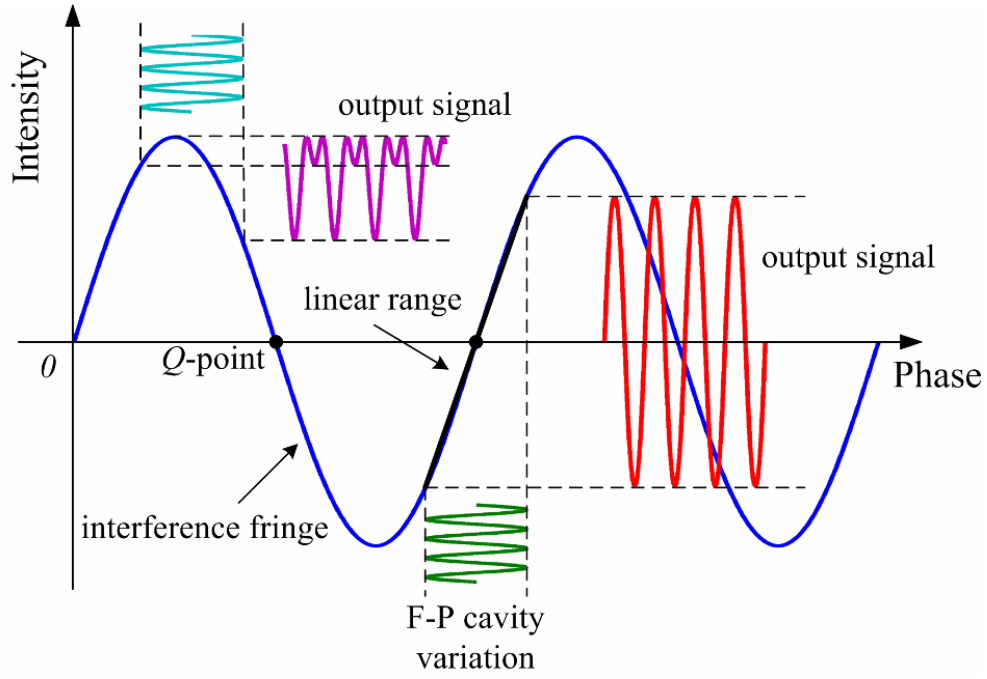

Figure 7.10 Interferometric intensity trace demodulation method with different operating point.

In this method, the maximum measurement range corresponds to a phase change no more than π/2. So the maximum detectable cavity length variation should satisfy the condition

$$\Delta L_{\max} \le \frac{\lambda_o}{8}, \tag{7.31}$$

where λ_o is the operating wavelength.

7.3 All-optical PAS gas detection based on EFPI

7.3.1 Sensing system

The principle for EFPI based gas detection is PAS. The gas detection process can be divided into three steps:

1) Light energy is absorbed by the sensing gas in the F-P cavity and generates a localized heat production via photoacoustic effect, which heats the gas in the cavity to induce a uniform pressure;
2) The laser wavelength is modulated to generate a periodic acoustic pressure wave. The acoustic pressure applied on the diaphragm to cause it deformed back and forth periodically;
3) The periodic deformation of diaphragm modulates the F-P cavity length. Thus the reflected light intensity of the EFPI is varied periodically, which can be measured to determine the gas concentration.

Therefore, the all-optical gas sensing system based on EFPI in our experiment is displayed in Figure 7.11. A distributed feedback (DFB) laser with wavelength tuned to the target absorption line of sensing gas and modulated at a frequency f acts as the excitation light source to be absorbed by the gas and generate the PA wave. Both of the detection light and excitation light are coupled to the sensor head through optical fiber via a coupler and a circulator. The sensor head is a diaphragm-based EFPI with a small cavity between the fiber end and the inner surface of diaphragm. Gas can diffuse into the cavity through a small hole in the ferrule. Periodic light absorption in this F-P cavity generates an acoustic pressure wave via photoacoustic effect. The acoustic pressure applied on the diaphragm to make it deformed periodically, which can be measured by monitoring the reflected light intensity of this EFPI. The optical intensity from the source laser is prevented by a tunable bandpass filter. The second

harmonic of the reflected intensity, which is proportional the acoustic pressure in the F-P cavity by properly selecting the operating point of the EFPI, is detected by a lock-in amplifier. The operating point of the EFPI is controlled by tuning the wavelength of the detection light via a computer to achieve optimal acoustic pressure sensitivity.

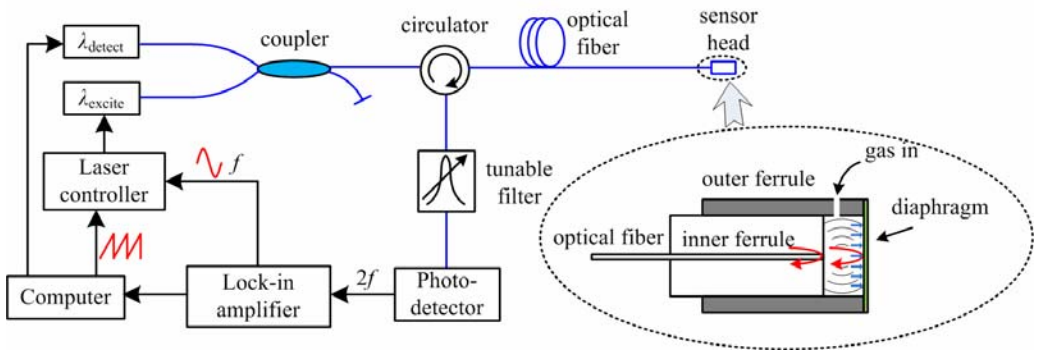

Figure 7.11 Diagram of the gas sensing system including the close-up figure for the sensor head. Blue lines show the optical path and black arrows depict the electrical path directions

7.3.2 Fabrication of sensor head

The most widely used material for fabricating the diaphragm of an EFPI pressure sensor is silica due to its favorable characteristics and easy bonding with optical fiber. It can be fabricated by wet-etching [13-16], direct cleaving and fusion splicing [17], or reactive ion etching the silicon substrate [18]. The thickness of a silica diaphragm is usually in the range of ~ μm. In order to improve the sensitivity of an EFPI based pressure sensor, two approaches are usually employed: reducing the diaphragm thickness or using diaphragm material with a lower Young's modulus. For the former case, typical representatives are nano-thick silver film [19, 20] or graphene diaphragm [21]. While for the latter case, polymer diaphragm with low Young's modulus can be used as the sensing element [22-25].

Considering the small Young's modulus and easy fabrication process, we select a polymer diaphragm as our sensing material of EFPI. The fabrication of the sensor head can be composed by the following three main steps:

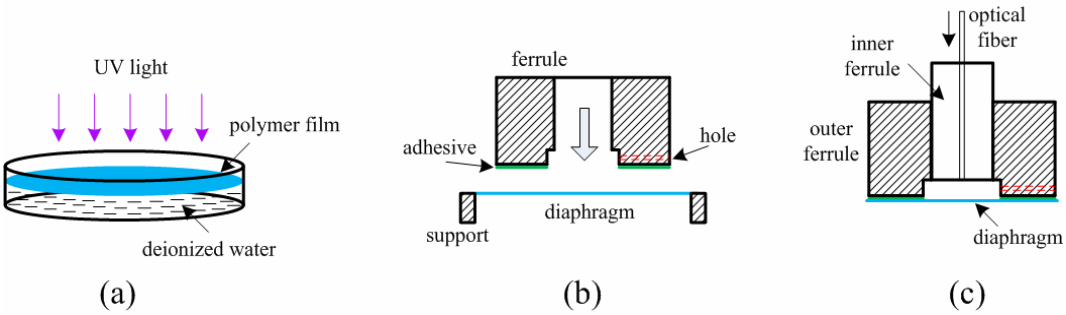

Figure 7.12 Fabrication process for the sensor head.

1) Fabricate the polymer diaphragm. The diaphragm is made of UV cured polymer film (NOA68, Norland Products) due to its small Young's modulus (E=0.138 GPa) and easy fabrication. A drop of polyimide (~4 mm^3) is dispensed into the deionized water in a Petri dish with a diameter of 10 cm [23, 24]. The polyimide floats on the surface of water and spreads out to form a thin film as shown in Figure 7.12 (a). By observing the coloration of the polymer film and controlling the spreading time, a thin polymer film with thickness down to μm or even nm can be obtained. Then an ultraviolet (UV) light shines the polyimide film to make it cured. The cured polyimide film is lifted up carefully from the water with a support and heated in an oven (set to 50 °C) to evaporate the residual water to make the film strong enough. The diameter of the dispensed film is about 5 cm, therefore the thickness of the diaphragm is estimated to be ~ 2 μm.

2) Prepare of ferrules and stick the diaphragm to the end of the outer ferrule. A plastic ferrule is fabricated with a shape as shown in Figure 7.12 (b). The inner diameter of the cavity is 2.5 mm and the front section of the cavity is a little bit wider (2.75 mm) to facilitate the gas diffusing into the cavity from the side opening. A thin layer of low-expansion adhesive is covered on the end of the

outer ferrule by spin coating. Then the ferrule slowly approaches the polymer diaphragm until in touch with it. The diaphragm will be adhered on the end of the ferrule as the sensing element.

3) Form the F-P cavity and fix the components of sensor head. After the diaphragm bonded on the end of the outer ferrule, a ceramic inner ferrule with outer diameter of 2.5 mm and inner diameter of 125 μm, a general optical fiber with end cleaved flat plug in, is moved into the outer ferrule step by step as shown in Figure 7.12 (c). Meanwhile, the reflected optical intensity is monitored by the system demonstrated in Figure 7.8 until an interferometric spectrum with good visibility appears in the OSA as shown in Figure 7.13. The FSR is ~ 6.9 nm and the length of the formed F-P cavity is calculated to be ~172 μm.

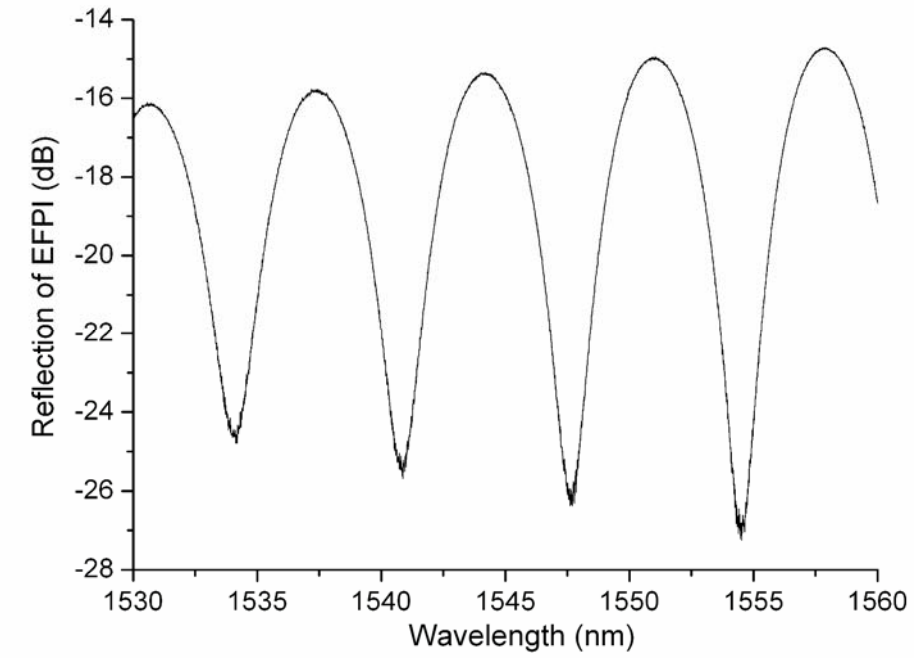

Figure 7.13 Reflection spectrum of the diaphragm-based EFPI.

7.3.3 Acoustic pressure response

To evaluate the acoustic pressure response of our sensor head, we built up a

measurement system as shown in Figure 7.14. A loudspeaker driven by a signal generator provides an acoustic wave that applies on the sensor head. Light from a tunable laser coupled to the sensor head to quantitate the amount of diaphragm deformation by the reflected light. A spectrum analyzer is used to determine the frequency distribution of the output signal.

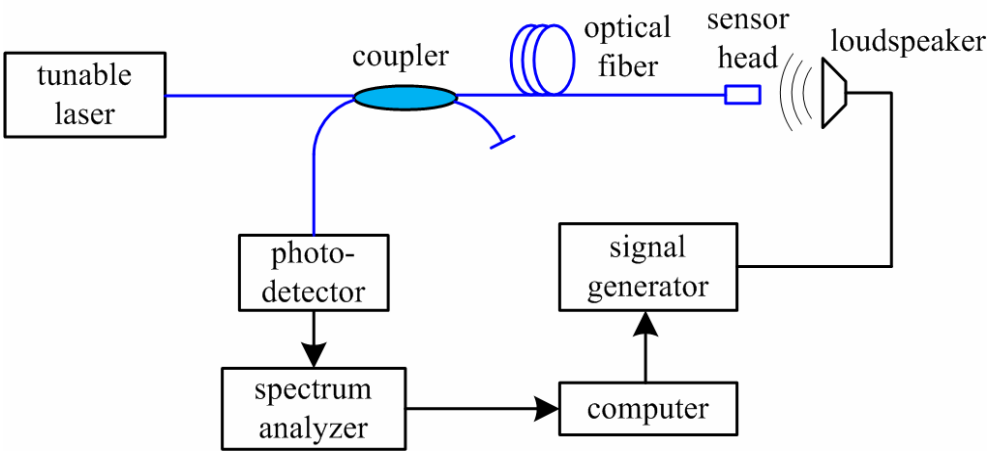

Figure 7.14 Schematic for the acoustic pressure response of diaphragm-based EFPI acoustic sensor.

The laser wavelength is tuned to the *Q*-point (1550.9 nm) of the EFPI as indicated in Figure 7.13. The voltage of the signal generaor is set to 1 V with frequency swept from 300 Hz to 9.5 kHz. The power spectral density (PSD) for an acoustic frequency of 2.75 kHz is shown in Figure 7.15. The signal-to-noise ratio (SNR) is estimated to be 48 dB between the peak power density and the average noise floor of the adjacent frequency. And the frequency corresponding to the peak PSD is equal to the frequency of acoustic pressure, indicting that only the first harmonic of the diaphragm deformation is effectively excited. For different acoustic frequency, the peak value of the power spectrum is plotted as shown in Figure 7.16. It is obvious that the diaphragm achieves a first order oscillation at around 754 Hz. And the acoustic sensor shows a relatively flat frequency response from 2.5 kHz to 6 kHz. The fluctuation of the frequency response curve might due to the unequal

acoustic generation effcient of loudspeaker for different frequency.

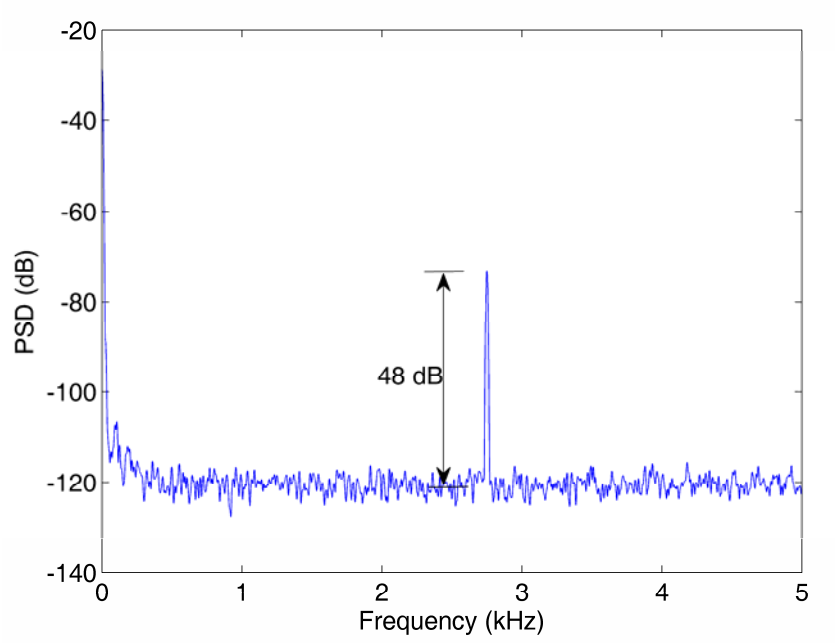

Figure 7.15 Power spectral density of the diaphragm-based EFPI acoustic sensor at frequency 2.75 kHz.

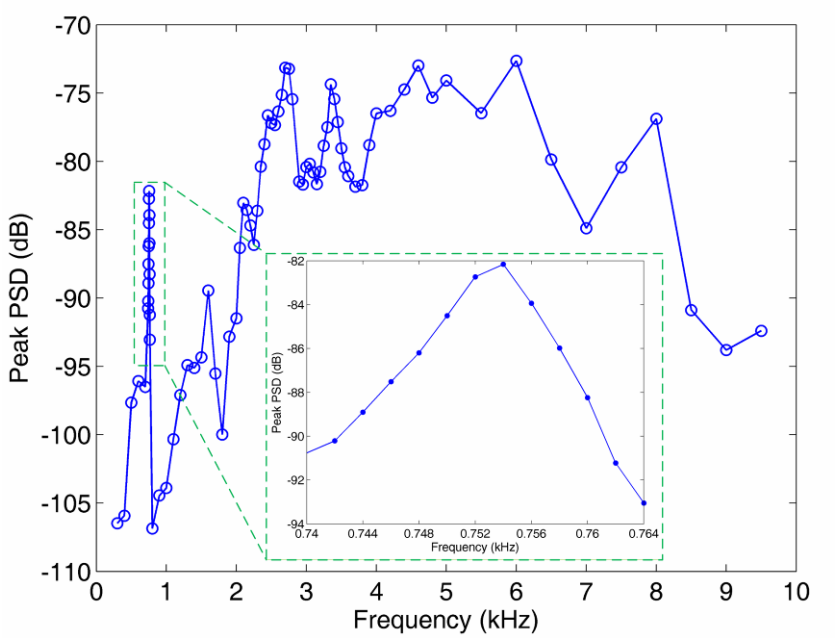

Figure 7.16 Peak PSD for different acoustic frequency with fixed acoustic amplitude.

With the acoustic frequency fixed at 2.75 kHz, the output signals of the EFPI demodulated at its first harmonic is measured with different acoustic pressure amplitude controlled by the driving voltage of loudspeaker. It reveals that the output signal is perfectly proportional to the acoustic pressure, indicating the stability and linearly operation at 1550.9 nm of our acoustic sensor. Because the absolute amplitude of the acoustic pressure is unable to be precisely measured in our laboratory currently, we can not be able to give a quantitative sensitivity of our acoustic sensor.

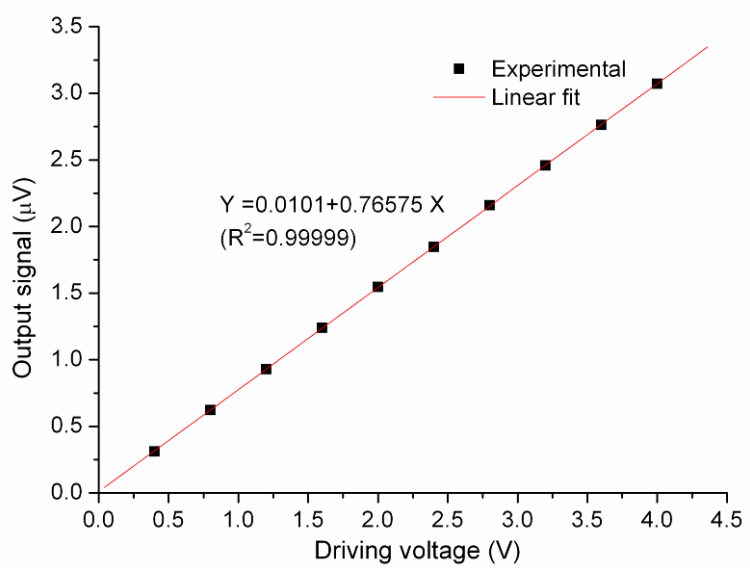

Figure 7.17 First harmonic signal of EFPI depended on the driving voltage of loudspeaker at 2.75 kHz.

7.3.4 All-optical gas detection

All-optical gas detection by using this kind of miniature pressure sensor is first proposed and experimentally carried out in this work. The acoustic generation and detection both happen in the small cavity of EFPI. The principle governing this approach is photoacoustic spectroscopy and diaphragm-based EFPI acoustic pressure response. The experiment setup has been demonstrated in section 7.3.1 already. The

sensing gas is acetylene with a concentration of 1%. The wavelength of the excitation laser is tuned to 1530.37 nm, corresponding to the P(9) absorption line of acetylene in the near-IR range. The absorption line strength is ~1.211×10^{-20} $cm^{-1}/(mol\ cm^{-2})$ [26]. The detection laser wavelength is tuned to 1556.1 nm, corresponding to the *Q*-point of EFPI interference fringe, with a laser power of 4 mW. The experiment is carried out at atmospheric pressure and room temperature. The excitation laser power used in the PAS absorption is 8 mW. The modulation frequency is set to be 200 Hz with a modulation current of 30 mA, and the time constant is 10 s with a filter slope 18 dB/octave.

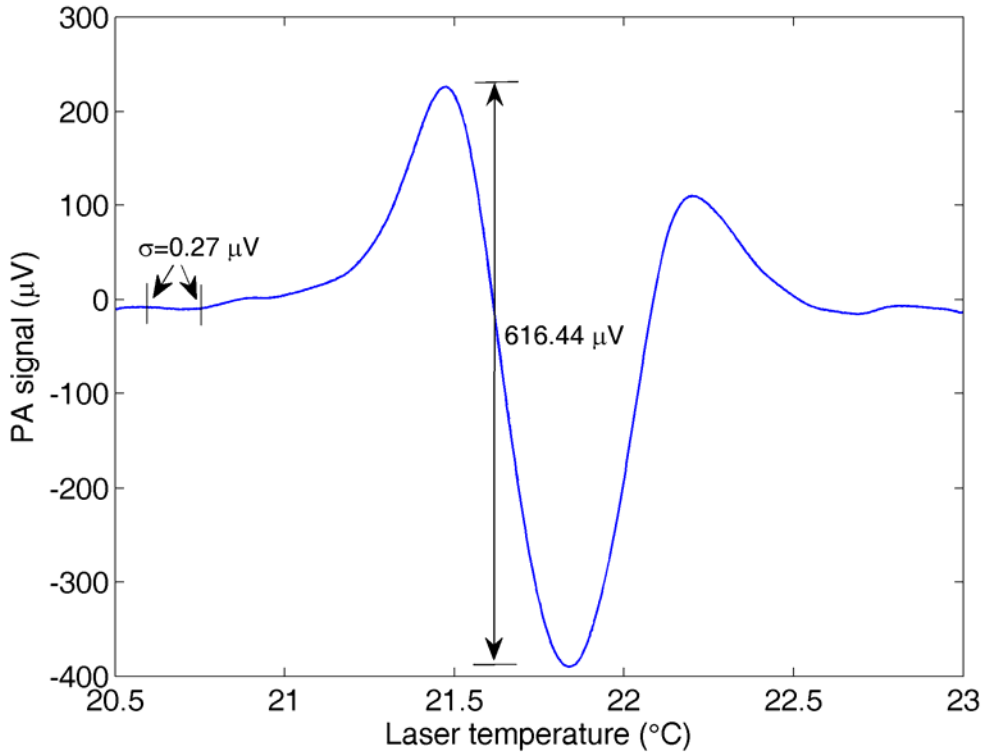

Figure 7.18 PA signal with laser temperature tuned around the center of the target absorption line.

The detected 2*f* PA signal from reflection of EFPI is plotted as in Figure 7.18 with source laser wavelength tuned across the absorption line by controlling the laser

temperature. The maximum acoustic signal appears at laser temperature of ~ 21.8 °C, and the peak-to-peak value of the signal is measured to be 616.44 μV. The noise is estimated to be the standard deviation of the PA signal in the off-line non-absorption spectral region as depicted in Figure 7.18. Thus a SNR of 2,314 is obtained, indicating a detectable concentration limit of 4.3 ppmv for acetylene by our all-optical sensing system. The sensitivity could be further enhanced by using larger laser power, better assembling the sensor head, optimizing the diaphragm and suppressing the effect of light intensity variation induced diaphragm deformation. The signal demodulation method could be improved to stabilize the EFPI operation point, which is significantly important in harsh environment measurement.

PA generation by non-acoustic-resonance within a closed cell is first demonstrated in experiment, and the sensitivity of this all-optical gas sensing system is found to be comparable with most of the PA gas detection method based on space coupled acoustic resonance cell and separated electrical [1-5] or optical [6-8] acoustic detection techniques. In addition, it is found possible for acoustic generation and detection in an identical cell for the first time to the best of our knowledge. This promises a useful application for small space (in mm scale) gas detection. Moreover, the all-optical measurement system shows significant advantages over other PA methods on remote and multiplex gas detection.

7.4 Summary

In this chapter, an all-optical PAS gas detection approach is first proposed by using a miniature diaphragm-based EFPI. The brief principle of FPI and acoustic response of diaphragm is introduced. A polymer film with low Young's modulus is employed as the sensing diaphragm with an effect diameter of 2.75 mm and thickness of ~2 μm. PAS gas detection with this polymer-diaphragm-based EFPI demonstrated a minimum detectable acetylene concentration of 4.3 ppmv, with potential

enhancement means suggested. This kind of all-optical gas sensor might find applications in small space gas detection and multiplex gas sensing areas.

References of Chapter 7

1. L. Hao, J. Han, Q. Shi, J. Zhang, J. Zheng, and Q. Zhu, "A highly sensitive photoacoustic spectrometer for near infrared overtone," *Rev. Sci. Instrum.* 71, 1975-1980 (2000).
2. M. E. Webber, M. Pushkarsky, and C. K. N. Patel, "Fiber-amplifier-enhanced photoacoustic spectroscopy with near-infrared tunable diode lasers," *Appl. Opt.* 42, 2119-2126 (2003).
3. S. Schilt, A. Vicet, R. Werner, M. Mattiello, L. Thevenaz, A. Salhi, Y. Rouillard, and J. Koeth, "Application of antimonide diode lasers in photoacoustic spectroscopy," *Spectrochim. Acta Part A* 60, 3431-3436 (2004).
4. A. A. Kosterev, Y. A. Bakhirkin, R. F. Curl, and F. K. Tittel, "Quartz-enhanced photoacoustic spectroscopy," *Opt. Lett.* 27, 1902-1904 (2002).
5. A. A. Kosterev, F. K. Tittel, D. V. Serebryakov, A. L. Malinovsky, and I. V. Morozov, "Applications of quartz tuning forks in spectroscopic gas sensing," *Rev. Sci. Instrum.* 76, 043105 (2005).
6. K. Wilcken and J. Kauppinen, "Optimization microphone for photoacoustic spectroscopy," *Appl. Spectroscopy* 57, 1087-1092 (2003).
7. V. Koskinen, J. Fonsen, K. Roth, and J. Kauppinen, "Progress in cantilever enhanced photoacoustic spectroscopy," *Vib. Spectrosc.* 48, 16-21 (2008).
8. Q. Wang, J. Wang, L. Li, and Q. Yu, "An all-optical photoacoustic spectrometer for trace gas detection," *Sens. Actuators B* 153, 214-218 (2011).
9. S. G. Lipson, H. Lipson, and D. S. Tannhauser, *Optical Physics*, 3rd ed. (Cambridge U. Press, London, pp. 248, 1995).

10. M. di Giovanni, *Flat and Corrugated Diaphragm Design Handbook*, (Marcel Dekker, New York, 1982).
11. A. Rossetti, R. Codeluppi, A. Golfarelli, M. Zagnoni, A. Talamelli, and M. Tartagni, "Design and characterization of polymeric pressure sensors for wireless wind sail monitoring," *Sens. and Actuators A* 167, 162-170 (2011).
12. J. Xu, *Fiber-optic sensor systems for acoustic measurements*, Ph.D. Thesis, (Virginia Polytechnic Institute and State University, 2005).
13. D. Donlagic and E. Cibula, "All-fiber high-sensitivity pressure sensor with SiO_2 diaphragm," *Opt. Lett.* 30, 2071-2073 (2005).
14. E. Cibula, S. Pevec, B. Lenardic, E. Pinet, and D. Donlagic, "Miniature all-glass robust pressure sensor," *Opt. Express* 17, 5098-5106 (2009).
15. Y. Zhu, K. L. Cooper, G. R. Pickrell, and A. Wang, "High-temperature fiber-tip pressure sensor," *J. Lightwave Technol.* 24, 861- 869 (2006).
16. J. Xu, X. Wang, K. L. Cooper, and A. Wang, "Miniature all-silica fiber optic pressure and acoustic sensors," *Opt. Lett.* 30, 3269-3271 (2005).
17. X. Wang, J. Xu, Y. Zhu, K. L. Cooper, and A. Wang, "All-fused-silica miniature optical fiber tip pressure sensor," *Opt. Lett.* 31, 885-887 (2006).
18. W. Wang, N. Wu, Y. Tian, C. Niezrecki, and X. Wang, "Miniature all-silica optical fiber pressure sensor with an ultrathin uniform diaphragm," *Opt. Express* 18, 9006-9014 (2010).
19. F. Xu, D. Ren, X. Shi, C. Li, W. Lu, L. Lu, L. Lu, and B. Yu, "High-sensitivity Fabry-Perot interferometric pressure sensor based on a nanothick silver diaphragm," *Opt. Lett.* 37, 133-135 (2012).
20. F. Guo, T. Fink, M. Han, L. Koester, J. Turner, and J. Huang, "High-sensitivity, high-frequency extrinsic Fabry-Perot interferometric fiber-tip sensor based on a thin silver diaphragm," *Opt. Lett.* 37, 1505-1507 (2012).
21. J. Ma, W. Jin, H. L. Ho, and J. Y. Dai, "High-sensitivity fiber-tip pressure

sensor with graphene diaphragm," *Opt. Lett.* 37, 2493-2495 (2012).

22. E. Cibula and D. Đonlagic, "Miniature fiber-optic pressure sensor with a polymer diaphragm," *Appl. Opt.* 44, 2736-2744 (2005).
23. S. Nesson, M. Yu, and X. Zhang, "Miniature fiber optic pressure sensor with composite polymer-metal diaphragm for intradiscal pressure measurements," *J. Biomed Opt.* 13, 044040 (2008).
24. H. Bae, X. M. Zhang, H. Liu, and M. Yu, "Miniature surface-mountable Fabry-Perot pressure sensor constructed with a 45° angled fiber," *Opt. Lett.* 35, 1701-1703 (2010).
25. Q. Wang and Q. Yu, "Polymer diaphragm based sensitive fiber optic Fabry-Perot acoustic sensor," *Chin. Opt. Lett.* 8, 266-269 (2010).
26. L. S. Rothman, I. E. Gordon, A. Barbe, D. C. Benner, P. F. Bernath, M. Birk, V. Boudon, L. R. Brown, A. Campargue, J.-P. Champion, K. Chance, L. H. Coudert, V. Dana, V. M. Devi, S. Fally, J.-M. Flaud, R. R. Gamache, A. Goldman, D. Jacquemart, I. Kleiner, N. Lacome, W. Lafferty, J.-Y. Mandin, S. T. Massie, S. N. Mikhailenko, C. E. Miller, N. Moazzen-Ahmadi, O. V. Naumenko, A. V. Nikitin, J. Orphal, V. I. Perevalov, A. Perrin, A. Predoi-Cross, C. P. Rinsland, M. Rotger, M. Simeckova, M. A. H. Smith, K. Sung, S. A. Tashkun, J. Tennyson, R. A. Toth, A. C. Vandaele, J. V. Auwera, "The HITRAN 2008 molecular spectroscopic database," *J. Quant. Spectrosc. Radiat. Transf.* 110, 533-572 (2009).

Chapter 8

Conclusion and future work

8.1 Conclusion

In this thesis, we have investigated the gas sensing techniques based on photoacoustic spectroscopy, mainly the quartz-enhanced photoacoustic spectroscopy (QEPAS) and its association with fiber-optic devices. Four main contributions are addressed in this thesis as: (1) numerically optimizing of the spectrophone parameters of QEPAS by simulating the multi-physical processes in the spectrophone; (2) experimentally investigating on the combined effect of wavelength modulation and residual intensity modulation in QEPAS; (3) proposing quartz-enhanced evanescent-wave photoacoustic spectroscopy method for gas detection; and (4) investigating all-optical gas detection based on photoacoustic spectroscopy by using a diaphragm-type EFPI.

After introducing PAS and acoustic detection based on a quartz tuning fork (QTF) in detail, we developed a numerical multi-physical model to investigate the acoustic coupling and enhancement in the QEPAS spectrophone based on finite element method. The numerical model was introduced in detail to set up the connection between the acoustic resonance and the piezoelectric properties of the QTF. The dependence of acoustic signal on the spectrophone dimension is simulated. It is found that the dimension of the tubes of micro-resonator and the gap between them greatly affects the acoustic coupling efficiency in the resonator. And the vibration of the QTF also interacts with the acoustic wave and results in its new

distribution and resonance. Finally, a set of parameters for the optimized performance of the spectrophone are suggested.

A complete experimental investigation of QEPAS gas detection method was carried out. By considering the effect of residual intensity modulation for a real semiconductor laser, we quantitatively studied the principle of wavelength modulation method with second harmonic detection. The experimental results agree well with theoretical prediction, which provides a useful guidance for modulation and demodulation parameters selection. The minimum detectable gas concentration is estimated to be 2 ppmv for acetylene with a DFB laser power of 8.44 mW. In addition, we developed some efficient methods in laboratorial PAS gas sensing investigation, including fiber-optic interferometric method for the determination of laser modulation information, gas concentration calibrating method in gas filling process, etc.

We proposed a novel evanescent-wave photoacoustic spectroscopy method for gas detection with a tapered OMNF. It is demonstrated that the evanescent field of an OMNF can be used for light absorption in target gas to generate photoacoustic pressure wave. Associated with a QTF-based acoustic detection approach, we successfully achieved a detectable C_2H_2 concentration limit of 178 ppmv by using this novel EPAS method with a 1.1-μm-diameter tapered optical fiber, corresponding to a normalized noise equivalent absorption coefficient of 1.5×10^{-6} cm^{-1} $W/Hz^{1/2}$ at atmospheric pressure. Possible improvement methods, including thinner fiber, larger laser power, additional resonate method, or other high sensitive detection method, were also suggested. The compact size, well optical confinement property, free tailored mode field, easy access to the fiber network of OMNFs promise a bright future for this novel method.

Inspired by all-optical acoustic detection method based on EFPI, we developed an all-optical approach for photoacoustic spectroscopy gas detection by using a

miniature diaphragm-based EFPI. We creatively propose the idea of integrating the acoustic generation and detection simultaneously in a compact FPI cavity. By fabricating a μm-scale-thick polymer film and using it as the sensing diaphragm of EFPI, we achieve a minimum detectable gas concentration of 4.3 ppmv for acetylene from the output demodulation signal by using an 8-mW near-IR DFB laser. Possible means to improve the sensitivity was suggested. This method possesses the advantages of high sensitivity of PAS and all-optical properties of fiber-optic devices, and might find important applications in small-space gas detection and remote or multiplex gas sensing areas.

8.2 Future work

PAS provides a versatile approach for trace gas detection, which has achieved great development in the past decade. The numerical simulation and experimental demonstration in this thesis supply a useful guidance for the better understanding of the physical process in PAS and optimal selecting of spectrophone dimensions and modulation parameters. The optical micro/nano fiber based evanescent-wave photoacoustic spectroscopy method and diaphragm-based EFPI all-optical gas detection approach demonstrate novel realization means of PAS in all-optical fiber-based communication systems. The future work can be suggested as follows:

1) Investigation on the molecular relaxation effect in the PAS gas detection. In most cases, the molecular relaxation from the excited ro-vibrational state to sample heating may be regarded as instaneous due to the much faster process of it compared with the laser modulation period. Thus there is no consequence on the PA signal. However, in some particular gas mixture, such as H_2O and CO_2, the relatively longer relaxation time can strongly influence the PA generation. Further more, for a high frequency modulation as in QEPAS, the molecular relaxation also becomes unneglectable. The investigation of molecular relaxation may help understanding the

physical process in PAS and improving the gas sensing efficiency;

2) Enhancement of the acoustic signal and finding more sensitive acoustic detection technique in evanescent-wave PAS. By reducing the fiber diameter, we can effectively increase the optical power in the evanescent field. With an additional acoustic resonator as in conventional PAS, the acoustic signal could be further enhanced. Replacing the QTF-based acoustic detection, an alternative fiber-optic acoustic detection technique, such as interferometric method, will be explored to improve the gas sensing ability of the system;

3) Optimizing the diaphragm-based EFPI all-optical PAS gas sensing method. The sensitivity of the gas sensing is directly related to the dimension and quality of diaphragm. By improving the diaphragm fabrication quality, advancing the sensor head assembling and packaging technique, optimizing the diaphragm dimension, the gas detection sensitivity could be considerably enhanced. Considering the influence from environment, the stabilizing of the operation point of the FPI in signal demodulation is necessary and important, which could be realized either by enhancing the mechanical properties of the diaphragm, for instance, coating a thin metal layer on the surface of the diaphragm to reduce the random vibration of it in detection environment, or by introducing a feedback circuit to monitor the phase variation of the interferometer and instaneously tune the detection wavlength accordingly. The modification of the F-P cavity based gas cell structure might also influence the sensitivity of the system;

4) Developing the all-optical multi-component and multiplexing gas sensing system. Considering the advantages of our all-optical gas sensing methods, evanescent-wave PAS and diaphragm-type EFPI based PAS, in fiber-optic network, we will explore the capability of our sensing system for multi-component and multiplexing gas sensing. This technique will be important in remote multi-point simultaneous gas monitoring and multiple species gas detection.